THE UNIVERSITY
of EDINBURGH

Investigating miR-214 as a pro-fibrotic mediator in renal fibrosis and its potential as a therapeutic target via effective *in vivo* modelling of chronic kidney disease

James O'Sullivan

BSc. (Hons)

Submitted in fulfilment of the requirements of the degree of Doctor of Philosophy in the College of Medicine and Veterinary Medicine, University of Edinburgh

Centre for Cardiovascular Sciences, The Queen's Medical Research Institute, College of Medicine and Veterinary Medicine, University of Edinburgh

September 2019

Author's Declaration

I declare that this thesis was wrote entirely by myself and is composed of work carried out by myself, with the following exceptions. The work presented in this thesis has not been submitted for any other degree or professional qualification. For the purposes of my training, the majority of STNx surgeries for the chapter 4 study were carried out by Dr. Laura Denby. Sarah Finnie, Andrew Boyd, and Dr. Laura Denby assisted with the cull of animals in studies presented in chapters 3 and 4. Echocardiography imaging (chapter 4) was carried out by preclinical imaging technician Adrian Thompson (analysis of echocardiograph was carried out by myself). Biochemical analysis of serum and urine for albumin, creatinine, urea, and phosphate was carried out by Howie Forbes in the QMRI specialist biochemical analysis service. rUUO (chapter 5) surgeries were carried out by Gary Borthwick and Dr. Laura Denby, with Dr. Laura Denby carrying out sham and UUO group surgeries, while Gary Borthwick carried out the rUUO group surgeries. In the bulk rUUO RNA sequencing, RNA was extracted from whole kidney cortex, yield quantified via NanoDrop and quality assessed via Aglient Bioanalyser by Dr. Laura Denby and Carolynn Cairns. In relation to the RNA sequencing of FACS-isolated renal cell populations (chapter 5), the protocol for preparing renal tissue for FACS, the use of the flow cytometer, RNA extraction, RNA quality and yield assessment via Aglient Bioanalyser, and amplified cDNA synthesis was carried out by Dr. Laura Denby and Carolynn Cairns. For RNA sequencing (chapter 5), library preparation, sequencing of libraries and quality control was carried out by Genewiz. IRI (chapter 5) and FACS process was carried out by Dr. Victoria Banwell, with RNA extraction carried out by myself and Dr. Victoria Banwell.

James O'Sullivan
September 2019

Acknowledgements

To my supervisor, Dr. Laura Denby, thank you for giving me the opportunity to learn and grow as a scientist over these four years. The advice and guidance you gave, as well as the space to explore my own ideas and interests, has allowed me to get to where I am today. Thank you to Prof. Andy Baker and Dr. Bryan Conway for the invaluable contributions and collaborations.

For providing the funding that allowed me to do a PhD in the first place, I owe a debt of gratitude to Medical Research Scotland. I thank Regulus Therapeutics for generously co-sponsoring my PhD and for inviting me to a three-month placement in their lab, which was a great experience.

Thank you to the other PhD students and staff who made the QMRI a bit more fun. Particularly to Rachel for the long coffee-breaks, to Andrew for the random chats in the lab, and to Francesca for sharing my office-related woes!

Many members of my large family have, in some way, helped me get to the point where I'm finishing writing a PhD thesis, but a few in particular stand out.

Thank you to my parents, who supported the earlier stages of this lengthy education of mine. During a recession was a pretty inconvenient time to go to college in Dublin, but we made it work. Thanks to Chloe and Conor, for always being there. Thank you to my Nanny O'Sullivan, for always, always, being there. To my Ada Wickham, thank you for telling me all the stories, teaching me so much about the world from a young age, and, of course, for bringing me to check the buoys. I owe a lot of the curiosity that drove me towards science to you.

Non scholæ, sed vitæ discimus.

Table of Contents

List of Figures

List of Tables

Abstract

Chronic kidney disease (CKD) is a prevalent health condition in the UK and worldwide. CKD is defined as the progressive decline of renal filtrative capacity over time. High rates of cardiovascular dysfunction and related mortality are observed in patients with CKD. Renal fibrosis is the final common pathway though which all CKD, regardless of the initiating insult. Renal fibrosis, defined as excess collagenous matrix deposition that restricts renal filtrative capacity, is a complex process involving multiple cell types, biological pathways, cytokines and other pro-fibrotic factors such as microRNAs (miRNAs).

miRNAs are small non-coding RNA which post-transcriptionally regulate gene expression via inhibition of target mRNA translation. MicroRNA-214-3p (miR-214) has been proposed to be a key pro-fibrotic miRNA in renal fibrosis. Increased miR-214 expression is found in CKD patient urine and kidney biopsies, correlating with degree of fibrosis, mirroring the increase observed in several *in vitro* and *in vivo* models. Knockdown of miR-214 expression in the unilateral ureteral obstruction (UUO) model of renal fibrosis resulted in an 86% reduction in fibrosis, although the mechanism behind this remained largely unknown. Therefore, the hypothesis presented in this thesis is that miR-214 functions as a pro-fibrotic miRNA in renal fibrosis and effective *in vivo* modelling will allow for the investigation of its mechanism and assessment of its potential as a therapeutic target in progressive chronic kidney disease.

The aims of this thesis are as follows. Firstly, to profile the refined mouse subtotal nephrectomy (STNx) model as a progressive model of CKD. Secondly, to evaluate an anti-miR-214 compound *in vitro*. Thirdly, to assess the therapeutic potential of anti-miR-214 as an intervention in STNx. Fourthly, to profile the miRNA and gene expression changes observed in individual renal cell populations in UUO and reversible UUO (rUUO). Lastly, to use the generated data to explore potential pro-fibrotic mechanisms of miR-214 in renal fibrosis on a cell-population specific basis.

Subtotal nephrectomy is an *in vivo* model of CKD, which, unlike UUO, allows for the measurement of clinically-relevant renal functional parameters, produces glomerulosclerosis and cardiovascular dysfunction, and has a history of successful translation of findings to clinical practice. The refined subtotal nephrectomy (STNx) 10-week model presented here attempts to overcome downsides in the traditional model; performed as a single-surgery with improved survival, animal welfare and consistent outcomes. The STNx model was fully characterised and then used to assess the effects of miR-214 inhibition (via anti-miR) in this more translatable model of CKD. The anti-miR-214 compound, provided by Regulus Therapeutics, was first assessed *in vitro*, where its affinity for miR-214 was found to be high and a reduction in pro-fibrotic gene expression was observed in TGFβ-stimulated renal fibroblasts.

Intervention with anti-miR-214 in STNx was initiated at 6-weeks post-STNx to assess anti-miR-214 efficacy in a situation where renal fibrosis and dysfunction were already present, as diagnosis and therapeutic intervention in CKD usually do not occur until renal fibrosis and dysfunction are already present. Here, anti-miR-214 intervention did not produce any significant changes across a number of renal and cardiovascular parameters measured compared to control anti-miR. Lack of efficacy may have been due to the timing of the intervention, lack of anti-miR penetration to the appropriate cell types, or lack of efficacy of anti-miR-214 in STNx in general.

As miR-214 is known to have diverse and even opposing roles in different cell types and pathologies, elucidating the expression of miR-214 in renal cell types may be critical to understanding its mechanisms in renal fibrosis. In order to address this, the expression of miR-214 was examined in a cell specific and temporal manner using the reversible UUO (rUUO) experimental model. This allowed for analysis of renal injury and resolution of renal injury. From the rUUO model, 4 cell populations known to play a role in renal fibrosis and injury resolution were FACS sorted and underwent RNA sequencing for miRNA and gene expression. miR-214 was found to be significantly enriched in Pdgfrβ^{+} (myofibroblast-like) cells in the kidney in comparison

to proximal tubular epithelial cells, endothelial cells and tissue-resident macrophages, indicating myofibroblasts are the primary site of mechanistic interest. Bioinformatic analysis revealed several predicted miR-214 targets in Pdgfrβ^{+} cells, indicating miR-214 may act as an anti-apoptotic and/or pro-proliferative factor in these cells in the context of renal fibrosis.

In conclusion, the development and profiling of STNx provided a valuable platform for the assessment of anti-miR-214 as a therapeutic intervention in CKD, allowing the measurement of a variety of clinically-relevant parameters including renal fibrosis. Anti-miR-214, despite displaying efficacy *in vitro*, did not ameliorate any renal or cardiovascular phenotypes induced by STNx. Four cell populations relevant to renal fibrosis were sorted from rUUO kidneys and RNA-sequencing carried out to discover the gene and miRNA expression profiles in these cell types in renal injury and injury resolution. miR-214 was found to be significantly enriched in Pdgfrβ^{+} (myofibroblast-like) cells. Bioinformatic analysis of miR-214 targets in this cell population suggests miR-214 may have an anti-apoptotic and/or pro-proliferative role.

Lay Summary

Chronic kidney disease (CKD) is a serious and prevalent health condition globally, estimated to affect between 8 and 16% of the adult population. As the risk of developing CKD rises with age, CKD is expected to become more prevalent in wealthy countries as the population ages in the coming years. Globally, in 2015, 1.2 million deaths from kidney failure occurred, a 35% increase since 2005. Therefore, new and more effective treatments for CKD are needed. In CKD, the ability of the kidneys to filter the blood progressively declines over time. CKD is typically only diagnosed when a significant decline in renal function has already occurred. Eventually, kidney function becomes so poor that renal replacement therapy (such as dialysis or transplantation) is required restore the body's ability to filter the blood. Importantly, CKD patients are at higher risk of cardiovascular disease and this is the leading cause of death in these patients.

There are many underlying conditions that can trigger CKD, such as diabetes and hypertension (high blood pressure). In CKD, as the kidney is damaged, the kidney tries to repair the damage by producing a scar. This scarring known as fibrosis, which develops progressively as renal function declines. Therefore, halting or reversing the build-up of renal fibrosis may be an effective way to control the progression of CKD.

In order to study kidney dysfunction and how this scarring of the kidney occurs, animal models are used to recapitulate the disease as accurately as possible. Typically, kidney dysfunction is triggered in these animals (often mice or rats) through surgical methods. These animal models can be used to discover new genes or other molecules that are associated with kidney dysfunction.

MicroRNAs (miRNAs) are molecular mediators of a wide-variety of biological processes. In animal models of kidney dysfunction, the amount of fibrosis in the kidney was found to correlate with the level of miRNA-214 (miR-214) in the kidney.

This correlation was found to also be present in CKD patients. When miR-214 was blocked in an animal model of kidney dysfunction using a drug, 87% less fibrosis was found in the kidneys of these mice. Therefore, this thesis aimed to uncover how blocking miR-214 resulted in less fibrosis, and further evaluate if blocking miR-214 could be an effective treatment for CKD patients.

A variety of animal models exist in relation to kidney disease, each with advantages and disadvantages for their use. The most common model is unilateral ureteral obstruction (UUO), a fast and reliable model which requires relatively little surgical skill. This was the model in which blocking miR-214 with a drug was initially found to result in 87% less kidney fibrosis. However, although popular, the UUO model does not recapitulate CKD as fully as other models. UUO does not allow for the assessment of kidney function though urine and blood measurements, which are critically important measurements which doctors use to assess and manage CKD patients. Additionally, cardiovascular disease does not occur in UUO. As it is important to investigate how/if a new drug to treat CKD influences these factors, this thesis sought to investigate a drug which blocks miR-214 in an animal model which recapitulates these aspects of CKD.

Subtotal nephrectomy is a model of CKD typically performed in rats or mice. This model allows the measurement of kidney function through analysis of the urine and blood from these animals. Cardiovascular disease also develops in these animals. Subtotal nephrectomy was used in the development of ACE inhibitors, a very commonly used family of drugs in the treatment of CKD. However, a large portion of animals subjected to this procedure die before the study is intended to end (up to ~50%). Therefore, in this thesis, surgical methods used to produce subtotal nephrectomy were adapted from traditional methods in an attempt to increase the survival and welfare of these animals, while still modelling CKD effectively. The resulting model was referred to as STNx and <8% of mice subjected to this model died

as a result of the procedure. STNx was found to successfully model CKD, with kidney fibrosis, kidney dysfunction and cardiovascular disease.

The STNx model was then used to test a drug which blocked miR-214 in the kidney when kidney dysfunction typical of patients when diagnosed was present, e.g. protein in the urine. However, this drug did not decrease kidney fibrosis, improve kidney function, or prevent cardiovascular disease. These results suggest that blocking miR-214 may not be an effective treatment for CKD when the disease is established, but more research is needed to confirm this. In addition, further research into miR-214, uncovering where in the kidney it is present, was carried out to understand why miR-214 levels increase in response to kidney fibrosis.

List of Abbreviations

2'-OMe	2’-O Methyl
3’UTR	3 prime untranslated region
αSMA	Alpha-smooth muscle actin
AAC	Abdominal aorta constriction
ACE	Angiotensin converting enzyme
ACR	Albumin:creatinine ratio
Acta2	Actin alpha 2, smooth muscle
ADMSC	Adipose-derived mesenchymal stem cell
AGE	Advanced glycation end product
Ago	Argonaute
Ahdc1	AT hook, DNA binding motif, containing 1
AKI	Acute kidney injury
AKT	AKT Serine/Threonine Kinase
ARRIVE	Animal Research: Reporting of In Vivo Experiments
ATCC	American Type Culture Collection
ATF4	Activating transcription factor 4
ATG12	Autophagy Related 12
ATG5	Autophagy Related 5
ATP	Adenosine triphosphate
Atxn1l	Ataxin 1 like
Baz2a	Bromodomain adjacent to zinc finger domain 2A
BC	Body condition score
Bcl2	B cell leukemia/lymphoma 2
BIM1	Bcl-2 interacting mediator of cell death
BMM	Bone-marrow monocyte
BMSC	Bone-marrow mesenchymal stem cell
CAD	Coronary artery disease
CD	Collecting duct
CD31	Cluster of differentiation 31
CD45	Cluster of differentiation 45
CD73	Cluster of differentiation 73
cDNA	Complimentary DNA
cET	Constrained ethyl
circRNA	Circular RNA
CKD	Chronic Kidney Disease
CKD-EPI	Chronic Kidney Disease Epidemiology Collaboration
CKD-MBD	CKD-Mineral Bone Disorder
cKO-214	Conditional knockout of miR-214 in the proximal tubules
CM	Cardiomyocyte
Co-SMAD	Common medator SMAD

Col1a1	Collagen type I alpha 1 chain
Col3a1	Collagen type 3 alpha 1 chain
Col4a1	Collagen type 4 alpha 1 chain
COX-2	Cyclooxygenase-2
CPM	Counts per million reads
CPT1	Palmitoyltransferase 1
CRS	Cardiorenal syndrome
CSF1	Colony Stimulating Factor 1
CSLC	Cancer stem-like cell
Ct	Cycle threshold
CTGF	Connective-tissue growth factor
CTNNBIP1	Catenin beta interacting protein 1
DAMP	Danger-associated molecular patterns
DAPI	4’,6-diamidino-2-phenylindole
dds	DESeq dataset object
DGCR8	DiGeorge Syndrome Critical Region Gene 8
DKD	Diabetic kidney disease
Dkk3	Dickkopf WNT signaling pathway inhibitor 3
DNA	Deoxyribonucleic acid
Dnm3os	DNM3 opposite strand/antisense RNA
dNTP	Deoxyribonucleotide triphosphate
DPX	Distyrene, Plasticiser, Xylene
DT	Diphtheria toxin
EC	Endothelial cell
ECM	Extracellular matrix
EDTA	Ethylenediaminetetraacetic acid
eGFR	Estimated glomerular filtration rate
EGFR	Epidermal growth factor receptor
EKV	ECG-gated Kilohertz Visualization
EMT	Epithelial to mesenchymal transition
endoMT	Endothelial to mesenchymal transition
eNOS	Endothelial nitric oxide synthase
EPC	Endothelial progenitor cell
EPO	Erythropoietin
ERK	Extracellular signal–regulated kinases
ESC	Embryonic stem cell
ESKD	End-stage kidney-failure
ET	Ejection time
Exp5	Exportin-5
Ezh2	Enhancer of zeste 2 polycomb repressive complex 2 subunit
FACS	Fluorescence-activated cell sorting

FAO	Fatty acid β-oxidation
Fbn1	Fibrillin 1
FBS	Foetal bovine serum
FC	Fold-change
FDA	Food and Drug Administration
FGF-23	Fibroblast growth factor 23
FMO	Fluorophore minus one
FoxD1	Forkhead box D1
FOXM1	Forkhead Box M1
FOXO1	Forkhead Box O1
FPKM	Fragments Per Kilobase of transcript per Million mapped reads
FRET	Fluorescence resonance energy transfer
Gapdh	Glyceraldehyde-3-phosphate dehydrogenase
Gata4	GATA binding protein 4
Gata6	GATA binding protein 6
GBM	Glomerular basement membrane
gDNA	Genomic DNA
GFB	Glomerular filtration barrier
GFR	Glomerular filtration rate
Gli1	GLI family zinc-finger 1
GSR	Glutathione-disulfide reductase
GTP	Guanosine triphosphate
H3K9ac	H3 lysine 9 acetylation
HBSS	Hank's Balanced Salt Solution
HD	Huntington’s Disease
HFSC	Hair follicle stem cell
Hh	Hedgehog
HK2	Human proximal tubular cell line
HO-1	Heme oxygenase 1
HSC	Hepatic stellate cell
HTT	Huntingtin gene
HUVEC	Human umbilical vein endothelial cell
IFNγ	Interferon gamma
Igdcc3	Immunoglobulin superfamily DCC subclass member 3
IGV	Integrative Genomics Viewer
IL-1	Interleukin-1
IL-15	Interleukin-15
IL-18	Interleukin-18
IL-1β	Interleukin-1 beta
IL-34	Interleukin-34
IL-6	Interleukin-6

IL-8	Interleukin-8
ILK	Integrin-linked kinase
ILK	Integrin-linked kinase
iNOS	Inducible nitric oxide synthase
IOD	Integrated Optical Density
IRI	Ischemia reperfusion injury
IV CT	Isovolumic contraction time
IV RT	Isovolumic relaxation time
KIM-1	Kidney injury molecule-1
Klf12	Kruppel Like Factor 12
LPS	Lipopolysaccharide
LTBP	Latent TGFβ binding protein
LTL	Lotus Tetragonolobus Lectin
LV	Left ventricle
MAPK	Mitogen-activated protein kinase
MCP-1	Monocyte chemoattractant protein-1
MDRD	Modification of Diet in Renal Disease (2006 study)
Mef2c	Myocyte enhancer factor 2C
MEK	Mitogen-activated protein kinase kinase
MGFR	Marker Gene Finder in RNA-seq data
MI	Myocardial infarction
MIF	Macrophage migration inhibitory factor
miR	microRNA
miRNA	microRNA
Mmp14	Matrix metallopeptidase 14
Mmp2	Matrix metallopeptidase 2
MMT	Macrophage-to-myofibroblast transition
MOE	Methoxyethyl
MOMP	Mitochondrial outer membrane permeability
MPI	Myocardial performance index
mRNA	Messenger RNA
MSC	Mesenchymal stem cell
mt-Nd4l	NADH dehydrogenase 4L, mitochondrial
mt-Nd6	NADH dehydrogenase 6, mitochondrial
Mtf-2	Mitofusin-2
mTORC1	Mechanistic target of rapamycin complex 1
Myo18a	Myosin XVIIIA
Myocd	Myocardin
NC3Rs	UK National Centre for Replacement, Refinement and Reduction of Animals in Research
Ncx-1	Sodium/calcium exchanger-1
NFκB	Nuclear factor kappa-B

NHS	National health service
NICE	UK National Institute for Health and Care Excellence
NLRP3	Nucleotide-binding domain, leucine-rich-containing family, pyrin domain-containing-3
NMD	Nonsense-mediated mRNA decay
NPC	Neural progenitor cell
NRK49F	Normal rat renal fibroblast cell line
Nrxn3	Neurexin 3
OAT	Organic anion transporter
Osr1	Odd-skipped related transcription factor 1
p-adj	Adjusted p-value
PAAT	Pulmonary artery acceleration time
PAMP	Pathogen-associated molecular pattern
PASMC	Pulmonary artery smooth muscle cell
PBS	Phosphate buffered saline
PCA	Principle component analysis
PCR	Polymerase chain reaction
PDGF	Platelet-derived growth factor
PDGFRβ	Platelet-derived growth factor receptor beta
PECAM-1	Platelet/endothelial cell adhesion molecule-1
Pen/strep	Penicillin/streptomycin
Pgf	Placental growth factor
PI3K	Phosphatidylinositol 3-kinase
Pik3cb	Phosphatidylinositol-4,5-bisphosphate 3-kinase catalytic subunit beta
Plxna2	Plexin A2
POR	Cytochrome p450 oxidoreductase
PP2Ac	Protein phosphatase 2A catalytic subunit
PPAR	Peroxisome proliferator-activated receptor
PPARGC1A	PPAR-γ coactivator-1a
Ppia	Peptidylprolyl isomerase A
PPL	Project licence
Ppm1a	Protein Phosphatase Magnesium Dependent 1A
Pptc7	PTC7 protein phosphatase homolog
Pre-miRNA	Precursor-miRNA
pri-miRNA	miRNA primary transcript
PS	Phosphorothioate
PTEC	Proximal tubular epithelial cell
PTEN	Phosphatase and tensin homolog
PTH	Parathyroid hormone
Qk	Quaking
Qki	Quaking isoform

QMRI	The Queen's Medical Research Institute
qRT-PCR	Quantitiative real-time PCR
QS5	QuantStudio 5
RAAS	Renin-angiotensin-aldosterone system
RAGE	Receptor for advanced glycation end products
RanGTP	Ran guanosine triphosphate
RANTES	Regulated Upon Activation, Normally T-Expressed, And Presumably Secreted
RASAL1	RAS protein activator like 1
Rcsd1	RCSD domain containing 1
Rho	Rhodopsin
RIN	RNA Integrity Number
RISC	RNA-induced silencing complex
rlog	regularised log
RNA	Ribonucleic acid
RNA-seq	RNA-sequencing
ROS	Reactive oxygen species
Rplp0	Ribosomal protein lateral stalk subunit P0
RQ	Relative quantification
RT	Reverse-transcription
rUUO	Reversal of unilateral ureteral obstruction
Rybp	RING1 and YY1 Binding Protein
SDF-1	Stromal cell-derived factor 1
SEM	Standard error of the mean
Sema4d	Semaphorin 4D
Sept4	Septin4
SIPA	Single Primer Isothermal Amplification
SMAD	homologue of C.elegans SMA protein and the D.Melanogaster mothers against decapentaplegic protein
SMAD2	Mothers against decapentaplegic homolog 2
SMAD3	Mothers against decapentaplegic homolog 3
SMAD4	Mothers against decapentaplegic homolog 4
Smg7	SMG7 Nonsense Mediated mRNA Decay Factor
Snail-1	Snail family transcriptional repressor 1
STAR	Spliced Transcripts Alignment to a Reference
$STHdh^{Q111/111}$	Striatal neurons Huntington's Disease model
STN	Subtotal nephrectomy
STNx	Single-surgery subtotal nephrectomy
Sufu	SUFU negative regulator of hedgehog signalling
SURF	Shared University Research Facility
TAC	Transverse aortic constriction

Tbx5	T-box binding protein 5
Tcf4	Transcription factor 4
TFAP2A	Transcription factor AP-2, alpha
TGFβ	Transforming growth factor β
TGFβRI	TGFβ receptor type I
TGFβRII	TGFβ receptor type II
TNFR1	TNF receptor 1
TNFR2	TNF receptor 2
TNFα	Tumour necrosis factor α
TRBP	TAR RNA-binding protein
Treg	Regulatory T-lymphocyte
TWEAK	TNF-related weak inducer of apoptosis
u6	U6 small nuclear RNA
UTC	Untreated control
UUO	Unilateral Ureteral Obstruction
VEGF	Vascular endothelial growth factor
vSMC	Vascular smooth-muscle cell
VTI	Velocity time integral
Wnt	Wingless-related integration site
XBP1	X-box binding protein 1
XIAP	X-linked inhibitor of apoptosis proteins
Xotx2	Xenopus Orthodenticle homeobox 2 S homeolog
Xvsx1	Xenopus visual system homeobox 1

Chapter One

General Introduction

1.1: Renal physiology

The kidney is an organ with multiple functions. The kidney is responsible for filtering metabolic waste from the blood, such as urea, creatinine, the products of haemoglobin and hormone breakdown, to name just a few.[1] Certain drugs are primarily excreted from the body by the kidney, for example ketamine and fentanyl.[1,2] The kidneys regulate water and electrolyte balance in the blood, to ensure these are maintained at an appropriate level to support homeostatic function of other organ systems.[1] In this way, arterial blood pressure is also regulated, as total blood volume is affected by water and sodium content.[1] Vasoactive substances generated by the kidneys also aid in the regulation of blood pressure by controlling vascular tone.[1] The kidneys are the primary source of erythropoietin (EPO), a peptide hormone which stimulates the production of red blood cells in the bone marrow.[1] The kidneys also participate in vitamin D synthesis and gluconeogenesis.[1]

Three distinct anatomical areas exist in the kidney: the cortex, medulla, and papilla.[3] The functional unit of the kidney is the nephron (Fig 1.1.1).[3] Blood is supplied to the glomerular capillaries of the nephron via the afferent arteriole, exiting the via the efferent arteriole.[3] The vascular tone of these arterioles modulates glomerular capillary pressure and glomerular plasma flow, receiving input from the sympathetic nervous system and vasoactive factors such as angiotensin II.[3]

The glomerulus is a highly specialised capillary bed designed for filtering the blood, allowing an ultrafiltrate to pass through the Bowman's space and into the tubular portion of the nephron.[3] The glomerulus is composed mainly of specialised endothelial cells, specialised epithelial cells (podocytes) and a glomerular basement membrane.[3] The cooperation of these components allows a size and charge-selective barrier to be maintained, inhibiting the filtration of larger substances such as proteins and cells, as well as anionic molecules.[3]

Glomeruli are located in the cortical region, however, glomeruli located in close proximity to the outer medulla are referred to as juxtamedullary glomeruli.[3] Efferent arterioles from the cortical glomeruli branch to form the peritubular capillary network, whereas those from juxtamedullary glomeruli form the vasa recta, a capillary loop which supplies blood to the renal medulla.[3] These post-glomerular capillaries are in close proximity to the tubular components of the nephron, thus supplying them with nutrients, delivering certain waste products for excretion and allowing for reabsorption of electrolytes, nutrients and water which were filtered by the glomerulus.[3]

The composition of the glomerular filtrate which is passed into the tubular component of the nephron is subject to progressive alteration as it passes through the different tubular segments.[3] Approximately 60-80% of the solute and water in the glomerular filtrate is reabsorbed via the proximal tubule.[3] Electrolytes such as Na^+, K^+, $HCO3^-$, Cl^-, PO_4^{3-}, Ca^{2+}, and Mg^{2+} as subject to reabsorption by the proximal tubule, as well as amino acids, glucose, citric acid cycle intermediates and low molecular weight proteins.[3] These reabsorption processes occur via active transporters and passive diffusion (in the case of water).[3] The proximal tubules also participate in the concentration-dependant transport of anions and cations from the post-glomerular capillaries the into proximal tubular cells, followed by secretion into the tubular fluid.[3]

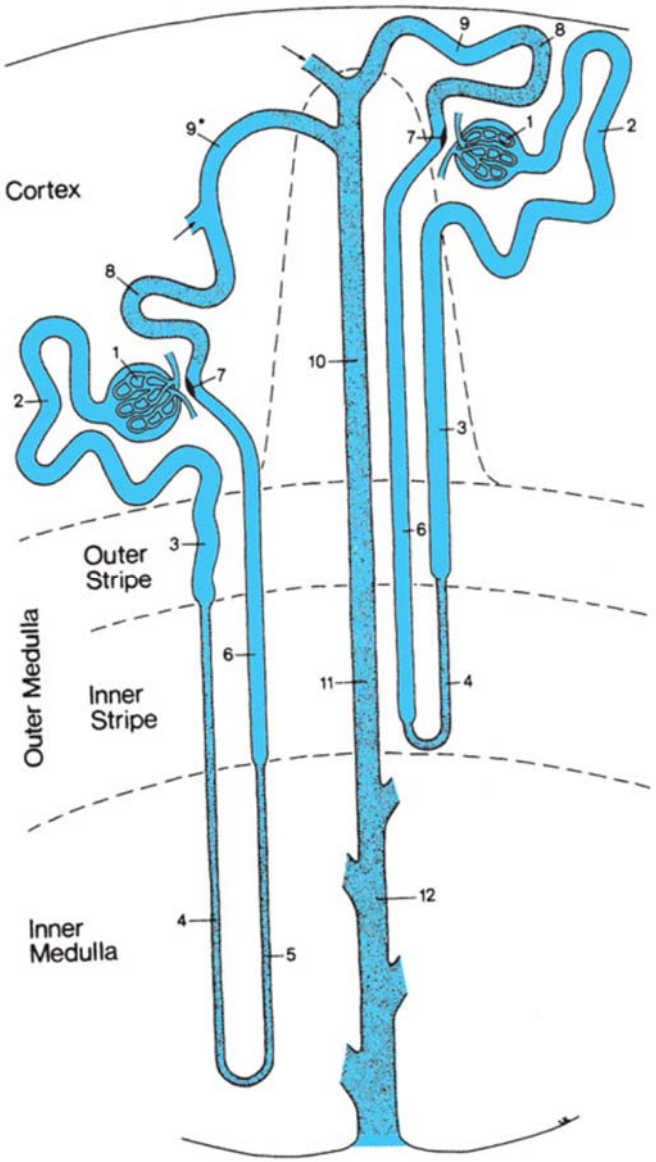

Fig 1.1.1: **The nephron**.[3] 1 = Renal corpuscle (including the glomerulus and Bowman's capsule), 2 = proximal convoluted tubule, 3 = proximal straight tubule, 4 = descending thin limb, 5 = thin ascending limb, 6 = thick ascending limb, 7 = macula densa, 8 = distal convoluted tubule, 9 = connecting tubule, 9* = connecting tubule of the juxtamedullary nephron, 10 = cortical collecting duct, 11 = outer medullary collecting duct, 12 = inner medullary collecting duct.

The loop of Henle (composed of the descending and ascending thin, and ascending thick limbs) then carries out processes relating to the regulation of urinary concentration.[3] The thin descending limb has high permeability to water and low permeability to electrolytes and urea, allow the reabsorption of these here. The thin ascending limb allows reabsorption of Na^+ and Cl^- via passive diffusion, but is relatively impermeable to water. The thick ascending limb allows reabsorption of Na^+ and Cl^- via active transport, but is impermeable to water.[3] The macula densa is located between the end of the thick ascending limb of the loop of Henle and the early distal tubule.[3] The macula densa detects the tubular fluid solute concentration and reduces the rate of glomerular filtration (via inducing afferent arteriole contraction) if increased solute concentrations are detected, thus maintaining electrolyte concentration in the blood in cases where tubular reabsorption processes are compromised.[3]

The tubular fluid then progresses to the distal tubule, a relatively water impermeable region where the majority of the remaining Na^+, K^+, and Cl^- is reabsorbed.[3] The late distal tubule, cortical collecting tubule, and medullary collecting duct then regulate the final urinary concentration and volume.[3] Any remaining Na^+ is reabsorbed, while K^+ and H^+ are secreted, in the late distal tubule and cortical collecting tubule. The variable permeability of the medullary collecting duct to water regulates the final concentration of the urine.[3]

1.2: Chronic kidney disease

Chronic kidney disease (CKD) is a prevalent condition worldwide. It is most consistently estimated to affect between 11-13% of the population globally,[4] although estimations between 8-16% of the adult population have been reported.[5] Increased prevalence is observed in aging populations, with over 20% of people over 65 years of age and 35% of people over 70 in the USA.[6,7] As population demographics across many developed countries shift towards a higher portion of older individuals,[8] CKD incidence may rise in years to come. The Global Burden of Disease (2015) study estimated that 1.2 million people died from kidney failure in 2015, a 35% increase from 2005.[9]

CKD can be simplistically defined as a progressive decline in glomerular filtration rate (GFR) over time. Functional criteria for CKD is GFR of <60mL/min per 1.73m^2 for over 3 months, while structural criteria are kidney damage for over 3 months (with albuminuria being the most common marker).[7] Staging of CKD (stage 1-5) is based on estimated GFR (eGFR), which declines as CKD progresses.[10] Once end-stage kidney-failure (ESKD) has been reached, the kidneys no longer have the capacity to adequately filter the blood, resulting in renal replacement therapy (dialysis) or transplantation being necessary.[11] Risk of cardiovascular mortality, coronary heart disease, stroke, and heart failure all increase as GFR (predicted by creatinine) declines.[12]

There is a significant economic burden associated with the treatment of CKD, worldwide.[5,7] In the UK, NHS England reported that in 2009-2010, an estimated £1.44-1.45 billion was spent managing CKD (~1.3% of total NHS spending). Renal replacement therapy (dialysis) accounted for greater than 50% of this cost, despite this being provided to only 2% of CKD patients.[13]

1.3: Markers of CKD

1.3.1: Creatinine

The measurement of serum creatinine is the current standard clinical practice for the estimation of GFR in patients,[10] therefore making it a critical tool in the diagnosis and clinical management of CKD. The use of circulating creatinine as a measure of glomerular filtration rate is based on our knowledge of renal physiology. The nephron is the functional unit of the kidney, responsible for filtering the blood and producing urine.[14] Therefore, the following equation can be used in GFR measurement: GFR = (U_x x V) / P_x, where U_x is the concentration of substance X in the urine, V is the urine flow-rate, and P_x is the concentration of substance X in the blood plasma.[15] This equation applies in situations where substance X, an ideal substance, is freely-filtered by the glomerulus, is not affected by tubular secretion or reabsorption processes, or metabolised at any point between its filtration by the glomerulus and its measurement in the urine.[15] An example of such a substance is inulin, the measurement of which in the urine (along with continuous infusion) remains the gold-standard method for GFR determination.[16] However, as this is a cumbersome and expensive method to use clinically, an endogenously produced substance to use is desirable.[15,16]

Creatinine expresses multiple characteristics of an ideal substance for which to estimate GFR.[17] Creatinine is produced in the muscles as by-product of homeostatic metabolism at a constant rate (20 mg/kg per day for adults),[15] is freely-filtered by the glomerulus, is not re-absorbed, and is not metabolised in the kidney.[17] However, some tubular secretion occurs,[15] meaning GFR may be over-estimated by creatinine measurement. There are two main equations for the estimation of GFR from serum creatinine, the 2006 Modification of Diet in Renal Disease (MDRD) study equation and the 2009 Chronic Kidney Disease Epidemiology Collaboration (CKD-EPI) equation.[18] The CKD-EPI equation has been shown to be more accurate and a better prognostic indicator than the MDRD equation.[18] In 2014, the UK National Institute for

Health and Care Excellence (NICE) recommended the use of the newer CKD-EPI equation for the diagnosis and staging of CKD.

1.3.2: Cystatin C

UK and international guidelines recommend that diagnosis of early-stage CKD, without the presence of albuminuria, be confirmed with GFR estimation using cystatin C.[19] This is in an effort to combat the over-diagnosis of CKD in healthy patients which can result from the use of creatinine to estimate GFR. Cystatin C is produced in all nucleated cells in the body at a constant rate, as it functions as a cysteine proteinase.[20] It functions as a serum marker of GFR due to being freely filtered by the glomerulus and having minimal extrarenal elimination.[20] Multiple studies have confirmed it to be a more sensitive marker of GFR than creatinine[20–23] and it has been suggested that the use of cystatin C, along with creatinine and ACR, offers increased predictive accuracy for progression to end-stage renal disease and all-cause mortality over the use of creatinine or ACR alone.[24]

1.3.3: Albuminuria

Albuminuria, usually measured by urinary albumin:creatinine ratio (ACR), is another tool commonly used in the clinic to stratify the CKD patient population and (together with other measures) predict prognosis.[25,26] Evidence exists for albuminuria as an independent risk factor for all-cause mortality, cardiovascular mortality, cardiovascular disease and CKD progression.[25] It has been suggested that albuminuric CKD patients with additional detectable markers of glomerular damage are likely to progress, while those with markers of tubulointerstitial damage are less likely.[27]

Albumin is a globular protein produced and excreted by the liver.[28] It is the most abundant protein in human plasma.[28] Under normal conditions, albumin filtration is largely restricted by the glomerulus, while any that does get through undergoes proximal tubular reabsorption.[29] Albuminuria has long been used as a marker of renal damage, as damage to the glomerular filtration barrier leads to leakage of albumin

into the urine as size and change selectivity are lost.[30–32] Properties of each component of the glomerular filtration barrier (the endothelium, glomerular basement membrane, and podocytes) are thought to contribute to the normal resistance to filtration of albumin and other large proteins. Therefore, dysfunction in each of these (most notably podocytes), along with increased intraglomerular hydrostatic pressure, are thought to underlie the increased albumin filtration observed in renal damage.[29] Inflammatory cytokines and adipokines are known to contribute to this, for example tumour necrosis factor α (TNFα), interleukin-6 (IL-6), leptin, and adiponectin.[29] In the podocytes in particular, exposure to increased serum albumin has been reported to cause albumin endocytosis, increased TGF-β (transforming growth factor beta) signalling, increased COX-2 (cyclooxygenase-2) expression, apoptosis relating to endoplasmic stress, and actin cytoskeleton reorganisation.[33]

Damage to the proximal tubular epithelial cells is also likely to contribute to albuminuria.[34] Under normal conditions, albumin which makes it through the glomerulus is reabsorbed by the proximal tubule, where it can be metabolised or transported to peritubular capillaries.[34] This reabsorption is largely via receptor-mediated endocytosis, heavily involving receptors megalin and cubilin.[29] Mutations and knockout studies involving these receptors have demonstrated increased albuminuria.[35]

Evidence also exists to suggest albuminuria is a driving factor in CKD, as opposed to simply being a consequence of it.[35] The increased uptake of albumin in tubular cells has been shown to be cytotoxic, as well as inducing expression of chemokines (MCP-1[36]), vasoactive substances (reactive oxygen species[37] and endothelin[38]) and pro-fibrotic substances (TGFβ[39], TNFα[40], IL8[41] and collagens[42]).[32,43] Together, these changes are thought to lead to tubulointerstitial dysfunction and fibrosis.[32]

				Persistent albuminuria categories Description and range		
				A1	A2	A3
				Normal to mildly increased	Moderately increased	Severely increased
				<30 mg/g <3 mg/mmol	30-300 mg/g 3-30 mg/mmol	>300 mg/g >30 mg/mmol
GFR categories (ml/min/1.73m2) Description and range	G1	Normal or high	≥90			
	G2	Mildly decreased	60-89			
	G3a	Mildly to moderately decreased	45-59			
	G3b	Moderately to severely decreased	30-44			
	G4	Severely decreased	15-29			
	G5	Kidney failure	<15			

Fig 1.3.1: **Prognosis of CKD by GFR and albuminuria categories: KDIGO 2012**. eGFR and albuminuria are used to predict prognosis in CKD patients. Green = low risk of poor outcomes (if no other makers of kidney disease present, no CKD), yellow = moderately increased risk, orange = high risk, red = very high risk.

1.3.4: Serum phosphate

Serum phosphate levels are important in the management of CKD. As one of the many roles of the kidney is to regulate phosphate levels, disturbances in this are commonly observed in CKD.[44] Phosphate is filtered from the blood via glomerular filtration before being reabsorbed with high efficiency by the proximal tubule. As GFR begins to decline, parathyroid hormone (PTH) and fibroblast growth factor 23 (FGF-23) levels increase, triggering reduced phosphate reabsorption, thus compensating for the decreased GFR and maintaining phosphate levels in the blood.[44] However, once GFR declines to 30 ml/minute/1.73 m^2 or less, these adaptive mechanisms can no longer maintain blood-phosphate levels within a normal range, leading to hyperphosphatemia.[45] This hyperphosphatemia, along with adaptive mechanisms

once intended to maintain levels, result in a number of adverse effects in CKD patients.[45] These are known to contribute to CKD-Mineral Bone Disorder (CKD-MBD),[46] vascular calcification,[47] endothelial dysfunction,[48] and left-ventricular hypertrophy.[49] Hyperphosphatemia is a well-established risk-factor for all-cause mortality, cardiovascular disease, and renal disease in the general population, as well as predicting future development of end-stage kidney disease (ESKD) in then-healthy individuals.[44] Phosphate levels also correlate with all-cause and cardiovascular mortality in dialysis patients.[44]

1.3.5: Serum urea

Urea is small molecule which results from the breakdown of protein and nitrogen.[50] Uremia is a term used to describe the build-up of nitrogenous waste products in the blood of patients with renal insufficiency.[51] Among these waste products, urea is the most abundant molecule and is therefore used as a marker of uremic syndrome.[50–52] *In vitro* experiments have found urea to have effects on multiple cell types (often deleterious) such as: medullary collecting duct cells,[53] medullary cells,[54] adipocytes,[55] vascular smooth muscle cells,[56] intestinal epithelial cells,[57] aortic endothelial cells,[58] and pancreatic β-cells.[59]

1.4: Cardiorenal syndrome

Cardiorenal syndrome (CRS) is the general term given to the phenomenon where acute or chronic dysfunction the kidney induces dysfunction in the heart (or vice-versa).[60] Cardiorenal syndrome (CRS) is classified into five different types (table 1.3.1).[60–62] CRS associated with CKD is classified as CRS type 4.

Table 1.4.1: **Classification of cardiorenal syndrome based on the Consensus Conference of the Acute Dialysis Quality Initiative**.[60–62]

Type	Name	Description
1	Acute cardiorenal syndrome	Acute worsening of cardiac function leading to decreased kidney function
2	Chronic cardiorenal syndrome	Long-term abnormalities in cardiac function leading to decreased kidney function
3	Acute renocardiac syndrome	Acute worsening of kidney function causing cardiac dysfunction
4	Chronic renocardiac syndrome	Long-term abnormalities in kidney function leading to cardiac disease
5	Secondary cardiorenal syndrome	Systemic conditions causing simultaneous dysfunction of the heart and kidney

Epidemiological data clearly demonstrates a strong link between renal dysfunction and cardiovascular dysfunction.[63] Increased risk of cardiovascular morbidity and mortality is predicted by decreased renal function.[63] This risk is also bi-directional. For example, heart failure patients are also at increased risk of renal impairment due to low cardiac output causing renal ischemia.[64]

Cardiorenal syndrome is of significant clinical importance, as CKD has been identified as an independent risk-factor for adverse cardiovascular outcomes.[65] In fact, adverse cardiovascular events are the cause of death in almost 50% of patients with CKD, with increased cardiovascular risk being observed in CKD stages 2-5.[66] Conversely, over 60% of congestive heart failure patients are observed to develop CKD.[67] In CKD cohorts, cardiac hypertrophy is a key feature. Cardiac hypertrophy, as assessed via

echocardiography, is the most commonly diagnosed cardiac abnormality in CKD patients and is also the strongest independent predictive marker of CVD-related mortality in this patient population.[68–73] Cardiac hypertrophy is diagnosed in ~40% of patients with renal insufficiency, rising as renal function declines, to ~75% at ESKD.[69]

A number of possible mechanisms have been demonstrated to be involved in CRS type 4, including activation of the renin-angiotensin-aldosterone system (RAAS), volume overload, sodium retention, endothelial dysfunction, anaemia and inflammation, resulting in morphological changes in cardiac tissue and blood vessles.[74,75]

1.5: Renal Fibrosis

Renal fibrosis can be simplistically defined as the build-up of excessive extracellular matrix (ECM) in the renal parenchyma.[76] Renal fibrosis is the result of maladaptive repair processes which were initiated in an attempt to restore renal architecture or function in response to renal injury.[77,78] Although the underlying aetiology of CKD can differ significantly from patient to patient, renal fibrosis is referred to as the final common pathway through which all chronic kidney disease progresses.[76,79] Increased renal fibrosis scores in patients with CKD is correlated with decline in renal function, as it is considered a key factor in the progression towards ESKD.[80] The key histological hallmarks of renal fibrosis are tubulointerstitial fibrosis and glomerulosclerosis,[81,82] with tubulointerstitial fibrosis being considered the more important indicator of CKD severity and progression.[80] Glomerulosclerosis is characterised by the loss of capillaries and accumulation of ECM in the glomeruli.[82] Tubulointerstitial fibrosis is excessive accumulation of ECM in the tubulointerstitial space.[83] The development and progression of renal fibrosis is complex, with individual cell types (fig 1.5.1) having unique and interlinking roles, involving cytokines, inflammation and other factors.[77,78,81,84]

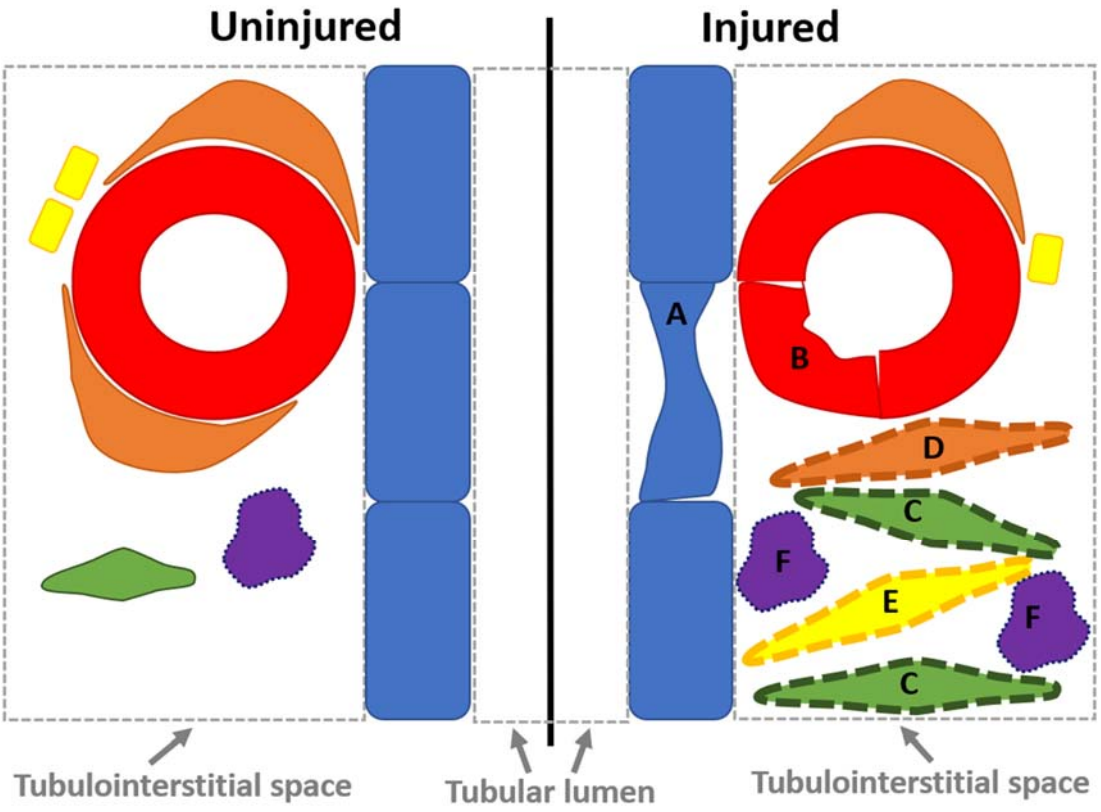

Fig 1.5.1: **Overview of various cell types in the uninjured and injured kidney**. Blue = proximal tubular epithelial cell (PTEC). Red = perivascular capillary, lined with endothelial cells. Purple = macrophage. Green = fibroblast (uninjured) or myofibroblast (injured, has thick dash border). Orange = pericyte or pericyte-derived myofibroblast (injured, thick dash border). Yellow = $Gli1^+$ perivascular progenitor cell or $Gli1^+$ cell-derived myofibroblast (injured, thick dash border). A = PTEC dedifferentiation. B = Endothelial activation. C = transdifferentiation of kidney resident fibroblasts into myofibroblasts and population expansion. D = pericyte detachment and transdifferentiation into myofibroblasts. E = $Gli1^+$ perivascular progenitor cell migration and differentiation into myofibroblasts. F = macrophage accumulation.

1.5.2: Cytokines and extracellular mediators in renal fibrosis

1.5.2.1: TGFβ

TGFβ (transforming growth factor-β) is extremely well-established as a key pro-fibrotic cytokine in renal fibrosis, TGF-β1 in particular.[85,86] TGF-β1 is synthesised and secreted by multiple cell types, where it is stored in an inactive form, bound to latent TGFβ binding proteins (LTBPs) or fibrillins in extracellular matrix.[87] TGFβ can be activated by multiple factors, including integrins,[88,89] proteases,[88,90,91] reactive oxygen species (ROS),[88,92] and tactile force on the extracellular matrix (for example that produced by myofibroblast contractility).[87,93] Once in its active and unbound, form TGFβ then binds the extracellular membrane TGFβ receptor type II (TGFβRII), which recruits and activates TGFβ receptor type I (TGFβRI), which in turn phosphorylates receptor SMADs (R-SMADs) such as SMAD2 and SMAD3.[86] SMAD2/3 then form an oligomeric complex with SMAD4 (co-SMAD), which allows the complex to translocate to the nucleus and activate the expression of certain genes (in collaboration with a number of transcriptional co-factors).[86,94] For example, SMAD3 can bind to the promoter of collagen genes to induce transcription, leading to increased synthesis of collagens, which are important components of extracellular matrix.[95–97] Non-canonical (non-SMAD) pathways are also activated by TGFβ, including MAPK (mitogen-activated protein kinase) signalling (MEK, ERK, p38, c-Jun) pathways, Rho (rhodopsin) GTPase signalling (Rho, Rac, Cdc42), along with phosphatidylinositol 3-kinase (PI3K)/AKT and integrin-linked kinase (ILK) signalling.[85]

TGFβ expression has consistently been found to be elevated in patients with renal fibrosis, as well as in several animal and *in vitro* models of renal fibrosis.[85,86] Mechanistically, TGFβ has been found to induce disease-associated phenotypes in multiple cell types in the kidney.[86] TGFβ signalling can increase extracellular matrix (ECM) synthesis, decrease ECM degradation via inhibition of matrix metalloproteinases (MMPs), and induce myofibroblast activation, which can in-turn result in further increased ECM production.[97] Transgenic overexpression of TGFβ

alone has been found to result in renal fibrosis in mice.[85] Inhibition of TGFβ and/or TGFβ signalling by a multitude of methods has been demonstrated to protect against renal fibrosis in *in vivo* and *in vitro* models of renal fibrosis.[85]

1.5.2.2: Angiotensin II

The renin–angiotensin–aldosterone system (RAAS) is an important regulator of vascular tone and blood volume.[98] Angiotensinogen is converted to angiotensin I via renin, an enzyme produced in the kidney. Angiotensin I is then converted to angiotensin II, the active product, via angiotensin converting enzyme (ACE).[99]

Angiotensin II is the main peptide hormone of this system, which is known to act on a number of cell types in the kidney, including mesangial cells, tubular epithelial cells and interstitial fibroblasts.[100] Angiotensin II is considered to be a central mediator of renal fibrosis and inflammation.[101] It is known to have role in the development of glomerulosclerosis via inducing glomerular mesangial cell proliferation and hypertrophy,[100] while also being involved in tubulointerstitial fibrosis via promoting the phenotypic switch between fibroblasts and myofibroblasts which produce large amounts of extracellular matrix.[100] Angiotensin II also induces the expression of pro-fibrotic factors such as TGFβ, PDGF (platelet-derived growth factor), CTGF (connective tissue growth factor), TNFα (tumour necrotic factor alpha), and activation of NFκB (nuclear factor κ-B) signalling (known to have a role in renal fibrosis).[81] RAAS blockade (via ACE inhibition) is employed as the first-line therapeutic intervention in proteinuric chronic kidney disease cohorts, as superiority to other anti-hypertensive medications in slowing progression to ESKD and ameliorating proteinuria.[102]

1.5.2.3: TNFα

Tumour necrotic factor alpha (TNFα) is an important cytokine mediator of inflammation and fibrosis in renal disease.[103,104] Infiltrating macrophages are the primary source of TNFα in the injured kidney, although it can also be expressed by renal cells such as proximal tubular epithelial cells.[103,104] TNFα activates the transmembrane receptors TNFR1 (TNF receptor 1) and TNFR2 (TNF receptor 2), which result in the activation of signalling pathways which result in the expression of a number of pro-fibrotic and pro-inflammatory extracellular factors which promote the inflammation and fibrotic pathways which drive progressive renal injury.[104] TNFα expression has been found to be elevated in the kidneys of many CKD cohorts, and TNFα inhibition has been demonstrated to be efficacious in reducing albuminuria and slowing the progressive decline in renal function in multiple animal models of CKD.[103,105]

1.5.3: Fibroblasts in renal fibrosis

Myofibroblasts are a population of mesenchymal interstitial cells which appear in wound-healing or fibrosis.[106] In normal wound-healing, myofibroblasts are cleared via apoptosis upon resolution of the injury, however, in fibrosis the accumulation of myofibroblasts is progressive and persistent.[107–109] Increased myofibroblast accumulation has been associated with the progression of renal disease.[110]

Myofibroblasts are considered the primary source of extracellular matrix (ECM) production in renal fibrosis, although other cell types are also known to contribute.[111] In response to multiple exogenous stimuli, fibroblasts and other myofibroblast precursor cells transdifferentiate into myofibroblasts (Fig 1.5.1 C-E), which produce alpha-smooth muscle actin (α-SMA), increased ECM synthesis, form stress-fibre bundles (from actin and myosin), increase size of adhesion structures, proliferate, migrate and exhibit contractility.[112] TGFβ is the principle extracellular ligand which mediates myofibroblast activation in renal fibrosis, although many other extracellular

ligands are involved, such as angiotensin II, Wnt ligands, interleukin-1 (IL-1) and tumour necrosis factor (TNFα).[112] Fibroblast activation is also highly sensitive to mechanical stress, as this is used to sense tissue injury.[113]

In addition to initial fibroblast activation, TGFβ may play an important role in the sustained fibroblast activation seen in renal fibrosis.[114] Here, TGFβ inhibits RASAL1 (RAS protein activator like 1) gene transcription leading to its hypermethylation and therefore epigenetic inactivation. RASAL1 hypermethylation was observed in 100% of fibrotic fibroblasts in the kidney, with RASAL1 gene expression significantly lower than in non-fibrotic renal fibroblasts. As RASAL1 is an important negative regulator of Ras signalling, this suggests hyperactive Ras signalling is important in the sustained activation of myofibroblasts in renal fibrosis. In line with this, the authors found that inhibition of Ras signalling results in significantly reduced renal fibrosis in the folic acid *in vivo* model of renal fibrosis.

Although there is no single defining marker of the myofibroblast, surrogate markers can be used to identify them. αSMA (Acta2) is considered one of the best markers, as myofibroblasts up-regulate the expression of this in order to form the stress fibres needed to enable a key property of the myofibroblast, contractility.[111,115] A commonly used cell-surface marker is platelet-derived growth factor receptor-beta (PDGFRβ), as all myofibroblasts express this. However, pericytes and fibroblasts also express PDGFRβ.[111] Pericytes are contractile mesenchymal cells located in the vascular basement membrane, which are critical to the stability of the renal microvasculature.[116] Pericyte contractility allows for the regulation of capillary diameter and vascular tone.[116] Pericytes have a duel-role in promoting CKD progression.[116] Here, renal injury triggers pericyte detachment and migration to the interstitium and transdifferentiation into myofibroblasts, thus contributing to renal fibrosis, while pericyte loss also triggers peritubular capillary destabilisation, leading to endothelial cell activation and capillary rarefaction which ultimately exacerbates renal injury via increased hypoxia.

The origin of the myofibroblast in renal fibrosis has been the subject of much scrutiny in recent years. Asada *et al* (2011) conducted a lineage-tracing study which suggested tissue-resident fibroblasts in the kidney contributed >90% of myofibroblasts in UUO (unilateral ureteral obstruction).[117] Here, myelin protein zero (P0)-Cre mice were used to mark migrating neural crest cells, which were found to co-express fibroblast markers PDGFRβ and CD73 (cluster of differentiation 73) in the renal interstitium, suggesting kidney-resident mesenchymal cells have key roles in renal fibrogenesis. Humphreys *et al* (2010) conducted a lineage-tracing study which suggested renal pericytes to be a key myofibroblast-progenitor population, with >90% of myofibroblasts in UUO expressing pericyte linage marker FoxD1 (forkhead box D1).[118] However, as FoxD1 is expressed in migrating neural crest cells, it is likely that significant overlap between these and the P0-Cre cells traced by Asada *et al* (2011).

It has recently been demonstrated that a population of mesenchymal stem cell-like (MSC) perivascular cells expressing the Gli1 transcription factor have a large contribution to the myofibroblast pool in renal fibrosis.[119] These $GLI1^+$ MSCs reside in the microvasculature in direct contact with endothelial cells, as well as in the adventitia of large arteries.[119] $GLI1^+$ MSCs play an important role in maintaining peritubular capillary health, with knockout of these cells resulting in peritubular capillary rarefaction, endothelial cell activation, hypoxia and tubular epithelial cell injury.[120] These $Gli1^+$ MSCs were found to constitute a small percentage of the PDGFRβ cells present in the healthy adult kidney (0.02%), however, fate-tracing indicated ~45% of PDGFRβ-expressing cells in the injured kidney (UUO or IRI (ischemia reperfusion injury)) are derived from this $GLI1^+$ progenitor population.[119] Depletion of $GLI1^+$ cells significantly reduced collagen accumulation in renal fibrosis.[119]

Other sources of myofibroblasts have been suggested to have a smaller contribution to the pool of myofibroblasts in renal fibrosis. Myeloid lineage, bone-marrow-derived fibrocytes have been demonstrated to contribute between <0.1% and 35% of

myofibroblasts in UUO, although further study is required to clearly demonstrate the role of these cells in renal fibrosis.[116] LeBleu *et al* (2013) demonstrated that 65% of αSMA^+ cells in the UUO kidney were derived from the expansion of kidney-resident resident cells (or non-bone marrow derived cells), while 35% were bone marrow derived.[121] Endothelial to mesenchymal transition (endoMT) is a proposed mechanism through which endothelial cells can acquire a mesenchymal phenotype to contribute to the pool of myofibroblasts.[116] Lineage-tracing studies have estimated between 30-50% of myofibroblasts in the injured kidney result from endoMT, however, the Tie2 marker used to trace endothelial lineage can also be expressed on myeloid lineage cells and potentially pericytes.[111] Therefore, the overall contribution of endoMT is likely over-estimated. Other markers of endothelial linage used, such as Cdh5–Cre, suffer similar issues with specificity.[111] Macrophage-to-myofibroblast transition (MMT) has also been suggested as a source of myofibroblasts in progressive renal fibrosis, with the transition of M2a macrophages to myofibroblasts being catalysed by TGFβ1.[122] Epithelial to mesenchymal transition (EMT) in renal fibrosis is controversial and is likely to contribute <5% of the myofibroblast pool in UUO, if any contribution is indeed made by this process.[116]

1.5.4: Macrophages in renal fibrosis

Macrophages are a group of phagocytic innate immune cells which are involved in kidney homeostasis and response to acute and chronic renal injury.[122] The kidney contains a tissue-resident macrophage population, in addition to macrophages which differentiated from bone-marrow derived monocytes which arrive via blood circulation.[122,123] In acute and chronic renal injury, macrophages accumulate in the interstitial and glomerular spaces as a result of both infiltration from bone-marrow derived monocytes and proliferation of the kidney-resident macrophages (Fig 1.5.1 F).[122,124] In human CKD, macrophage accumulation correlates-well with the severity of tubular atrophy, tubulointerstitial fibrosis and glomerulosclerosis.[122]

Activated monocytes can adopt one of two polarisation states, M1 or M2.[125] M1-polarised macrophages are referred to as "classically activated," while M2-polarised macrophages are referred to as "alternatively activated."[125] However, simply categorising all macrophages into M1 or M2 categories is likely a significant over-simplification, as macrophage subsets with important functional differences are known to exist.[122]

Recruitment and local proliferation of circulating monocytes is known to make a large contribution to the overall pool of activated macrophages in the acutely injured kidney in animal models of renal injury, such as UUO, renal allograft rejection and diabetic kidney disease, with proliferation of tissue-resident macrophages having a lessor impact.[122,126–128] Certain chemokines have known roles in the recruitment of circulating monocytes to the kidney during kidney injury. Monocyte chemoattractant protein-1 (MCP-1) is a particularly important chemokine in this process, where it is released inflammatory sites and recruits monocytes which differentiate and contribute to the inflammatory response.[129] Genetic knockout of the CCR2 (MCP-1 receptor) significantly reduced macrophage accumulation and ameliorated renal injury in experimental ischemia-reperfusion injury (IRI).[130] Aside from chemokines,

activation of the compliment cascade can also recruit monocytes to the injured kidney.[122]

M1-polarised macrophages are referred to as pro-inflammatory and can be activated by pathogen-associated molecular patterns (PAMPs), such as bacterial (CpG) DNA or lipopolysaccharide (LPS), or danger-associated molecular patterns (DAMPs), which includes many pro-inflammatory cytokines (e.g. IL1, TNF, MIF (macrophage migration inhibitory factor)).[122] In this way, M1 macrophages can be involved in host-defence and acute inflammation. M1 is the predominant polarisation found in acute renal inflammation.[122] M1 macrophages are thought to exacerbate renal injury.[122] Inhibition of M1-polarising cytokines has been found to be protective in animal models of diabetic renal injury and glomerulonephritis and reduce M1 macrophage accumulation.[131,132] Administration of PAMPs or DAMPs in animal models of renal injury promotes M1 macrophage accumulation and promotes increased severity of renal injury phenotypes.[122] Taken together, these suggest M1 macrophage polarisation has a deleterious, injury-promoting, role to play in renal injury.

In animal models of renal injury, macrophage polarisation switches to predominantly M2 phenotypes.[122] For example, at 2-days post-IRI (the peak of renal injury) M1 macrophage number is at the highest it is observed to be at any point in this model, however, as the injury phase subsides and repair phase begins, M1 phenotype macrophage number decreases while M2 increases significantly.[122,133] M1 macrophages can switch phenotype to M2 during this transition.[122,133] The switch from M1 to M2 has also been observed in mouse models of AKI (acute kidney injury) and UUO.[122] This switch from M1 to M2 polarisation was also found to be of critical importance to the recovery from AKI.[122,134] In line with this observation, depletion of macrophages prior to IRI results in a less severe phenotype, as opposed to the depletion 3-5 days post-IRI (as the M1-M2/injury-repair switch takes place) where decreased tubular proliferation and diminished repair is observed.[122,133] However, in animal models where chronic renal injury is present, or in human CKD, significant

evidence exists to suggest M2 macrophages to be deleterious and pro-fibrotic.[122] The number of glomerular M2 macrophages (expressing CD163) in diabetic kidney disease patients correlated with the degree of interstitial fibrosis, tubular atrophy and glomerulosclerosis, while interstitial M2 macrophages (expressing CD68) correlated with GFR stage and albuminuria.[122,135] Number of M2 ($CD163^+$) macrophages were also found to correlate with degree of fibrosis in immunoglobulin A (IgA) nephropathy[122,136] and chronic kidney allograft injury.[122,137] In a severe IRI mouse model which leads to CKD, depletion of the (majority M2) macrophage infiltrate is protective against progressive interstitial collagen deposition (with reduced TGFβ expression). However, re-introduction of specifically M2c macrophages reversed the anti-fibrotic effects of macrophage depletion, suggesting this subset of M2 macrophages may be responsible for the pro-fibrotic effects of M2 macrophages in progressive renal fibrosis.[122,138] TGFβ1 has been demonstrated to promote the transition of M1 macrophages into M2c macrophages, as well as promoting M2a macrophages transitioning into myofibroblasts (macrophage-to-myofibroblast transition, MMT).[122]

1.5.5: Proximal tubular epithelial cells in renal fibrosis

The renal tubules and tubulointerstitial area constitute a large portion of total kidney volume, with proximal tubular mass contributing over 50% of the total kidney volume.[139,140] Three segments of the proximal tubule exist (S1, S2 and S3).[141] S1 is thought to act as the main sensor of renal injury, and modulates the response of S2 and S3.[140,142] S1 also has the highest potential to protect itself from oxidative injury, via HO-1 (heme oxygenase 1) and sirtuin 1 up-regulation, whereas S2 and S3 do not have this ability.[140]

Renal tubular injury has been suggested to be a key contributor to the progression of AKI to CKD. The severity and frequency of injury to the proximal tubular epithelial cells (PTECs) has been demonstrated to correlate with the degree of AKI to CKD progression and long-term prognosis, in a mouse model of specific PTEC injury.[143] Here, a transgenic mouse with proximal tubule-specific expression of the diphtheria toxin (DT) receptor in the S1 and S2 segments of the proximal tubular epithelium was created and DT was used to induce specific proximal tubular cell injury. A single high dose of DT resulted in severe tubular injury characterised by loss of brush boarder, caspase-3 expression (indicating increased apoptosis), and PTECs detached from basement membrane, with increased kidney injury molecule-1 (KIM1) expression and decreased expression of markers of differentiated PTECs (magalin, organic anion transporter 1 and 3 (OAT1 and OAT3)).[143] This injury alone resulted in increased myofibroblast accumulation in the tubulointerstitial space, notably in the areas surrounding injured (KIM1 or caspase-3 expressing) PTECs, as well as increased macrophage infiltration. A single low-dose of DT induced mild proximal tubular injury and interstitial fibrosis, which by 5-weeks post-injury had resolved, with tubular regeneration and myofibroblast transition to fibroblast having taken place. However, repeated low-dose DT administration resulted in a severe phenotype and did not reverse over time.[143] Together, these data suggest proximal tubular injury can act as a driver of renal fibrosis, with the potential for reversal of fibrosis being negatively

correlated with extent of proximal tubular damage and that regeneration of PTECs may be a key step in recovery of fibrosis.

Following renal injury and PTEC loss, the surviving PTECs de-differentiate and migrate along the tubular basement membrane to the site(s) of injury, where they proliferate to regenerate the lost PTECs to maintain nephron structure and functionality.[139,144] However, injured PTECs can also undergo cell cycle arrest in the G2/M phase and acquire a secretory, pro-fibrotic phenotype which drives renal fibrosis (Fig 1.5.1 A).[139]

Cellular senescence and de-differentiation of PTECs in response to AKI has also been reported as being a key step in the transition between AKI and CKD. Here, PTECs arrest in the G2/M phase of the cell cycle and acquire a secretory phenotype, producing pro-fibrotic factors TGFβ and connective-tissue growth factor (CTGF).[145,146] Inhibition of G2/M checkpoint-enforcing proteins *in vitro* results in decreased tubular expression of TGFβ and CTGF.[146] Renal fibrosis in response to IRI was also found to be significantly reduced when the number of PTECs in G2/M cell cycle arrest was reduced (by ~50-60%) via administration of a p53 inhibitor.[146]

Injured PTECs have been demonstrated to secrete a variety of extracellular factors.[139] These include pro-inflammatory cytokines such as IL-1β, IL-6, IL-15, IL-16, IL-18, IL-34, TNF-α, CSF1 (colony stimulating factor 1), TWEAK (TNF-related weak inducer of apoptosis), Fas ligand, VEGF (vascular endothelial growth factor) and CTGF, which induce a wide variety of effects in the injured kidney, such as inducing the expression of more pro-inflammatory and pro-fibrotic factors, macrophage and T-cell recruitment, macrophage M2 polarisation induction, and apoptosis.[139] Chemokine expression is also induced, with injured PTECs being a major source of MCP1/CCL2, RANTES/CCL5 (Regulated Upon Activation, Normally T-Expressed, And Presumably Secreted), and fractalkine/CX_3CL1, along with being a source of IL8, SDF-1 (stromal cell-derived factor 1) and CXCL5, therefore promoting monocyte/macrophage and leukocyte chemotaxis.[139] Increased expression of a number of pro-fibrotic factors has

been observed in injured PTECs, including TGFβ, platelet-derived growth factor (PDGF), CTGF, VEGF, Wnt (wingless-related integration site) ligands, hedgehog (Hh) ligands, Notch signalling ligands, angiotensin II, Endothelin-1, Complement components, and miR-21-containing exosomes, leading to myofibroblast differentiation and proliferation, PTEC de-differentiation, endothelial cell proliferation, macrophage recruitment, RAAS activation, and ECM accumulation.[139]

PTECs are highly metabolically active cells, with a high number of mitochondria per cell.[147] Fatty acid β-oxidation (FAO) is the primary source of energy in PTECs and its dysregulation has been implicated as being a key component of renal fibrosis.[147] Many highly metabolic cell types utilise FAO as it produces more ATP (adenosine triphosphate) per molecule metabolised than glycolysis.[147] In order to facilitate FAO, fatty acids are taken up into the tubules via long-chain fatty acid transporter CD36 and transport to the mitochondria is facilitated by carnitine palmitoyltransferase 1 (CPT1), which conjugates fatty acids to carnitine, the rate-limiting enzyme in FAO.[147,148] The key transcription factors which control the expression of proteins related to FAO are peroxisome proliferator-activated receptors (PPARs) and PPAR-γ coactivator-1a (PPARGC1A).[147,149] In healthy PTECs, fatty acid uptake is tightly controlled, along with metabolism of fatty acids and the rate of FAO-related protein synthesis, to avoid excess intracellular lipid accumulation.[147] As reported by Kang *et al* (2015),[147] transcriptomic analysis of fibrotic vs health human kidney samples revealed significant decreases in FAO-related genes in fibrotic kidneys vs healthy. Similar deficits in FAO were observed in two separate mouse models of renal injury (tubular-specific overexpression of Notch1 intracellular domain and folic acid). As FAO deficits are likely to lead to increased intracellular lipid accumulation, the potential impact of lipid accumulation alone on fibrosis development as assessed using a transgenic mouse with tubular epithelial cell-specific overexpression of CD36, but this was found to not induce renal fibrosis or increase susceptibility to renal fibrosis using animal models.[147] Inhibition of FAO in PTECs results in increased apoptosis, de-differentiation and expression of collagens. Stimulating the PTECs with

TGFβ mimicked this, in a SMAD3-dependant manner, via inhibition of PPARGC1A expression, leading to down-regulation of key FAO pathway components such as CPT1.[147] Tubular-specific overexpression of PPARGC1A, or pharmacological activation of PPARGC1A, significantly reduced PTEC apoptosis, reduced KIM1 expression, reduced renal fibrosis development, improved FAO, and improved renal function, indicating FAO deficits may be a key part of PTEC injury and renal fibrosis in general.[147]

Injury to the proximal tubule and tubulointerstitial fibrosis may also result from glomerular injury and dysfunction.[115] One proposed mechanism for revolves around injured glomeruli allowing excess amounts of protein (notably albumin) to pass through the glomerular filtration barrier.[115] This protein is then reabsorbed by the PTECs, which, in excessive amounts, trigger PTEC injury, leading to increased excretion of pro-inflammatory mediators and PTEC apoptosis.[115] However, the extent to which this process contributes to tubulointerstitial fibrosis chronic kidney disease development and progression *in vivo* is unknown. Another proposed mechanism is extension of local glomerular injury to the proximal tubule.[115] Here, glomerular injury leads to podocyte loss and the formation of a tuft adhesion between the glomerular basement membrane and parietal epithelium. This leads to protein filtrate being misdirected into the interstitial space, causing inflammation and fibrosis between the proximal tubule and its basement membrane, leading to tubular atrophy. Also, the glomerulotubular junction may become blocked by proliferating glomerular crescent or inflammatory cells, thus blocking the passage of glomerular filtrate to the tubules and forming atubular glomeruli, leading to tubular trophy and interstitial fibrosis.[115]

1.5.6: Endothelial cells in renal fibrosis

The endothelium is a layer of endothelial cells (ECs) which is typically has a major role in supporting the vasculature by lining blood and lymphatic vessels.[150] This property is of notable importance in the kidney, as it is a highly vascularised organ with a high demand for blood-supply.[150] However, the kidney is also host to diverse EC populations which have distinct roles in kidney physiology and disease.[151] The kidney possesses 3 main endothelia; the glomerular endothelium, the microvascular endothelium within peritubular capillaries, and the endothelium which lines larger arterial and venous blood vessles.[150]

The glomerular endothelium is a highly fenestrated, glycocalyx-covered endothelial membrane which assists in the sieving properties of the glomerular filtration barrier and the maintenance of podocyte structure.[150] The glycocalyx is heavily enriched with negatively charged proteoglycans, which via glycosaminoglycan binding (chiefly hyaluronic acid) anchors the glomerular endothelium to the glomerular basement membrane (GBM).[150] The GBM, synthesised by the glomerular ECs, is a thick extracellular matrix which sits between the glomerular endothelial cells (which line the glomerular capillaries) and the podocytes which exist within the urinary space.[152] GBM integrity, along with glomerular EC and podocyte function is essential in the maintenance of selective permeability of the glomerular filtration barrier (GFB), allowing the flow of small solutes and plasma water while restricting larger plasma proteins such as albumin.[152] Increased urinary albumin, a prominent feature of CKD, is a marker of reduced selectivity of the GFB, resulting from dysfunction in at least one of its three components.[150,152]

The microvascular endothelium exists in peritubular capillaries, where it facilitates the transportation of reabsorbed components and supports epithelial cell function. Peritubular capillaries are a key part of the post-glomerular microvasculature.[153] Cortical peritubular capillaries arise from the glomerular efferent arterioles[154] and

provide a way for re-absorbed components of the glomerular filtrate to return to the blood circulation, as well as supply oxygen and nutrients to the tubular epithelial cells.[153] In peritubular capillaries, endothelial cells sit on the vasculature-side of a basement membrane, with pericytes and tubular epithelial cells on the other side of the membrane (Fig 1.5.1).[150] Peritubular ECs have sieving properties, controlling what passes though the endothelium, which results from its highly fenestrated and glycoprotein-enriched structure.[150] Pericytes are also important in maintaining peritubular capillary function, as they can promote capillary restriction to regulate cortical and medullary blood flow, regulate capillary permeability, participate in angiogenesis and can transdifferentiate into myofibroblasts which contribute to renal fibrosis.[150]

Another role of ECs in the kidney is to produce and secrete angiocrine factors, which are extracellular factors that signal to other ECs in juxtacrine fashion or to non-endothelial cells (such as tubular epithelial cells and interstitial fibroblasts) in paracrine fashion.[155] Angiocrine signalling is involved in supporting tissue homeostasis and regeneration.[155] These angiocrine factors also support a local population of resident renal progenitor/stem cells, which are important in mediating tissue repair to prevent fibrosis.[150,156] ECs can be activated by a number of stimuli, such as renal injury, inflammation, oxidative stress, or uremic toxins (Fig 1.5.1 B).[150] Here, activated ECs lose their anti-inflammatory and anti-coagulant phenotype and acquire a pro-inflammatory and pro-coagulant phenotype. In response to damage to the endothelium, adjacent ECs proliferate to replace lost cells, as well as endothelial progenitor cells being recruited to the site of injury. However, this response is impeded in the activated endothelium.[150] Two types of EC activation can occur.[150] Type I activation is fast, with ECs responding within minutes of receiving the activating stimulus (such as cytokines, thrombin, compliment c5b-9, or reactive oxygen species) to trigger the exocytosis of Weibel–Palade bodies to release pro-thrombotic, inflammatory and vasoactive factors. Type II activation is slower as it is dependent on gene expression changes, and is triggered by long-term exposure to

activating factors such as cytokines (for example TNFα or IFNγ (interferon gamma)), PAMPs or products of haemolysis such as haemoglobin or haem, resulting in the increased cell surface expression of adhesion molecules such as ICAM1, VCAM1 or E-selectin, and decreased expression of protective molecules such as thrombomodulin.[150] These responses cause a number of responses which are detrimental to overall endothelial health, glycocalyx breakdown, reactive oxygen species (ROS) generation which can damage further ECs, EC cell death and detachment from the endothelium, with reduced capacity for EC proliferation and decreased survival or incorporation of endothelial progenitor cells.[150]

Rarefaction of peritubular capillaries is a consistent feature of human renal fibrosis and in animal models of renal fibrosis, with renal fibrosis leading to this regardless of the underlying fibrosis trigger.[157] The extent of peritubular capillary loss correlates with fibrosis severity in clinical CKD cohorts, as well as in several animal models of renal fibrosis.[158] Peritubular capillary rarefaction makes a significant contribution to chronic hypoxia, which is thought to be a key contributor to the progression of CKD.[154] Pro-angiogenic/EC survival factors (such as VEGF) which normally contribute to the maintenance of the endothelium were found to be down-regulated in animal models of renal fibrosis,[157] while anti-angiogenic factors such as thrombospondin-1 and endostatin or pro-apoptotic factors such as TNFα, IL1 and Fas ligand were up-regulated.[158] ECs have been found to proliferate in response to early renal injury, however, this is followed shortly by increased EC apoptosis.[158] The downstream effects of decreased GFR in CKD can also have pro-apoptotic effects on peritubular ECs.[153] Here, decreased sheer stress in the peritubular capillaries results in peritubular capillary rarefaction, as mechanisms exist to remove “unused” capillaries. Decreased filtration also lowers the oxygen demand of the proximal tubular epithelial cells as less active reabsorption processes need to take place, resulting in a weaker hypoxic and pro-angiogenic stimulus and capillary regression. Tubular cell apoptosis, de-differentiation and G2/M cell cycle arrest can also contribute to capillary

rarefaction in this way, in addition to the decreased VEGF secretion from tubular epithelial cells.

Pericyte function is coupled to renal EC function. Genetic knockout of pericyte expression via an inducible transgenic mouse results in endothelial damage by day 10, with irreversible perivascular capillary rarefaction following.[159] Following AKI, distance between pericytes and ECs can increase before pericytes detach from the capillary, leading to instability in the microvasculature and capillary rarefaction.[159] Moreover, detached pericytes can transdifferentiate into myofibroblasts which contribute to interstitial fibrosis (which can lead to capillary rarefaction as discussed), and this process can deplete the local progenitor cell population (GLI^+) which function to replenish interstitial and vascular cells (Fig 1.5.1 E + D).[159]

1.6: Animal models of renal injury

1.6.1: Unilateral ureteral obstruction (UUO)

UUO is one of the most commonly used murine surgical models of renal fibrosis.[160] Favourable characteristics of this model include the relative simplicity of the surgery, the short-duration of the model (minimising animal maintenance costs), the relatively high consistency and reproducibility of results, the fact it can be successfully carried out in any strain of mouse, and the fact that it's a well-validated model of renal fibrosis.

In a relatively simple surgical protocol, the peritoneal cavity of the mouse is opened via laparotomy and the ureter of one of the kidneys is ligated using surgical suture.[161] As a result, urine can no longer pass into the bladder and instead builds up in the kidney, leading to the rapid development of fibrosis over the course of 4 to 14 days.[162–164]

The changes in renal blood flow and ureteral pressure which result from the initial ureteric obstruction occur in three phases. Firstly, ureteral pressure and renal blood flow increase together over ~1.5 hours. Secondly, over the course of ~3.5 hours, ureteral pressure continues to increase while renal blood flow declines. Thirdly, both ureteral pressure and renal blood flow decrease progressively over time, with significantly lower rates than pre-obstruction being observed by 18 hours post-obstruction.[165] Increased vasoconstriction of the afferent arteriole has been demonstrated to occur in post-obstruction, with this resulting in decreased ureteral pressure via decreased effective filtration pressure.[165,166] Mechanistically, increased vasoconstrictor (such as angiotensin II) and decreased vasodilator (such as inducible nitric oxide synthase (iNOS)) expression has been implicated in producing this increased afferent arteriole pressure.[165,167]

Significant increase in intratubular pressure occurs in the early phases of UUO, which normalises as renal blood flow declines (as this reduces GFR).[168] However, this initial intratubular pressure applies significant mechanical stress on the tubular epithelial cells, which develop a flattened appearance, which causes cell injury and apoptosis.[168] *In vitro* studies have demonstrated the effects of increased mechanical stress on tubular epithelial cells, which involve down-regulation of antioxidant catalase, leading to build-up of intracellular hydrogen peroxide and oxidative stress, thus activating caspase-dependant apoptosis.[168] Although decreased renal blood flow in UUO decreases intratubular pressure, it also promotes hypoxia in the kidney, which is known to promote apoptosis in tubular epithelial cells.[168,169] Tubular cell de-differentiation, G2/M cell cycle arrest and secretory phenotype gain is also observed in UUO.[146,160]

Progressive peritubular capillary rarefaction is also observed in UUO (from ~3 days post-UUO), indicating endothelial cell death and dysfunction takes place.[170] As reviewed above, injured tubular epithelial cells and endothelial cells secrete a number of pro-fibrotic, pro-inflammatory and pro-apoptotic factors by the tubular epithelial cells, including TGFβ1, Angiotensin II, IL-1, TNFα, and MCP-1[168]

Significant accumulation of interstitial macrophages occurs in UUO, initially recruited by chemokine expression by cells in the injured kidney and increased cell adhesion factor expression by activated endothelial cells.[160] Interstitial macrophage accumulation is evident by 3 days post-UUO, with large increases in interstitial macrophage cell count taking place by 7 and 14 days post-UUO.[170] As reviewed above, these macrophages can act as key mediators of renal fibrosis, amplifying the expression of pro-fibrotic factors.

The preceding pro-fibrotic changes in the kidney result in significant accumulation of activated fibroblasts (myofibroblasts) in the interstitium.[160] Myofibroblasts are the primary source of tubulointerstitial collagenous extracellular matrix (ECM), the

excess accumulation of which defines renal fibrosis.[160] Increased myofibroblast count and collagen synthesis is observable from 3 days post-UUO, with significant renal fibrosis and large expansion of the myofibroblast and macrophage populations having occurred by day 7 post-UUO.[160]

As eluded to, the cellular composition of the kidney is subject to change over the course of UUO. For example, 0.17% ± 0.10 of tubules were found to be atrophic in the sham kidney, while this figure rose to 32.57% ± 3.14 at 7-days post-UUO.[171] Alongside this, interstitial fibroblast and macrophage counts increase significantly by 7-days post-UUO compared to sham, with αSMA^+ myofibroblasts increasing from ~1% of the interstitial area in sham to ~6%, and $F4/80^+$ interstitial macrophage count increasing by ~20-fold.[170] Therefore, caution must be exercised when assessing gene expression changes on the basis of sham vs UUO expression, as changes in cell count may influence this.

1.6.2: Reversal of unilateral ureteral obstruction (rUUO)

Multiple attempts have been made over the years to adapt the UUO model for the study of renal injury resolution.[161,172–174] The general hypothesis is that removing the obstruction after allowing renal injury (to varying degrees) to develop may allow resolution of the renal injury to take place over time, enabling the study of regenerative pathways activated in the kidney during this time.

Multiple surgical methods have been employed to produce a reversible unilateral ureteral obstruction (rUUO). Cochrane *et al* (2005) first published an rUUO model where the ureter was clamped for 10 days using a surgical clamp, before being released and the mice allowed to recover for 1, 2, 4 or 6 weeks.[172] However, out of the 11 animals subjected to 10-day UUO and 6-weeks recovery via this methods, bilateral renal function was not measurable in 7 of these animals due to low urine flow from the previously obstructed kidney, which may indicate damage to the ureter had occurred due to the clamp and that ureteral obstruction may not have been fully alleviated by this method.[172] Chaabane *et al* (2012) used a silicone catheter device to fold the ureter, inducing UUO for 7 days before removing the device, allowing the ureter to unfold and kidney to recover for 7 days.[175] This induced UUO with a success rate of 100%, however, only successful reversal of obstruction as only induced in 62% of animals.[175] Puri *et al* (2010) used a microvascular clamp (similarly to Cochrane *et al*) to induce UUO for 6 days.[176] It was found that leaving the clamp in one location for 6 days resulted in successful reversal of obstruction in <20% of animals, whereas when the clamp was moved to a new location along the ureter every 2 days, the success rate increased to >70%.[176] This suggests the ureter is quite susceptible to injury which prevents successful complete restoration of urine flow post-obstruction. Tapmeier *et al* (2008) presented an rUUO method with a >96% rate of successful complete-reversal of ureter obstruction, involving surgical re-implantation of the ureter into the bladder after 7 days of obstruction.[173] This technique is substantially more technically difficult than ureter clamp-based methods, as it requires the UUO surgery to be carried out in a specific manner and careful re-implantation of the

ureter into the bladder, but the rate of success makes it an attractive method in comparison. Hesketh *et al* (2014) successfully reproduced the methods of Tapmeier *et al* (2008).[161] At one-week post-ureteric reimplantation, the previously obstructed kidney can be observed to be decompressed as the flow of urine had been successfully restored (Fig 1.6.2).

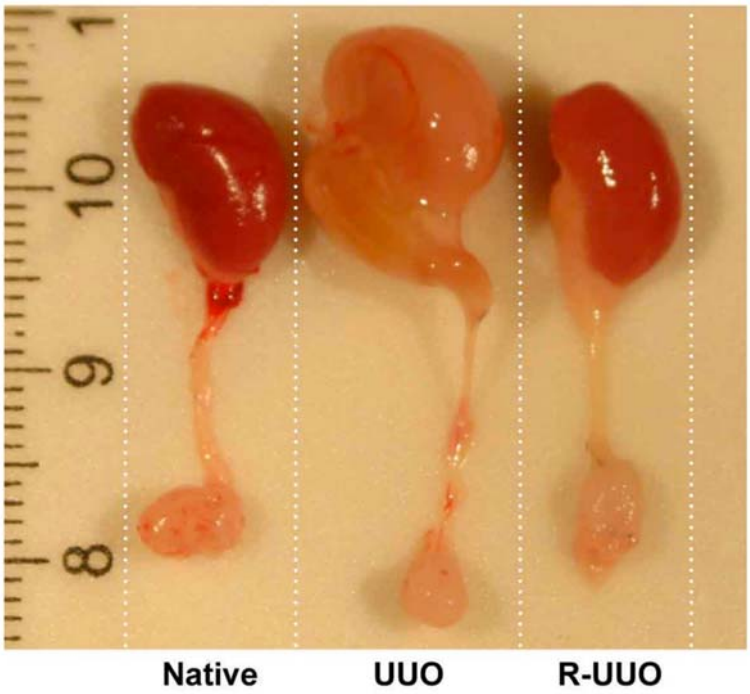

Fig 1.6.2: **Kidneys with attached baladder from mice subjected to sham, UUO, or rUUO surgery**. Native = sham-operated. UUO = 7-day UUO. rUUO = 1-week post-rUUO surgery (after 7-day UUO).[161]

1.6.3: Subtotal nephrectomy

Subtotal nephrectomy (STN), also known as 5/6 nephrectomy, partial nephrectomy, the remnant kidney model, or simply experimental CKD, is an *in vivo* model of chronic kidney disease. Progressive renal injury in this model is driven by a significant reduction in the volume of renal parenchyma, produced by surgical removal of one kidney (nephrectomy) and reduction of renal mass of the contralateral kidney via one of two main methods.[81] The most common methods are surgical removal of ~2/3rd of the contralateral renal mass from the top and bottom poles, or complete ligation of two branches of the renal artery which results in tissue infarction in ~2/3rd of the kidney, with surgical removal being the more common of the two.[81,177] Traditionally, surgeries on each kidney were performed as two separate surgeries, 1-2 weeks apart (Fig 1.6.3).[81,177]

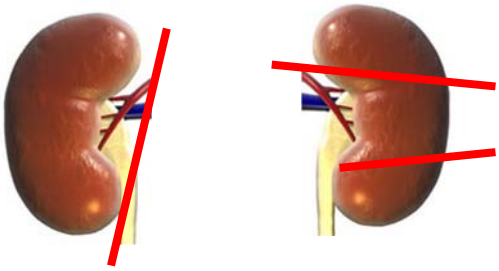

Fig 1.6.3: **Surgical schematic of subtotal nephrectomy**. Red lines indicate where incisions take place. One kidney is removed (left) and the top and bottom poles of the contralateral kidney (right) are removed.

STN being performed on animals dates back to 1889, with STN first being carried out on dogs using surgical removal of a portion contralateral renal mass.[177,178] However, this was of limited success as no changes in urea excretion was detected. More success was obtained in 1899 when three quarters of canine renal mass removal resulted in polyurea and wasting.[177,179] STN has since been performed on a number of non-murine model animals, such as rabbits, cats, sheep and goats.[177] For most of its history, rats have been the predominant model organism on which STN was carried out, with the first such publication dating back to 1936.[177,180] Here, 1-2 weeks

after unilateral nephrectomy, the top and bottom poles of the contralateral kidney were ligated and removed. However, an extremely high mortality rate was associated with the procedure, with only 6 out of 100 rats surviving the surgeries. Platt *et al* (1952) made slight alterations to the surgical protocol in order to reduce mortality rates, such as performing the nephrectomy second and not ligating the renal poles before removal.[177] Further adaptations have been employed over the years to refine the surgery, such as methods to reduce bleeding during the surgeries and the administration of post-operative fluids, but the majority of the surgical methods are largely unchanged.[177]

STN has more recently been performed and characterised in mice, although susceptibility to the model has been found to vary greatly between strains of mice, with the commonly used C57 black strain being highly resistant and sv129 and CD-1 strains being more susceptible.[181]

STN produces a sudden substantial decrease in the number of functional nephrons available, which triggers a number of pathophysiological events.[182] This loss of nephrons also occurs in CKD (albeit over a longer period of time) and results in the decline in renal function which characterises the disease.[183] In order to compensate for the decreased nephron availability and therefore reduced capacity to filter the blood, the remaining nephrons compensate in two main ways: i) nephron hypertrophy and ii) increased filtrative capacity. Cellular hypertrophy or hyperplasia are responsible for the hypertrophy observed in response to STN.[184] Single-nephron GFR increases to obtain a hyperfiltrative phenotype.[183] Here, arteriolar tone decreases, with afferent arteriolar tone decreasing more than efferent arteriolar tone, therefore increasing pressure in the glomerular capillaries and resulting in increased glomerular plasma flow (GFR).[185] Although this compensates for the significant decrease in GFR caused by nephron loss, intraglomerular hypertension in the long term becomes one of the main pathogenic triggers in the model.[183]

Therapeutic intervention with antihypertensive agents to reduce intraglomerular hypertension inhibit future renal dysfunction and injury.[185]

The RAAS is of notable importance to the pathology of STN. ACE inhibitors (which block the formation of angiotensin II), have been found to have larger impacts on intraglomerular pressure reduction than other anti-hypertensive agents, and consistently protect against progressive renal injury in STN.[186] Considerable variation in the susceptibility to developing CKD in response to STN is observed between different mouse strains, with C57 black mice being highly resistant while sv129 mice are sensitive.[181] The reason for this may be related to the renin gene, with C57 black mice having one copy and sv129 having two, resulting in 100-fold higher renin concentrations in the plasma of sv129 mice[81,187]

Intraglomerular hypertension may lead to progressive renal injury through a number of mechanisms. Increased "leakiness" of the glomerular filtration barrier is observed in response to this, owing to increased size of glomerular membrane pores, leading to a reduction in the capacity for size-selectivity of proteins.[185] Therefore, increased protein occurs in the glomerular filtrate, which is then reabsorbed by proximal tubular epithelial cells.[185] This intracellular protein overload can cause apoptosis and dysfunction in tubular epithelial cells, leading to interstitial inflammation (with macrophage infiltration being a prominent feature), interstitial fibrosis, and ultimately nephron loss, which further reduces the filtrative capacity of the remaining renal tissue and forms a cycle through which progressive renal injury is produced.[185] Glomerulosclerosis and glomerulomegaly are prominent features of this model.[177]

STN allows for the measurement of renal functional parameters which are of critical importance in the clinical management of CKD, such as urinary albumin:creatinine ratio (ACR), serum creatinine and serum phosphate.[186] STN also has a history of successful translation of results to the clinic, with multiple therapeutic strategies trialled in STN later being successfully deployed in the management of human CKD,

such as ACE inhibitors, which are currently the primary therapeutic intervention.[102,177,188–191]

Cardiorenal syndrome, similar to what is observed in clinical CKD cohorts, is observed in animals subjected to STN. Significant variability exists in the literature in regard to the cardiac effects of STN, likely resulting from inconsistent methods, model duration, and model organism or strain used. The most consistent findings are cardiac hypertrophy and systemic hypertension, with some studies showing diastolic dysfunction.[189,190,192–197] This provides a platform for the assessment of potential therapeutic interventions in CKD on cardiorenal endpoints such as hypertension, especially if methods could be standardised between studies.

1.6.4: Ischemia reperfusion injury (IRI)

Ischemia reperfusion injury in humans is a prevalent cause of acute kidney injury (AKI).[198] This can be modelled *in vivo* using mice, rats, rabbits, dogs and pigs.[198] Here, unilateral or bilateral IRI can be carried out by clamping off the blood supply to one or both kidneys, respectively, for a short period of time.[198] This causes PTEC injury and apoptosis, along with endothelial cell activation, leading to up-regulation of pro-inflammatory mediators and subsequent influx of pro-inflammatory cells.[198] If renal injury from the initial IRI is severe enough, mice will develop progressive renal fibrosis over a number of weeks.[198]

1.7: microRNA

microRNAs (miRNAs) are small (19-24 nucleotide) single-stranded non-coding RNA which primarily function as post-transcriptional repressors of gene expression.[199] First discovered in 1993, miRNAs have had a substantial impact on our understanding of how gene expression is regulated.[199] miRNAs have since been demonstrated to have a role in a wide variety of biological processes, including development, normal body system homeostasis and physiology, as well as in many disease states.[199] miRNAs have been proposed and explored as therapeutic interventions and biomarkers in many pathologies.[200–205]

1.7.1: miRNA biogenesis and function

miRNA biogenesis begins with RNA polymerase II-mediated transcription of the miRNA gene, forming the miRNA primary transcript (pri-miRNA).[206] Pri-miRNA are long transcripts (often >1kb) which contain a 33-35bp double-stranded stem, a terminal loop, and single-stranded 3' and 5' tails. Multiple transcription factors have been found to positively or negatively regulate the transcription of miRNA primary transcripts.[206] The expression of miRNA-encoding genes are also known to be subject to epigenetic regulation (for example, DNA methylation or histone modification).[206,207] Additionally, miRNAs themselves have been shown to regulate the transcription of miRNA host genes via regulation of transcription factor expression.[206]

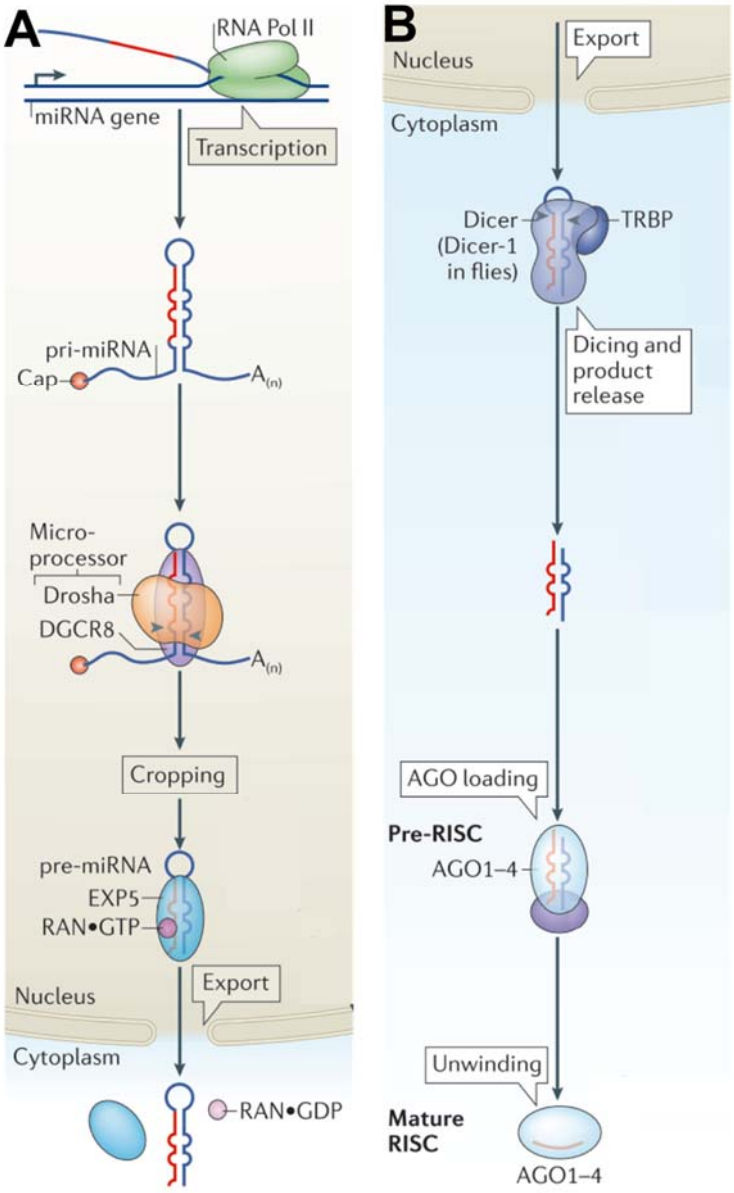

Fig 1.7.1: **miRNA biogenesis pathway**. A = biogenesis within the nucleas. B = biogenesis within the cytoplasm. Primary miRNA transcript (pri-miRNA) is produced from the miRNA host gene before being cropped by the microprocessor complex, forming the pre-miRNA, which is then exported into the cytoplasm via exportin-5 (EXP5), in a GTP-dependant process. The pre-miRNA is then cleaved by Dicer to form a double-stranded RNA duplex which is then loaded into the RISC (RNA-Induced Silencing Complex). A single-stranded mature miRNA-RISC complex is then formed and can bind target mRNA to modulate gene expression.[206]

A number of steps are required to process the pri-miRNA into mature miRNA. The microprocessor complex, consisting of two main proteins, Drosha and DGCR8 (DiGeorge Syndrome Critical Region Gene 8), is the first factor involved in pri-miRNA processing.[206,208] Drosha, the catalytic subunit, is a nuclear RNase III enzyme, while DGCR8 is a double-stranded RNA binding protein.[206,208] The activity of the microprocessor complex is known to be subject to regulation by certain factors, for example, p53 and SMAD3 promote microprocessor activity, while oestrogen signalling (ER-α) inhibits activity.[207] Also, many auxiliary factors facilitate or inhibit the processing of specific miRNA or miRNA processing in general.[206,207]

Drosha cleaves the pri-miRNA at a site which is ~11bp from the basal junction (the site at which the stem loop begins, near the single-stranded RNA tails) and ~22bp from the apical junction (where the terminal loop begins), leaving a ~60-100 nucleotide small hairpin structure called the precursor-miRNA (pre-miRNA).[206,207] A 2 nucleotide overhang is present at the 3' end. A complex is then formed with Ran guanosine triphosphate (RanGTP), which facilitates the interaction with Exportin-5 (Exp5), a substrate-specific nuclear membrane transporter, which transports the pre-miRNA out of the nucleus and into the cytoplasm.[209] Exp5 directly binds correctly processed pre-miRNA only (recognising the 2 nucleotide 3' overhang), releasing it from Drosha, and therefore acting as a quality control factor as well as nuclear export factor.[209] GTP (guanosine triphosphate) is hydrolysed during transport of the pre-miRNA through Exp5, thus releasing it on the cytoplasmic side.[206] Nuclear levels of RanGTP are high, while cytoplasmic levels are low, facilitating the release of the pre-miRNA in the cytoplasm after transport.[209]

Cytoplasmic processing begins with the Dicer-TRBP (TAR RNA-binding protein) complex.[206] Dicer is another RNase III, which binds and cleaves the double-stranded RNA of the pre-miRNA.[206] TRBP is a double-stranded RNA binding protein which facilitates the interaction between the pre-miR and Dicer.[206] Dicer can bind and recognise the 3' 2 nucleotide overhang or the 5'-terminal phosphate group at the end

of the pre-miR and cleave it at a certain number of nucleotides away (~22), near the terminal loop, thus forming a double-stranded RNA duplex.[206,210]

Next, the RNA-induced silencing complex (RISC) is formed. Here, the RNA duplex being loaded onto one of four Argonaute (AGO) proteins in an ATP-dependant process.[206] The duplex then unwinds and one strand is ejected from the complex and degraded, thus, along with a number of auxiliary proteins, forming the mature RISC complex.[206,211] Target mRNA are recognised via complimentary (or semi-complimentary) matching of the miRNA seed sequence (a sequence 2-7 nucleotides from the 5' end), located on primarily the 3'UTR (untranslated region) of the mRNA.[211] Translation of the target mRNA is then repressed, and/or mRNA breakdown can occur.[212]

Selection of which strand is kept and which is discarded is made based on relative thermodynamic stability at the 5' end, with the less stable strand usually being selected to be the guide strand, with the discarded strand being referred to as the passenger strand.[206] Another factor is the nucleotide which is located at position one, with AGO proteins having a preference for nucleotide U.[206] However, strand-selection is not consistent with these rules all the time, which results in the passenger strand being retained some of the time.[206] Mature miRNAs are denoted as -5p or -3p (for example, miR-1-5p) depending on which strand was retained by the AGO protein, with 5p being the most common guide strand.[213] However, certain miRNAs, such as miR-214, have the 3p strand as the guide strand and 5p as the passenger.[213] In addition, the predominant guide strand can switch (called arm switching) depending on tissue type , for examples, miR-145-5p is most abundant in the brain, testes and ovaries, while miR-145-3p is most abundant in embryonic tissue samples.[206,213] Arm switching has been suggested to be related to alternative Drosha processing which results in modified thermodynamic stability of duplex ends.[206,213]

1.7.2: miRNA in development

miRNAs are known to play important roles in development and organogenesis, with, for example, Dicer knockout mice dying at embryonic day 7.5.[214] Here, abnormal morphology was observed in the majority of organs and a global lack of stem cells.[199] Embryonic stem cells (ESCs) are cells which can differentiate into many different cell lineages.[215,216] The regulation of self-renewal and differentiation of these ESCs is of critical importance to development, and these processes have been demonstrated to be modulated by miRNAs in many instances.[216] Expression of certain miRNAs are high in ESCs and decline as differentiation occurs (such as the miR-302 family), while the opposite pattern is found in other miRNAs (for example let-7 and miR-145).[216] ESC enriched miRNAs such as miR-302 have been found to be up-regulated by key pluripotency-related transcription factors and are involved in maintaining the self-renewal, multipotent phenotype of ESCs.[216] This is in contrast to miRNA such as Let-7, which is enriched in differentiated cells and functions to inhibit key factors involved in the maintenance of pluripotency.[216]

miRNAs have been found to be of critical importance to cardiac differentiation, in particular miR-1 and miR-133.[215] These miRNAs are expressed at the early stages of when embryonic stem cells (ESCs) select the cardiac mesoderm lineage and function to inhibit endoderm and neuroectoderm differentiation while promoting differentiation towards a cardiac lineage.[215]

Renal development is highly complex, involving the coordinated growth and differentiation of multiple cell types, many of which are highly specialised renal cell types.[217] A plethora of genes are regulated in a site-specific and temporally-sensitive fashion to facilitate kidney organogenesis.[217] For example, Osr1 (odd-skipped related transcription factor 1) is expressed in the intermediate mesoderm and has a role in the establishment of the nephron progenitors.[217,218] miRNAs are known to be important in renal development and the maintenance of differentiated cell types. Conditional knockout of Dicer in nephron-linage cells results in premature

termination of nephrogenesis.[217] Certain miRNAs are highly expressed in the adult kidney and may be involved in the maintenance of kidney homeostasis. For example, miR-30 has been found to inhibit Snail-1 (snail family transcriptional repressor 1) expression to promote the terminal differentiation of renal epithelial cells.[217]

1.7.3: miRNA in disease and as therapeutic targets

miRNAs have been implicated in a vast array of disease states, from motor neuron diseases to cancers.[219–222] A number of miRNAs have been suggested to be involved in pro-fibrotic and anti-fibrotic pathways in renal fibrosis.[223–227] Due to this, there has been considerable interest in exploring miRNA as therapeutics in a variety of contexts. Although no miRNA-based therapeutics are currently approved, a number of clinical trials are ongoing in FDA (Food and Drug Administration) phase I and phase II.[228] miRNA-based therapeutics can be assigned to two categories: miRNA mimetics and miRNA inhibitors (anti-miRs).[229]

miRNA mimetics typically are synthetic double-stranded RNA with the same sequence as a particular miRNA, which aim to increase expression and activity of said miRNA.[229] The structure of the pre-miRNA is mimicked, with the goal being the synthetic miRNA will be processed by endogenous miRNA maturation machinery and be assembled into a functional RISC complex.[230] miRNA mimetics typically require the use of additional delivery systems, such as liposomes, lipoprotein-based carriers or nanoparticles, for their effective delivery to their site of action.[231] miRNA mimetics have been of particular interest in cancer, where restoring the expression of tumour-suppressor miRNA has been found to be advantageous in *in vitro* and pre-clinical *in vivo* models.[229] The first miRNA mimetic clinical trial was a miR-34 mimetic, developed by Synlogic, with potential application as an anti-cancer drug, as miR-34 has been found to be a tumour-suppressor miRNA which is down-regulated in many cancers.[231] However, the trial was halted in phase I due to serious, immune-related, adverse events occurring.[231] A miR-29b mimetic, developed by miRagen Therapeutics, is currently in phase I trials, with future applications in the prevention of keloid and

scar tissue.[228,231,232] Enhanced targeting of site of delivery using a "TargomiR" has also been used in a recently completed phase I trial. Here, a miR-16 mimetic was delivered to mesothelioma patients in a delivery vesicle, utilising an anti-EGFR (epidermal growth factor receptor) antibody, as high EGFR expression is consistently observed in lung cancers.[228]

miRNA inhibitors, or anti-miRs, are single-stranded oligonucleotides with a sequence which is complementary to that of the mature target miRNA.[229] Anti-miRs bind their target RNA and therefore prevent said miRNA from interacting with its target genes.[229] Anti-miRs can be employed in situations where a certain miRNA is up-regulated and is involved in promoting a certain pathology. Unlike miRNA mimetics, anti-miRs do not necessarily require additional delivery systems and can be administered dissolved in saline solution.[231] A number of modifications to the oligonucleotide backbone have been implemented to streamline the suitability of these compounds for therapeutic intervention.[233] Modifications have been introduced to confer resistance to nucleases, improve binding affinity with the target miRNA, and improve accumulation in certain organ systems.[233]

Anti-miR compounds typically accumulate in high concentrations in the kidney and liver, making these organs particularly easy to target, although anti-miRs have also been found to accumulate in peripheral tissues such as the heart, lungs, spleen and bone marrow to a degree which allows them to be pharmacologically active at these sites.[233]

Several clinical trials involving anti-miRs are currently ongoing.[228] Anti-miR-122, developed by Santaris Pharma/Roche, is in phase II trials in patients with hepatitis C. Recruitment for phase II trials for anti-miR-155, developed by miRagen Therapeutics, as an intervention in cutaneous T-cell lymphoma are currently underway. Phase II trials for anti-miR-21, developed by Regulus Therapeutics with partner Genzyme (Sanofi), in Alport syndrome are ongoing. Anti-miR-92, developed by miRagen

Therapeutics, is in phase I trials, with future applications in promoting wound healing and treating heart failure. anti-miR-10b has been announced as a clinical candidate by Regulus Therapeutics, with potential as a therapeutic in glioblastoma multiforme. Anti-miR-17 is being developed by Regulus Therapeutics, currently in stage I clinical trials, for future application in the treatment of autosomal dominant polycystic kidney disease.[234]

1.8: miR-214 in development, disease and homeostasis

The miR-214 cluster is a highly evolutionarily conserved cluster of miRNAs (conserved across vertebrates[235]) produced from the long non-coding RNA (lncRNA) Dnm3os (DNM3 opposite strand/antisense RNA), which is a 7.9-kb antisense transcript to the 14th intronic region of the Dynamin-3 (Dnm3) gene on mouse chromosome 1 (Fig 1.8.1).[236–238]

Dnm3os functions as a primary transcript (pri-miRNA) from which miR-214-3p (major strand), miR-214-5p (minor strand), miR-199a-5p (major strand) and miR-199a-3p (minor strand) are produced.[236,237] In addition, miR-199a can also be produced from an antisense transcript to the 16th intronic region of Dynamin-2 on mouse chromosome 9.[238] Dnm3os has also been suggested to have functions independent of the miRNAs it hosts, with it being implicated in epigenetic regulation, for example promoting permissive histone modifications (such as H3K9ac (H3 lysine 9 acetylation)) at the promoters of proinflammatory genes (such as IL6) in macrophages in diabetes mellitus.[239]

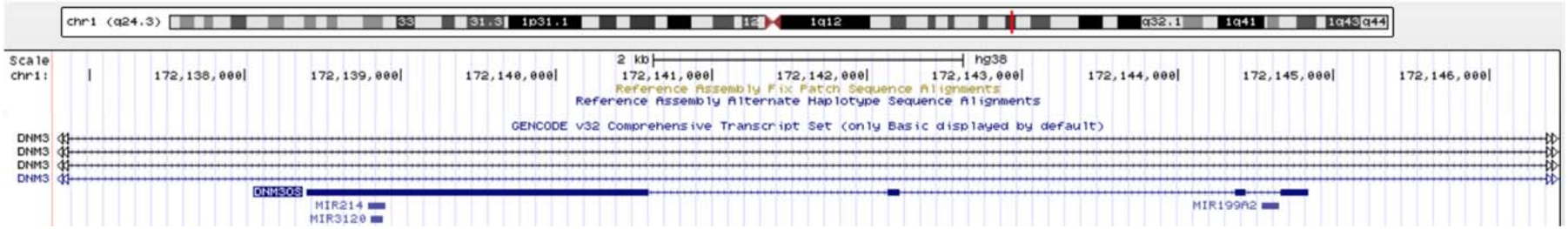

Fig 1.8.1: **Human genomic locus containing the miR-214 cluster as viewed in UCSC Genome Browser**. Genomic region viewed = chr1:172,136,786-172,146,451. Human Dec. 2013 (GRCh38/hg38) assembly used.

The miR-214-3p mature sequence is conserved across many vertebrate species, including homo sapien (human/hsa), mus musculus (mouse/mmu), rattus norvegicus (rat/rno), xenopus laevis (African clawed frog/xla), anolis carolinensis (Carolina anole lizard/aca), macaca mulatta (rhesus macaque/mml), gadus morhua (Atlantic cod/gmo), dasypus novemcinctus (nine-banded armadillo/dno), and columba livia (rock dove/cli) (Fig 1.8.2).

```
hsa-miR-214-3p      ACAGCAGGCACAGACAGGCAGU
mmu-miR-214-3p      ACAGCAGGCACAGACAGGCAGU
rno-miR-214-3p      ACAGCAGGCACAGACAGGCAG-
xla-miR-214-3p      ACAGCAGGCACAGACAGGCAG-
aca-miR-214-3p      ACAGCAGGCACAGACAGGCAGU
mml-miR-214-3p      ACAGCAGGCACAGACAGGCAG-
gmo-miR-214-3p      ACAGCAGGCACAGACAGGCAG-
dno-miR-214-3p      ACAGCAGGCACAGACAGGCAGU
cli-miR-214-3p      ACAGCAGGCACAGACAGGCAGU
                    **********************
```

Fig 1.8.2: **Alignment of the mature miR-214-3p sequences from 9 species**. Clustal Omega 1.2.4 used to align sequences. Mature miRNA sequences obtained from miRBase.org. * = same nucleotide present at this position in each sequence. - = no nucleotide present at this position.

miR-214 has been implicated in an extremely wide variety of pathologies, homeostatic processes and developmental contexts, encompassing an array of cell types. Table 1.8.1 provides an overview of published literature on miR-214, with the exceptions of cardiac dysfunction and cancer. Here, miR-214 has been found to play a deleterious or positive role in a variety of contexts, with many overlapping (and often contradictory) mechanisms.

Table 1.8.1: **Published reports of miR-214 being mechanistically involved in biological processes or pathologies.**

Pathology/ context	Up or down	Promote or inhibit	Cell type(s)	Pathways
Loss of protective autophagy in atherosclerosis[240]	Up	Promotes	Endothelial cells (ECs)	Inhibits autophagy genes (ATG5, ATG12)
Cutaneous T-cell lymphomas[241]	Up	Promotes	T-cells	Inhibits tumour suppressor Klf12
Salt-sensitive hypertension[242]	Up	Promotes	Renal epithelial cells, outer medulla	Inhibits eNOS
Liver fibrosis[243]	Up	Promotes	hepatic stellate cells (HSC)	Inhibits Sufu to promote HSC activation
Ischemia/reperfusion injury in myoblasts[244]	Up	Inhibits	Myoblasts	Inhibits pro-apoptotic and autophagy genes
Endometriosis fibrosis[245]	Down	inhibits	Endometrial stromal cells	Unclear. Inhibits collagen expression
Proximal tubular cell epithelial to mesenchymal transition (EMT)[246]	Up	Promotes	Human proximal tubular cell line (HK2)	Promoted EMT via E-cadherin inhibition
Bone-marrow mesenchymal stem cell differentiation to osteoblasts[247]	Down	Inhibits	Bone-marrow mesenchymal stem cells (BMSCs)	Inhibits ATF4
Bone marrow monocyte differentiation to osteoclasts[248]	Up	Promotes	Bone-marrow monocytes (BMMs)	Inhibits PTEN
Neural progenitor cell differentiation in neurogenesis[249]	Up	Promotes	Neural progenitor cells (NPCs)	Inhibits Quaking (Qk) to inhibit self-

				renewal and promote differentiation
Embryonic stem cell differentiation to skeletal muscle[250]	Up	Promotes	Embryonic stem cell (ESCs)	Inhibits Ezh2.
Embryonic stem cell differentiation to vascular smooth muscle cells[251]	Up	Promotes	vascular smooth muscle cells (vSMCs)	Inhibits Quaking (Qk)
Retina bipolar cell differentiation[252]	Up	Promotes	Early Retina Progenitor Cells	Inhibits Xotx2 and Xvsx1 expression
Dendrite growth and complexity[236]	Up	Promotes	Hippocampal neurons	Inhibits Quaking (Qk)
Adipose-derived mesenchymal stem cell differentiation to fibroblasts during pelvic floor dysfunction[253]	Up	Promotes	Adipose-derived mesenchymal stem cells (ADMSCs)	Inhibits Mitofusin-2 (Mtf2)
Hypoxic pulmonary hypertension[254]	Up	Promotes	Pulmonary artery smooth muscle cells (PASMCs)	Inhibits PTEN to promote proliferation
Myocardiac apoptosis in ischemia/reperfusion injury[255]	Down	inhibits	Cardiomyocytes (CM)	Inhibits PTEN and Bim1 to inhibit apoptosis
Injury-induced vascular smooth muscle cell migration, proliferation and hyperplasia[256]	Down	Inhibits	vascular smooth muscle cells (vSMCs)	Inhibits NCKAP1 (required) to inhibit vSMC migration and proliferation
Fragmented mitochondria and loss of cell cycle control in Huntington's Disease (HD)[257]	Up	Promotes	Striatal neurons HD model ($STHdh^{Q111/111}$)	Inhibits Huntingtin gene (HTT) and Mtf2.
Parkinson's disease[258]	Down	Inhibits	Midbrain neurons	Inhibits α-synuclein gene expression

Gluconeogenesis[259]	Down	inhibits	Hepatocytes	Inhibits ATF4 to regulate FOXO1 activity
Endothelial cell angiogenesis[260]	----	Inhibits	Human umbilical vein endothelial cells (HUVECs)	Inhibits XBP1 to inhibit HUVEC proliferation and angiogenesis
Renal fibrosis[261]	Up	Promotes	Unknown	miR-214 inhibition significantly reduces renal fibrosis in UUO
Hepatocyte alcohol-induced oxidative stress[262]	Up	Promotes	Hepatocytes	Inhibits GSR and POR gene expression
Co-stimulation-dependant T-cell proliferation[263]	Up	Promotes	T-cells	Inhibits PTEN
Advanced glycation end product (AGE)-induced monocyte apoptosis delay[264]	Up	Promotes	Circulating monocytes	Inhibits PTEN
Tumour-induced Treg expansion[265]	Up	Promotes	Tregs	Inhibits PTEN
Acute kidney injury (IRI)/hypoxic injury to PTECs[266]	Up	Inhibits	IRI: unknown. NRK52E (rat PTEC)	Inhibits Dkk3 to activate Wnt/β-catenin to inhibit apoptosis
Mitochondrial dysfunction in CKD[267]	Up	Promotes	Mitochondria of proximal tubule	Inhibits mt-Nd4l and mt-Nd6
Propofol-induced neuroapoptosis[268]	Up	Inhibits	Hippocampal neuron cell line	Inhibits PTEN
Glomerular hypertrophy in diabetic nephropathy[269]	Up	Promotes	Glomerular mesangial cells	Inhibits PTEN to promote glomerular hypertrophy
Hair follicle stem cell differentiation and proliferation[270]	Down	Inhibits	Hair follicle stem cells (HFSCs)	Inhibits Ezh2, β-catenin, and Tcf4

miR-214 has been found to be involved in promoting the differentiation of multiple progenitor cells along a certain lineage, for example embryonic stem cells (ESCs) to skeletal muscle,[250] ESCs to vascular smooth-muscle cells (vSMCs),[251] Adipose-derived mesenchymal stem cells (ADMSCs) to fibroblasts (in a pathological context; pelvic floor dysfunction),[253] Early retina progenitor cells to retinal bipolar cells,[252] and the induction of neural progenitor cell differentiation during cortical development.[249] miR-214 was also found to inhibit the differentiation of bone-marrow mesenchymal stem cells (BMSCs) to osteoblasts,[271] and the differentiation of hair follicle stem cells,[270] with down-regulation of miR-214 being observed during these processes. The proposed mechanisms for how miR-214 promotes or inhibits the differentiation of these different cell types vary depending on the cell type, but include modulation of RNA-binding proteins (Quaking), modulating epigenetic regulation, modulating proliferation, and inhibiting genes which need to be repressed in the differentiation of that cell type (such as Xotx2 (Xenopus Orthodenticle homeobox 2 S homeolog) and Xvsx1 (Xenopus visual system homeobox 1) in bipolar cell differentiation). Together, these data demonstrate the pleiotropic nature of miR-214's actions, which can vary significantly depending on the cell type or context of its expression.

1.8.1: miR-214 in cardiac injury and disease

miR-214 is highly expressed in the heart.[272] In cardiac injury and disease, miR-214 has been demonstrated to play both a deleterious and protective role, depending on the underlying pathology, cell type, or injury model assessed.[272]

In cardiac hypertrophy, publications are conflicting, with miR-214 being suggested to act as both a pro and anti-hypertrophic factor.[272] miR-214 has been found to be up-regulated in animal models of cardiac hypertrophy which involve the administration of β-adrenergic agonists isoproterenol and phenylephrine, or abdominal aorta constriction (AAC, a model of pressure overload-induced hypertrophy).[272–276] Mechanistically, miR-214 has been suggested to promote cardiac hypertrophy in these models via Ezh2 (enhancer of zeste 2 polycomb repressive complex 2 subunit)

inhibition (causing altered epigenetic regulation of hypertrophy-associated genes), and promote hypertrophic heart failure due to inhibiting the angiogenesis (via inhibition of Xbp1 (X-box binding protein 1) and Vegf) which is necessary to sustain cardiac function in hypertrophy.[272,273,276] Supporting these proposed mechanisms, miR-214 has been demonstrated to impact Vegf expression, Xbp1 expression, angiogenesis, and Ezh2 expression by other independent studies in other biological contexts (table 1.8.1). However, decreased miR-214 expression is observed in the myocardium of patients with cardiac hypertrophy, a finding which was mirrored in *in vivo* and *in vitro* models of angiotensin II-induced cardiac hypertrophy, as well as transverse aortic constriction (TAC, pressure overloading model).[272,277] Here, miR-214 was found to be down-regulated in the cardiomyocytes in an NFκB-dependant fashion, which promoted hypertrophy via reduced inhibition of Mef2c (myocyte enhancer factor 2C), a transcription factor which a key role in cardiac hypertrophy. Mef2c has also been published as a miR-214 target in smooth muscle cell phenotype switching in pulmonary arterial hypertension.[278] Therefore, further studies are needed to elucidate the role of miR-214 in cardiac hypertrophy, especially in the context of chronic kidney disease.

In cardiac fibrosis, miR-214 again has been observed to have contrasting, pro-fibrotic or anti-fibrotic, roles depending on the drug used to induce fibrosis, isoproterenol vs angiotensin II respectively.[272] In the cardiac myofibroblasts responsible for the bulk of the ECM production in cardiac fibrosis, miR-214 is highly expressed.[272] In stimulation with angiotensin II, miR-214 expression decreases, while with isoproterenol stimulation expression increases.[272] Due to this, more studies would be required to better elucidate the role of miR-214 in cardiac fibrosis.

In comparison to cardiac hypertrophy and fibrosis, the role of miR-214 in ischemic heart injury (such as in myocardial infarction (MI)) is much less controversial.[272] Here, miR-214 acts as a cardioprotective miRNA post-MI via its inhibition of PTEN (phosphatase and tensin homolog), promoting cell survival, and Ncx1

(sodium/calcium exchanger-1), thus decreasing intracellular calcium-mediated cell death. Similarly, cardioprotective effects of miR-214 have been found in sepsis-induced myocardial injury.[279]

miR-214 is increased in the serum of coronary artery disease (CAD) patients, where it is a marker of CAD severity and mediator of pathogenesis via inhibition of Vegf in diseased endothelial progenitor cells (EPCs), leading to impaired angiogenesis.[272] miR-214 is thought to exacerbate pulmonary artery hypertension by promoting hypoxia-induced proliferation in pulmonary artery smooth muscle cells (PASMCs).[272,278,280] miR-214 has been demonstrated to promote atherosclerosis via the inhibition of protective autophagy in endothelial cells.[240] miR-214 is thought to promote salt-sensitive hypertension via inhibition of endothelial NOS (eNOS) in the kidneys.[242]

Therefore, although miR-214 may be likely to have a deleterious role in certain cardiovascular diseases (such as CAD, atherosclerosis and salt-sensitive hypertension), well demonstrated protective effects exist in the context of myocardial infarction and ischemic cardiac injury. miR-214 may also have a role in promoting or inhibiting cardiac hypertrophy and cardiac fibrosis. Due to this, application of miR-214 mimetics or inhibitors to the treatment of other disorders must consider the potential for adverse cardiovascular side effects, especially in pathologies with cardiovascular interactions.

1.8.2: miR-214 in cancer

miR-214 has been implicated in the pathogenesis, metastasis, and prognosis of a vast array of cancers.[281,282] Interestingly, miR-214 can act as an oncogenic factor or as a tumour-suppressor depending on the type of cancer, with conflicting reports being present in certain cancers.[281,282]

Increased miR-214 expression has been found in melanoma, osteosarcoma, lung cancer, prostate cancer, nasopharyngeal carcinoma, oral and tongue squamous carcinomas, T-cell lymphoma, and pancreatic cancer.[281,282] This increased expression has been associated with poor prognosis or metastasis in a number of cancers, including osteosarcoma and T-cell lymphoma.[281]

Decreased miR-214 expression has been found in hepatocellular carcinoma, adrenocortical cancer, cervical cancer, intrahepatic cholangiocarcinoma, prostate cancer, multiple myeloma, lymphomas of the primary central nervous system, cutaneous squamous cell carcinoma, bladder cancer, glioma, rhabdomyosarcoma, colorectal cancer, and papillary thyroid carcinoma.[281–283] This decreased expression has been associated with poor prognosis or metastasis in a number of cancers, including hepatocellular carcinoma, bladder cancer, glioma and colorectal cancer.[281]

miR-214 has a more ambiguous or controversial role in some cancers, where reports of both increased and decreased expression exist. These include breast cancer, gastric cancer, oesophageal squamous cell carcinoma, ovarian cancer and melanoma.[281,282] In some cancers, miR-214 expression increase and decrease have both been suggested to be indicators of poor prognosis or metastasis, such as melanoma, ovarian cancer and breast cancer.[281]

A variety of mechanisms and pathways are proposed for how miR-214 confers its pro or anti-cancer actions. These can vary greatly between cancer types. miR-214 has been demonstrated to increase cell survival and proliferation by inhibiting the pro-apoptotic factor Bim1 (Bcl-2 interacting mediator of cell death) in nasopharyngeal carcinoma,[281,284] or by inhibiting PTEN in gastric cancer.[281,285] Conversely, miR-214 has been observed to exert the opposite effect on cell survival and proliferation in breast cancer and hepatocellular carcinoma via inhibition of Ezh2, β-catenin, and Xbp1 in these cells.[281,286–289] miR-214-mediated inhibition of angiogenesis may also be relevant to hepatocellular carcinoma, in which miR-214 down-regulation is

associated with poor prognosis.[281,288] miR-214 promotes migration, invasion, extravasation from blood vessels and metastasis formation in melanoma.[282,290] Here, miR-214 knockdown was found to result in a 40-80% reduction in the mobility of these cells *in vitro*. This is in contrast cervical cancer, where miR-214 inhibits the migration and invasion of these cells (via inhibition of the oncogene FOXM1 (Forkhead Box M1)).[291] Resistance to cisplatin-induced apoptosis has reportedly been modulated by miR-214 also, either increasing or decreasing resistance depending on the type of cancer. miR-214 expression increases *resistance* to cisplatin in ovarian cancer, osteosarcoma and tongue squamous cell carcinomas,[281,292–294] while increasing cisplatin *sensitivity* in non-small cell lung cancer, esophageal squamous cancer, and breast cancer.[295–297]

miR-214 has also been implicated in the regulation of "stemness" or self-renewal capabilities in cancer stem-like cells (CSLCs). CSLCs are multipotent cells with high capacity for self-renewal and resistance to radiation and chemotherapy, which have been suggested to be a source of cancer cells.[298] For example, miR-214 is highly expressed in lung adenocarcinoma-associated CSLCs, where it promotes stemness and self-renewal of these cells by inhibiting catenin beta interacting protein 1 (CTNNBIP1, a negative regulator of Wnt/β-catenin signalling) expression.[298] miR-214 has also been suggested to contribute to the stemness or self-renewal capacity in epithelial ovarian cancer stem cells[299] and hepatic cancer stem cells,[300] through regulating PTEN (promoting Akt signalling) and TFAP2A (Transcription factor AP-2 alpha, a transcription factor with roles in cell growth and differentiation[301]) expression respectively.

Taken together, the varied and often opposing roles of miR-214 observed in cancers speak to the critical importance of cell type and cellular context on how miR-214 exerts an effect. This suggests that in order to study the potential mechanisms of miR-214, investigation of multiple cell types even within the same disease should be considered separate investigations.

1.8.3: miR-214 in renal dysfunction

miR-214 expression is up-regulated in kidney biopsies taken from CKD patients in comparison to healthy controls and correlates with severity of proteinuria and degree of fibrosis.[267,302] miR-214 expression is also increased in animal models of renal fibrosis, such as UUO, IRI, mesangial proliferative glomerulonephritis, and salt-sensitive hypertension.[302,303] *In vitro* models of renal fibrosis, such as TGFβ-stimulation of NRK52E cells (rat proximal tubular epithelial cells) or CRL-2753 cells (rat fibroblasts), miR-214 expression has also been reported to increase.[303]

miR-214 has been reported to be up-regulated in the urine, glomeruli and kidneys in general of patients with diabetic kidney disease (DKD).[224,304,305] Under high glucose conditions, miR-214 has been suggested to promote hypertrophy in PTECs and glomerular mesangial cells, which are key features of DKD.[269,306,307] Here, miR-214-mediated inhibition of PTEN promotes Akt and mTORC1 (Mechanistic target of rapamycin complex 1) activity, therefore promoting cellular hypertrophy in high-glucose conditions. It is unclear if this mechanism applies to non-diabetic kidney disease.

Denby *et al* (2014) reported that genetic knockout or anti-miR-mediated inhibition of miR-214 in the UUO model results in a 93% or 86% reduction in fibrosis respectively.[261] This was a key study which suggested a strong association between miR-214 expression level and degree of renal fibrosis present. However, certain questions need to be answered before the results of this study could be extrapolated to answer the ultimate question of miR-214's potential as a therapeutic intervention in renal fibrosis. Firstly, as the UUO model does not allow for the measurement of markers of renal function, it is unknown if miR-214 has potential efficacy in ameliorating these (although the reduction in tubulointerstitial fibrosis and tubular cell apoptosis would suggest it may). Secondly, due to the lack of glomerulosclerosis and glomerulomegaly in UUO, this study could not assess how any potential miR-214-glomerular interactions may affect renal dysfunction or fibrosis. Thirdly, cardiorenal

syndrome is not modelled by UUO. This is of particular significance to the clinical application of anti-miR-214, as cardiorenal syndrome is a common cause of mortality in CKD patients, while miR-214 has been suggested to play important protective and pathological roles in many forms of cardiovascular disease and cardiac injury. Investigating miR-214 in the context of renal dysfunction-induced cardiovascular dysfunction may be an integral part of evaluating the potential safety of anti-miR-214 intervention in CKD. Fourthly, as miR-214 expression was inhibited or genetically abated prior to initiation of renal injury in this study, it is unclear if miR-214 will function as an effective therapeutic if expression is inhibited after renal dysfunction and fibrosis are already present. This is of considerable importance as CKD diagnosis and therapeutic intervention normally only take place once a significant decline in renal function has already took place. Fifthly, as miR-214 is known to have vastly different functions depending on cell type and biological or pathological context, key to understanding its pro-fibrotic mechanism will be uncovering which cell types in the kidney are relevant to miR-214 in renal fibrosis, and how/if this mechanism differs between different cell types.

miR-214 has been suggested to be protective rather than deleterious in the context of acute kidney injury.[266] The authors found that miR-214 expression was increased in kidneys subjected to IRI, as well as NRK52Es (rat PTEC cell line) subjected to hypoxia. miR-214 was proposed to inhibit Dkk3 (Dickkopf WNT signaling pathway inhibitor 3), therefore promoting Wnt/β-catenin signalling activation, which protected PTECs from hypoxia-induced apoptosis.[266] These results somewhat parallel the anti-apoptotic/protective nature of miR-214 in ischemic cardiac[272] or myoblast[244] injury. However, as the authors demonstrated this effect by administering a miR-214 mimic to further increase expression in IRI, it remains unclear as to if the miR-214 expression increase induced by IRI alone is sufficient to confer protective effects in this context. Further study (most notably with miR-214 knockdown) is required to understand the role of miR-214 in this context.

miR-214 has been observed to have a role in the delay of apoptosis in advanced glycation end products (AGE)-treated monocytes in CKD patients.[264] AGEs are known to cause inhibition of monocyte and macrophage apoptosis, therefore promoting inflammation and inflammatory-response. [264] AGEs accumulate in a variety of contexts, such as diabetes, renal dysfunction, and aging.[264] AGEs are proposed to play a deleterious role in conditions such as dialysis-related amyloidosis and atherosclerosis via inhibition of monocyte or macrophage apoptosis.[264] miR-214 was found to be up-regulated in monocytes in response to AGE-stimulation, where it inhibited apoptosis via PTEN inhibition. miR-214 expression was found to be >140-fold higher in monocytes derived from CKD patients in comparison to healthy donor controls. Over-expression of miR-214 in these cells significantly inhibited apoptosis, while knockdown promoted apoptosis.[264] Therefore, miR-214 may have a deleterious role in CKD in inhibiting monocyte or macrophage apoptosis, which may be especially relevant in pathologies such as dialysis-related amyloidosis, although more study is required to confirm this.

The role of miR-214 in the proximal tubule during renal fibrosis has more recently been elucidated by Bai *et al* (2019).[267] It was found that miR-214 is highly enriched in the mitochondria relative to the cytoplasm of the PTECs, where it's expression increases in multiple *in vivo* and *in vitro* models of renal fibrosis/CKD. Mitochondrial genes mt-Nd4l (NADH dehydrogenase 4L, mitochondrial) and mt-Nd6 (NADH dehydrogenase 6, mitochondrial) were validated as direct miR-214 targets in PTECs subjected to models of CKD. miR-214 was found to induce PTEC-apoptosis and contribute to metabolic dysfunction via disruption of mitochondrial oxidative phosphorylation, thus contributing to progression of the renal injury. Conditional knockout of miR-214 in the proximal tubules (cKO-214) ameliorates these effects, as does inhibition via anti-miR. cKO-214 mice were found to have a 50% reduction in miR-214 expression in the renal cortex of sham animals. Interestingly, although significantly reduced compared to wild-type, marked renal fibrosis appeared to still be present in the cKO-214 kidneys. The authors scored fibrosis in the cKO-214 7-day

UUO kidneys at ~1.2%, with wild-type UUO at ~2.5%. In contrast, Denby *et al* (2014) scored miR-214 global knockout 7-day UUO kidneys at ~0.35%, with wild-type UUO at ~3.35%. This may suggest knockout of miR-214 in all cell types in the kidney is more effective at inhibiting fibrosis development than PTEC-specific knockout. However, as different histological stains (Masson's trichrome vs picrosirius red) and different mouse genetic backgrounds (sv129 vs C57 black) were used by Bai *et al* (2019) and Denby *et al* (2014) respectively, these results may not be directly comparable. Unfortunately, Bai *et al* (2019) did not repeat the cKO-214 UUO experiment using anti-miR-214-mediated knockdown, instead using an albumin-overload model of CKD, as anti-miR-214 resulted in a 90% knockdown in miR-214 expression in the kidneys of sham-operated mice. A parallel study of renal fibrosis in miR-214 PTEC-specific knockout vs global knockout may better elucidate the contribution of miR-214 in the PTECs vs other renal cell types to renal fibrosis.

Therefore, outside the specific context of DKD, PTECs have been the focus of much of the study carried out into miR-214 in renal fibrosis. The contribution of miR-214 to the function or dysfunction in other cell types in renal fibrosis remains to be explored. Given the well-established pleotropic effects of miR-214 on different cell types and in different pathological contexts, this may be of critical importance to fully understanding its pro-fibrotic mechanisms in the kidney. Important aspects to the assessment of miR-214 as a therapeutic target are its influence on cardiovascular injury and disease in a CKD context, its ability to influence renal function, and its suitability as an intervention when renal dysfunction and fibrosis are already present in the kidney.

1.9: Aims of this thesis

Genetic knockout or anti-miR-mediated knockdown of miR-214-3p has been found by Denby *et al* (2014) to significantly inhibit the development of renal fibrosis in the UUO model. However, the UUO model does not allow for the measurement of clinically-relevant markers of renal function or model cardiorenal syndrome.

Therefore, the hypothesis of this thesis is miR-214-3p is an effective therapeutic in chronic kidney disease and the investigation of its mechanism may provide insights into renal fibrosis.

Aims:

1. To characterise the single-step subtotal nephrectomy (STNx) model in terms of CKD phenotype produced, evaluating renal fibrosis, markers of renal function and cardiorenal syndrome.
2. To evaluate the therapeutic potential of anti-miR-214 in the STNx model, when administered after renal fibrosis was already present.
3. To use the reversible UUO model to decipher the cell population-specific expression and differential regulation of miR-214-3p in renal injury and reversal of injury, along with uncovering cell population-specific pro-fibrotic mechanisms of miR-214-3p.

Chapter Two

Materials & Methods

2.1: Common Materials

FBS (foetal bovine serum) – Gibco, 10500064.

Ethanol – Fischer Scientific, E/0650DF/17.

Xylene – Fischer Scientific, X/0200/17.

PBS/DPBS (Dulbecco's phosphate buffered saline) – Gibco, 14190-094.

2.2: Cell Culture

All cell culture experiments were performed under a biological safety class II laminar flow hood using aseptic technique. Two cell lines were used: HeLa and NRK49F. The HeLa cell line is the oldest and one of the most prominent human cell lines available,[308] having being cultured from an adenocarcinoma in 1951.[309] NRK49F is a rat renal fibroblast cell line. The NRK49F cell line was first established by Larco *et al* in 1978, immortalising fibroblasts obtained from normal rat kidney using murine sarcoma virus.[310] Cells were obtained from ATCC (American Type Culture Collection, Manassas, VA, USA).

2.2.1: Culture Conditions and Growth Medium

Cells were grown in 175cm^2 (T175) cell culture flasks (Corning, CLS431080) in cell culture incubators at 37^{o}C in 95% CO2, 5% O2. The following media was used for HeLa cell growth: DMEM (Gibco, 11995040) supplemented with penicillin (100 U/mL, Gibco 15070063), streptomycin (100 µg/mL, Gibco 15070063), and FBS (10% v/v, Gibco 10500064). The following media was used for NRK49F cell growth: DMEM:F12 (Gibco, 11320033) supplemented with penicillin (100 U/mL, Gibco 15070063), streptomycin (100 µg/mL, Gibco 15070063), and FBS (10% v/v, Gibco). All media, reagents and transfection mixes are heated to 37^{o}C in a water bath before being used, unless otherwise stated.

Cells were allowed to reach ~80% confluence in 175 cm^2 flasks before being passaged. To passage, media was removed and cells were washed with sterile PBS before being incubated in 3 mL of 0.25% (v/v) trypsin with 2.21 mM EDTA in HBSS (Corning, 25053CI) for 5 minutes. Trypsinised cells were transferred to a 50 mL falcon tube where the trypsin was neutralised in 10mL of cell growth media and spun down at 1000G for 5 minutes to form a pellet of cells. Cells were then re-suspended in 10 mL of cell growth media and each 175 cm^2 flask was seeded with 1 mL of this suspension and a further 24 mL of growth media was added.

2.2.2: Transfection of cultured cells

For all transfections, a 6x concentrated mix of OptiMEM (Gibco, 31985047) + oligonucleotide (Regulus Therapeutics) + transfection reagent (Lipofectamine LTX/PLUS (Invitrogen, 15338100) for plasmids, Lipofectamine RNAiMAX (Invitrogen, 13778500) for oligonucleotides) was initially created. This allowed for the transfection reagent(s) and the oligonucleotide to interact in a small volume of liquid to facilitate complex formation. The 6x concentrated mix was allowed to sit for 20 minutes before being diluted to 1x concentration by adding the appropriate volume of pen/strep-free media. 1x transfection mix was then added to the cells and allowed to sit for at least 6 hours. The transfection mix was then aspirated, cells were washed and media containing pen/strep was added.

2.3: Methods of *in vitro* analysis

2.3.1: *In vitro* analysis of anti-miR oligonucleotide compound miR-214-3p binding capacity

HeLa cells were used in this experiment. 175 cm^2 flasks were seeded at $3.5*10^6$ cells per flask and allowed to proliferate overnight. Cells were then transfected with a luciferase construct which contained a sequence complimentary to the miR-214-3p seed sequence, as well as a miR-214-3p expression plasmid. Multiple concentrations of luciferase and expression plasmids were transfected for optimisation purposes, along with a control where 0 µg of either compound was transfected. 2.5 µg of luciferase and 5 µg of expression plasmids were found to be optimal to produce a miR-214 inhibition dose-response curve. To transfect, a transfection mix was prepared in 500 µL OptiMEM (Gibco, 11058021), which consisted of 5 µL of Lipofectamine LTX (Invitrogen, 15338100) and 1 µL of PLUS reagent (Invitrogen, 15338100) per 1 µg of total plasmid. The transfection mix was allowed to sit for 10 minutes before 7.5 mL of transfection media (DMEM + 10% v/v FBS, no penicillin/streptomycin) was added. Cells in 175 cm^2 flasks were washed in PBS twice before 8mL of transfection mix + transfection media was added and allowed to incubate for 6 hours. Cells were then washed in PBS twice before being trypsinised and plated in black side/clear bottom 96-well plates (Corning, 3610) at 7500 cells per well in growth media (DMEM + 1% v/v pen/strep + 10% v/v FBS) and were allowed to proliferate overnight.

Six oligonucleotide compounds were transfected at a gradient of doses, with no transfection taking place in rows A and H or columns 1 and 12 (due to potential inaccuracy in florescent measurements taken in wells at the edge of the plate). Oligonucleotide compounds were transfected for 6 hours in OptiMEM + Lipofectamine RNAiMAX (Invitrogen, 13778500) in transfection media (DMEM + 10% v/v FBS, no penicillin/streptomycin), 100 µL per well. Serial dilutions were used to produce a gradient of concentrations at which each of the oligonucleotides were

transfected at, with the initial concentration being 17 nM, diluted 1:3 a total of 8 times (Fig 2.4.1). LightSwitch Luciferase Assay Kit (Switchgear Genomics, LS100) was used to induce luciferase luminescence, which was detected using an automated 96-reader.

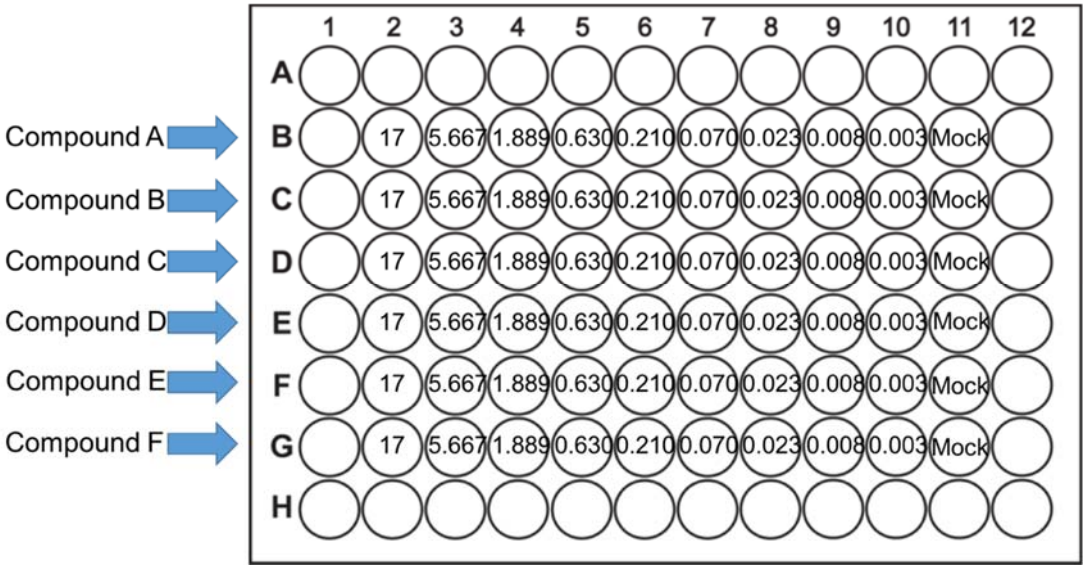

Fig 2.3.1: **Plate map for oligonucleotide transfection.** Rows B-G = one oligonucleotide transfected per row. Rows 2-10 = concentrations (nM) of oligonucleotide transfected, produced via serial dilutions (1:3) from row 2. Row 11 = mock transfected, no oligonucleotide added to transfection mix. Compound F = control anti-miR.

2.3.2: *In vitro* cell culture model of renal fibrosis.

NRK49F cells were used for these experiments. Cells were plated (at passage 4) in cell growth media (DMEM:F12 1:1 + 10% v/v FBS + 1% v/v pen/strep) at $2.5x10^4$ cells per well in 6-well plates (Corning, CLS3516) and allowed to proliferate for 24 hours. Cells were then serum-starved for 48 hours by aspirating growth media, washing in PBS, then placing 2 mL of low FBS media (DMEM:F12 + 0.1% v/v FBS + 1% v/v pen/strep) per well. Anti-miR-214 and control anti-miR oligonucleotide compound (compounds A and F, respectively, as in Fig 2.3.1) were transfected for 6 hours at 1 nM and 0.5 nM concentrations using Lipofectamine RNAiMAX. For each concentration of each oligonucleotide, 3 wells were treated with recombinant human TGFβ1 (Sigma-Aldrich, T7039) at 20 ng/µL per day for 3 days, and 3 wells were left untreated. Media was replaced on all cells with each treatment of TGFβ. RNA was extracted 24 hours after the third treatment with TGFβ.

2.4: Gene and miRNA expression analysis

2.4.1: RNA extraction

RNA extraction was carried out using RNeasy 96 Kit (Qiagen, 74182) for cell culture experiments or RNeasy mini kit (Qiagen, 74106) for samples derived from *in vivo* experiments, according to manufacturer instructions. All steps, bar centrifugation, took place in a fume hood unless otherwise stated.

When extracting RNA from cultured cells, the cell culture media was aspirated and 700 µL of Qiazol was added per well in a 6-well plate. This was allowed to sit for 5 minutes at room temperature, to provide adequate time for the Qiazol to lyse the cells and liberate RNA. The cell culture plate was then tilted and the surface of each well washed with the Qiazol present, before being placed in 1.5 mL Eppendorf tubes. Samples were stored at -80^{o}C until required or used immediately.

When extracting RNA from animal tissue, the sections of tissue were placed in a RNase-free 2 mL Eppendorf tubes with 700 µL Qiazol and one 5 mm stainless steel bead (Qiagen, 69989). The Eppendorfs were loaded into the TissueLyser II (Qiagen, 85300) and were homogenised for 1 minute 30 seconds at 25 Hz. If required, samples were homogenised for a further 1 minute 30 seconds at 25 Hz. Samples were stored at -80^{o}C until required or used immediately.

Samples in Qiazol were stored at -80^{o}C were allowed to fully thaw on ice prior to RNA extraction. 140 µL of chloroform was added to each Eppendorf before shaking for 10 seconds and allowing this mixture to sit for 2 minutes. The Eppendorf tubes were then spun down at 4^{o}C for 15 minutes at 12000 x g, allowing three phases to separate. The lower, organic, phase contained proteins, the interphase (middle) contained DNA, while the upper aqueous phase contained RNA. The upper aqueous phase was removed using a p1000 pipette, with care being taken not to disturb the interphase or lower phase, and placed in a new nuclease-free 1.5 mL Eppendorf tube. 1.5 times

the volume of upper aqueous phase collected of 100% ethanol was added and mixed by pipetting up and down 2-3 times before being transferred to an RNeasy mini column. Columns were spun down at room temperature for 15 seconds at 8000 x g and flow through was discarded.

DNA digest was then carried out to remove any contaminating genomic DNA present. Using RNase-free DNase Set (Qiagen, 79256) according to manufacturer instructions, 10 µL of DNase enzyme was added to 70 µL of RDD buffer, with 80 µL of this mixture being added per sample and allowed to sit for 15 minutes at room temperature. This is important as certain Taqman gene expression probes can detect genomic DNA and therefore the presence of this may cause downstream analysis of gene expression to be inaccurate.

700 µL of RWT buffer was then added and spun down at room temperature for 15 seconds at 8000 x g and flow through discarded. 500 µL of RPE buffer was then added and spun down at room temperature for 15 seconds at 8000 x g and flow through discarded. 500 µL of RPE buffer was again added before centrifugation at room temperature for 2 minutes at 8000 x g. Columns were then transferred to clean collection tubes and spun down for 1 minute at 16000 x g to ensure as much residual liquid as possible was removed from the column, as this could contaminate the RNA yield. Finally, to elute the RNA bound to the columns, nuclease-free water was added to the column and allowed to sit for 1 minute at room temperature. The volume of nuclease-free water added varied depending on the expected RNA yield, for example, 40 µL was used when extracting RNA from animal tissues while 20 µL was used when extracting from cultured cells. The columns were spun down at room temperature for 1 minute at 8000 x g, and to maximise RNA yield, the resulting elute was re-added to each column, allowed to sit for 1 minute, then was spun down at room temperature for 1 minute at 8000 x g. The resulting elute was immediately placed on ice or placed in a -80^{o}C freezer for longer-term storage.

2.4.2: RNA quantification and standardisation

If necessary, RNA was allowed to fully thaw on ice. RNA was kept on ice at all times to protect against RNA degradation. NanoDrop 1000 Spectrophotometer (Thermo Fisher Scientific) was used to determine RNA concentration (ng/µL) and observe the presence or absence of certain contaminants from the RNA extraction process. RNA concentration was then standardised, using nuclease-free water, to a single concentration in all samples to streamline downstream analysis (typically 200 ng/µL when RNA yields were sufficient).

2.4.3: Reverse transcription

For gene expression analysis, cDNA was synthesized using Applied Biosystems High-Capacity cDNA Reverse Transcription Kit (Applied Biosystems, 4368813). Between 500 ng and 1 µg of RNA was added to each cDNA synthesis reaction depending on the minimum RNA yield achieved from each experiment. Reagents and RNA were allowed to fully thaw on ice and remained on ice until being placed in the thermal cycler. Reagents and RNA were added (as per table 2.4.1) to a nuclease-free 96-well plate to achieve a final reaction volume of 20 µL per sample. On each cDNA plate, a reverse-transcription (RT) control was used, where the volume of multiscribe added to non-control samples was replaced with nuclease-free water. The 96-well plate was sealed using an adhesive PCR plate seal (Thermo Scientific, 11570274) and spun in a plate centrifuge at 500 x g for 20 seconds.

A thermal cycler was used to produce the following conditions: 25^{o}C for 10 minutes to permit random hexamers to anneal, then 48^{o}C for 30 minutes for reverse transcription to take place, then 95^{o}C for 5 min to halt reverse transcription via reverse transcriptase denaturation, before sample temperate was cooled to 4^{o}C and removed from the thermal cycler. If >800 ng of RNA was added per reaction, the resulting cDNA was diluted 1:3 with nuclease-free H_2O. cDNA was stored at -20^{o}C.

Table 2.4.1: **Reagents used for cDNA synthesis.**

Reagent	µL per reaction
10x reverse-transcription buffer	2
2.5 mM MgCl2	4.4
10 nM dNTPs	4
2.5 µM Random Hexamers	1
0.4 U/µL RNase inhibitor enzyme	0.4
25 U/µL Multiscribe™ Reverse Transcriptase	0.5
Nuclease-free H_2O	2.7
RNA	5

For miRNA expression analysis, RNA stocks were diluted to 2 ng/µL using nuclease-free H_2O. To reverse transcribe miRNA to cDNA, the TaqMan™ MicroRNA Reverse Transcription Kit (Applied Biosystems, 4366596) was used. 5 ng of RNA was loaded per reaction. Reagents and RNA were allowed to fully thaw on ice and remained on ice until being placed in the thermal cycler. Reagents and RNA were added (as per table 2.4.2) to a nuclease-free 96-well plate to achieve a final reaction volume of 7.5 µL per sample. In contrast to cDNA synthesis, miRNA reverse transcription was carried out using a specific reverse-transcription primer for each miRNA. The 96-well plate was sealed using an adhesive PCR plate seal (Thermo Scientific, 11570274) and spun in a plate centrifuge at 500 x g for 20 seconds.

A thermal cycler was used to produce the following conditions: 16^{o}C for 30 minutes to permit the primer to anneal, then 42^{o}C for 30 minutes for reverse transcription to take place, then 85^{o}C for 5 min to halt reverse transcription via reverse transcriptase denaturation, before sample temperate was cooled to 4^{o}C and removed from the thermal cycler. The reverse-transcription (RT) product was stored at -20^{o}C.

Table 2.4.2: **Regents used for mRNA reverse transcription.**

Reagent	µL per reaction
100 mM dNTPs	0.075
MultiScribe™ Reverse Transcriptase, 50 U/µL	0.5
10x Reverse Transcription Buffer	0.75
RNase Inhibitor, 20 U/µL	0.095
RT primer	1.5
Nuclease-free H_2O	2.08
RNA at 2 ng/µL	2.5

For cDNA synthesis from RNA yield sources, such as from FACS-isolated cell populations from renal tissue (section 5.3), a separate cDNA synthesis/amplification kit and protocol was used: Ovation RNA-Seq V2 (Nugen, 7102-32). This kit allowed for the input of purified total RNA in the range of 500 pg to 100 ng per reaction. 776 pg of RNA was added per reaction.

The use of this kit involved 3 steps: first strand cDNA synthesis, second strand cDNA synthesis, and SIPA (single primer isothermal amplification) amplification. In first strand cDNA synthesis, DNA/RNA chimeric primers bind to the 5' portion of the mRNA Poly-A tail or randomly across the mRNA, with reverse transcriptase extending the 3' end of the DNA portion of the primer. Therefore, the resulting first strand cDNA/mRNA hybrid had a unique RNA sequence at the 5' end of the cDNA strand. In second strand synthesis, the mRNA within the mRNA/cDNA hybrid was fragmented, thus creating priming sites for DNA polymerase to synthesise a second strand, complimentary to the first strand, including the 5' unique sequence of the first strand chimeric primers. Therefore, a double stranded cDNA with a unique DNA/RNA heteroduplex at the 5' end was synthesised. In SIPA amplification, RNase H was used to cut the 5' DNA/RNA heteroduplex, resulting in the production of a specific DNA sequence to which first SIPA primer binds. DNA polymerase then initiates replication of the cDNA from the 3' end of the SIPA primer. RNase H was again used to cut the

RNA site at the 5’ end of the newly synthesised cDNA strand, thus exposing a binding site for SIPA primers to initiate the next round of synthesis. This process is repeated, resulting in rapid amplification of SPIA cDNA.

Table 2.4.3: **Reagents used for Ovation RNA-Seq V2 cDNA synthesis.**

	Reagent	µL per reaction
First strand synthesis:		
	First Strand Primer Mix	2
	First Strand Buffer Mix	2.5
	First Strand Enzyme Mix	0.5
Second strand synthesis:		
	Second Strand Buffer Mix	9.7
	Second Strand Enzyme Mix	0.3
SIPA amplification:		
	SPIA Primer Mix	10
	SPIA Buffer Mix	20
	SPIA Enzyme Mix	10

Table 2.4.4: **Thermal cycler conditions for Ovation RNA-Seq V2 cDNA synthesis.**

Step	Cycling conditions
First strand synthesis	65°C – 2 min, 4°C – 1 min, 25°C – 10 min, 42°C – 10 min, 70°C – 15 min, hold at 4°C.
Second strand synthesis	4°C – 1 min, 25°C – 10 min, 50°C – 30 min, 80°C – 20 min, hold at 4°C.
SIPA amplification	4°C – 1 min, 47°C – 60 min, 80°C – 20 min, hold at 4°C.

2.4.4: Quantitative real-time PCR (qRT-PCR)

Quantitative real-time PCR was used to analyse gene and miRNA expression. Taqman Gene Expression or Taqman miRNA Expression assays (Thermo Fischer) for each specific gene or miRNA were used, along with TaqMan Universal Master Mix II (Thermo Fischer)(Table 2.4.5). A list of Taqman gene and miRNA expression assays used can be found in table 2.4.6.

Each reaction (10 µL total volume) was pipetted into a well of a 384-well plate, with each sample from the cDNA plate being added in technical duplicate to account for potential variation in gene or miRNA expression caused by pipetting. For each 384-well plate, and each set of cDNA, a housekeeper gene was also added. A housekeeper gene is one which remains stable in expression between each of the experimental conditions and was later used in the analysis of qRT-PCR results. For each Taqman assay, two negative controls were used. Firstly, a blank control where no cDNA was pipetted (this volume replaced with nuclease-free water) and secondly, where cDNA from the RT-control was used. These control for potential Taqman assay or nuclease-free water contamination with cDNA or genomic DNA and contamination in the cDNA synthesis/reverse-transcription, respectively.

Table 2.4.5: **Reagents used for Taqman gene/miRNA expression analysis.**

Reagent	µL per reaction
TaqMan Universal Master Mix II	5
TaqMan Gene/miRNA Expression Assay	0.5
Nuclease-free water	3.1
cDNA	1.4

Once pipetting was complete, the 384-well plate was then sealed with MicroAmp Optical Adhesive Film (Applied Biosystems, 4311971) and spun down at 500 x g for 20 seconds. The plate was then placed in the QuantStudio 5 (QS5) Real-Time PCR System (Thermo Fischer) and subjected to the following cycling conditions: 95^{o}C for 10 minutes, then 40 cycles of 95^{o}C for 15 seconds, followed by 60^{o}C for 1 minute.

Taqman qRT-PCR functions as a semi-quantitative measure of gene or miRNA expression via the detection of fluorescence. The Taqman system consists of a double-stranded DNA template (cDNA/RT product), a Taqman probe, target gene/miRNA-specific primers, and Taq polymerase enzyme. Taqman probes contain a fluorophore at the 5' end and a quencher at the 3' end. While the Taqman probe is in its baseline, intact, state, light produced by the QS5 excites the fluorophore and causes it to fluoresce, however, this is not detectable due to this fluorescent energy being transferred to the quencher in a process known as fluorescence resonance energy transfer (FRET). The QS5 initially increases temperature to 95^{o}C to denature the DNA template, then cools to allow the primers and Taqman probe to bind. Taq polymerase then begins synthesis of complimentary DNA strands, which at a certain point will meet the Taqman probe which is bound to a specific sequence matching the target gene of interest. As Taq polymerase possesses exonuclease activity, it degrades the Taqman probe as the extension phase of the PCR progresses. As a result, the 5' fluorophore is released and is no longer in close proximity to the 3' quencher, meaning its fluorescence can then be detected by the QS5. With each cycle of denaturation and cooling, more cDNA is produced by the PCR primers and Taq polymerase, resulting in degradation of more bound Taqman probe which in turn results in more detectable fluorescence. The QS5 measures this fluorescence and outputs which cycle (out of 40) the fluorescence was first detected at a statistically significant threshold, called cycle threshold (Ct), with Ct value being inversely proportional to expression.

To analyse qRT-PCR-derived gene or miRNA expression results, a number of steps were taken. Firstly, blank and RT controls were checked to ensure gene/miRNA expression in these samples was undetectable or very low (>38 Ct). Secondly, technical duplicates were averaged to produce an average Ct for each gene/miR for each sample. Thirdly, gene/miRNA expression was normalised to housekeeper gene expression. Here, the Ct value for the housekeeper gene was subtracted from the gene/miRNA Ct value in the corresponding sample, producing a ΔCt for each gene/miR in each sample. Fourthly, statistical analysis was performed on ΔCt values, as detailed in section 2.20. For illustrative purposes, an experiment with two groups (control and treatment) will be used. Fifthly, ΔCt values were normalised to the average ΔCt for the control group. Here, ΔCts for all samples in the control group were averaged to produce an average control ΔCt value. This average control ΔCt value was then subtracted from each individual ΔCt value from the control and treatment groups, producing a ΔΔCt for each sample. Sixthly, an RQ (relative quantification) value for each sample was determined via the following formula: $RQ = 2^{-\Delta\Delta Ct}$. This RQ value then corresponds to fold-change from the average expression detected in the control group. Seventhly, RQ values were plotted using GraphPad Prism 6.

Table 2.4.6: **Taqman gene or miRNA expression assays used.**

Target	Species	ID
Ppia	Mouse	Mm02342430_g1
Pdgfrβ	Mouse	Mm00735546_m1
Col1a1	Mouse	Mm00801666_g1
Col3a1	Mouse	Mm01254476_m1
Col4a1	Mouse	Mm01210125_m1
Acta2	Mouse	Mm00725412_s1
Mmp2	Mouse	Mm00439498_m1
Mmp14	Mouse	Mm00485054_m1

Tgfβ1	Mouse	Mm01178820_m1
Tgfβr1	Mouse	Mm00436964_m1
Il1β	Mouse	Mm00434228_m1
Tnf	Mouse	Mm00443258_m1
Gapdh	Mouse	Mm99999915_g1
Qk	Mouse	Mm00498991_m1
Sept4	Mouse	Mm00448225_m1
Ppm1a	Mouse	Mm00725963_s1
Smg7	Mouse	Mm01304560_m1
Rybp	Mouse	Mm04203868_g1
Mef2c	Mouse	Mm01340842_m1
miR-21-5p	Mouse	000397
miR-214-3p	Mouse	002306
u6	Mouse	001973
miR-212-3p	Mouse	002551
miR-874-5p	Mouse	465187_mat
miR-874-3p	Mouse	002268
Col1a1	Rat	Rn01463848_m1
Col3a1	Rat	Rn01437681_m1
Col4a1	Rat	Rn01482927_m1
Ctgf	Rat	Rn01537279_g1
Acta2	Rat	Rn01759928_g1
Fbn1	Rat	Rn01514895_m1
Rplp0	Rat	Rn03302271_gH
Let-7a-5p	Rat	000379
miR-214-3p	Rat	000517

2.5: Methods of *in vivo* investigation

2.5.1: Care and maintenance of mice

Mice were group-housed, maintained on a 12-hour day-night cycle and provided access to started chow and water *ad libitum*, as well as environmental enrichment. ARRIVE (Animal Research: Reporting of In Vivo Experiments) guidelines were adhered to for all animal work.

2.5.2: Subtotal nephrectomy (STNx) surgery

The single-step subtotal nephrectomy (STNx) surgical mouse model of chronic kidney disease carried out was the result of adaptations to existing subtotal nephrectomy protocol available, most notably the entire procedure being carried out as a single surgery as opposed to as two separate surgeries. 6-8-week old, male, 129S2/SV mice (Envigo) were used for this animal model unless otherwise stated. The procedure, as well as the post-surgical care and maintenance, followed an approved guideline as agreed with the UK Home Office as stated on PPL P1204DF30.

Mice were selected to receive sham or STNx surgery using an online random number generator (random.org).

Surgical packs were prepared and autoclaved prior to surgery, consisting of heavy blue paper towels, cotton-buds and medical gauze. All surgical instruments were sterilised via autoclave prior to surgery. Where possible, a separate set of surgical instruments was prepared per mouse, otherwise a table-top surgical instrument steriliser was used to re-sterilise instruments between surgeries.

Prior to surgery, the surgical area was prepared. Firstly, a heat mat was placed on the bench to minimise loss of body temperature during surgery and the surgical area was prepared on top of this. Sterile blue paper towel was placed on top of the heat mat and surrounding area, on which only sterile items were placed. The required sterile

surgical instruments were laid out on the blue paper towel, as well as medical gauze, cotton-buds and an aliquot of sterile water to dampen the cotton-buds where necessary. A surgical blanket was also prepared from a sterile blue paper towel to minimise body temperature loss during surgery, which contained a window through which all surgical procedures were carried out. Spongiostan (Ethicon) was cut into small segments and put on a sterile part of the blue paper towel. A lamp was placed facing the surgical area for added visibility. An anaesthetic rig was obtained to induce and maintain anaesthesia during surgery using inhalational isoflurane. A nose cone was secured at the surgical area to maintain anaesthesia during surgery. Immediately prior to surgery, the surgeon put on sterile surgical gloves. After each surgery, the surgical area was replaced with sterile materials.

Anaesthesia was induced using inhalational isoflurane by placing the mouse in an induction chamber, after which the animal was weighed, shaved (the areas around where the flank incisions were to be introduced) and had the shaved areas wiped down with 70% v/v ethanol to remove lose hair and sterilise the area. The mouse was then placed on the prepared surgical area, with its nose placed in the nose cone of the anaesthetic rig. Lacri-lube (Allergan) was placed on the eyes to prevent drying and reflexes were tested immediately before surgery to ensure adequate anaesthesia was induced. Ibuprofen and buprenorphine were administered at this time for post-surgical pain relief.

The mouse was turned on its left side to initiate the procedure. An initial flank incision into the abdomen was made above the kidney using surgical scissors and extended via blunt dissection. Using cotton-buds tipped in sterile water, the kidney was located and carefully manoeuvred close to the incision with organ holders. Using surgical forceps, the adrenal glands were then blunt dissected away from the kidney so as to not remove them while removing the kidney. The renal peduncle was clamped off with a surgical clamp. Using surgical thread, two tight knots were tied between the clamp and the kidney. The kidney was removed using surgical scissors, cutting just

above the location of the knots, taking care to remove remaining renal tissue. The clamp was then carefully removed and signs of bleeding checked for. The abdomen was then closed with biodegradable surgical thread and skin clips used to close the outer incision.

The mouse was then placed on its right-hand side. An incision was made and kidney located in the same manner as previously described, with extra care being made to avoid damaging the fragile liver located just above this kidney. Again, adrenal glands were blunt dissected away from the kidney to avoid removal. The renal artery and vein were carefully clamped off, with a high degree of vigilance to avoid clamping the ureter. It is important that blood-flow to the kidney is clamped off for the shortest amount of time possible (no longer than 5 minutes). Using small surgical scissors, renal mass was removed from the top of the kidney by cutting just above the renal blood supply (Fig 2.5.1). Renal mass was removed from the bottom in the same way, however with special caution being taken to avoid severing (or even nicking) the ureter. The previously cut to size spongiostan was quickly placed on the kidney after removal of each (top and bottom) section. The clamp was then carefully removed, allowing blood circulation to return to the kidney. To allow the spongiostan to assist in the clotting of blood on the face of the surgical incisions, the spongiostan was gently held in place for ~1-2 minutes before subsequent steps were carried out. Slowly, the kidney was manoeuvred back into place in the abdomen, taking care to not displace the spongiostan during this process. Cotton-buds dipped in sterile water may be used to re-moisturise the abdominal wall to make this process more manageable. The flank incision was then closed as previously described.

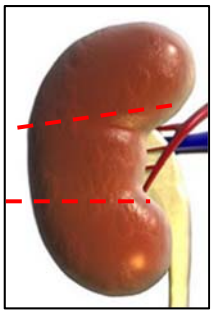

Fig 2.5.1: **Removal of renal mass from top and bottom sections of kidney.** Red broken lines indicate where incisions were made to remove mass from above the top line and below the bottom line.

Post-surgery, mice were placed in a hotbox at 23^{o}C for 5 days, containing mashed food in the cage to allow the mice to eat without having to reach up to the dry food store at the top of the cage. Mice were given a second dose of analgesics 24-hours post-surgery. At 7-days post-surgery, the surgical skin clips were removed.

Animal health following STNx was closely monitored using an animal condition scoring sheet (table 2.5.2). Mice were checked three times per day for the first three-days post-surgery, then twice per week afterwards.

Table 2.5.2: **Animal condition scoring criteria for STNx.** A cumulative score of 5 for any individual mouse resulted in a mandatory cull for health reasons. BC = body condition score, with BC1 being emaciated and BC5 being obese.[311]

General appearance:	**Score**
Normal	0
Slightly unkempt	1
Moderate piloerection	2
Marked piloerection (staring coat)	3
Slightly hunched	1
Markedly hunched	3
Weight and BC score:	**Score**
Normal - < 5% loss and/or BC3	0
Body wt. 5-10% loss and/or BC3/2	1
Body wt. 10-15% loss and/or BC2	2
Body wt. 15-20% loss and/or BC2/1	4
Body wt. ≥ 20% loss and/or BC1	5
Clinical signs:	**Score**
Soft stools	2
Laboured respiration	2
Dull, pale eyes	1
Semi-closed eyes	2
Less inquisitive than normal	1
Little interaction with peers	3
Totally “uninterested”/cold to the touch	5
Tremors/convulsions	5
Marked dehydration (skin pinch test)	4

2.5.3: Urinary analysis through the use of metabolic cages

Metabolic cages were used to collect urine for biochemical analysis during STNx studies. Here, mice were placed in individual cages overnight with water and standard chow available *ad libitum*. Urine for each individual animal was collected and stored at -20^{o}C until required.

2.5.4: Assessment of cardiac structure and function via echocardiography

Echocardiography was carried out by University of Edinburgh pre-clinical imaging facility technician Adrian Thompson as part of the STNx anti-miR-214 study detailed in chapter 4. Echocardiography took place at 2 time-points: 6-weeks post-surgery (immediately prior to the first dose of anti-miR or control was administered) and 10-weeks post-surgery. Mice were anaesthetised with inhalational isoflurane during the procedure. Hair on the chest and upper abdomen was removed using hair removal cream to enable a clear image to be obtained. Lacri-lube (Allergan) was placed on the eyes to prevent drying. The mouse was then placed on a heat pad and tail pinch performed to confirm anaesthesia. A rectal thermometer was inserted to monitor body temperature throughout the procedure, which was maintained at 37^{o}C ± 0.5^{o}C by adjusting the heat pad temperature. Electrode gel was placed on each of the four paws and were taped to the ECG electrodes. Warm ultrasound gel was applied to the chest area of the mouse, with bubbles in said gel being avoided as these can interfere with obtaining a clear image. VisualSonics Vevo 770 High-Resolution In Vivo Micro-Imaging System (FujiFilm) was used to record data for future analysis. A parasternal long-axis view of the heart was used to obtain EKV (ECG-gated Kilohertz Visualization) over one cardiac cycle. Spectral Doppler was carried out in parasternal short-axis view and used to assess mitral valve and pulmonary artery blood-flow. Doppler sample volume was placed across the mitral valve for measurement of E (early) and A (late, atrial) wave velocity and deceleration time. Doppler sample volume was placed at mid-left ventricular level to measure isovolumic contraction (IV CT) and isovolumic relaxation (IV RT) times, ejection time (ET) and myocardial performance index (MPI). Parasternal short-axis view of the pulmonary artery was used to obtain

spectral Doppler measurements of pulmonary artery acceleration time (PAAT) and velocity time integral (VTI).

Analysis of echocardiography data was carried out using VisualSonics software (FijiFilm)(Fig 2.5.3). For EKV analysis, trace lines were drawn along the epicardial and endocardial borders at both end systole and end diastole. Left ventricle (LV) major axes were also traced at end systole and end diastole by drawing a line from the LV apex endocardium or LV apex epicardium, to the mitral valve line. These resulted in the measurement of the following parameters: endocardial volume at diastole (µL), endocardial volume at systole (µL), endocardial stroke volume (µL), ejection fraction (%), fractional area change (%), endocardial area change (mm^2), cardiac output (mL/min), average cardiac wall thickness (mm), and LV mass (mm^2).

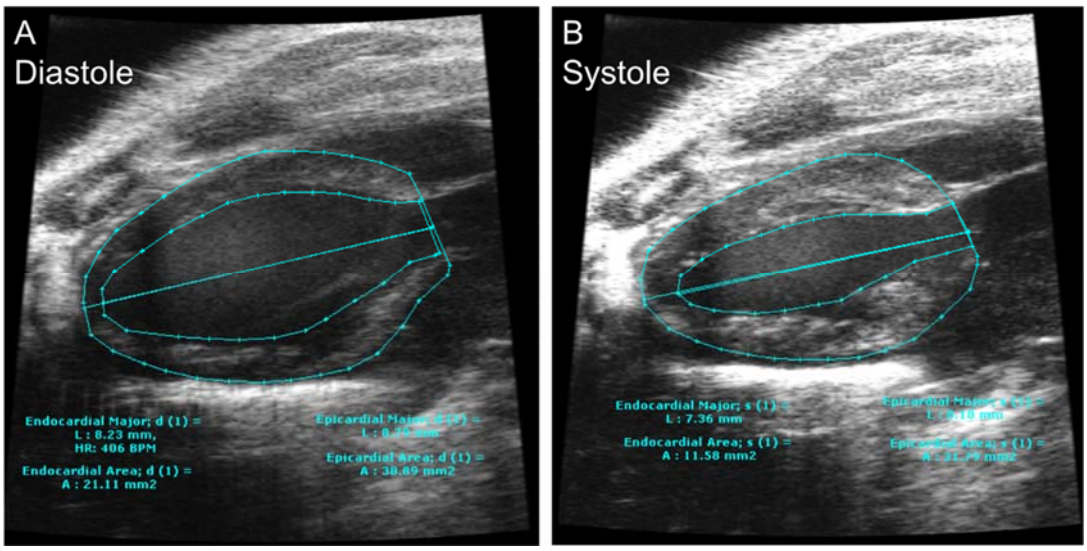

Fig 2.5.3: **Analysis of EKV echocardiography using VisualSonics software.** A = end diastole, B = end systole. At both end diastole and end systole, the following was carried out: Endocardial area (mm^2) was measured via drawing trace lines along the endocardial border, epicardial area (mm^2) was measured via drawing trace lines along the epicardial border, endocardial major length (mm) was measured via drawing a line from the endocardial apex to the mitral valve line, and epicardial major length (mm) was measured via drawing a line from the epicardial apex to the mitral valve line.

2.5.5: Blood pressure measurement

Assessment of blood-pressure was carried out via a non-invasive tail-cuff method.[312] Mice were placed in a hot-box at 32^{o}C for 5-10 minutes before being placed in custom-made apparatus to secure the mouse during blood-pressure measurement. The mouse was allowed to acclimate to the apparatus before the tail-cuff was placed on the upper part of the tail, close to but not in contact with the body. Custom software was then used to record blood pressure.

2.5.6: Reversal of UUO surgical methods

The reversal of UUO (rUUO) model was performed as detailed in Hesketh *et al* (2014),[161] with the exception that inhalational isoflurane was used for anaesthesia. The surgical area, use of surgical instruments, and analgesics used was as described in relation to STNx. Prior to each surgery, anaesthesia was induced in an induction chamber, the mouse was weighed, shaved, wiped with 70% v/v ethanol to remove lose hair, Lacri-lube (Allergan) was applied to the eyes, analgesics were administered and the mouse was placed on its back (supine position) on the surgical area, with its snout in the anaesthetic nose cone, limbs secured to surgical area with low-tack adhesive tape and covered with a surgical blanket. Toe/tail-pinch reflexes were measured immediately prior to making the initial surgical incision to ensure sufficient anaesthesia has been induced.

In the initial surgery, UUO is performed as followed. Access to the peritoneal cavity is provided via midline laparotomy. The left ureter is isolated and ligated near the bladder using 6/O black braided silk suture, thus obstructing the ureter and preventing urine from flowing into the bladder. A soft-walled silicone plastic tubing with 1 mm internal and 2 mm external diameter was placed around the ureter and secured with 6/O black braided silk suture. This prevented expansion and damage of the ureter which may impede the future rUUO surgery and/or successful reversal of injury. The intestines were placed back in the peritoneal cavity and the incision was closed using 5/O black braided silk suture and skin clips. The mice were allowed to

recover in a hot box for 24 hours. Sham surgery was performed by opening the peritoneal cavity and locating the left ureter. Sham and UUO groups were sacrificed at 7-days after this procedure, whereas the rUUO groups were subjected to a second surgery at 7-days post the original surgery.

For the rUUO surgery, the mice and surgical conditions were prepared as per the previous surgery. Skin clips and stiches were removed to open the peritoneal cavity. The left ureter was isolated and the plastic tubing around the ureter was removed. The ureter was cut just above the suture and liquid was allowed to drain onto a sterile piece of surgical gauze. The ureter was then re-implanted into the bladder, thus allowing urine to flow into the bladder and reversing the UUO injury. The peritoneal cavity was closed and mice allowed to recover as in the previous surgery. Mice were sacrificed at 7, 14, and/or 28 days post-rUUO surgery.

2.5.7: Animal sacrifice and tissue collection

2.5.7.1: Subtotal nephrectomy

Animals were sacrificed via schedule one methods (CO_2 chamber for 5 minutes with confirmation of death via cervical dislocation). The abdomen was opened using surgical scissors, then the chest cavity was opened to expose the heart. Blood was drawn from the heart using a 23-gadge needle and syringe and placed in a 1.5 mL Eppendorf tube. The blood was allowed to clot for ~1 hour before being spun down in a centrifuge at 3000 x G for 15 minutes. Serum was taken from the top of the Eppendorf (without disturbing the blood clot), placed in a clean 0.5 mL Eppendorf and stored at -80^{o}C. The mice were perfused through the heart with 3 mL of PBS until the liver became pale. This removes blood from the organs which may otherwise interfere with histological staining. The right tibia was measured with a ruler and the length noted.

The heart was removed and weighed before being cut (horizontally) into 3 sections. The top section and bottom sections were placed in 1.5 mL Eppendorf tubes in liquid nitrogen for later RNA or protein extraction respectively. These samples were later transferred from liquid nitrogen to long-term storage at -80^{o}C. The middle section was placed in 10% v/v formalin for 24 hours before being transferred to 70% v/v ethanol. Tissue sections in 70% v/v ethanol were then sent to QMRI SURF histology for embedding in paraffin blocks.

The remnant kidney was removed and fatty deposits were removed using scissors before being weighed. The kidney was cut (horizontally) into 3 sections and these were processed as the heart sections were. The liver, spleen and lungs were processed as per table 2.5.4.

When processing sham kidneys, the left kidney (matching the STNx) was taken. The top and bottom poles were removed prior to processing, as to resemble the STNx kidneys.

Table 2.5.4: **Sacrifice of mice post-STNx and tissue collection.**

Organ	Weighed	RNA	Protein	Histology
Kidney	✓	✓	✓	✓
Heart	✓	✓	✓	✓
Liver	✓	✓	✓	✓
Spleen	✓	✓	✓	✕
Lungs	✕	✓	✓	✕

2.5.7.2: rUUO

Mice were sacrificed via schedule one methods (CO_2 chamber for 5 minutes with confirmation of death via cervical dislocation). The abdomen was opened using surgical scissors, then the chest cavity was opened to expose the heart. The mice were perfused through the heart with 3 mL of PBS until the liver became pale. The left kidney which UUO or rUUO surgery was performed on was removed, with the contralateral kidney being discarded. The left kidney was also taken from sham mice, with the contralateral kidney discarded. The kidney capsid was removed and slices taken horizontally for RNA, protein, FACS and histology. RNA and protein slices were placed in 1.5 mL Eppendorfs and snap-frozen in liquid nitrogen. Slices for FACS were collected in FACS buffer and placed on ice. Slices for histology were placed in 10% v/v formalin for 24 hours, then placed in 70% v/v ethanol and sent for embedding in paraffin blocks down downstream analysis.

2.5.8: Biochemical analysis

Biochemical analysis of mouse serum and urine was carried out by Dr. Howie Forbes at the QMRI SURF Specialist Assay Service. 100 µL of serum and 150 µL of urine was provided per mouse. Serum and urine were analysed for creatinine, albumin, urea, calcium and phosphate content.

2.6: Fluorescence-activated cell sorting (FACS)

Prior to starting, FACS buffer, RPMI media and digestion solution were prepared, and water bath was set to 37^{o}C. RPMI media, prepared in a cell culture hood, contained RPMI 1640 media (Gibco, 11875093), 10% v/v FBS and 1% v/v pen/strep. FACS buffer consisted of PBS, 10 mL FBS and 5 mL 0.1M EDTA. RPMI media and FACS buffer were maintained at 4^{o}C. Digestion solution consisted of collagenase II (Sigma C6885) at 0.425 mg/mL, collagenase D (Roche 11088882001) at 0.625 mg/mL, dispase (Gibco 17105-041) at 1 mg/mL, and DNase (Roche 10104159001) at 30 µg/mL.

The kidney sections were chopped with a scalpel and 4 mL digestion buffer was added to the chopped tissue, the mixture was then transferred to 50 mL gentleMACS C tubes (Miltenyi Biotec, 130-093-237). These were then placed in a gentleMACS Dissociator (Miltenyi Biotec). The gentleMACS tubes were then placed in a shaking water bath at 37^{o}C at 120 RPM for 30 minutes, before again being placed in gentleMACS Dissociator. At this point, digestion was stopped by adding 4 mL of FACS buffer, as tissue homogenisation was complete.

The tissue was then filtered through 100 µM, 70 µM and 40 µM gauge filters (Falcon, 352360, 352350, and 352340 respectively). The filtered single-cell suspension was then centrifuged at 500 x g for 5 minutes at 4^{o}C and the supernatant aspirated with a stripette without disturbing the pellet of cells. The pellet was resuspended in red blood cell lysis buffer (abcam, ab204733), with the reaction neutralised after exactly 1 minute by adding 15 mL of FACS buffer. This lysed auto-florescent red blood cells which may have otherwise interfered with FACS. Cell suspension was again centrifuged at 500 x g for 5 minutes at 4^{o}C.

The single-cell suspensions were resuspended in 1 mL FACS buffer and counted before being plated in a 96-well round-bottom plate (Corning 3799), with the appropriate rat anti-mouse antibodies added (table 2.6.1). The following controls

were implemented: unstained cells, single-stain, and FMO (fluorophore minus one). For each experimental group, 1 well was allocated to be not stained with any antibody (unstained control) and 1 well was allocated to be the FMO (fluorophore minus one) per antibody. A single stain control for each conjugated antibody was added to the plate, with compensation beads (Bioscience 01-222-41) added instead of cells to ensure antibody binding. Once the cells were plated, the plate was centrifuged at 500 x g for 3 minutes at room temperature. The supernatant was discarded and 25 µL of blocking solution was added per well (mouse FC block (x2 concentration), BD biosciences 553141) and incubated at 4°C for 20 minutes.

A mastermix was created containing each antibody used, which was added to the non-control wells. For each FMO, all antibodies minus one were added as appropriately. A single antibody was added per single-stain well. Antibodies were mixed by pipetting up and down and allowed to incubate in the dark for 30 minutes at 4°C. Cells were then washed in 120 µL of FACS buffer and centrifuged at 500 x g for 3 minutes at room temperature, before the supernatant was removed and cell pellets disturbed via vortexing the plate. Cells were washed again via the same method and resuspended in 150 µL of FACS buffer and transferred to FACS tubes (Falcon 352008). For live/dead staining, DAPI (4',6-diamidino-2-phenylindole) was added to each FACS tube at 1:1000 dilution immediately prior to sorting.

Table 2.6.1: **Antibodies used in FACS**.

Antibody	Fluorophore	Cat. number	Company	Dilution
PDGFRβ	PE	136006	Biolegend	1:50
CD31	Bright violet 605	102427	Biolegend	1:100
CD45	APC	561018	BD Bioscience	1:100
F4/80	PE Cy7	25480182	eBioscience	1:100
LTL	PITC	FL1321	Vector	1:200

Dead cells were first gated out. Cells were then gated based on CD45, with PDGFRβ, LTL and CD31 being sorted from the CD45 negative population, while F4/80 was sorted from the CD45 positive population. F4/80^{hi} were sorted while F4/80^{lo} were not.

Cells were FACS sorted into RLT buffer and the following RNA extraction protocol was followed. This was done to maximise yield and allow for extraction of miRNA. RNeasy Plus Micro Kit (Qiagen, 74034) was used, with pure molecular-grade ethanol (Honeywell, E7023-500mL) used for all steps requiring the use of ethanol, including making up RWT and RPE buffers. All centrifugation steps take place at room temperature. Cells sorted into 350 µL RLT buffer were allowed to sit at room temperature for no longer than 30 minutes before initiating RNA extraction. Cells were vortexed for 10 seconds before being transferred to gDNA (genomic DNA) eliminator columns, where they were centrifuged at 1000 x g for 30 seconds. The gDNA eliminator column was then discarded and 1.5 times the volume present in the collection tube of ethanol was added and mixed by pipetting up and down. Up to 700 µL was this was added to RNeasy MinElute Spin Columns. Columns were centrifuged at 10000 x g for 30 seconds and the flow-through discarded. The remainder of the ethanol-containing mixture was added to the column (if applicable) and centrifuged as previous. 700 µL of RWT buffer was added per column, centrifuged for 30 seconds at 10000 x g and flow-through discarded. 500 µL of RPE buffer was added per column, centrifuged for 30 seconds at 10000 x g and flow-through discarded. 500 µL of RPE buffer was again added per column, centrifuged for 2 minutes at 10000 x g and flow-through discarded. The columns were then placed in new collection tubes and centrifuged at 17000 x g for 1 minute. To elute the RNA, 17 µL of nuclease-free water was added per column and centrifuged for 1 minute at 10000 x g. To maximise yield, the 17 µL of RNA-containing water was then re-added to the column, allowed to sit for 1 minute and then centrifuged at 10000 x g for 1 minute. The resulting RNA was stored at -80^{o}C.

2.7: Histological staining

Tissue sections were fixed for 24 hours in 10% v/v formalin and embedded in paraffin blocks by QMRI SURF. 3 µM slices of tissue were taken from paraffin blocks using a microtome and placed in a water bath at 45^{o}C for ~1 minute before being placed on a 1 mm thick glass slide (Clarity, C360). Slides were baked at 65^{o}C overnight to melt the paraffin and ensure tissue section adherence to the slide.

Slides were deparaffinised via the following protocol:

- 100% xylene for 5 minutes.
- 100% xylene for 5 minutes.
- 100% ethanol for 5 minutes.
- 100% ethanol for 5 minutes.
- 90% ethanol for 5 minutes.
- 80% ethanol for 5 minutes.
- 70% ethanol for 5 minutes.
- dH_2O for 5 minutes.

Once deparaffinised, slides were not allowed to dry until staining was complete.

Picrosirius red staining was carried out using Abcam picrosirius red staining kit (ab150681), according to manufacturer protocol in a flume hood. Deparaffinised slides were placed in picrosirius red stain for 1 hour, then dipped 5 times each in two changes of acetic acid solution (provided by kit), washed and dehydrated two changes of 100% ethanol, then cleared in 100% xylene. Glass coverslips (VWR, 631-0880) were mounted on the slides using DPX mounting medium (Sigma-Aldrich, 06522). Any bubbles were removed by gently pressing on the glass slide. Slides were allowed to dry overnight before being removed from the fume hood.

Whole-tissue sections were imaged at 20x magnification using ZEISS Axio Scan.Z1 slide scanner. Picrosirius red staining was then quantified using Image-Pro Premier 9.2 (Media Cybernetics). Here, areas of positive (red) staining were selected, while areas without positive staining were deselected. Image-Pro Premier applies a colour-match algorithm to select areas of the image which closely match the area selected by the user. This process was continued until all positive (red) staining was selected by Image-Pro Premier. Integrated Optical Density (IOD) of the areas selected (selected_IOD) was provided as an output by Image-Pro Premier. IOD is the average intensity/density of the selected areas, derived via the formula IOD = area x average density. The total IOD of the whole image (total_IOD) was also measured. Results were presented as the % of positive staining (selected_IOD) in the whole image (total_IOD); formula: (selected_IOD/total_IOD)*100.

2.8: Statistical analysis

All data generated was subjected to Grubbs outlier test; outliers were removed from analysis as specified. $P < 0.05$ was considered significant in all statistical tests used. Comparisons between two data points was carried out using a two-tailed student's t-test. A paired t-test was used for repeat measures, whereas unpaired as used in all other cases. For comparisons involving three or more data points, one-way ANOVA with Tukey's multiple comparison test was carried out. Tukey's multiple comparison test compared each group to each of the other groups. For Figure 3.2.2 B, sham vs STNx were compared at each time point with correction for multiple comparisons via Holm-Sidak method. All other comparisons in chapter 3 were unpaired, two-tailed t-tests. In section 4.2, an n of 3 (3 independent repeats of the experiments) was not achieved, so no statistical analysis was carried out. In section 4.3, all comparisons were via unpaired, two-tailed t-tests. In section 4.4, sham and STNx + PBS groups were compared via Student's t-test (unpaired, two tailed), while STNx + PBS, STNx + anti-miR-214, and STNx + control anti-miR groups were compared via one-way ANOVA with Tukey's multiple comparison test. Analysis was carried out in this way to allow sham vs STNx + PBS to assess changes induced by the STNx surgery, while comparison between the three STNx groups allowed for assessment of anti-miR-214 interaction with the parameter being measured in comparison to the two controls (PBS or control anti-miR). In Figure 4.4.7, paired t-tests were used to assess changes albumin:creatinine ratio detected in the urine when measured at 6-weeks post-surgery and 10-weeks post-surgery within each group. Statistical analysis of RNA-sequencing data (see 2.9) was carried out using DESeq2 R package.

2.9: RNA-sequencing

Three separate RNA sequencing (RNA-seq) experiments are presented in this thesis.

Firstly, RNA-seq of bulk mouse kidney cortex at sham, 7-day UUO, rUUO 1-week (1-week post-reversal of a 7-day UUO injury), rUUO 2-week (2 weeks post-reversal of a 7-day UUO injury), and rUUO 4-week (4 weeks post-reversal of a 7-day UUO injury). n=4 per group, with each n being a different mouse. RNA extraction was carried out as outlined in section 2.4. RNA quality was assessed via Agilent RNA 6000 Nano Kit (Agilent Biotechnologies 5067-1511), with RIN (RNA Integrity Number) values of >9.5 (out of 10) being sent for sequencing. small RNA sequencing and gene RNA sequencing (via poly-A pulldown) library preparation, sequencing and read quality control was carried out GeneWiz. Reads were mapped to the mm10 transcriptome using RSEM,[313] which determined raw read count and FPKM (Fragments Per Kilobase of transcript per Million mapped reads) for each gene in each sample. Statistical analysis to determine differential expression data between groups was carried out on raw read counts via DESeq2 R package. For each pair of experimental groups (e.g. sham vs UUO), DESeq2 generated a fold-change and adjusted p-value for each gene.

Secondly, gene expression RNA-seq (poly-A pulldown) of 4 cell populations FACS-sorted from mouse kidney cortex at sham, 7-day UUO, and rUUO 2-week (2 weeks post-reversal of a 7-day UUO injury). n=4 per group, with each n being a different mouse. The four cell populations were LTL (proximal tubular epithelial cells), CD31 (endothelial cells), F4/80^{hi} macrophages, and Pdgfrβ (fibroblast-like cells). FACS sorting and RNA extraction were carried out as outlined in section 2.6. RNA quality was assessed via Agilent RNA 6000 Nano Kit (Agilent Biotechnologies 5067-1511), with RIN (RNA Integrity Number) values of >9.5 (out of 10) being sent for sequencing. Library preparation, sequencing and read quality control was carried out GeneWiz. Reads were mapped to the mm10 transcriptome using RSEM,[313] which determined raw read count and FPKM (Fragments Per Kilobase of transcript per Million mapped

reads) for each gene in each sample. For visualisation purposes, reads were aligned to the mm10 genome using STAR (Spliced Transcripts Alignment to a Reference), prepared for visualisation with BigWig, and visualised using Integrative Genomics (IGV) viewer. Statistical analysis to determine differential expression data between groups was carried out on raw read counts via DESeq2 R package. For each pair of experimental groups (e.g. sham vs UUO) in each cell population, DESeq2 generated a fold-change and adjusted p-value for each gene. The pheatmap R package was used to generate all heatmaps, with FPKM values used.

Thirdly, small RNA sequencing was carried out on 4 cell populations FACS-sorted from mouse kidney cortex at sham, 7-day UUO, and rUUO 2-week (2 weeks post-reversal of a 7-day UUO injury). n=4 per group, with each n being a different mouse. The four cell populations were LTL (proximal tubular epithelial cells), CD31 (endothelial cells), F4/80^{hi} macrophages, and Pdgfrβ (myofibroblast-like cells). FACS sorting and RNA extraction were carried out as outlined in section 2.6. RNA quality was assessed via Agilent RNA 6000 Nano Kit (Agilent Biotechnologies 5067-1511), with RIN (RNA Integrity Number) values of >9.5 (out of 10) being sent for sequencing. Library preparation, sequencing and read quality control was carried out GeneWiz. Reads were aligned to the mm10 transcriptome and raw read counts per miRNA per sample generating using Shortstack.[314] Statistical analysis to determine differential expression data between groups was carried out on raw read counts via DESeq2 R package. For each pair of experimental groups (e.g. sham vs UUO) in each cell population, DESeq2 generated a fold-change and adjusted p-value for each miRNA. To normalise for differences in sequencing depth between samples, raw read counts were converted to CPM (counts per million). CPM was used for all analysis and outputs (such as heatmaps) downstream of the initial DESeq2 differential analysis, including heatmaps generated and enrichment analysis performed.

2.9.1: Principle component analysis (PCA)

PCA was carried out using DESeq2 and ggplot R packages. A DESeq dataset object (dds) summarising the gene expression data in each sample was created using DESeq2, i.e. this contains expression data for the top 1000 gene or miRNAs in each sample, along with additional information such as which group (sham, UUO or rUUO) each sample belongs to. To aid visual detection of outlier samples in the data, regularised log (rlog) transformation was applied to the dds object prior to generation of the PCA plot, producing a variance-stabilising effect and normalising for library size differences between samples.

2.9.2: Filtering data to remove very lowly expressed genes and contamination from each cell population

The rUUO FACS sorted population gene expression data was initially filtered for contaminating gene expression, i.e. genes which were observed in a certain cell population despite not normally being expressed in this population. These typically were genes highly expressed in other renal cell populations. To identify these genes, the dataset generated by Park *et al* (2018),[315] a single-cell RNA-seq dataset generated from mouse kidneys, was used. Genes found by Park *et al* (2018) to be specific to the following cell types were filtered from all 4 cell populations: podocytes, loop of Henle, distal convoluted tubule, collecting duct principal cell, collecting duct intercalated cell and collecting duct transient cell. In addition, genes found by Park *et al* (2018) to be specific to the proximal tubule were filtered from the $CD31^{+}$, $F4/80^{hi}$, and $Pdgfr\beta^{+}$ cell populations.

Genes with an average expression of <1 FPKM across all experimental groups (sham, UUO, and rUUO) were filtered out (removed). This was carried out in each individual cell population.

2.9.3: Manual clustering of gene/miRNA expression data into gene/miRNA sets based on expression patterns between experimental groups

To characterise differential gene (5.3) and miRNA (5.4) expression between experimental groups, each gene or miRNA was assigned to one of ten gene/miRNA sets. The three experimental groups were sham, UUO, and rUUO. Expression change between sham and UUO groups was first considered. Here, genes/miRNAs with any positive fold-change and an adjusted p-value of <0.05 were assigned as “up” between sham and UUO, while genes/miRNAs with any negative fold-change and an adjusted p-value of <0.05 were assigned as “down” between sham and UUO. Genes/miRNAs with an adjusted p-value of >0.05, regardless of fold-change, were assigned as no significant change (ns) between sham and UUO. Expression change between UUO and rUUO was then assessed as previously described, with each gene/miRNA assigned into one of three categories. Expression change between sham and rUUO was also assessed in the same way. These data were combined to produce 10 groups in total, to which each gene/miRNA belongs to 1 group only (table 2.9.1).

Table 2.9.1: **Criteria for gene/miRNA expression dataset assignment.** UP = increased expression from group x to y. DN = decreased expression from group x to y. NS = no significant change between group x and y. u = sham vs UUO. r = UUO vs rUUO. p-adj = adjusted p-value. ---- = not considered.

Gene set	Sham v UUO fold-change	Sham v UUO p-adj	UUO v rUUO fold-change	UUO v rUUO p-adj	Sham v rUUO fold-change	Sham v rUUO p-adj
UPu_DNr	Any positive	<0.05	Any negative	<0.05	----	----
UPu_UPr	Any positive	<0.05	Any positive	<0.05	----	----
UPu_NSr	Any positive	<0.05	----	>0.05	Any positive	<0.05
DNu_UPr	Any negative	<0.05	Any positive	<0.05	----	----
DNu_DNr	Any negative	<0.05	Any negative	<0.05	----	----
DNu_NSr	Any negative	<0.05	----	>0.05	Any negative	<0.05
NSu_DNr	----	>0.05	Any negative	<0.05	Any negative	<0.05
NSu_UPr	----	>0.05	Any positive	<0.05	Any positive	<0.05

2.9.4: Identification of enriched gene and miRNA expression

The MGFR (Marker Gene Finder in RNA-seq data) R package[316] was used to identify marker (or "enriched") genes/miRNAs in each cell population. Marker genes/miRNAs were identified for each cell population in sham, UUO and rUUO. That is, marker genes/miRNAs were identified by the MGFR package by comparing expression in each of the four cell types, with expression at sham, UUO, and rUUO being compared separately. Firstly, marker genes in the sham groups were detected, then marker genes in the UUO groups were detected separately, followed by the rUUO groups. Only genes/miRNAs which were found to be markers of a given cell type in all three experimental groups (sham, UUO, and rUUO) were presented in this thesis as marker (or enriched) genes/miRNAs.

2.9.5: Identification of predicted miRNA targets

The MultimiR R package was used to fetch data on predicted miRNA targets from the following databases: DIANA-microT-CDS (version 5), ElMMo (version 5), MicroCosm (version 5), miRanda, miRDB (version 5), PicTar (version 2), PITA (version 6), TargetScan (version 7.1). A species must be specified to run a MultimiR query.

MultimiR was provided with a miRNA of interest (e.g. miR-214-3p) and a list of genes. MultimiR then scanned the list of genes for predicted binding sites for the input miRNA, in each of the available databases. The list of gene provided were genes which displayed an expression pattern which opposed that of the miRNA, in the cell population of interest. For example, in the Pdgfrβ^{+} population, miR-214-3p expression was found to significantly increase from sham to UUO, then no significant change was detected between UUO and rUUO groups. Therefore, the list of genes provided to MultimiR to accompany the miR-214-3p search were Pdgfrβ genes which significantly decreased between sham and UUO, and remained significantly repressed in rUUO (Pdgfrβ_DNu_NSr).

Chapter Three

Characterisation of the Single-Surgery Mouse Subtotal Nephrectomy (STNx) Model of CKD

3.1: Introduction

Subtotal nephrectomy, also known as 5/6 nephrectomy, the remnant kidney model, or simply experimental CKD, is a rodent model of CKD. It was originally developed for use in rats, but has more recently been adapted for use in mice.[177] This model has traditionally been carried out as two separate surgeries, with removal of one kidney in one surgery, followed by ablation of contralateral renal mass 1-2 weeks later.[177,186,196,197,317] Subtotal nephrectomy has been associated with poor animal welfare as evidenced by high mortality rate[177,196] and significantly decreased bodyweight in the weeks following surgery.[181,194,197] In this chapter, a single-step surgery subtotal nephrectomy (STNx) is presented.

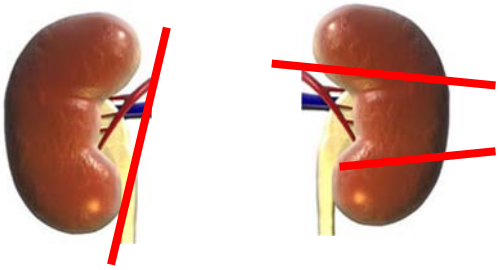

Fig 3.1.1: **Surgical schematic of subtotal nephrectomy**. Red lines indicate where incisions take place. One kidney is removed (left) and the top and bottom poles of the contralateral kidney (right) are removed.

Hypothesis:

The refined subtotal nephrectomy method models the renal and cardiovascular dysfunction present in CKD patients, along with a lower mortality rate and improved animal welfare compared to traditional subtotal nephrectomy methods.

Aims:

1. Profile animal welfare and mortality rate in STNx.
2. Assess the fibrotic and functional consequences of STNx on the kidney.
3. Assess the hypertrophic impact of STNx on the heart.
4. Assess the ability of STNx to model chronic kidney disease in C57 black background mice.

3.2: STNx in 129S2/SV mice

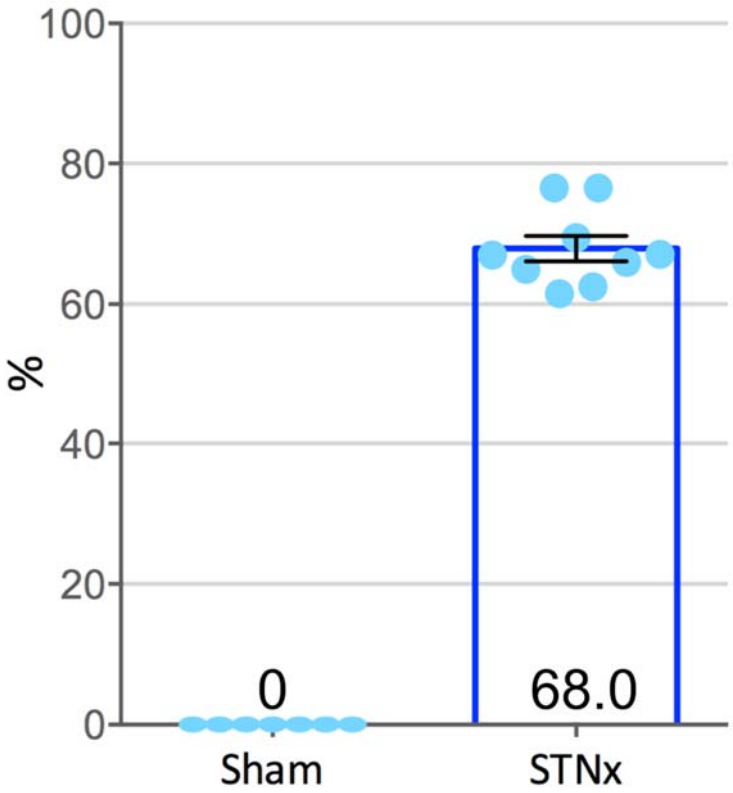

Fig 3.2.1: **Estimated percentage of total renal mass removed during the STNx surgery**. Each mouse which underwent STNx had one kidney removed and a portion of the contralateral kidney removed. Removed tissue was weighed and used to estimate the percentage of the total renal mass removed during the surgery. Sham: n=7, STNx: n=9. Plotted as mean ± SEM.

The percentage of total renal mass removed during each surgery was estimated (Fig 3.2.1). This procedure allows for constant monitoring of the consistency of the surgery within a study, as well as across multiple studies. It has been reported that variability in the amount of renal tissue remaining after subtotal nephrectomy surgery is a major factor in the variability in the model itself,[177] therefore, monitoring this is critical in ensuring consistency in the model.

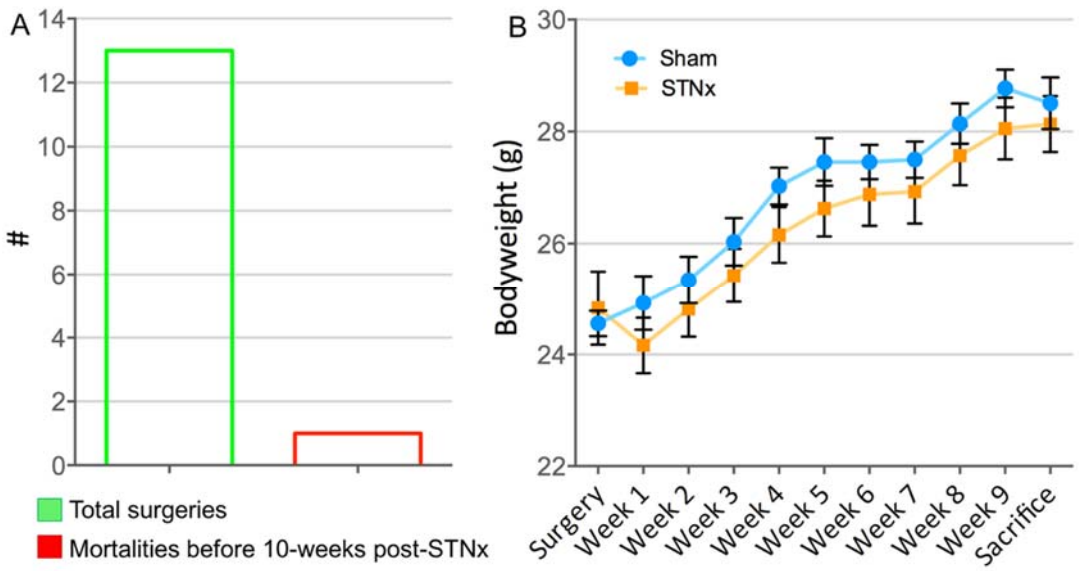

Fig 3.2.2: **Animal welfare in STNx.** A = Mortality rate in animals subjected to STNx. B = Animal bodyweight across the study. Sham: n=7, STNx: n=11. B = plotted as mean ± SEM, statistical analysis via student's t-test (unpaired, two-tailed) carried out separately baseline and cull time-points.

Out of 13 STNx surgeries performed, 1 animal was culled at 3-days post-surgery due to poor health as defined by a score of 6 on the animal condition scoring sheet (table 3.2.1). Therefore, a mortality rate of 7.69% was observed in animals subjected to STNx in this study (Fig 3.2.2 A). All mice which received sham operation successfully recovered from anaesthesia and 0 mortalities were recorded before sacrifice at 10-weeks post-surgery.

1 animal was not processed for tissue at the end of the experiment, resulting in n=11 for STNx and n=7 for sham in the results presented in section 3.2. This mouse was used to attempt to measure glomerular filtration rate, but as it was unsuccessful, this procedure was not attempted in the remaining mice.

At 7-days post-surgery, mice were weighed one per week until sacrifice at 10-weeks post-surgery (Fig 3.2.2 B) and assigned an animal condition score (table 3.2.1). At no time-point did weight significantly differ between sham and STNx groups.

General appearance:	Score
Normal	0
Slightly unkempt	1
Moderate piloerection	2
Marked piloerection (staring coat)	3
Slightly hunched	1
Markedly hunched	3
Weight and BC score:	**Score**
Normal - < 5% loss and/or BC3	0
Body wt. 5-10% loss and/or BC3/2	1
Body wt. 10-15% loss and/or BC2	2
Body wt. 15-20% loss and/or BC2/1	4
Body wt. ≥ 20% loss and/or BC1	5
Clinical signs:	**Score**
Soft stools	2
Laboured respiration	2
Dull, pale eyes	1
Semi-closed eyes	2
Less inquisitive than normal	1
Little interaction with peers	3
Totally “uninterested”/cold to the touch	5
Tremors/convulsions	5
Marked dehydration (skin pinch test)	4

Table 3.2.1: **Animal condition scoring criteria for STNx**. A cumulative score of 5 for any individual mouse results in a mandatory cull for health reasons. BC = body condition score, with BC1 being emaciated and BC5 being obese.[311]

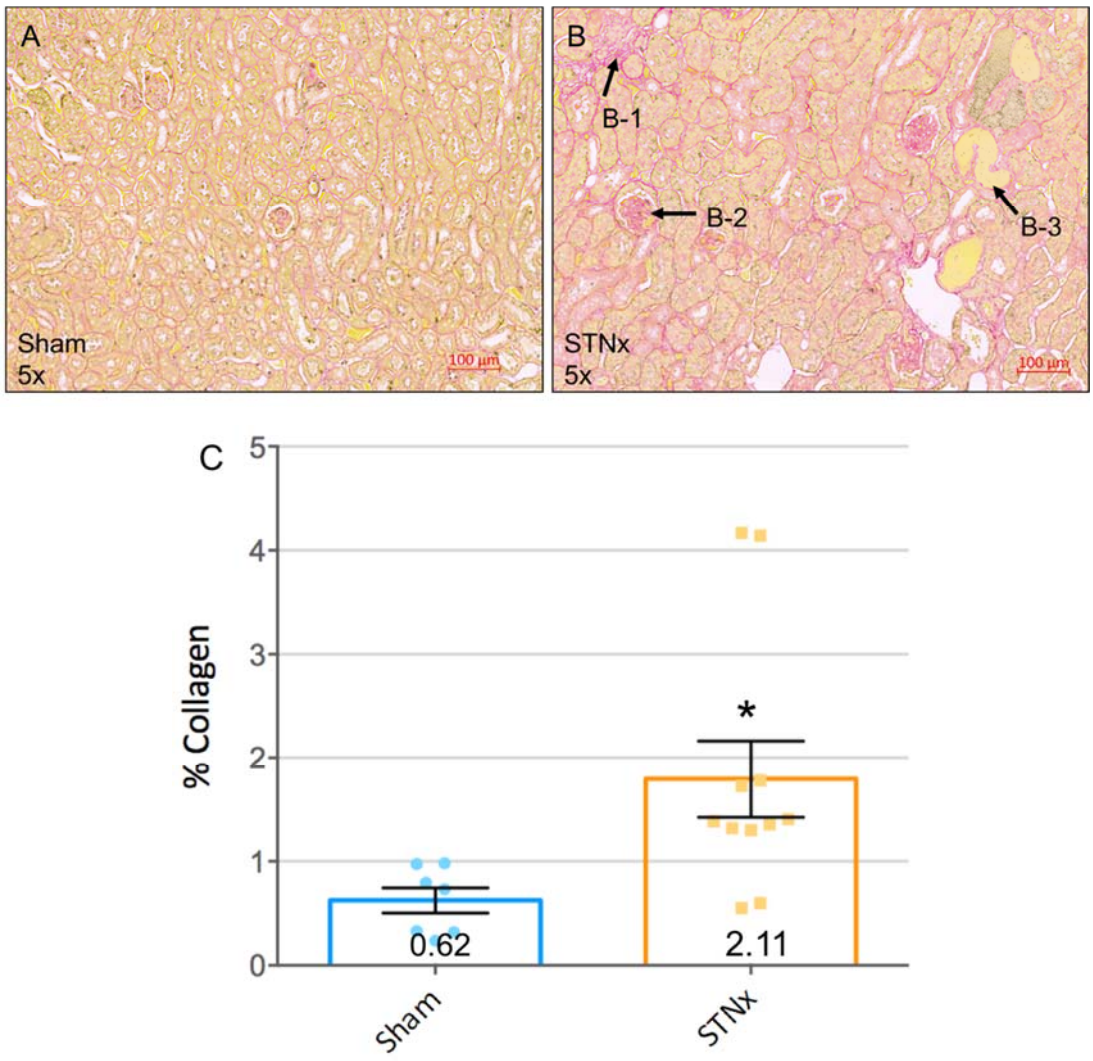

Fig 3.2.3: **Renal total collagen expression at 10-weeks post-surgery.** A = Sham exemplar image. B = STNx exemplar image. C = Quantification of total collagen expression. 3 µM slices were taken from paraffin-embedded kidney tissue before deparaffinisation and staining with picrosirius red for total collagen. Exemplar images (A-B) are provided at 5x magnification. B-1 = Tubulointerstitial fibrosis, B-2 = glomerulosclerosis, B-3 = tubular dilatation. Quantification of collagen expression was carried out using Image-Pro Plus 7. Sham: n=7. STNx: n=11. Plotted as mean ± SEM. Sham and STNx compared via student's t-test (unpaired, two-tailed). * = $P \leq 0.05$.

At 10-weeks post-surgery (Fig 3.2.3), mice subjected to STNx had significantly increased total renal collagen in comparison to sham-operated mice (0.62 % ± 0.12 SEM to 2.11 ± 0.37). This equalled a 3.4-fold increase in total collagen expression, indicating significant renal fibrosis was present.

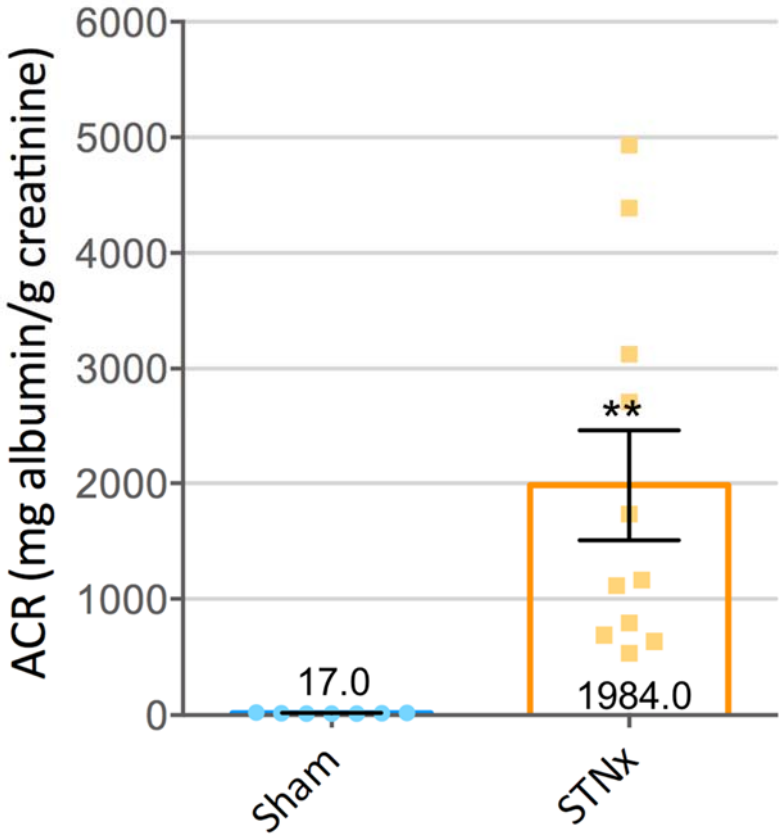

Fig 3.2.4: **Urinary albumin:creatinine ratio (ACR) at 10-weeks post-STNx.** Urine was collected overnight via metabolic cages. Albumin and creatinine content was determined via in-house biochemical analysis service. Sham: n=7, STNx: n=11. Plotted as mean ± SEM. Sham and STNx compared via student's t-test (unpaired, two-tailed). ** = P ≤ 0.01.

A significant increase in urinary ACRs was detected between sham and STNx groups (17 mg/g ± 1.3 SEM to 1984 ± 475) at 10-weeks post-surgery (Fig 3.2.4).

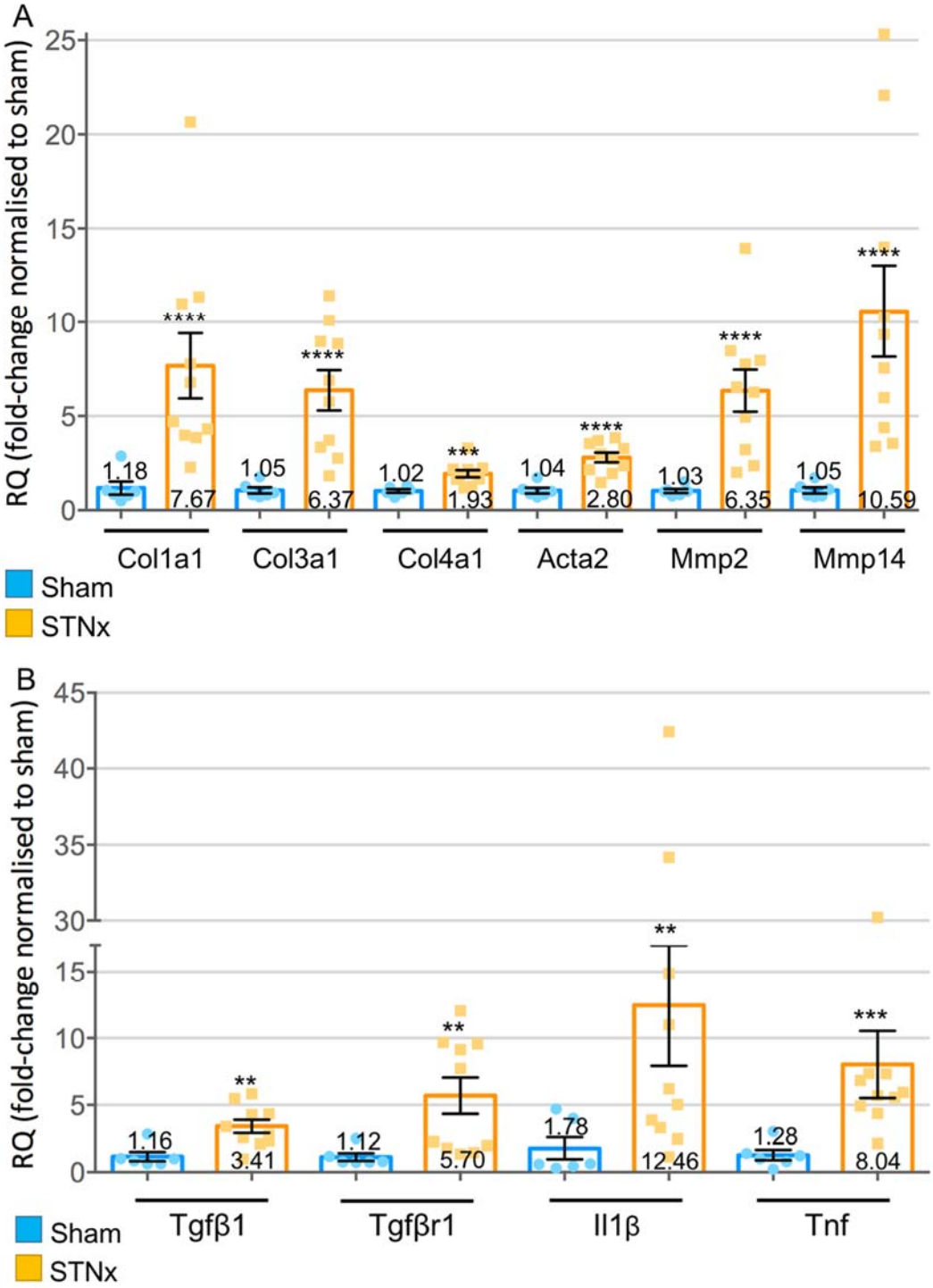

Fig 3.2.5: **Renal gene expression profile at 10-weeks post-surgery.** Quantitative real-time PCR (qRT-PCR) was carried out with specific Taqman probes for each gene, normalised to housekeeper Ppia (peptidylprolyl isomerase A). Sham: n=6, STNx: n=10. Plotted as mean ± SEM. Sham and STNx compared via student's t-test (unpaired, two-tailed). ** = P ≤ 0.01, *** = P ≤ 0.001, **** = P ≤ 0.0001.

A significant increase in the expression of several genes was detected between sham and STNx (Fig 3.2.5 A-B). These included collagen genes (Col1a1 (collagen type I alpha 1 chain), Col3a1 (collagen type 3 alpha 1 chain) and Col4a1 (collagen type 4 alpha 1 chain)), α-smooth muscle actin (Acta2), matrix metallopeptidase genes (Mmp2 and Mmp14), cytokines (Tgfβ1, Il1β and Tnf) and TGFβ receptor type 1 (Tgfβr1).

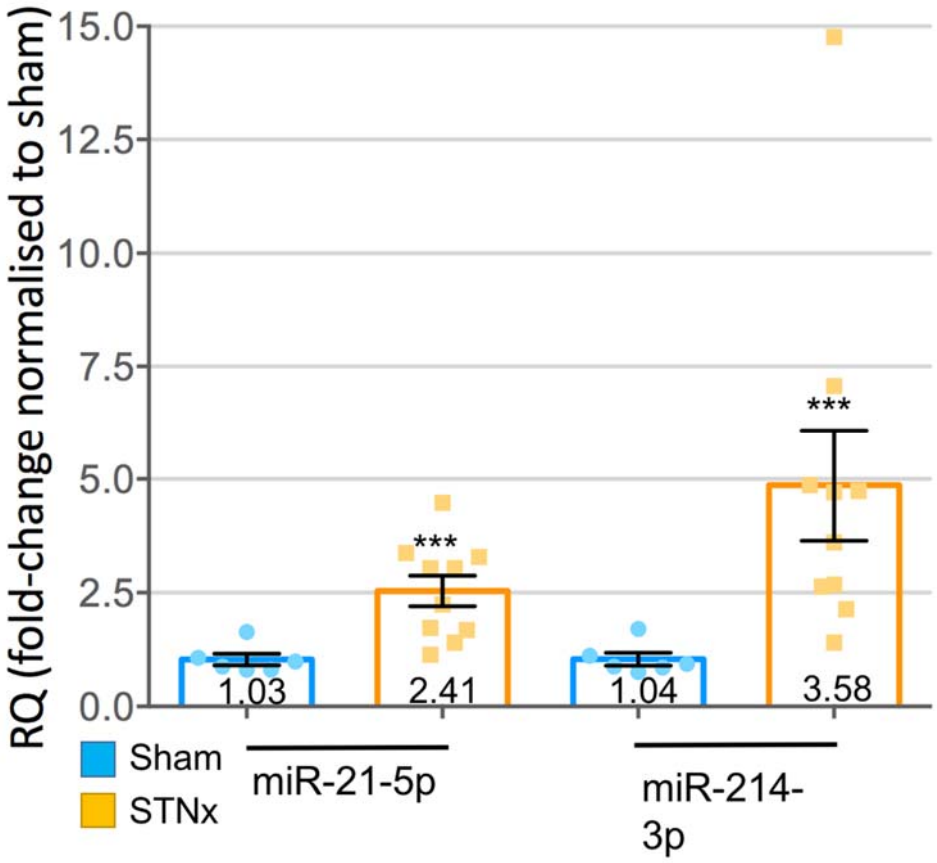

Fig 3.2.6: **Renal pro-fibrotic miRNA expression at 10-weeks post-surgery.** Quantitative real-time PCR (qRT-PCR) was carried out with specific Taqman probes for each miRNA, normalised to housekeeper u6 (u6 small nuclear RNA). Sham: n=6, STNx: n=10. Plotted as mean ± SEM. Sham and STNx compared via student's t-test (unpaired, two-tailed). *** = P ≤ 0.001.

A significant increase in renal expression of pro-fibrotic miRNAs[261] miR-21 (2.41-fold) and miR-214 (3.58-fold) was detected between sham and STNx groups at 10-weeks post-surgery (Fig 3.2.6).

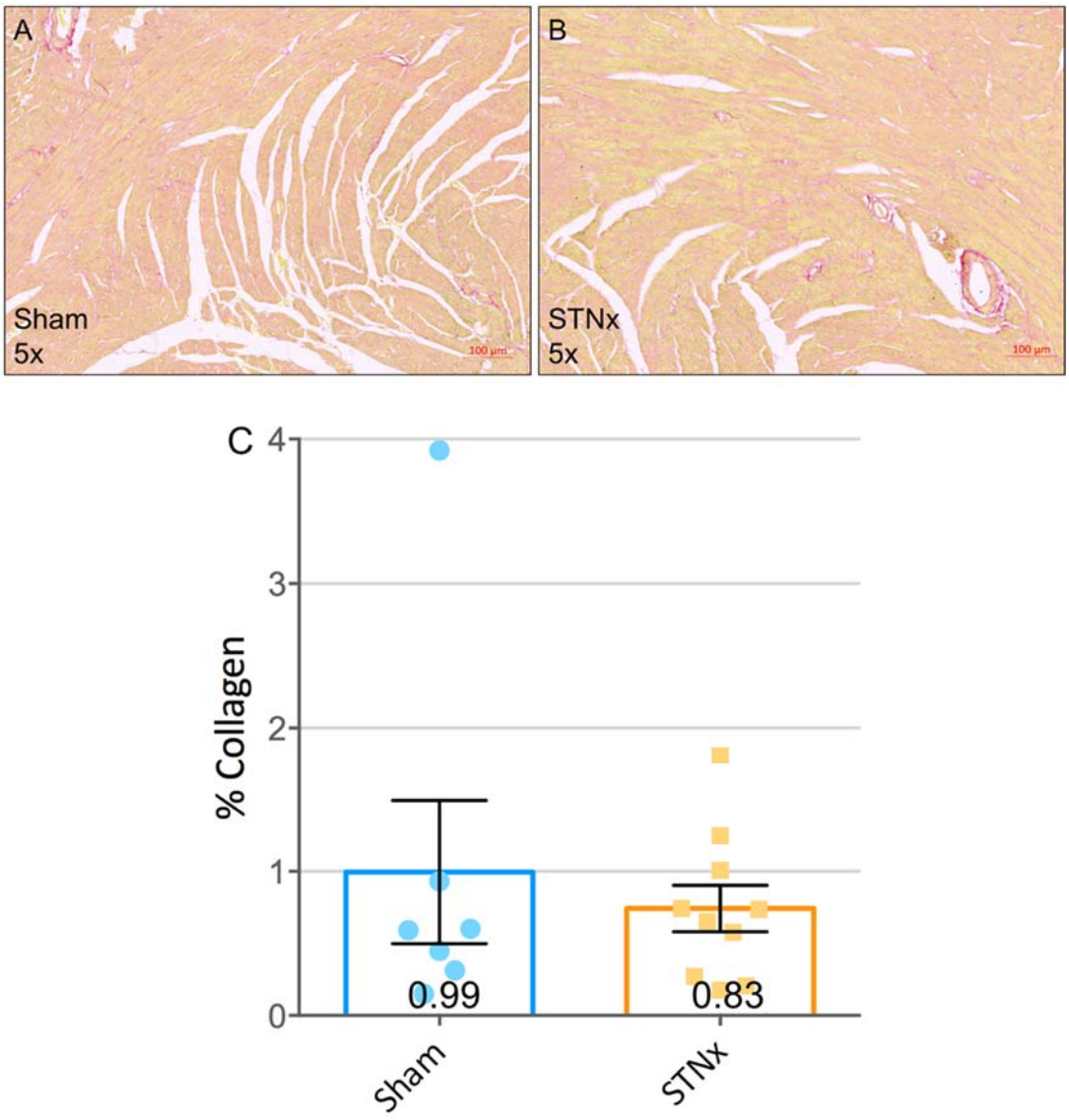

Fig 3.2.7: **Cardiac total collagen expression at 10-weeks post-surgery.** A = Sham exemplar image. B = STNx exemplar image. C = Quantification of total collagen expression. 3 µM slices were taken from paraffin-embedded heart tissue before deparaffinisation and staining with picrosirius red for total collagen. Exemplar images (A-B) are provided at 5x magnification. Quantification of collagen expression was carried out using Image-Pro Plus 7. Sham: n=7. STNx: n=10. Plotted as mean ± SEM. Sham and STNx compared via student's t-test (unpaired, two-tailed).

At 10-weeks post-surgery, no significant difference in cardiac total collagen expression was detected between sham and STNx groups (Fig 3.2.7).

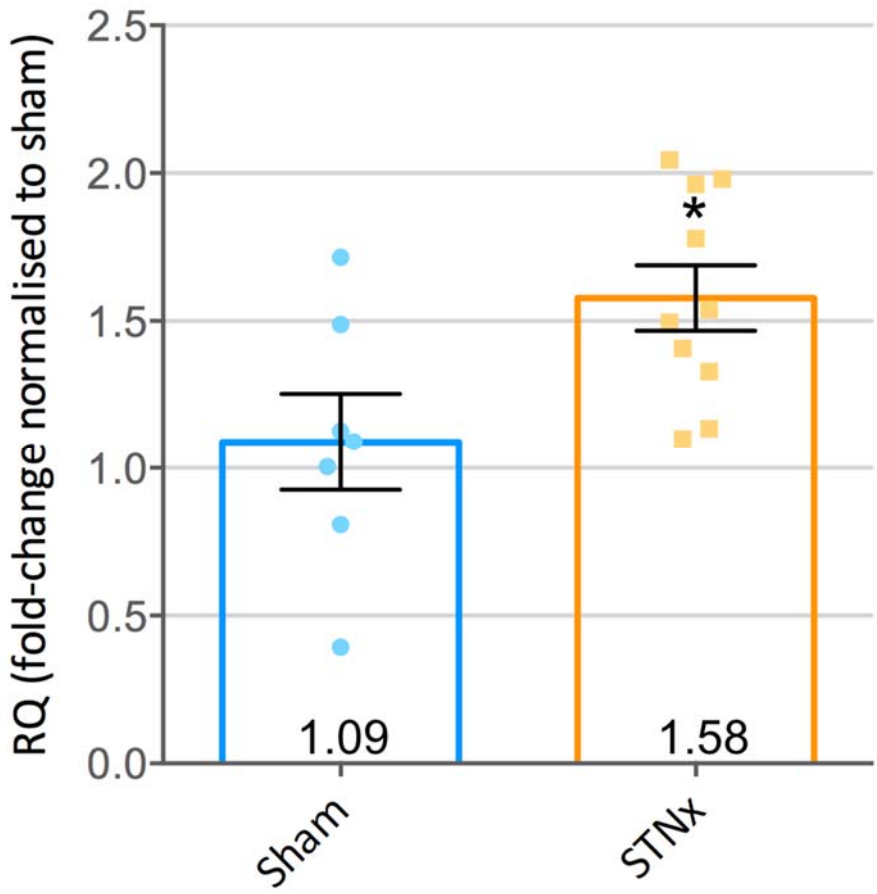

Fig 3.2.8: **Cardiac miR-214-3p expression at 10-weeks post-surgery.** Quantitative real-time PCR (qRT-PCR) was carried out with specific Taqman probe for each miR-214-3p, normalised to housekeeper u6. Sham: n=6, STNx: n=10. Plotted as mean ± SEM. Sham and STNx compared via student's t-test (unpaired, two-tailed). * = $P \leq 0.05$.

A significant increase in miR-214-3p was detected in the hearts of animals subjected to STNx, in comparison to sham, 10-weeks post-surgery (Fig 3.2.8).

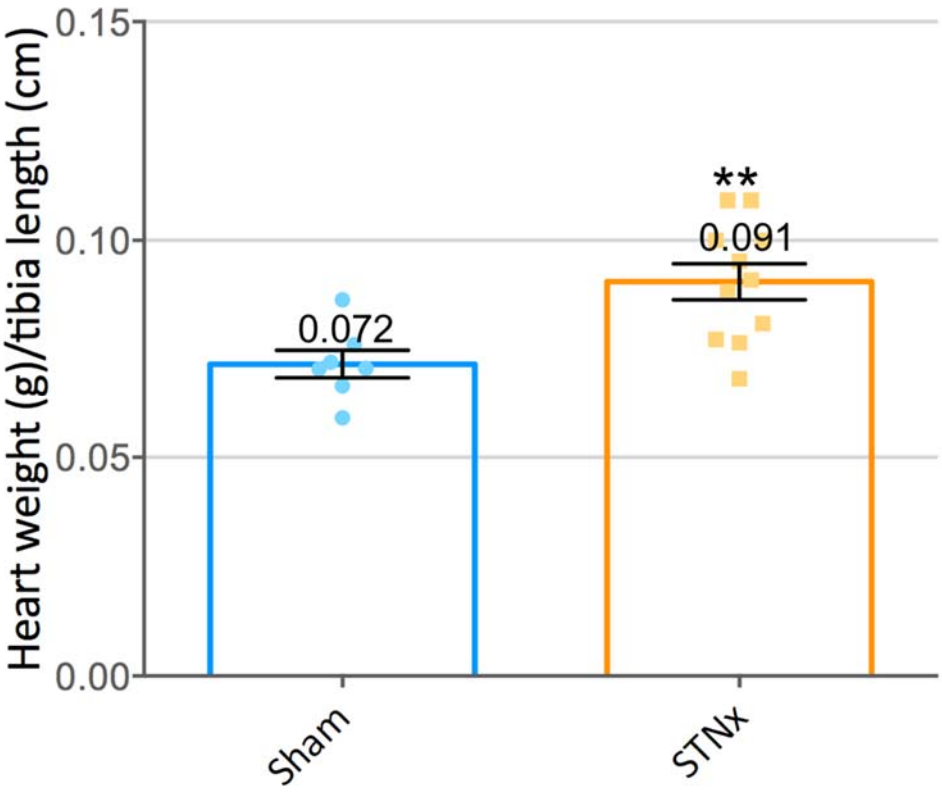

Fig 3.2.9: **Heart weight at sacrifice (10-weeks post-surgery), normalised to tibia length.** Sham: n=7, STNx: n=11. Plotted as mean ± SEM. Sham and STNx compared via student's t-test (unpaired, two-tailed). ** = P ≤ 0.01.

A significant increase in heart weight (normalised to tibia length) was detected in animals subjected to STNx, in comparison to sham, 10-weeks post-surgery (0.072 g/cm ± 0.003 SEM to 0.091 ± 0.004). This 1.24-fold increase indicates cardiac hypertrophy had occurred by 10-weeks post-STNx (Fig 3.2.9).

3.3: STNx in a C57 black background

Traditional subtotal nephrectomy methods used in mice are known to be much less effective at producing renal dysfunction in certain strains, most notably C57 black.[181] However, C57 black is a commonly used background strain for genetically-altered mice and therefore, the ability to perform subtotal nephrectomy in this strain is desirable. To assess how STNx may perform in this situation, STNx was carried out on a Gli1 reporter mouse (Gli1 x Ai14) on a C57 black background.

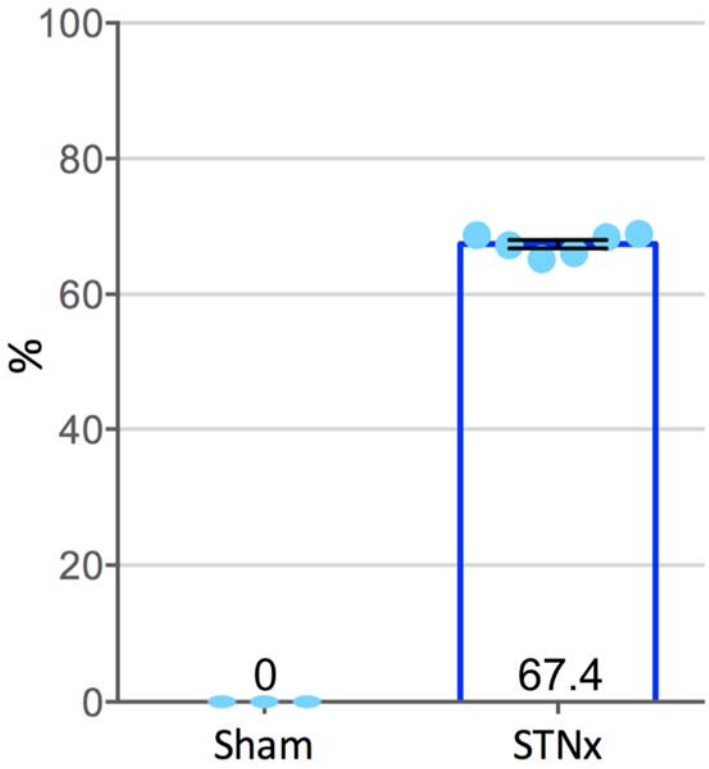

Fig 3.3.1: **Estimated percentage of total renal mass removed during the STNx surgery**. Each mouse which underwent STNx had one kidney removed and a portion of the contralateral kidney removed. Removed tissue was weighed and used to estimate the percentage of the total renal mass removed during the surgery. Sham: n=3, STNx: n=6. Plotted as mean ± SEM.

A consistent portion of renal tissue was removed from each mouse subjected to STNx surgery, 67.4% ± 0.62 SEM (Fig 3.3.1).

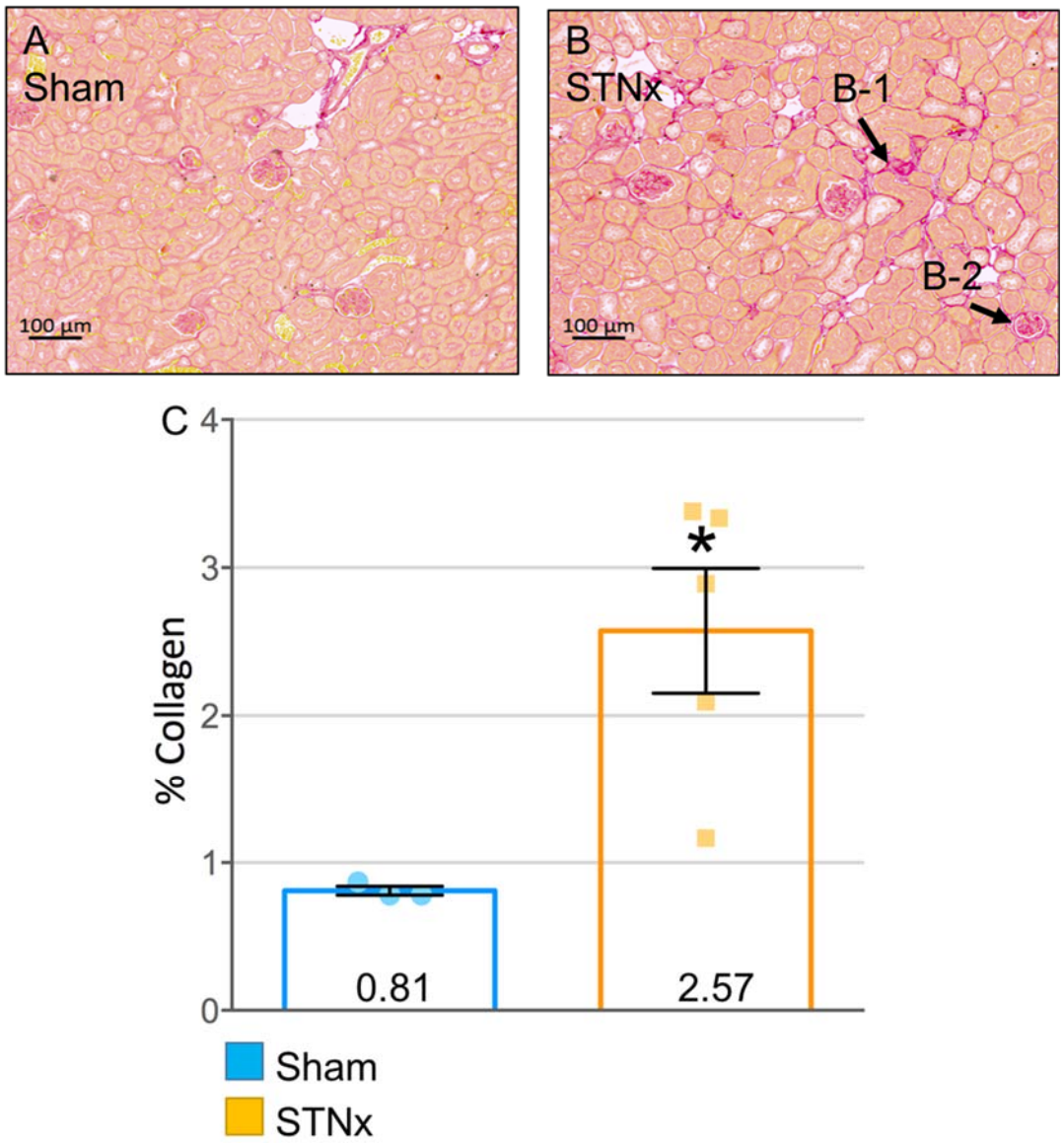

Fig 3.3.2: **Total renal collagen expression in Gli1 reporter mice subjected to STNx.** A = Sham exemplar (5x magnification). B = STNx exemplar (5x magnification). C = Quantification of Picrosirius red stain. 3 µM slices were taken from paraffin-embedded kidney tissue before deparaffinisation and staining with picrosirius red for total collagen. B-1 = Tubulointerstitial fibrosis, B-2 = glomerulosclerosis. Quantification of collagen expression was carried out using Image-Pro Plus 7. Sham: n=3. STNx: n=5. Plotted as mean ± SEM. Sham and STNx compared via student's t-test (unpaired, two-tailed). * = $P \leq 0.05$.

Significantly increased renal total collagen expression was detected at 10-weeks post-STNx in comparison to sham, via Picrosirius red stain quantification (Fig 3.3.2). Evidence of tubulointerstitial fibrosis and glomerulosclerosis was observed.

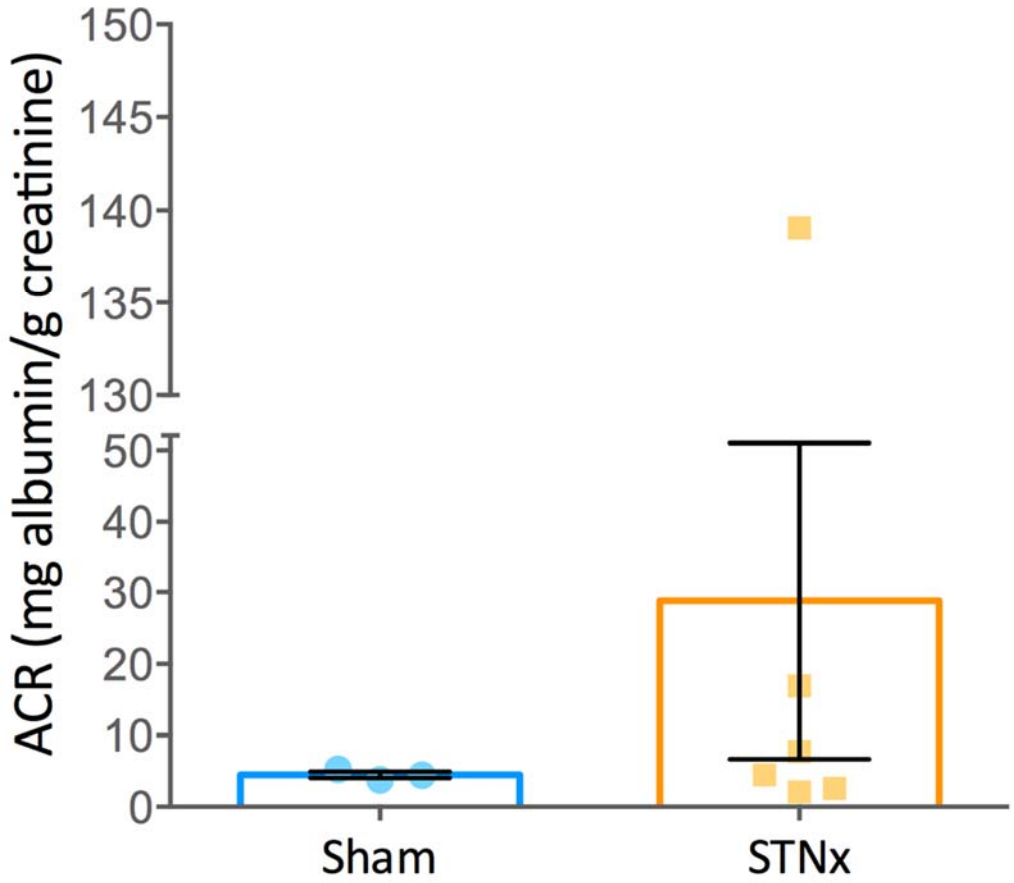

Fig 3.3.3: **Urinary albumin:creatinine ratio (ACR) at 10-weeks post-STNx in a C57 black background.** Urine was collected overnight via metabolic cages. Albumin and creatinine content was determined via in-house biochemical analysis service. Sham: n=3, STNx: n=6. Plotted as mean ± SEM. Sham and STNx compared via student's t-test (unpaired, two-tailed).

At 10-weeks post-surgery, no significant change in urinary ACR was detected in STNx mice in comparison to sham (Fig 3.3.3).

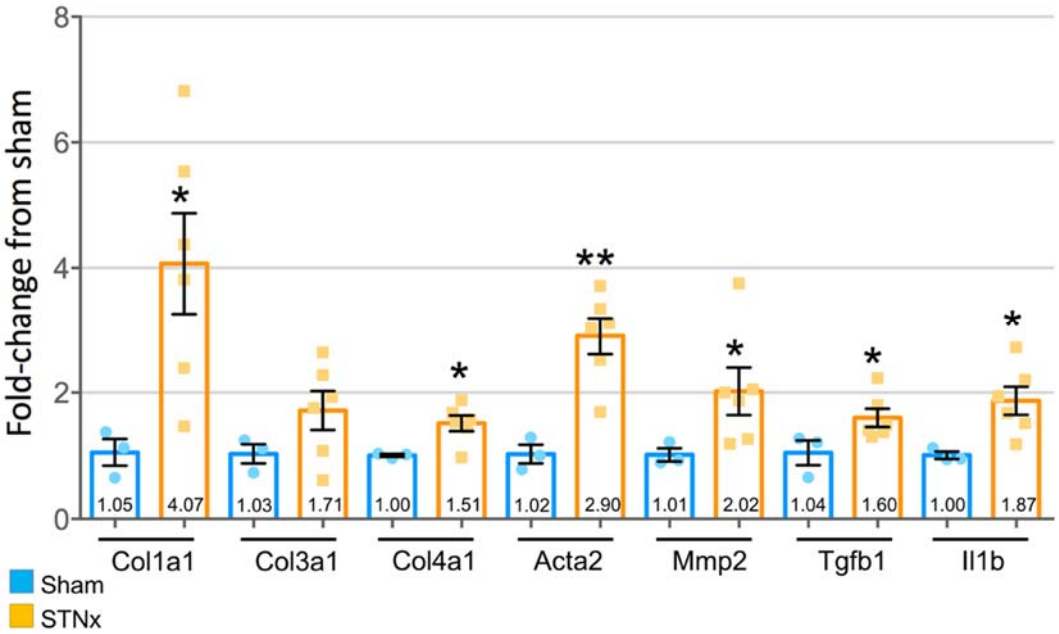

Fig 3.3.4: **Renal gene expression at 10-weeks post-STNx in C57 black background mice.** Quantitative real-time PCR (qRT-PCR) was carried out with specific Taqman probes for each gene, normalised to housekeeper Ppia. Sham: n=3, STNx: n=6. Plotted as mean ± SEM. Sham and STNx compared via student's t-test (unpaired, two-tailed). * = P ≤ 0.05 vs sham, ** = P ≤ 0.01 vs sham.

Significant increases in Col1a1, Col4a1, Acta2, Mmp2, Tgfβ1, and IL1β were detected in STNx kidneys at 10-weeks post-STNx vs sham, in C57 black background mice (Fig 3.3.4). No significant increase in Col3a1 was detected.

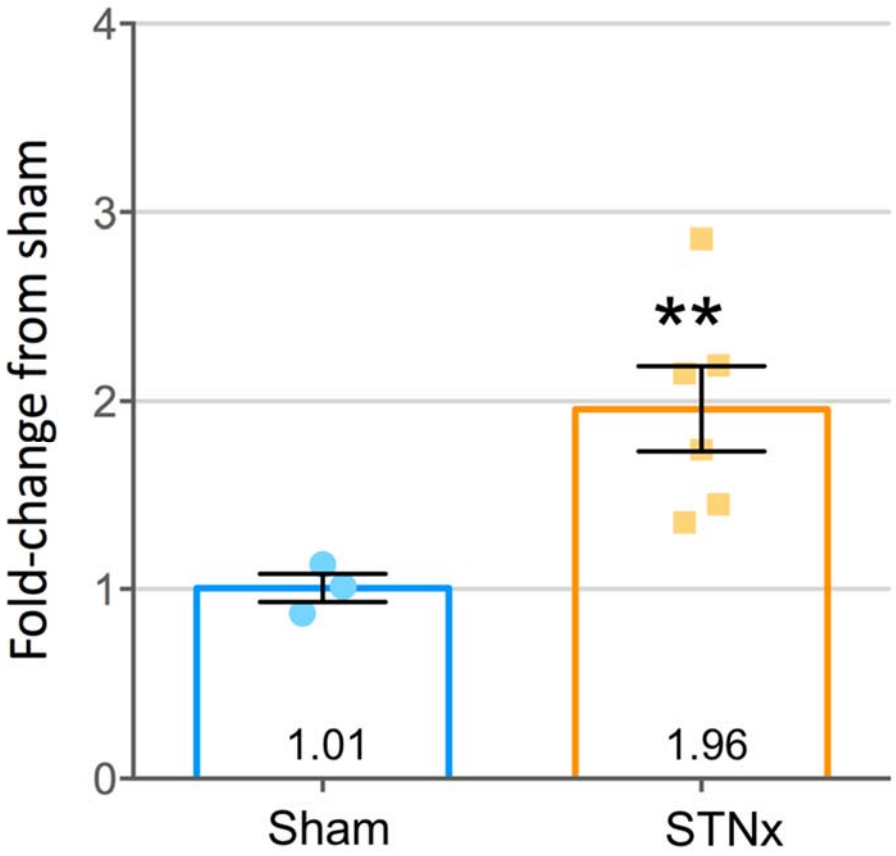

Fig 3.3.5: **Renal miR-214-3p expression at 10-weeks post-STNx in C57 black background mice.** Quantitative real-time PCR (qRT-PCR) was carried out with specific Taqman probes, normalised to housekeeper u6. Sham: n=3, STNx: n=6. Plotted as mean ± SEM. Sham and STNx compared via student's t-test (unpaired, two-tailed). ** = $P \leq 0.01$.

miR-214-3p was found to be significantly up-regulated in STNx kidneys at 10-weeks post-STNx in C57 black background mice (Fig 3.3.5).

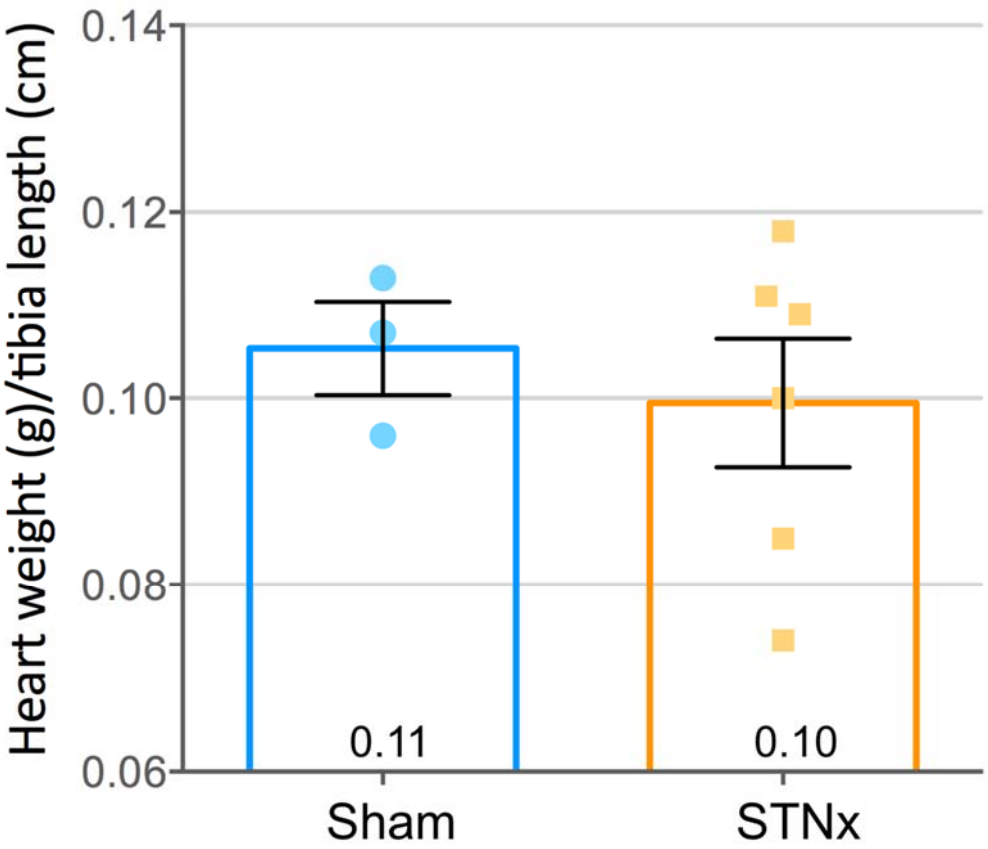

Fig 3.3.6: **Heart weight at sacrifice, 10-weeks post-STNx, normalised to tibia length in C57 black background mice.** Sham: n=3, STNx: n=6. Plotted as mean ± SEM. Sham and STNx compared via student's t-test (unpaired, two-tailed).

No significant change in heart weight at sacrifice was detected in STNx hearts in comparison to sham (Fig 3.3.6).

3.4: Discussion

In this chapter, an adapted subtotal nephrectomy mouse model (STNx) of CKD was characterised. The key difference between the surgical methods used and those previously published is the use of a single-surgery to perform both the nephrectomy and contralateral partial nephrectomy. Many papers have been published where nephrectomy is performed in one surgery, then 1-2 weeks later, resection of the poles or renal artery ligation is performed in a separate surgery.[160,186,190,195,197,318–325] Reducing the number of surgeries the mice are subjected to has a number of benefits. The length of time the mice need to spend on-procedure is decreased, meaning less money will be spent on maintaining the animals and results are obtained faster. Costs associated with surgery are reduced, as well as time spent performing surgery.

Animal welfare in response to STNx was closely monitored throughout the study using an animal condition scoring sheet (table 3.2.1), approved by the UK Home Office, on a weekly-basis. A cumulative score of 5 or higher results in a mandatory cull of the animal. For example, one animal was culled at 3-day post-STNx due to a score of 6 (slightly unkempt appearance (1), markedly hunched (3), body weight 10-15% loss (2)). Animal body condition scoring (BC), based on observation of the amount of flesh overlying bony protuberances, was also used in the health assessment of these animals throughout the study (table 3.2.1). This method has been demonstrated to be an accurate indicator of overall health status in mice.[311] Decreased weight in mice, also used in this study, has been shown to be an important determinant of health status.[311] Animals subjected to STNx were found to not differ in weight in comparison to sham animals at any time-point during the 10-weeks between surgery and sacrifice (Fig 4.2.2). This is in contrast to many other studies which use traditional (two-step, pole resection or renal artery ligation) subtotal nephrectomy protocols, which show subtotal nephrectomy animals having significantly decreased body weight in comparison to shams.[181,194,197] Therefore, the

presented methodology for carrying out a single-step subtotal nephrectomy in mice (STNx) was not associated with decreased animal welfare.

In addition, mortality rates associated with the traditional subtotal nephrectomy methods in mice are substantial, with reports as high as 43%[196] and >50%.[326] In comparison, a mortality rate of 7.69% was observed in STNx in mice (Fig 3.2.2 A), further suggesting STNx offers improved animal welfare vs traditional methods.

As expected, significant renal fibrosis was detected in STNx kidneys in comparison to sham at 10-weeks post-surgery (Fig 3.2.3). Classical hallmarks of renal fibrosis tubulointerstitial fibrosis and glomerulosclerosis[327] were observed. Tubular dilatation was also observed, which results from an increase in intraluminal pressure and cytoskeletal alterations.[328,329] These changes occurred in conjunction with increased urinary albumin:creatinine ratio (ACR) at 10-weeks post-surgery (Fig 3.2.4). These data indicate STNx successfully modelled renal fibrosis and renal dysfunction consistent with human CKD *in vivo.*

Renal transcriptomic profiling (Fig 3.2.5) revealed significant in several genes known to be associated with renal fibrosis in animals subjected to STNx. Increases in three collagen genes mirror what was seen histologically in Fig 3.2.3. Col1a1 and Col3a1 encode fibrillar collagens[330] which are important extracellular matrix components, secreted by myofibroblasts in the kidneys when a pro-fibrotic environment is present.[331] Col4a1 is an important basement membrane component,[332] suggesting possible basement membrane expansion in STNx kidneys. Acta2 is a marker of the formation of the myofibroblasts which increase in number in renal fibrosis and secrete excess extracellular matrix components.[333] Mmp2 has been suggested as a clinical biomarker, as increased expression has been observed to correlate with renal fibrosis and predicts risk of future decline in renal function.[334] Renal Mmp2 expression is also known to increase in *in vivo* models of renal dysfunction (diabetic nephropathy via streptozotocin,[335] ischemia-reperfusion injury,[336] lithium-induced

interstitial fibrosis,[337] anti-Ty1.1 nephritis,[338,339] and UUO).[340] Mmp14 is the predominant membrane type (1) matrix metalloproteinase (MT1-MMP) in the kidney, where it functions as the main activator of Mmp2 locally.[341] Increased expression of these genes indicate a pro-fibrotic transcriptomic profile is present in STNx kidneys, demonstrating the potential for STNx as a platform for the investigation of renal fibrosis where chronic renal dysfunction is present.

IL1β is thought to have a role in the activation of fibroblasts and mesenchymal stem cells into myofibroblasts the kidney, thus promoting renal fibrosis.[342] This effect has been observed in UUO, IRI and in clinical CKD samples.[342] Stimulation of human 3D kidney organoid cultures with IL1β is sufficient to initiate proximal tubular damage and tubulointerstitial fibrosis.[342] IL1β production in the kidney largely takes place in the dendritic cells and macrophages.[343] For production of IL1β to take place, activation of NF-κB signalling must occur to produce pro-IL1β, which requires NLRP3 (nucleotide-binding domain, leucine-rich-containing family, pyrin domain-containing-3) inflammasome activation to produce active caspase-1, which cleaves pro-IL1β to form mature IL1β.[343,344] Another product of active NF-κB signalling is Tnf.[343] Tnf is up-regulated in various clinical instances of CKD and its inhibition has been found to be therapeutic in multiple animal models of renal dysfunction, including subtotal nephrectomy.[103] Tnf promotes inflammation through activation of NF-κB signalling and recruits monocytes and macrophages to the renal interstitium, which in-turn produce cytokines such as Tgfβ.[345] Tgfβ is referred to as the master-regulator which drives fibrosis in chronic kidney disease, which has been established in cases of clinical CKD, a wide-variety of *in vivo* and *in vitro* models.[346] Intracellular Tgfβ signalling is initiated via Tgfβ receptor 1.[346] As IL1β, Tnf, Tgfβ1 and Tgfβr1 were found to be up-regulated in STNx, these indicate the pro-inflammatory and pro-fibrotic cytokine profile found in STNx recapitulates what is observed in other *in vivo* models of renal dysfunction and also in human CKD.

A novel observation was made in relation to the renal miRNA expression profile at 10-weeks post-STNx. Here, miR-21-5p and miR-214-3p were observed to be significantly increased in STNx. miR-21 is well-established to be a pro-fibrotic miRNA in the kidney and has been shown to be up-regulated *in vivo* in UUO and IRI.[347] miR-21 has been shown to be up-regulated in human kidneys where glomerulosclerosis, IgA nephropathy, diabetic nephropathy, interstitial fibrosis or atrophic tubules are present, as well as in acute kidney injury.[226] Knockdown of miR-21 via anti-miR oligonucleotide has been shown to significantly reduce interstitial fibrosis in a mouse model of Alport syndrome.[348] miR-214 has also been demonstrated to increase in models of renal fibrosis (UUO and IRI) and its knockdown in UUO using anti-miR oligonucleotide or genetic knockout has been shown to be anti-fibrotic.[261,303] Up-regulation of these miRNAs are in-line with other well-established models of renal injury and recapitulate changes which are consistently observed in cases of human renal dysfunction. This indicates STNx may be a promising model for future mechanistic or therapeutic intervention studies relating to miRNA in the context of chronic renal injury.

Aside from assessment of parameters related to the kidneys, some cardiovascular parameters were also measured. Cardiac hypertrophy, secondary to uremia, has been shown to occur in mice subjected to subtotal nephrectomy in many studies.[192,193,349,350] Cardiac hypertrophy is also common in patients with renal insufficiency, with nearly 75% of patients displaying this by the time dialysis is initiated.[192,351] Animals subjected to STNx were found to have significantly increased cardiac hypertrophy at 10-weeks post-surgery compared to shams (Fig 3.2.9), indicating STNx is consistent with other subtotal nephrectomy methods in modelling the uremic cardiac hypertrophy observed in human CKD. Increased miR-214-3p expression was also observed in hearts of animals subjected to STNx (Fig 3.2.8). The role of miR-214-3p in cardiac hypertrophy is controversial, with studies showing an increase or decrease in miR-214-3p expression in cardiac hypertrophy depending on underlying pathology of the model used or human condition assessed.[272] These data

indicate miR-214-3p expression increases in uremic cardiac hypertrophy, although no assessment if this increase is protective or deleterious can be made. As cardiac fibrosis (Fig 3.2.7) was not detected, it may be necessary to allow the model to run longer than 10-weeks post-surgery to observe this. One sham animal was found to have significant cardiac fibrosis present. Further characterisation of the cardiac effects of STNx through echocardiography and blood pressure assessment would be beneficial.

In comparison to STNx carried out in 129S2/SV mice, C57 black background mice had a notably blunted response to STNx on certain parameters. Up-regulation of many of the same genes (and miR-214-3p) in the kidney occurred in C57 black mice as in 129S2/SV, however, notably lower fold-changes were observed in these mice. One striking difference between the two strains were the urinary ACRs. No change was observed in C57 black mice in comparison to sham, with an average of ~30 mg/g, while 129S2/SV mice had an average ACR of 1984.0 mg/g at 10-weeks post-STNx. No increase in urinary ACR suggests no significant dysfunction was present in the kidneys of the C57 black animals when subjected to STNx. No evidence of cardiac hypertrophy was observed in C57 black animals, which may also be due to lack of renal dysfunction, as it has previously been reported that C57 black resistance to subtotal nephrectomy-induced cardiac dysfunction is at least partially dependant on the severity of renal dysfunction.[181] Together, these results suggest long-term renal dysfunction following STNx was not present in C57 black background mice, although renal fibrosis and pro-fibrotic gene expression were observable. Based on these results, C57 black background mice should be avoided when using the STNx model, although angiotensin II administration[181] may be used to sensitise these mice to STNx.

Conclusion:

The presented STNx model is a mouse model of CKD, refined by using a single-step surgery over traditional two-step methods. STNx was carried out as a 10-week model, which was well-tolerated and induced a number of indicators of renal dysfunction. Renal fibrosis and pro-fibrotic gene and miRNA expression were observed in STNx kidneys. Serum and urine biochemical analysis indicated significant renal dysfunction was present. Cardiovascular parameters indicated cardiorenal syndrome was developing in these mice. STNx in C57 black mice, a strain known to be resistant to developing renal dysfunction in response to subtotal nephrectomy, revealed a significantly blunted response to STNx in comparison to 129S2/SV mice.

Chapter Four

Anti-miR-214 as a Therapeutic Intervention in the STNx Model of CKD

4.1: Introduction

Anti-miRNA compounds are oligonucleotides designed to bind and neutralise specific miRNA via base-pairing with its seed region.[352–354] Several modifications to the oligonucleotide backbone have been utilised over the years to make improvements such as resistance to nuclease, increased target affinity, reduced innate immune response, improved pharmacokinetic profile and increased cellular uptake.[352,355] Despite these chemical modifications, inhibition of miRNA activity via the delivery of oligonucleotides has proven difficult in certain contexts, such as tumours in the central nervous system due to delivery across the blood-brain-barrier.[356] However, making use of the common phosphorothioate (PS) modification results in high renal accumulation of the anti-miR compound,[233] making targeted miRNA knockdown in the kidney therapeutically viable.

The anti-miR-214 compound used in the following *in vivo* studies, provided by Regulus Therapeutics, includes phosphorothioate (PS), 2'-OMe (2'-O Methyl), MOE (Methoxyethyl) and cEt (constrained ethyl) modifications to the 17-nucleotide backbone. PS offers improved nuclease resistance and increased binding to plasma proteins, thus reduced renal clearance. 2'-OMe and MOE both offer improved affinity for the target miRNA, nuclease resistance and decreased innate immune response. cEt modification has a strong effect on target binding affinity as well as further improved nuclease resistance.[352,355]

miR-214 inhibition via genetic knockout and oligonucleotide-mediated inhibition has been shown to be anti-fibrotic in the unilateral ureteral obstruction (UUO) model of renal fibrosis.[261] Due to the nature of the UUO model used in this study affecting a single kidney, the consequences of miR-214 inhibition on renal functional measures (such as albumin-creatinine ratio or serum creatinine)[10,357] or cardiorenal syndrome-related phenomenon (blood pressure, cardiac hypertrophy, cardiac fibrosis or cardiac function)[66,358–360] could not be investigated. The refined, single-step, subtotal

nephrectomy mouse model of chronic kidney disease (STNx), profiled in chapter 3, was selected for these *in vivo* studies due to its ability to model a number of these features of CKD. “Refined,” in this case refers to NC3Rs (UK National Centre for Replacement, Refinement and Reduction of Animals in Research) definition of refinement: “methods which minimise animal suffering and improve welfare.”[361]

The chronic nature of the STNx model allows for the initiation of anti-miR dosing at a time-point where renal fibrosis and increased miR-214 expression were already observable. In patients, CKD is commonly diagnosed using serum creatinine, a marker which alterations are only detectable when 40-50% of the renal parenchyma is damaged.[362] This, in addition to the non-specific symptoms produced by early-stage CKD, results in early diagnosis not being routine.[362,363] Therefore, from the perspective of testing a therapeutic intervention, dosing the compound from a time-point where renal dysfunction is already present will allow us to gain valuable information about translational potential.

Hypothesis:

Anti-miR-214 is an effective therapeutic intervention in chronic kidney disease.

Aims:

1. Evaluate anti-miR-214 and control anti-miR compounds in *in vitro* models of renal disease.
2. Determination of the optimal time-point post-STNx surgery for intervention with anti-miR-214 *in vivo*.
3. Investigate the effects of anti-miR-214 on the kidney in the STNx model.
4. Investigate the effects of anti-miR-214 on the heart in the STNx model.

4.2: *In vitro* analysis of anti-miR-214 and control anti-miR oligonucleotide compounds

Initially, a luciferase-based assay was used to investigate the capacity of anti-miR-214 compounds to bind miR-214-3p. This work was conducted in conjunction with Regulus Therapeutics while the author was on Industry placement. The assay system used consisted of two plasmid constructs, a luciferase reporter construct which contained a miR-214-3p binding site (complementary to the miR-214-3p seed sequence) and a miR-214-3p expression plasmid. The plasmids were co-transfected into HeLa cells 6 hours before the cells were trypsinised and plated in 96-well plates. The anti-miR compounds were transfected the following day utilising a range of doses and luminescence measured 24hrs later. The concept behind this assay system is: miR-214-3p produced by the miR-214 expression plasmid will inhibit luciferase expression via binding to the miR-214-3p seed-match region on the luciferase plasmid. When anti-miR-214 is transfected at a gradient of doses, it is expected that it will bind the miR-214-3p present in the cells, which will prevent miR-214-3p-mediated inhibition of the luciferase construct. Therefore, measured luminescence will increase with the affinity of the anti-miR-214 compound for miR-214-3p.

As expected, the control anti-miR did not induce any luminescence (Figure 4.2.1). Anti-miR-214 compounds B, C, D and E displayed affinity for miR-214-3p, with anti-miR-214 compound A displaying the greatest peak luciferase activity (Figure 4.2.1). The activity for compound A peaked at 3.18-fold the average value detected in the untreated control wells (wells which received no drug) at a dose of 0.21nM, compared to 0.71-fold for the control anti-miR at the same dose. From this data, anti-miR-214 compound A was selected for further in vitro and in vivo studies, along with the control anti-miR compound shown.

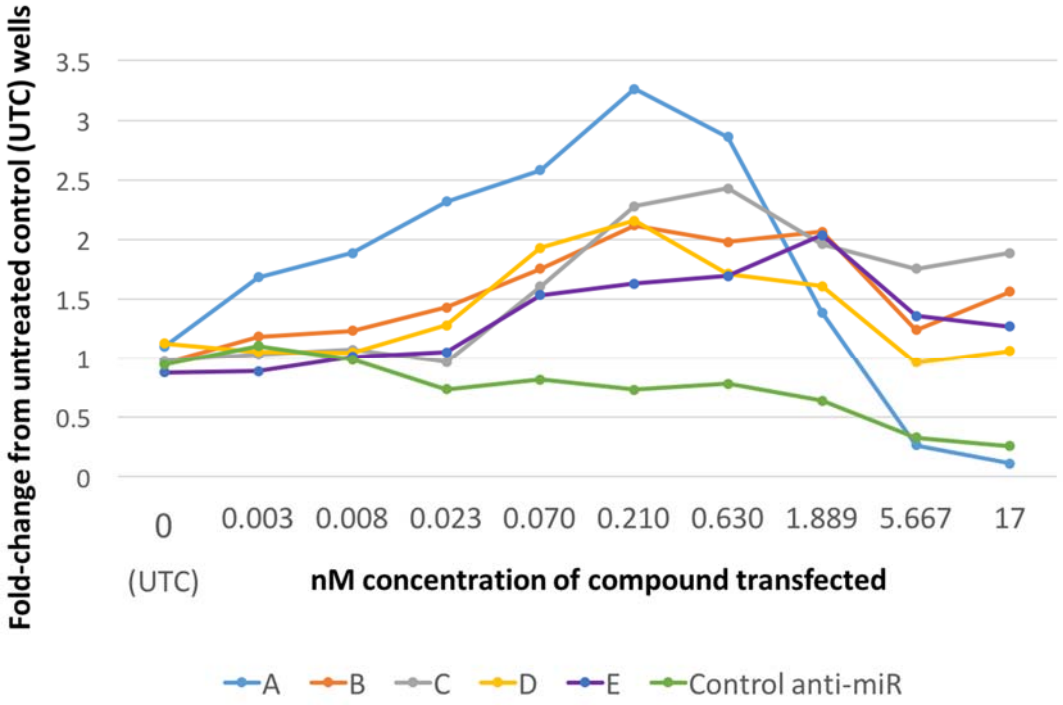

Fig 4.2.1: **Assessment of the miR-214-3p binding capacity of oligonucleotide compounds *in vitro.*** Luciferase-based miR-214 expression sensor system used to analyse the capacity of several oligonucleotide compounds to bind miR-214-3p. Oligonucleotides were transfected into HeLa cells containing luciferase-based miR-214-3p sensor in a gradient of doses (0.003-17nM). Luminescence detected was normalised to that of untreated control (UTC) wells (which received no oligonucleotide). Increased fold-change from UTC indicates increased inhibition or miR-214 by the compound. n=1. A-E = anti-miR-214 compounds.

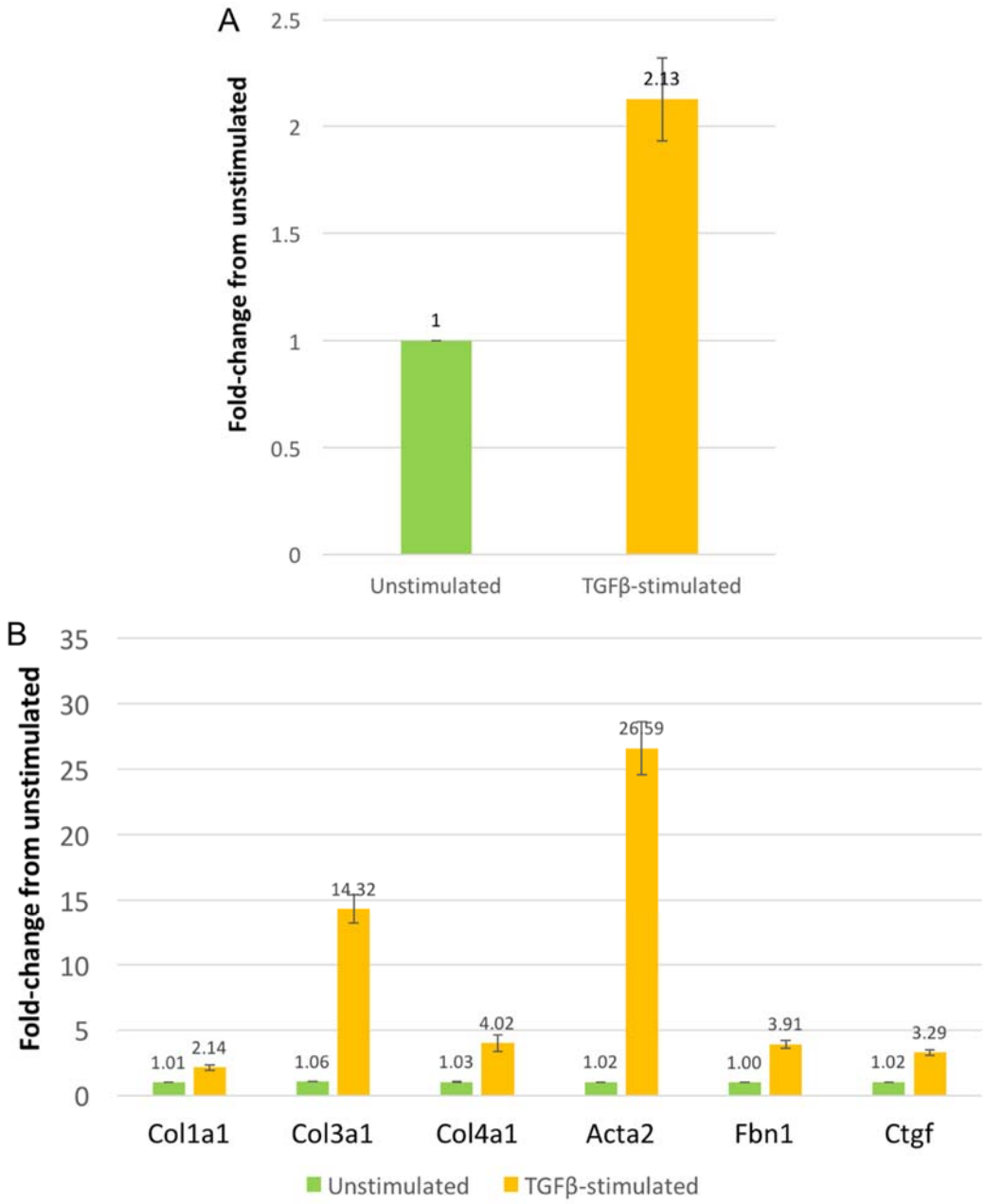

Fig 4.2.2: **miR-214-3p and pro-fibrotic gene expression in an in vitro model of renal fibrosis**. A = miR-214-3p expression. B = Pro-fibrotic gene expression. Rat renal fibroblast (NRK49F) cells were stimulated with TGFβ1 (10 ng/mL for 3 days) to model renal fibrosis *in vitro*. Quantitative real-time PCR (qRT-PCR) was carried out with specific Taqman probes for each miRNA or gene, normalised to housekeeper Let7 for miRNA and Rplp0 (ribosomal protein lateral stalk subunit P0) for genes. n=2. Plotted as mean ± standard deviation.

Following selection of anti-miR-214 compound A, the effect of this compound and a control anti-miR compound were evaluated in an *in vitro* model of renal fibrosis. Here, rat renal fibroblast (NRK49F) cells were stimulated with TGFβ1 in order to induce a pro-fibrotic phenotype which could be used to assess the potential impact of miR-214 inhibition. As these experiments took place during a time-limited placement at Regulus Therapeutics, only two repeats of the experiment (n=2) could be carried out. Therefore, no statistical analysis could be carried out. However, some clear trends are observed.

Prior to transfecting anti-miR compounds, it was established that stimulating NRK49F cells with TGFβ1 resulted in increased miR-214-3p expression and pro-fibrotic gene expression (Fig 4.2.2).

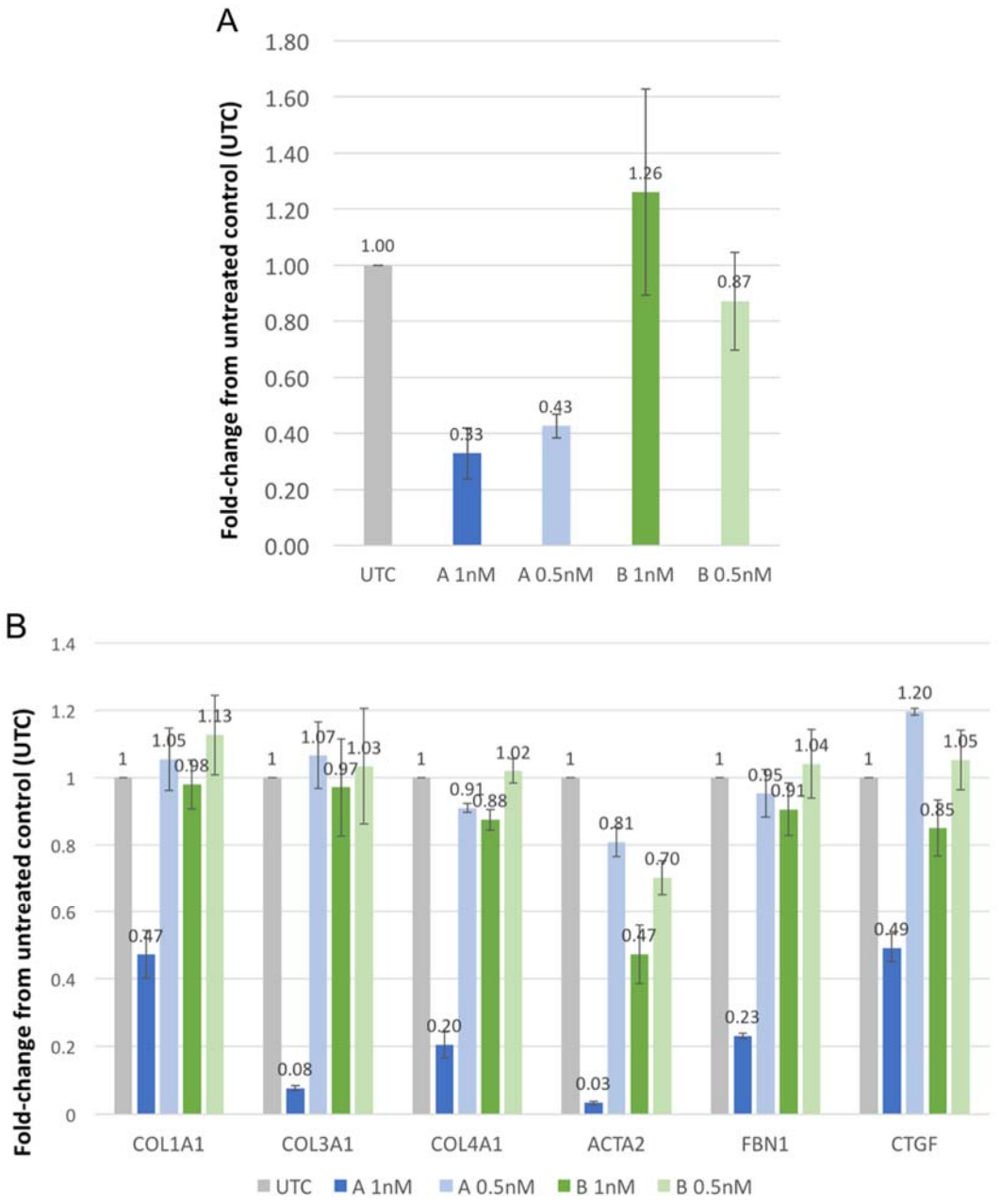

Fig 4.2.3: **The effect of anti-miR-214 and control anti-miR on an in vitro model of renal fibrosis.** A = miR-214-3p expression. B = Pro-fibrotic gene expression. Rat renal fibroblast (NRK49F) cells were transfected with anti-miR-214 (A - blue) or control anti-miR (B - green) at 1 nM and 0.5 nM concentrations, then stimulated with TGFβ1 at 10 ng/mL for 3 days. miR-214-3p and gene expression were assessed via quantitative real-time PCR (qRT-PCR), carried out with specific Taqman probes for each miRNA or gene, normalised to housekeeper Let7 for miRNA or Rplp0 for genes. n=2. Plotted as mean ± standard deviation.

To assess how anti-miR-214 could affect the molecular changes observed in Fig 4.2.2, anti-miR-214 and control anti-miR were transfected at 1 nM and 0.5 nM concentrations into NRK49F cells which were then stimulated with TGFβ1 (Fig 4.2.3). Here, miR-214-3p expression appeared to be knocked down by anti-miR-214 (compared to cells not transfected with an anti-miR) at both 1 nM and 0.5 nM concentrations, whilst control anti-miR at the same concentration had no clear effect (Fig 4.2.3). Pro-fibrotic gene expression (Col1a1, Col3a1, Col4a1, Acta2, Fbn1 and Ctgf) appeared to be knocked down with 1 nM of anti-miR-214 (A), while 0.5 nM had comparatively little effect (compared to cells not transfected with an anti-miR)(Fig 4.2.3). Both 1 nM and 0.5 nM concentrations of control anti-miR (B) appeared to have little effect on gene expression compared to cells not transfected with an anti-miR (Fig 4.2.3).

4.3: Assessing 6-weeks post-STNx as a time-point to initiate intervention with anti-miR-214 compound

In order to evaluate anti-miR-214 as a potential therapeutic intervention in CKD in the most stringent manner possible, the decision was made to initiate dosing with anti-miR-214 at a time-point where renal fibrosis had already been established. 6-weeks post-STNx was evaluated for its potential to be this time-point. Critical to the selection of this time-point was the observation of increased renal total collagen expression at the histological level and increased renal miR-214-3p expression.

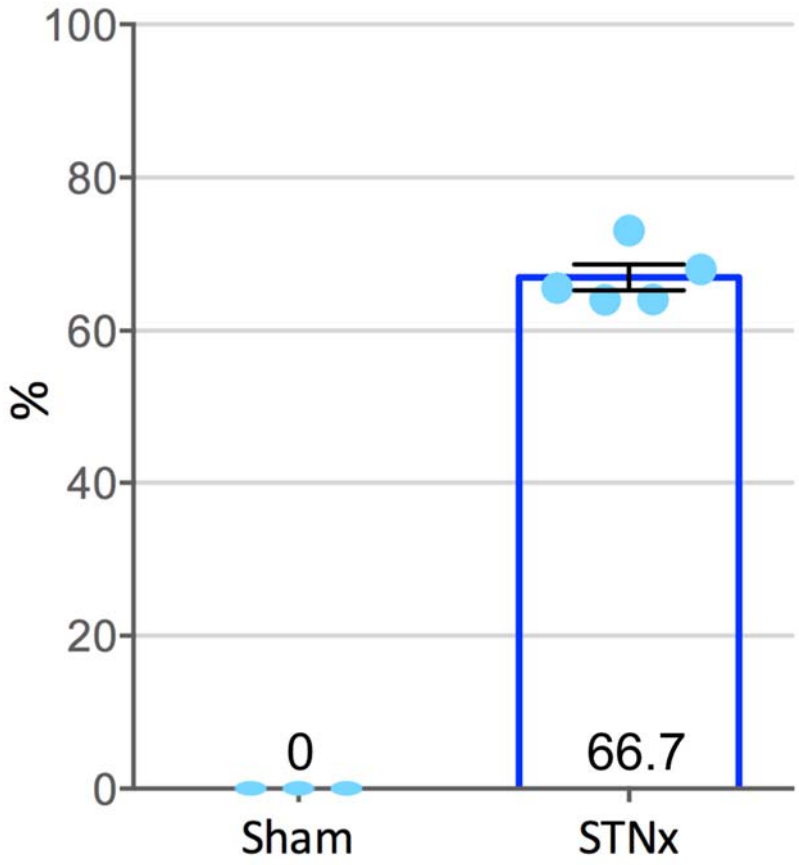

Fig 4.3.1: **Estimated percentage of total renal mass removed during the STNx surgery**. Each mouse which underwent STNx had one kidney removed and a portion of the contralateral kidney removed. Removed tissue was weighed and used to estimate the percentage of the total renal mass removed during the surgery. Sham: n=3, STNx: n=5. Plotted as mean ± SEM.

For quality control purposes, the estimated percentage of total renal mass removed during STNx surgery was calculated for each mouse. This was carried out by weighing the whole kidney removed to estimate the total renal mass present in the mouse. With the assumption that the contralateral kidney was the same weight as the whole kidney removed, the weight of the sections of tissue removed from the contralateral kidney were compared to the estimated total renal mass, obtaining a percentage of total renal mass removed.

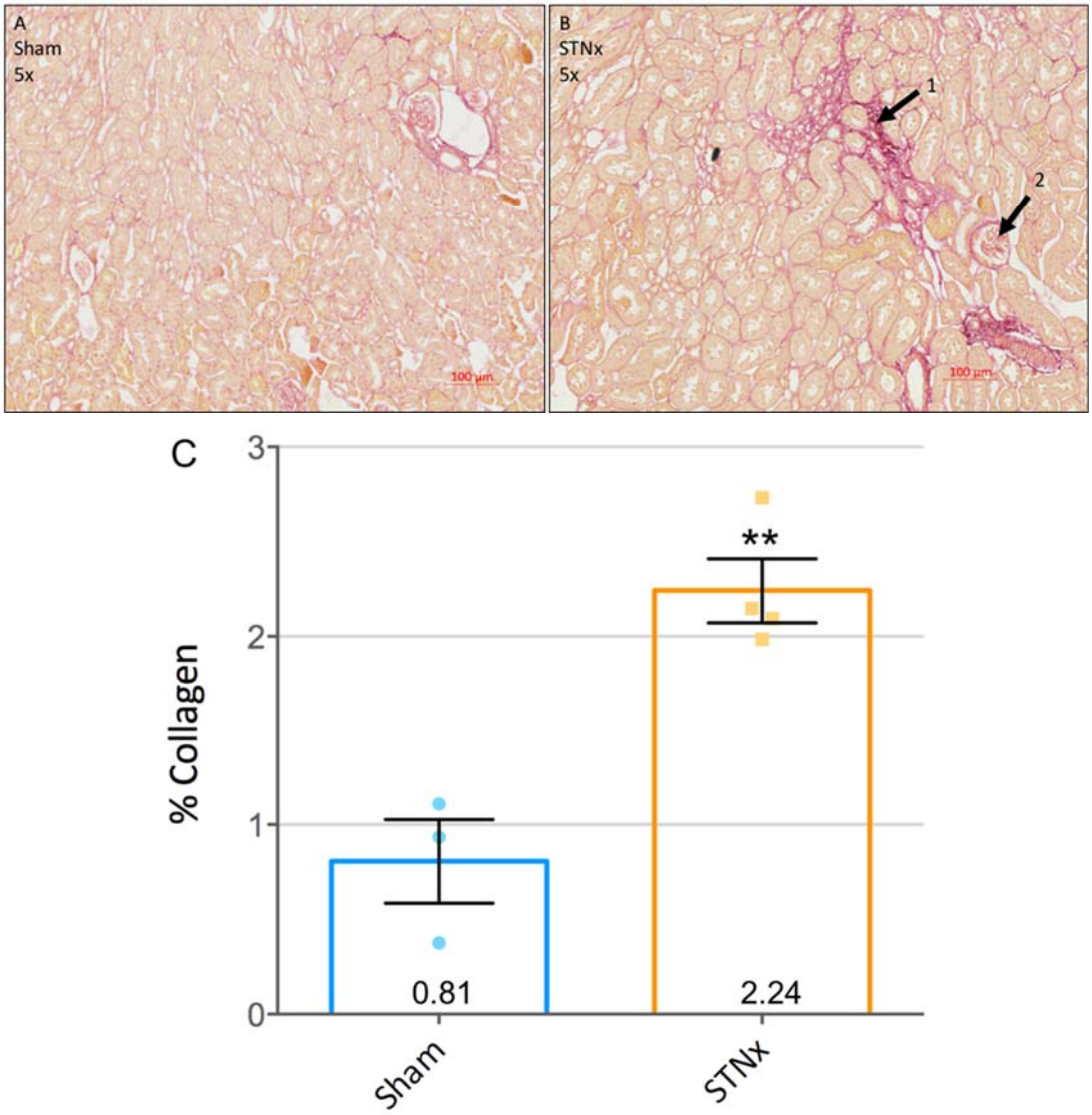

Fig 4.3.2: **Total collagen expression in the kidneys of mice 6-weeks post-STNx.** A = Sham exemplar image. B = STNx exemplar image. C = Quantification of total collagen expression. 3 µM slices were taken from paraffin-embedded kidney tissue before deparaffinisation and staining with picrosirius red for total collagen. Exemplar images (A-B) are provided at 5x magnification. 1 = Tubulointerstitial fibrosis, 2 = glomerulosclerosis. Quantification of collagen expression was carried out using Image-Pro Plus 7. Sham: n=3. STNx: n=4. Student's t-test (unpaired, two-tailed) was used for statistical analysis. ** = $P \leq 0.01$. Plotted as mean ± SEM.

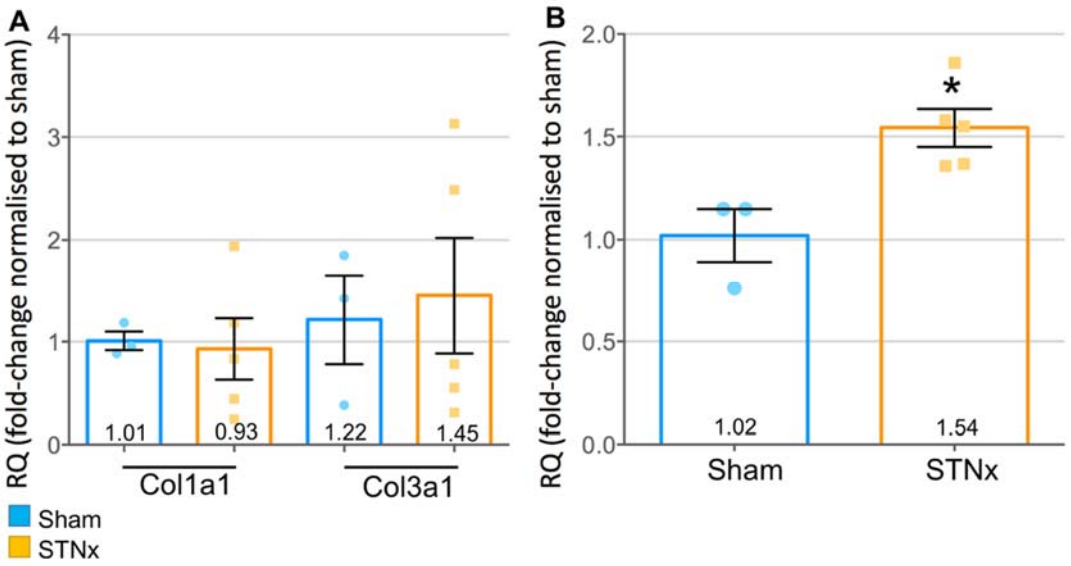

Fig 4.3.3: **Renal gene and miRNA expression at 6-weeks post-STNx**. A = Collagen gene expression. B = miR-214-3p expression. Quantitative real-time PCR (qRT-PCR) was carried out with specific Taqman probes for each gene or miR, normalised to housekeeper Ppia for genes and u6 for miRNA. Sham: n=3. STNx: n=5. Student's t-test (unpaired, two-tailed) was used for statistical analysis. * = $P \leq 0.05$. Plotted as mean ± SEM.

At 6-weeks post STNx a small but significant increase in renal collagen deposition was detected histologically in STNx mice compared to shams (0.81% ± 0.22 SEM to 2.24% ± 0.17 SEM), along with histological hallmarks of renal fibrosis (tubulointerstitial fibrosis and glomerulosclerosis) (Fig 4.3.2). This increase did not correlate with a significant increase in collagen gene expression in the kidney (Fig 4.3.3), however miR-214-3p was found to be significantly increased (1.02 ± 0.13 SEM to 1.54 ± 0.09 SEM).

4.4: Assessing the renal effects of anti-miR-214 intervention in STNx

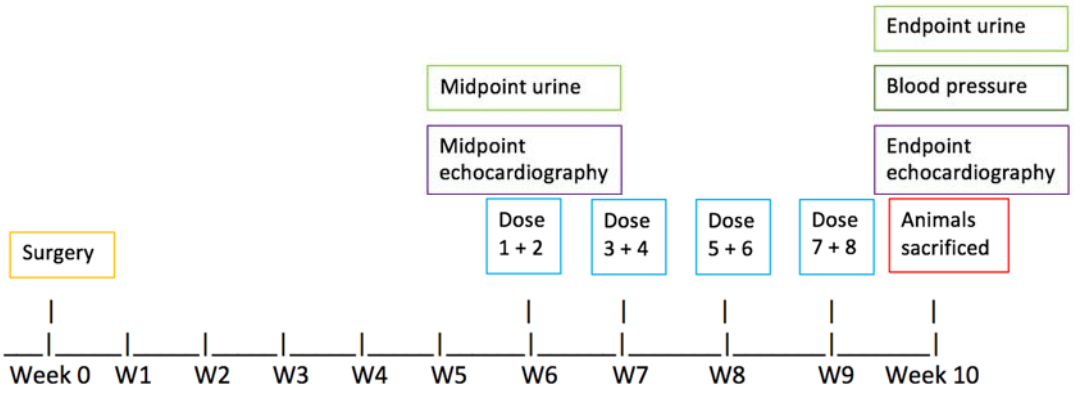

Fig 4.4.1: **Timeline of experimental procedures carried out on mice during this study (4.4 and 4.5).**

In order to evaluate the impact of anti-miR-214 compound A on a number of renal and cardiovascular parameters in the STNx model, male mice of the 129S2/Sv strain (n=41), aged 8 to 10-weeks old, were randomly selected to undergo sham (n=9) or STNx surgery (n=32). Randomisation carried out using random.org. Mice which received STNx surgery were then split into 3 intervention groups: Phosphate buffered saline (PBS, n=11), anti-miR-214 (n=11), or control anti-miR (n=10). Two animals subjected to STNx, prior to receiving any intervention, were culled due to poor health as defined as receiving an animal condition score which equalled or exceeded a maximum score, as agreed by the UK Home Office, allowed to continue on-procedure. One sham animal failed to recover from anaesthesia (inhalational isoflurane) after echocardiography. Therefore, the final group numbers were as follows: sham: n=8, PBS: n=10, anti-miR-214: n=11, and control anti-miR: n=9.

Statistical analysis between the groups was carried out as follows. Sham and STNx + PBS were compared via student's t-test (unpaired, two-tailed) to assess changes induced by the STNx model alone. STNx + PBS, STNx + anti-miR-214, and STNx +

control anti-miR groups were compared via one-way ANOVA with Tukey multiple comparison test (each group compared to each other group) to assess changes induced by anti-miR-214 compared to the two control interventions.

Anti-miR compounds and PBS were blinded by a laboratory technician prior to the study beginning and were referred to as X, Y and Z until the study was complete and all data had been analysed. STNx mice were assigned to one of the three groups based on their estimated percentage of total renal mass removed to try and match anticipated renal function across the groups. Once initiated at week-6, mice were dosed subcutaneously at 25 mg/kg twice per week for four weeks.

At 6-weeks post-surgery, prior to initial dosing, mice were placed in metabolic cages overnight to collect urine, as well as having echocardiography carried out. This was repeated, along with blood pressure measurement, at 10-weeks post-surgery just prior to being sacrificed.

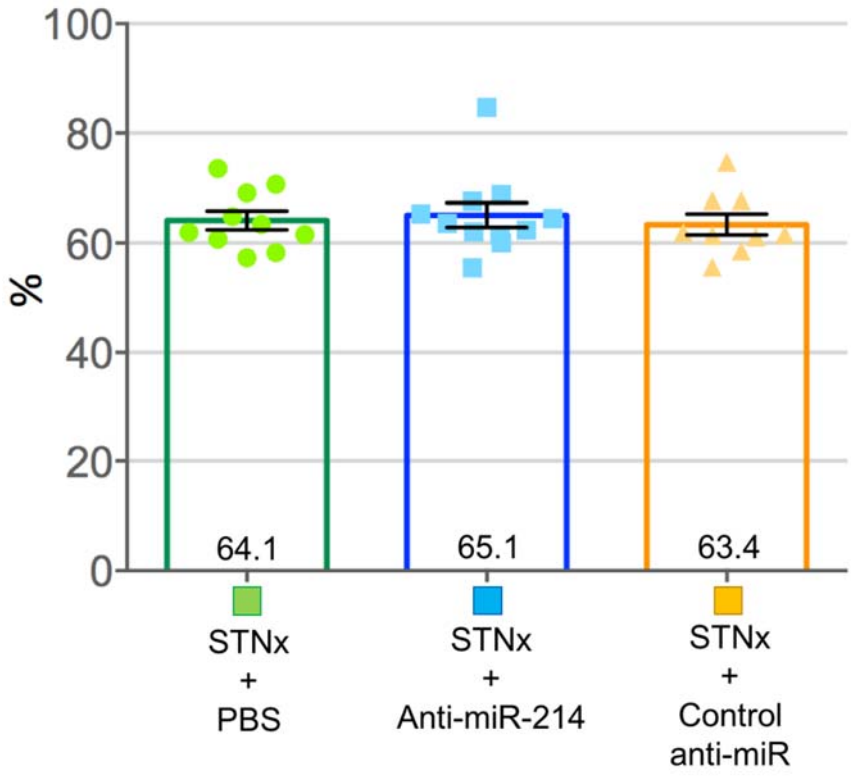

Fig 4.4.2: **Percentage of total renal mass removed during STNx surgery**. Each mouse which underwent STNx had one kidney removed and a portion of the contralateral kidney removed. This removed tissue was weighed and used to estimate the percentage of the total renal mass removed during the surgery. PBS: n=10, Anti-miR-214: n=11, Control anti-miR: n=9. Plotted as mean ± SEM. Statistical analysis via one-way ANOVA with Tukey multiple comparison test.

For quality control purposes, the estimated percentage of total renal mass removed during STNx surgery was calculated for each mouse. This was carried out with the same methodology as outlined in section 4.3. Between the three intervention groups, there was no significant difference found (Fig 4.4.2).

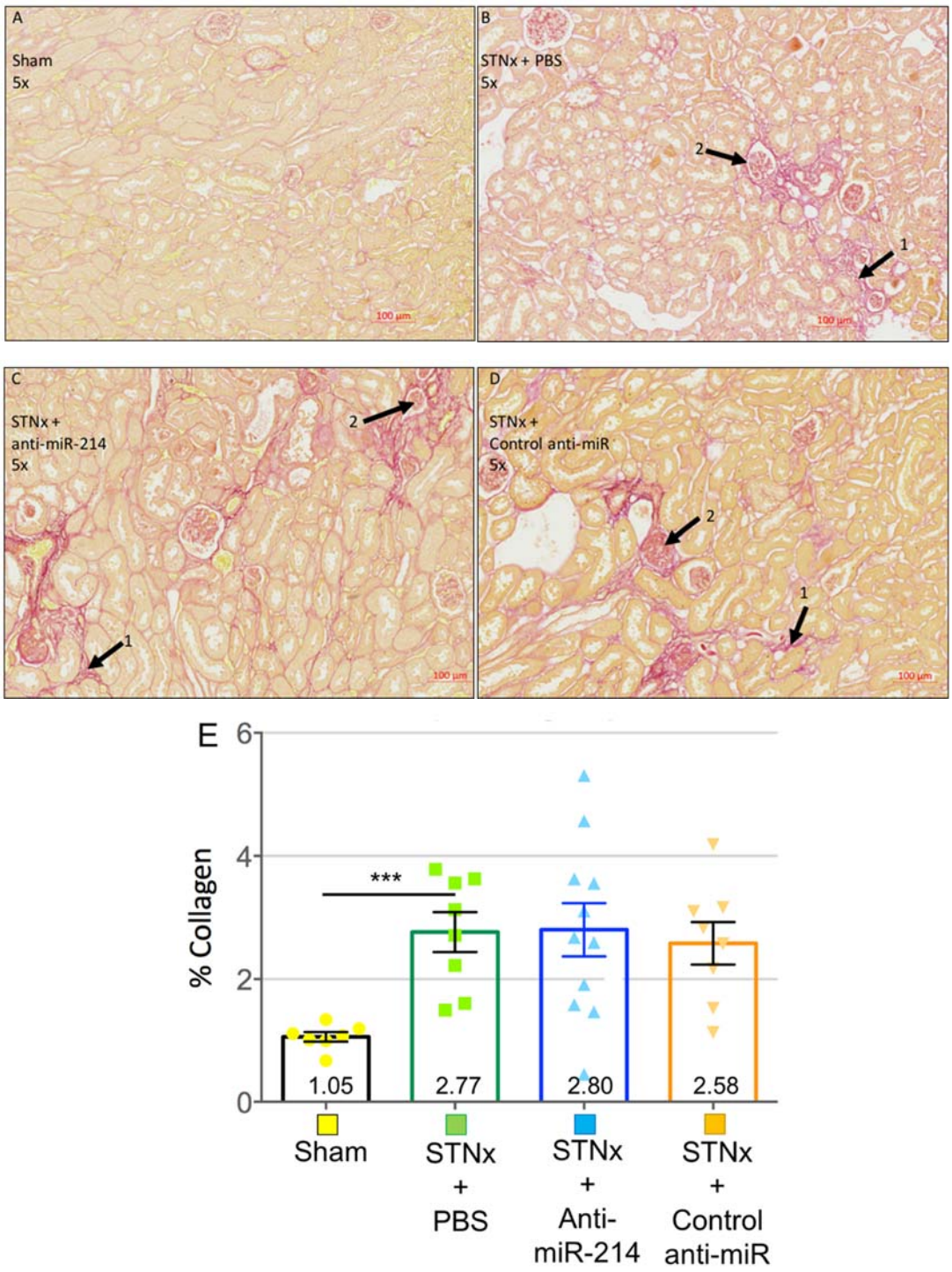

Fig 4.4.3: **Total collagen expression in mouse kidneys 10-weeks post-surgery.** A = Sham. B = STNx + PBS. C = STNx + anti-miR-214. D = Control anti-miR. E = Quantification of total collagen expression. 3 µM slices were taken from paraffin-embedded kidney tissue before deparaffinisation and staining with picrosirius red for total collagen. Exemplar images (A-D) are provided at 5x magnification. 1 =

Tubulointerstitial fibrosis, 2 = glomerulosclerosis. Quantification of collagen expression was carried out using Image-Pro Plus 7. Sham: n=7, PBS: n=8, Anti-miR-214: n=11, Ctrl anti-miR: n=8. Plotted as mean ± SEM. Statistical analysis: sham and PBS compared via student's t-test (unpaired, two-tailed). PBS, anti-miR-214 and control anti-miR groups compared via one-way ANOVA with Tukey multiple comparison test. *** = $P \leq 0.001$.

At 10-weeks post-surgery, mice which received STNx + PBS intervention had significantly increased renal fibrosis compared to sham (1.05% ± 0.08 SEM to 2.77% ± 0.32 SEM). No significant difference between each of the three intervention groups could be detected. Evidence of tubulointerstitial fibrosis and glomerulosclerosis could be detected in each of the STNx groups, regardless of which of the three interventions they received.

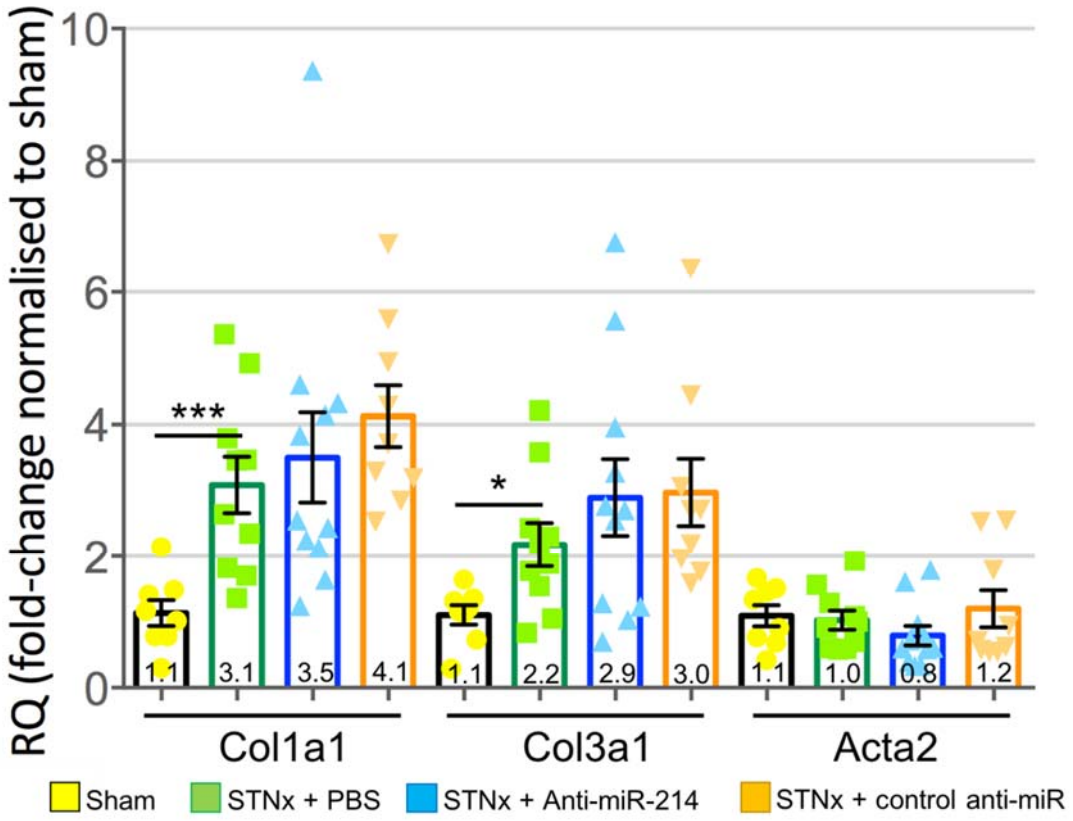

Fig 4.4.4: **Renal gene expression 10-weeks post-surgery**. Quantitative real-time PCR (qRT-PCR) was carried out with specific Taqman probes for each gene, normalised to housekeeper Ppia. Sham: n=8, PBS: n=10, Anti-miR-214: n=11, Ctrl anti-miR: n=9. Plotted as mean ± SEM. Statistical analysis: Sham and PBS compared via student's t-test (unpaired, two-tailed). PBS, anti-miR-214 and control anti-miR groups compared via one-way ANOVA with Tukey multiple comparison test. * = $P \leq 0.05$, *** = $P \leq 0.001$.

Analysis of expression of renal pro-fibrotic genes in at the RNA level revealed significant increases in Col1a1 (1.14 ± 0.20 SEM to 3.09 ± 0.43 SEM) and Col3a1 (1.11 ± 0.15 SEM to 2.18 ± 0.33 SEM) between sham and STNx + PBS intervention groups. Acta2 expression did not significantly change between sham and STNX + PBS groups (1.10 ± 0.16 SEM to 1.03 ± 0.14 SEM). When all three STNx + intervention groups were compared, no significant differences in Col1a1, Col3a1 or Acta2 were found between the groups.

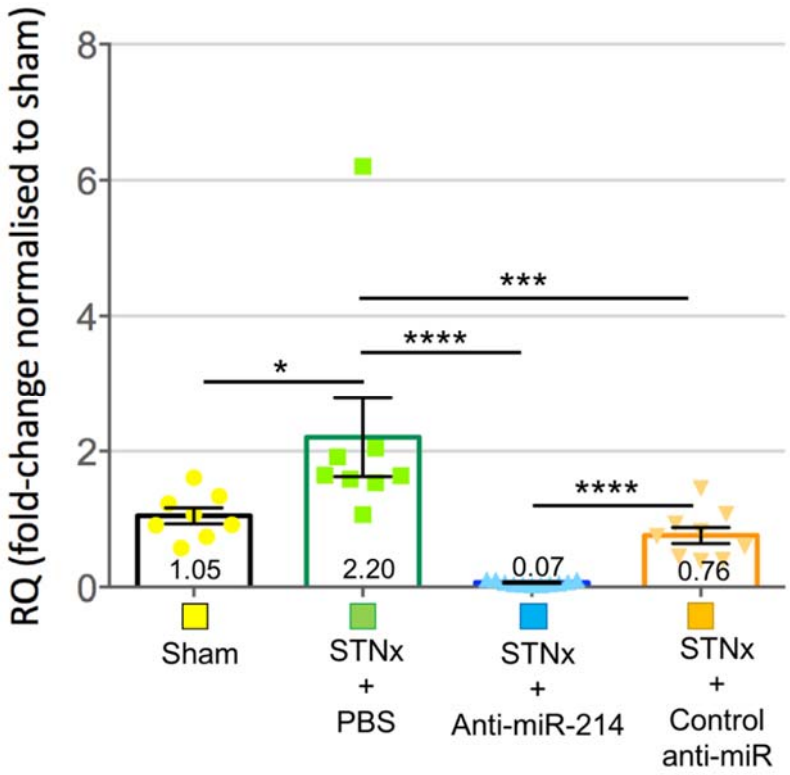

Fig 4.4.5: **Renal miR-214-3p expression 10-weeks post-STNx**. Quantitative real-time PCR (qRT-PCR) was carried out with specific Taqman probe, normalised to housekeeper u6. Sham: n=8, PBS: n=8, Anti-miR-214: n=11, Ctrl anti-miR: n=9. Plotted as mean ± SEM. Statistical analysis: Sham and PBS compared via student's t-test (unpaired two-tailed). PBS, anti-miR-214 and control anti-miR groups compared via one-way ANOVA with Tukey multiple comparison test. * = $P \leq 0.05$. ** = $P \leq 0.01$, **** = $P \leq 0.0001$.

Two animals from the PBS group were excluded from analysis due to RNA degradation (as evidenced by housekeeper U6 Ct value being 9-10 cycles higher in this sample) or being demonstrated to be a significant outlier ($P < 0.05$) by a Grubbs' test.

miR-214-3p in the kidney was found to be significantly upregulated between sham and STNx + PBS groups (1.05 ± 0.12 SEM to 2.20 ± 0.58 SEM) at 10-weeks post-surgery. miR-214-3p expression was significantly reduced by anti-miR 214 compound A and surprisingly was also somewhat suppressed in the control-anti-miR group.

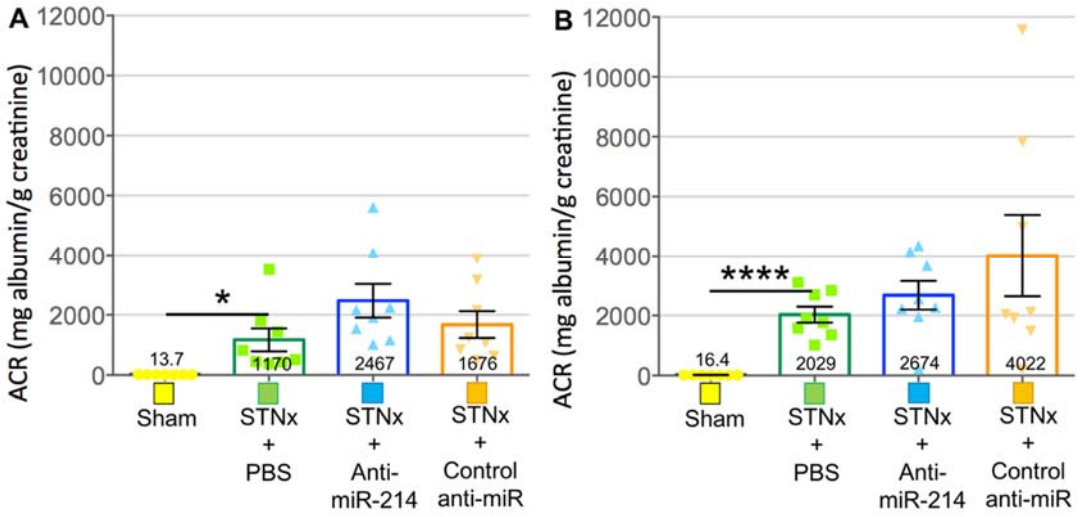

Fig 4.4.6: **Urinary albumin:creatinine ratio (ACR) at 6 and 10-weeks post-STNx**. A = 6-weeks post-STNx. B = 10-weeks post-STNx. Urine was collected overnight via metabolic cages. Albumin and creatinine content was determined via in-house biochemical analysis service. Sham: n=7, PBS: n=8, anti-miR-214: n=8, Control anti-miR: n=8. Plotted as mean ± SEM. Sham and PBS compared via student's t-test (unpaired, two-tailed). PBS, anti-miR-214 and control anti-miR groups compared via one-way ANOVA with Tukey multiple comparison test. * = $P \leq 0.05$, **** = $P \leq 0.0001$.

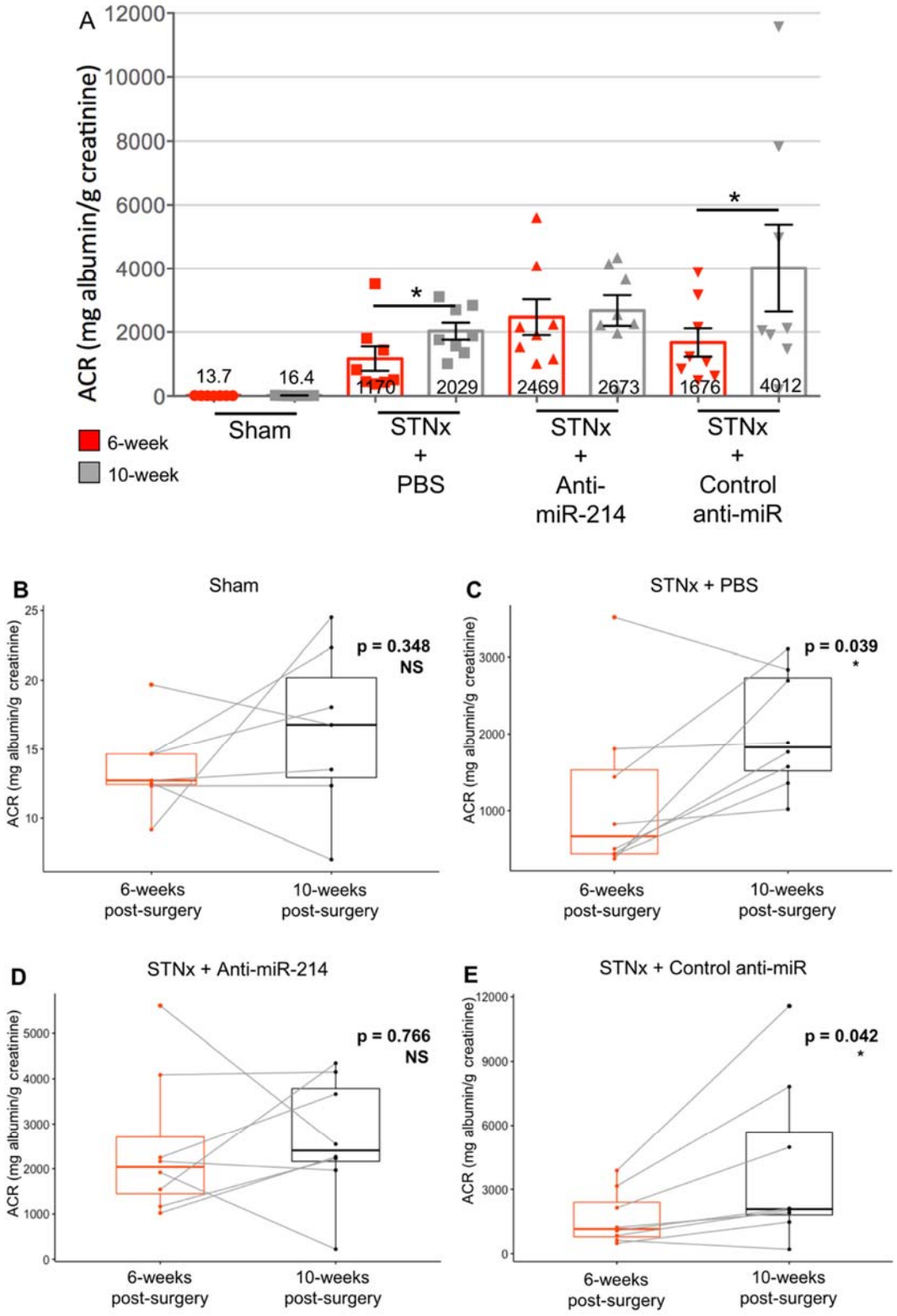

Fig 4.4.7: **Change in ACR from 6 to 10-weeks post-surgery.** A = Data from each of the four groups in bar-chart format. B-E = Boxplots for each group, lines are shown between 6 and 10-weeks post-surgery to demonstrate the change in each individual

animal's ACR between these two time-points. Urine was collected overnight via metabolic cages. Albumin and creatinine content were determined via in-house biochemical analysis service. Sham: n=7, PBS: n=8, anti-miR-214: n=8, Control anti-miR: n=8. Plotted as mean ± SEM. 6 and 10-weeks post-surgery compared via student's t-test (paired, two-tailed) for each group. * = P ≤ 0.05. B-E created using ggplot function within the ggpubr R package.

Urinary albumin:creatinine ratio (ACR) has long been used as a marker of renal damage.[30–32] ACR is an important marker in the clinic, commonly used to stratify the CKD patient population and predict prognosis.[25,26] At 6 and 10-weeks post-surgery, urine was collected from individual animals and analysed to determine ACR. Animals for which sufficient urine to determine ACR was not obtained at both 6 and 10-weeks post-surgery time-points were excluded from this analysis (sham: n=1, STNx + PBS: n=2, STNx + anti-214: n=3, STNx + control anti-miR: n=1).

A significant increase in ACR was detected between sham and STNx + PBS groups at (Fig 4.4.6 A) 6-weeks post-surgery (13.7 ± 1.2 SEM to 1170.4 ± 382.2) and (Fig 4.4.6 B) 10-weeks post-surgery (16.4 ± 2.3 SEM to 2028.5 ± 267.7). When the three STNx + intervention groups were compared at either 6-weeks (Fig 4.4.6 A) and 10-weeks (Fig 4.4.6 B) post-surgery, no significant differences were detected.

A paired t-test was carried out to investigate changes between 6-weeks and 10-weeks post-surgery within each of the four groups individually (Fig 4.4.7 A). No significant change in sham or STNx + anti-miR-214 ACRs were detected, while ACR was significantly increased between 6 and 10-weeks post-surgery in both STNx + PBS (1170.4 ± 382.2 to 2028.5 ± 267.7) and STNx + control anti-miR (1676.0 ± 444.1 to 4012.5 ± 1372.2) groups.

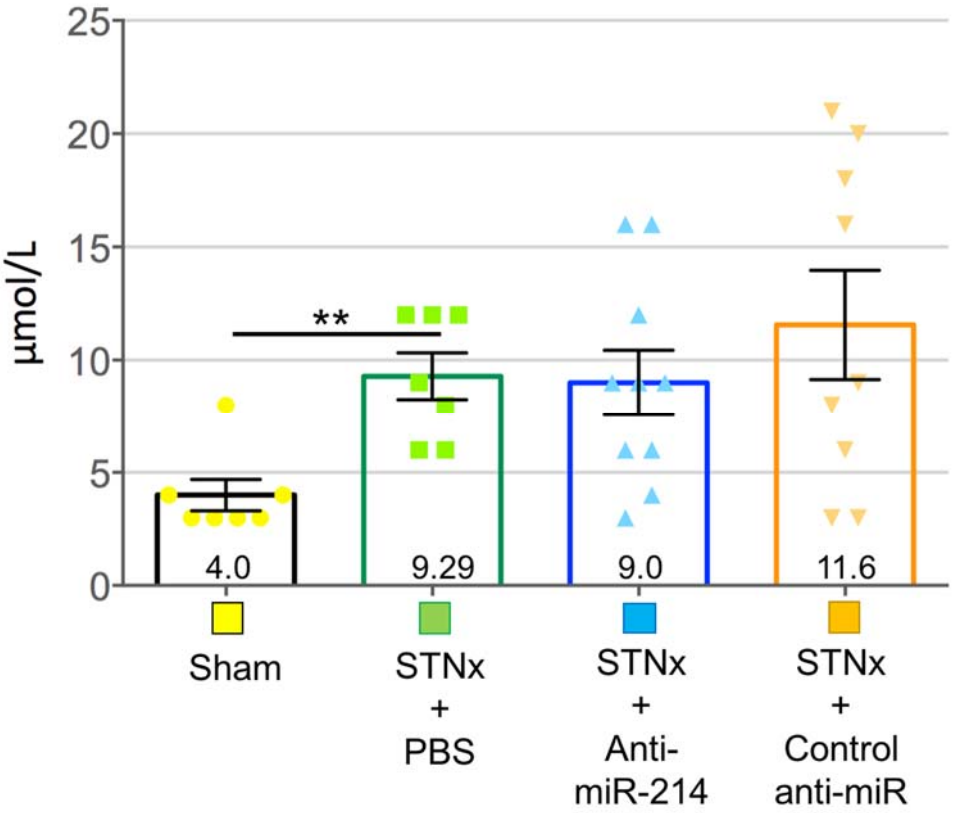

Fig 4.4.8: **Serum creatinine at 10-weeks post-STNx**. Serum was collected at cull. Creatinine content was determined via in-house biochemical analysis service. Sham: n=7, PBS: n=7, anti-miR-214: n=10, Ctrl anti-miR: n=9. Plotted as mean ± SEM. Sham and PBS compared via student's t-test (unpaired, two-tailed). PBS, anti-miR-214 and control anti-miR groups compared via one-way ANOVA with Tukey multiple comparison test. ** = $P \leq 0.01$.

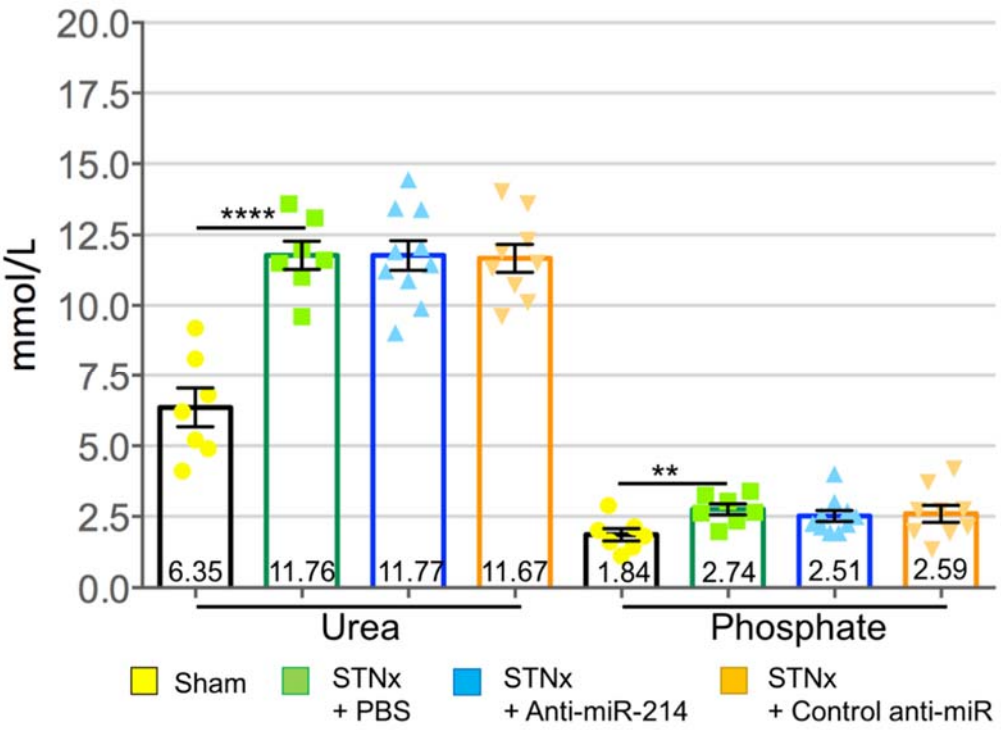

Fig 4.4.9: **Serum urea and phosphate at 10-weeks post-STNx**. Serum was collected at cull. Urea and phosphate content were determined via in-house biochemical analysis service. Sham: n=7, PBS: n=7, anti-miR-214: n=10, Ctrl anti-miR: n=9. Plotted as mean ± SEM. Sham and PBS compared via student's t-test (unpaired two-tailed). PBS, anti-miR-214 and control anti-miR groups compared via one-way ANOVA with Tukey multiple comparison test. ** = P ≤ 0.01, **** = P ≤ 0.0001.

Serum creatinine measurement is central to the diagnosis and staging of patients with CKD.[10] Urea is product of protein and nitrogen metabolism which is normally filtered from the blood by the kidneys, therefore increased serum concentrations are detected as renal function declines.[50,51] Clinically, serum phosphate concentrations are known to increase once renal function has significantly declined (GFR of 30 ml/minute/1.73 m2 or below).[45] Management of serum phosphate levels is considered an important aspect of clinical CKD management overall.[44,46,364]

At 10-weeks post-surgery, serum creatinine (Fig 4.4.8), urea and phosphate (Fig 4.4.9) were determined for each group. Comparing between sham and STNx + PBS groups, a significant increase was detected in serum creatinine (4.0 μmol/L ± 0.69 SEM to 9.29 ± 1.04), serum urea (6.35 mmol/L ± 0.70 SEM to 11.76 ± 0.50), and serum phosphate (1.84 mmol/L ± 0.22 SEM to 2.74 ± 0.19). When comparing between the three STNx + intervention groups, no significant changes were detected in serum creatinine, urea or phosphate.

4.5: Assessing the cardiovascular effects of anti-miR-214 intervention in STNx

Termed cardiorenal syndrome type 4, cardiovascular complications commonly occur in patients with CKD.[365] Cardiac hypertrophy, cardiac fibrosis and hypertension are frequently present in these patients, with cardiac dysfunction being a less common feature.[365] In order to assess the impact of miR-214-3p on these parameters, echocardiography, histological staining, and tail-cuff blood-pressure measurement were utilised, as well as cardiac weight at cull being taken.

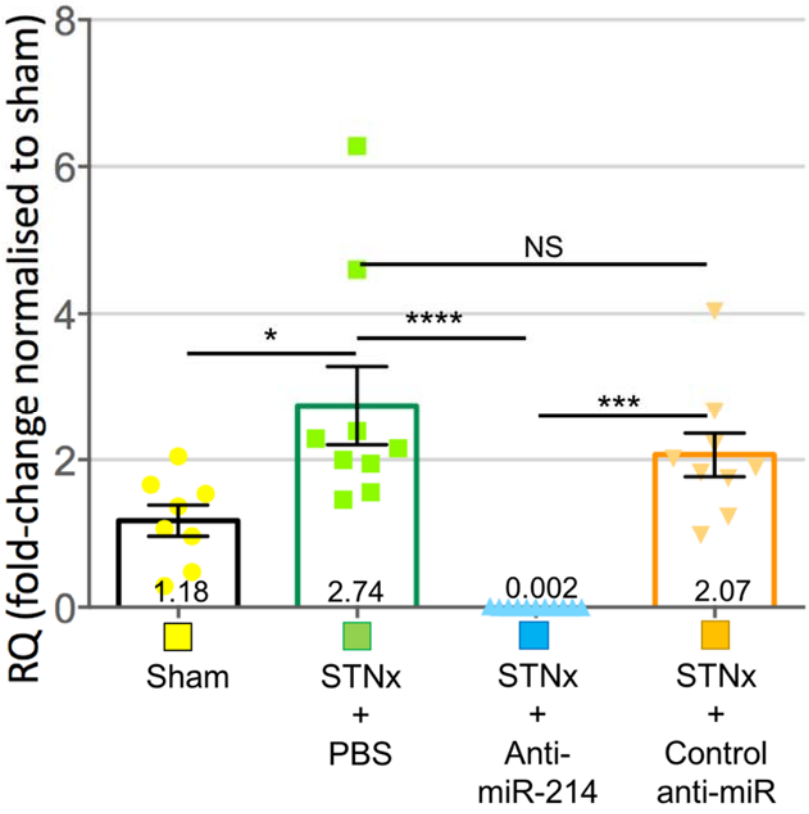

Fig 4.5.1: **miR-214-3p expression in heart tissue of mice 10-weeks post-STNx**. Quantitative real-time PCR (qRT-PCR) was carried out with specific Taqman probe, normalised to housekeeper u6. Sham: n=8, PBS: n=9, Anti-miR-214: n=11, Ctrl anti-miR: n=9. Plotted average ± SEM. Statistical analysis: Sham and PBS compared via student's t-test (unpaired, two-tailed). PBS, anti-miR-214 and control anti-miR groups compared via one-way ANOVA with Tukey multiple comparison test. * = $P \leq 0.05$. *** = $P \leq 0.001$, **** = $P \leq 0.0001$, NS = not significant ($P > 0.05$).

In the heart, miR-214-3p expression increased significantly between sham and STNx + PBS (1.18 ± 0.21 SEM to 2.74 ± 0.54). A significant decrease in miR-214-3p expression was detected when comparing the STNx + anti-miR-214 (0.002 ± 0.001) group with STNx + control anti-miR (2.07 ± 0.30) or STNx + PBS (2.74 ± 0.54) groups. No significant change in miR-214-3p expression was detected when comparing STNx + PBS and STNx + control anti-miR groups.

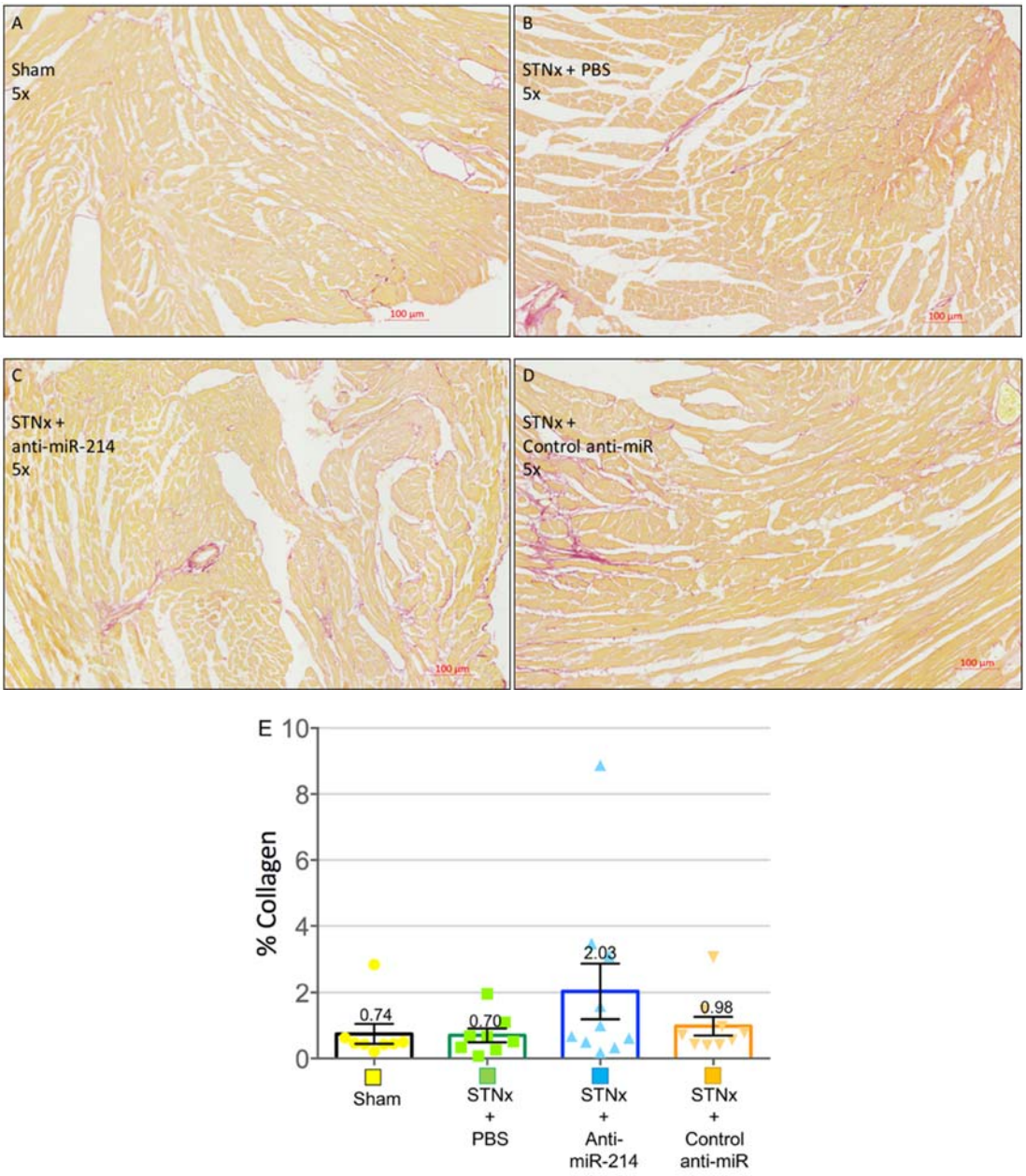

Fig 4.5.2: **Total collagen expression in mouse hearts 10-weeks post-surgery**. A = Sham. B = STNx + PBS. C = STNx + anti-miR-214. D = STNx + control anti-miR. E = Quantification of total collagen expression. 3 µM slices were taken from paraffin-embedded heart tissue before deparaffinisation and staining with picrosirius red for total collagen. Exemplar images (A-D) are provided at 5x magnification. Sham: n=8, PBS: n=8, Anti-miR-214: n=10, Ctrl anti-miR: n=9. Plotted as mean ± SEM. Statistical analysis: sham and PBS compared via student's t-test (unpaired, two-tailed). PBS, anti-miR-214 and control anti-miR groups compared via one-way ANOVA with Tukey multiple comparison test.

No statistically significant changes in cardiac fibrosis could be found at the histological level at 10-weeks post-STNx, regardless of intervention (Fig 4.5.2).

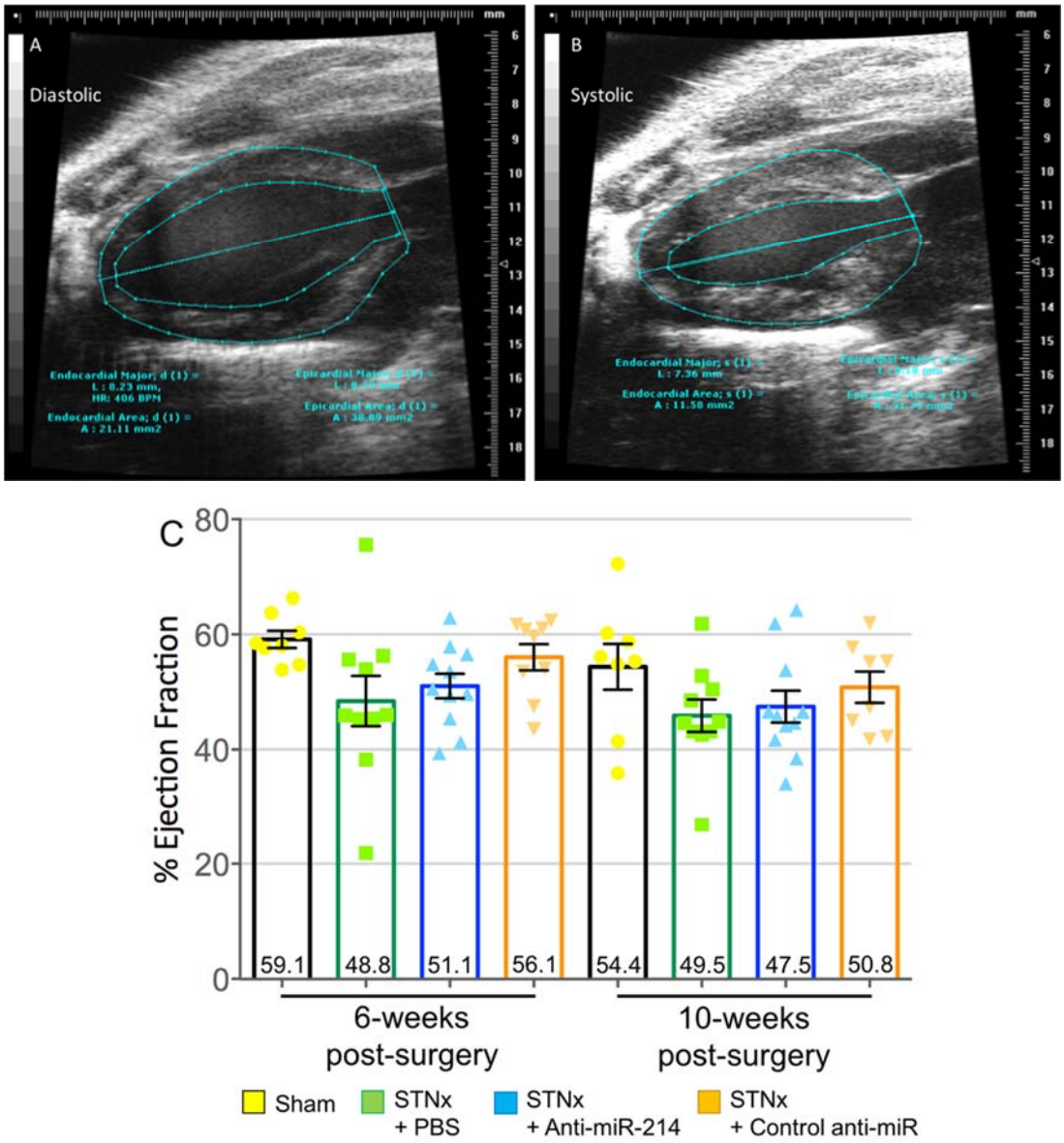

Fig 4.5.3: **Ejection fraction in mice subjected to STNx (via echocardiography).** A-B = Exemplar images of echocardiography EKV analysis using VisualSonics Vivo software. C = Ejection fraction. Sham: n=8, PBS: n=10, Anti-miR-214: n=11, Ctrl anti-miR: n=9. Plotted as mean ± SEM. Statistical analysis: sham and PBS compared via student's t-test (unpaired, two-tailed). PBS, anti-miR-214 and control anti-miR groups compared via one-way ANOVA with Tukey multiple comparison test. 6-weeks and 10-weeks post-surgery results analysed separately.

At both 6 and 10-weeks post-surgery, EKV analysis revealed no significant differences in cardiac ejection fraction were when comparing between sham and STNx + PBS groups, or when comparing between each of the three STNx + intervention groups.

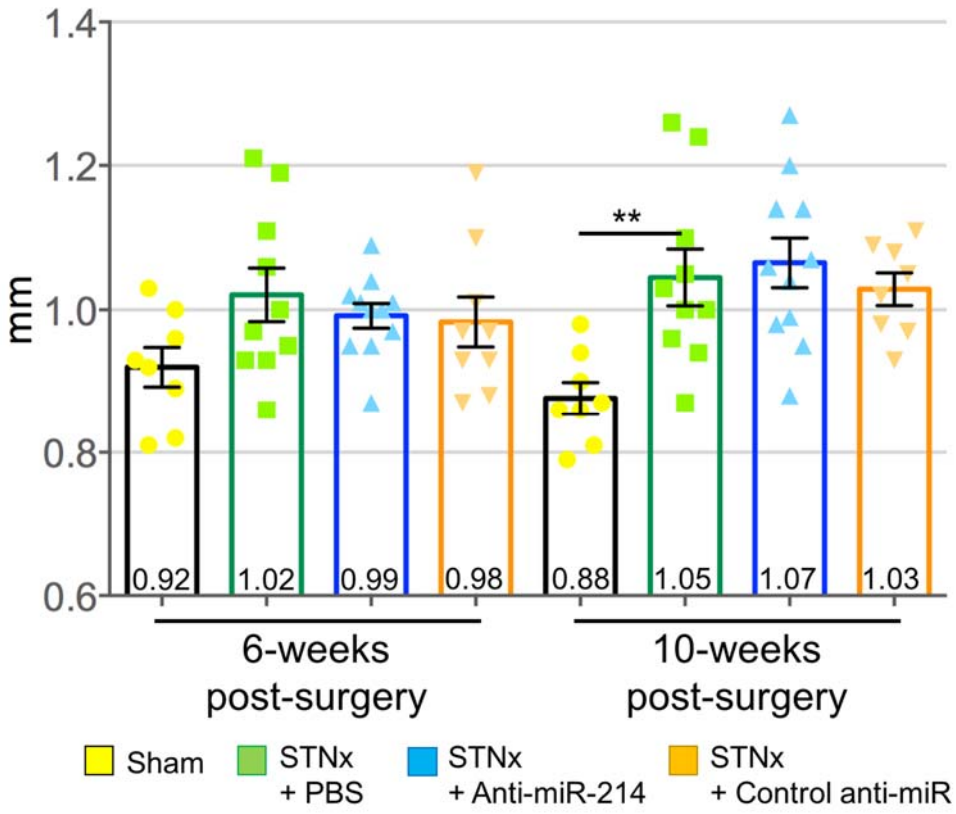

Fig 4.5.4: **Cardiac wall thickness in mice subjected to STNx (via echocardiography).** Sham: n=8, PBS: n=10, Anti-miR-214: n=11, Ctrl anti-miR: n=9. Plotted as mean ± SEM. Statistical analysis: sham and PBS compared via student's t-test (unpaired two-tailed). PBS, anti-miR-214 and control anti-miR groups compared via one-way ANOVA with Tukey multiple comparison test. 6-weeks and 10-weeks post-surgery results analysed separately. ** = $P \leq 0.01$.

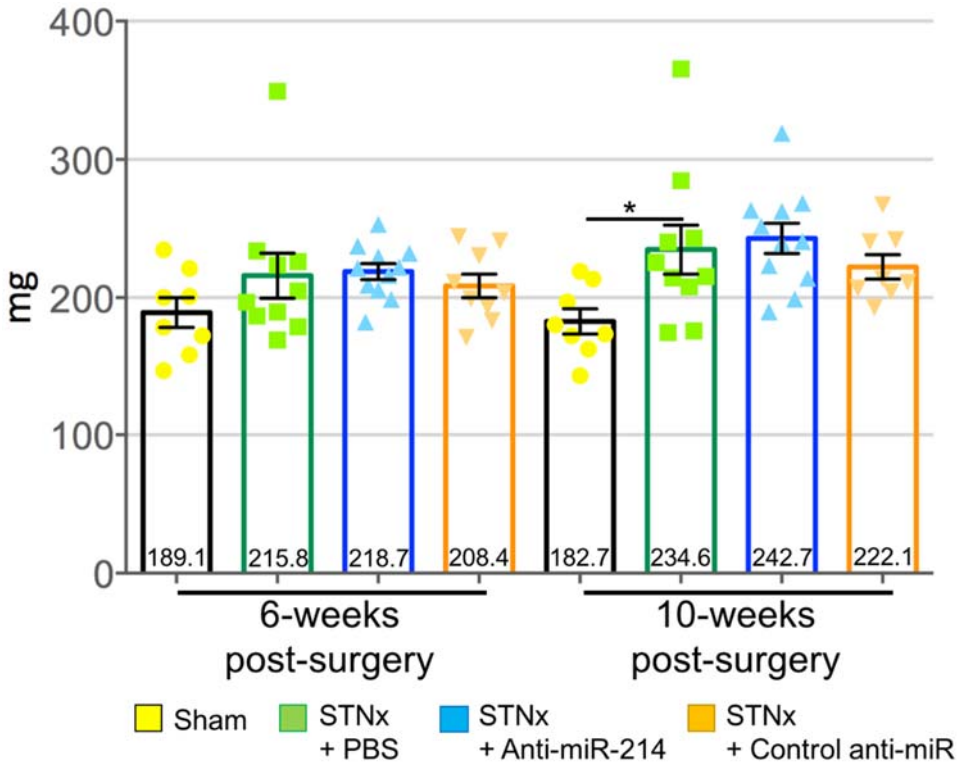

Fig 4.5.5: **Left ventricle mass in mice subjected to STNx (via echocardiography).** Sham: n=8, PBS: n=10, Anti-miR-214: n=11, Ctrl anti-miR: n=9. Plotted as mean ± SEM. Statistical analysis: sham and PBS compared via student's t-test (unpaired two-tailed). PBS, anti-miR-214 and control anti-miR groups compared via one-way ANOVA with Tukey multiple comparison test. 6-weeks and 10-weeks post-surgery results analysed separately. * = $P \leq 0.05$.

At 6-weeks post-surgery, EKV analysis revealed no significant differences in cardiac wall thickness (Fig 4.5.4) or left ventricle mass (Fig 4.5.5) between sham and STNx + PBS groups. However, at 10-weeks post-STNx, comparing between sham and STNx + PBS groups revealed a significant increase in cardiac wall thickness (0.88 mm ± 0.02 SEM to 1.05 ± 0.04) and left ventricle mass (182.7 mg ± 9.06 SEM to 234.6 ± 17.75). At both 6 and 10-weeks post-surgery, when comparing between each of the three STNx + intervention groups, no significant differences were detected in cardiac wall thickness or left ventricle mass.

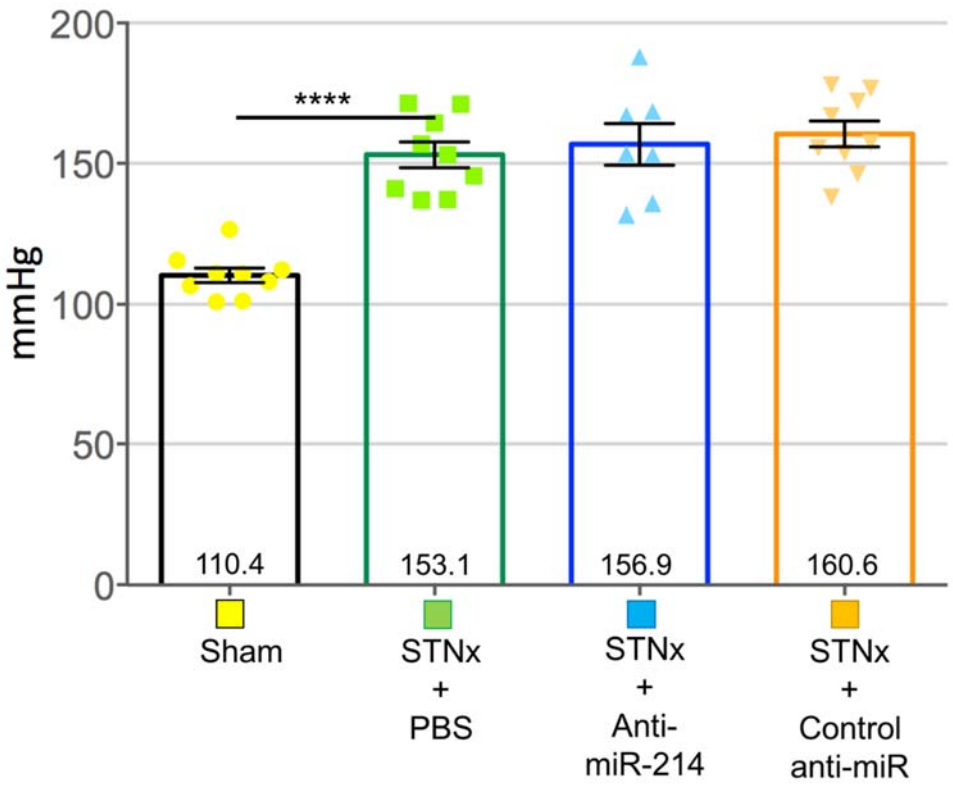

Fig 4.5.6: **Blood pressure in mice 10-weeks post-STNx (via tail cuff)**. Sham: n=9, PBS: n=9, Anti-miR-214: n=7, Ctrl anti-miR: n=9. Plotted as mean ± SEM. Statistical analysis: sham and PBS compared via student's t-test (unpaired, two-tailed). PBS, anti-miR-214 and control anti-miR groups compared via one-way ANOVA with Tukey multiple comparison test. **** = $P \leq 0.0001$.

At 10-weeks post-surgery, a significant increase in blood pressure was observed between sham and STNx + PBS groups (110.4 mmHg ± 2.61 SEM to 153.1 ± 4.60). When comparing between the three STNx + intervention groups, no significant difference in blood pressure was detected.

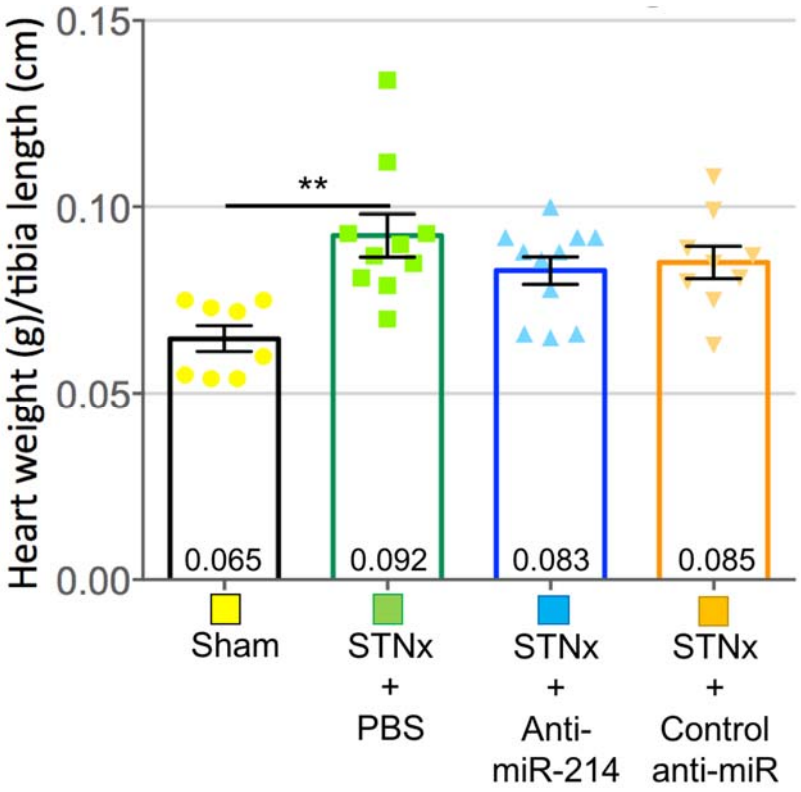

Fig 4.5.7: **Heart weight at cull normalised to tibia length**. Sham: n=8, PBS: n=10, Anti-miR-214: n=11, Control anti-miR: n=9. Plotted as mean ± SEM. Statistical analysis: sham and PBS compared via student's t-test (unpaired, two-tailed). PBS, anti-miR-214 and control anti-miR groups compared via one-way ANOVA with Tukey multiple comparison test. ** = $P \leq 0.01$.

At sacrifice, 10-weeks post-surgery, wet weight of each heart was taken and normalised to the tibia length of that animal. A significant increase was detected between sham and STNx + PBS groups (0.065 g/cm ± 0.003 SEM to 0.092 ± 0.006), however no significant differences were detected when comparing between the three STNx + intervention groups.

4.6: Discussion

In vitro experiments in section 4.2 were carried out at Regulus Therapeutics during a placement in second semester of PhD year one. A number of anti-miR-214 compounds, along with a control anti-miR, were provided at this time for analysis. This initial analysis was carried out using a luciferase-based miR-214 sensor system, where the compounds were compared on their ability to inhibit miR-214-3p interacting with an artificial miR-214-3p binding site (seed-sequence match) located on a luciferase expression plasmid (Fig 4.2.1). Multiple compounds were observed to inhibit miR-214, while this effect was not observed with control anti-miR. Compound A (RG4658) was selected by Regulus to be used in future experiments, along with the same control anti-miR used in Fig 4.2.1.

One limitation of the luciferase-based assay system used is that it is quite artificial in nature and lacks any cellular context, whilst also being carried out in HeLa cells. Therefore, it may be advantageous to build on this data by examining the anti-miR compounds in an *in vitro* model of renal fibrosis. TGFβ1-stimulation of normal rat renal fibroblast (NRK49F) cells was chosen due to availability of the cells along with TGFβ1-stimulation of this cell line being a commonly used *in vitro* model of renal fibrosis.[366–369] Although no statistical analysis could be carried out due to low n number (n=2), a number of trends in these data could be observed.

Upregulations in several fibrosis associated genes, along with increased miR-214-3p expression are observable in Fig 4.2.2. Col1a1 and Col3a1 are fibrillar collagens,[330] well-known to be secreted by fibroblasts in renal fibrosis.[367,370–373] Col4a1 is ordinarily a component of glomerular and tubular basement membranes, however it has been shown to be excreted by renal fibroblasts stimulated with TGFβ.[374] Acta2 (αSMA) is a marker of the myofibroblast differentiation[333] caused by the TGFβ in this model.[375–377] Fbn1 (fibrillin1) is secreted by fibroblasts in the kidney in response to TGFβ.[378–381] Ctgf is known to be upregulated in NRK49F cells in response to TGFβ[382] and has been

suggested to be an important mediator of renal fibrosis.[383–387] The trends in upregulation observed in these genes suggest myofibroblast activation was successfully modelled *in vitro*. The novel finding of an association of this with increased miR-214-3p expression is also interesting. These data provided a platform for investigation of anti-miR-214 and control anti-miR in an *in vitro* setting which is more relatable to the *in vivo* setting of renal fibrosis than the luciferase assay system provided.

Anti-miR-214 appeared to decrease the TGFβ-induced expression of miR-214-3p at both concentrations tested, while control anti-miR did not have any clear effect on this (Fig 4.2.3). This data was obtained via quantitative real-time PCR (qRT-PCR), a commonly used method of detecting oligonucleotide-mediated miRNA inhibition. However, this has been more recently demonstrated to be an imperfect method of detection, as the primer for miRNA reverse transcription may displace the bound anti-miR oligonucleotide.[383] Therefore, this data may not fully reflect the miR-214 inhibition caused by the anti-miR compounds. Despite this, trends towards amelioration of the TGFβ-induced induction of Col1a1, Col3a1, Col4a1, Acta2, Fbn1 and Ctgf gene expression were observable with 1 nM of anti-miR-214, but not with 1 nM of control anti-miR (bar an observable effect on Acta2 expression). Taken together, results outlined in section 4.2 provided a basis for further *in vivo* studies using these anti-miR compounds.

The control anti-miR provided for the STNx experiment had been previously used by Regulus as a control for anti-miR-214, where it was demonstrated to have no significant influence on major readouts which were of importance to assessing the therapeutic potential of anti-miR-214, such as renal collagen expression in UUO. The control anti-miR inhibits miR-33, which due to a lack of influence on renal collagen expression, appeared to be irrelevant to renal fibrosis and therefore functional as a control.

When anti-miRs were administered in the STNx model, qRT-PCR was used to detect miR-214-3p expression in the kidneys (Fig 4.4.5) and hearts (Fig 4.5.1) of the animals. In the kidney, control anti-miR significantly reduced miR-214-3p expression in STNx compared to PBS, whereas no difference in miR-214-3p expression between these two groups could be detected in the heart. Taken together, these results may indicate that knockdown of miR-33 may result in decreased miR-214-3p expression specifically in the kidneys of animals subjected to STNx. Insufficient evidence exists in this study to support a hypothesis as to how this may occur. As this data is derived from qRT-PCR, it is worth noting again that RT-primers may displace anti-miR oligonucleotides binding to miRNA and successfully carry out reverse-transcription,[383] meaning the true repression brought about by the anti-miR may not be reflected in qRT-PCR results. However, given that the control anti-miR was demonstrated to have no capacity to directly bind miR-214 using a luciferase-based miR-sensor system (Fig 4.2.1), it is unlikely that this caveat would apply to qRT-PCR-derived data showing decreased renal miR-214-3p in the control anti-miR group. Despite any reduction in miR-214-3p expression in the kidney caused by the control anti-miR, this had no measurable impact on the study, as no significant differences between the control anti-miR and PBS groups could be detected in any of the parameters measured.

In the study outlined in section 4.4, a PBS control intervention group was used in addition to the control anti-miR group. Comparisons between sham and STNx + PBS groups were carried out via t-test, separately from the other statistical analysis, and were used essentially as a measure of how the STNx model caused changes in the measured parameters without the influence of anti-miR interventions. This comparison constituted all the statistically significant results obtained in this study, bar miR-214-3p expression in the kidney and heart. In general terms, this indicates the model successfully induced renal dysfunction associated with CKD as expected, but anti-miR-214 had no significant impact on reversing or ameliorating the phenotype produced. This being in spite of a seemingly successful knockdown of miR-

214-3p (Fig 4.4.5) would suggest that miR-214-3p expression level has no impact on experimental CKD, although a number of possible explanations must be considered.

With no reference for miR-214 knockdown besides qRT-PCR derived from whole-kidney tissue RNA, it is unknown if the anti-miR-214 compound successfully reached all cell types in the kidney, and therefore that miR-214 was successfully knocked down in each cell type relevant to any pro-fibrotic mechanism miR-214 may possess. Regulus have previously shown that this anti-miR-214 compound in particular has significantly reduced renal fibrosis when administered in the UUO model, which would indicate that this anti-miR compound has the ability to reach the cells in the kidney needed to bring about the anti-fibrotic effects observed. In comparing this result in UUO to the STNx model, barriers exist in that the type of renal injury in these models is quite different and physical differences between the kidneys in each model may exist. However, given the hyperfiltration that is known to occur in the remnant kidney in subtotal (5/6th) nephrectomy models,[186] it seems unlikely that an anti-miR would have less ability to penetrate the kidney, especially considering the ~65% reduction in total renal mass would result in less renal mass in total to penetrate and potentially decreased excretion of the compound. With well-validated miR-214-3p direct targets involved in renal fibrosis or dysfunction not known at the time of this study and RNA-sequencing or gene expression microarrays being prohibitively expensive, assessing if miR-214 knockdown was functional in de-repressing target genes was not possible.

The time post-surgery at which anti-miR-214 intervention was initiated may also be a factor in the lack of efficacy detected. Anti-miR-214 significantly inhibited fibrosis in the UUO model when dosing began prior to UUO surgery[261], with miR-214 therefore being knocked down significantly early in (and prior to) the fibrotic process. Decreased renal fibrosis is also seen in the UUO model with miR-214 genetic knockout mice.[261] These were important pilot studies which demonstrated miR-214 inhibition as an anti-fibrotic target in the kidney. More recently, miR-214 knockdown

via anti-miR has been shown to be protective against renal injury in an albumin-overload model of CKD, as well as tubular-specific genetic knockout of miR-214 being protective in ischemia-reperfusion injury and UUO.[267] However, CKD patients are commonly only diagnosed when renal impairment is already significant,[362,363] therefore it would be critical to understand how a potential therapeutic intervention would perform when initiated in these conditions.

In contrast to UUO, renal injury is developed over a longer period of time in the STNx model. The intention of this study was to exploit this and intervene at a time-point where some renal dysfunction had already been established. Based on data from previous runs of the STNx model, 6-weeks post-STNx had been observed to be the typical time-point at which abnormal urinary albumin:creatinine ratio (ACR) began to be observed, so this time-point was therefore investigated as a potential time-point to begin intervention (section 4.3). Increased renal fibrosis and miR-214-3p expression were observed and therefore this time-point was chosen. However, as mentioned, no significant differences between the anti-miR-214 group and either the control anti-miR or PBS groups could be detected. Therefore, the possibility must be considered that anti-miR-214 intervention may only be effective if initiated early in the fibrotic process (or even before it has begun), which would indicate anti-miR-214 may not be an effective anti-fibrotic agent in most CKD patients. A follow-up STNx study using a genetic knockout or initiation of anti-miR dosing prior to surgery would enhance our understanding of time-sensitivity in relation to miR-214 as an anti-fibrotic target. Another possible explanation is that 6-weeks post-STNx is too late in the course of the model for any therapeutic to show efficacy, or that the 4-week window between initiation of intervention and sacrifice of the animals is insufficient to observe a therapeutic effect. The use of a positive control intervention (known to be therapeutic in CKD and subtotal nephrectomy, for example an ACE inhibitor[190]) at 6-weeks post-STNx may be a useful tool in dissecting time-sensitivity for therapeutic efficacy in the model in general from time-sensitivity of specifically anti-miR-214 intervention.

Although no significant results were obtained when comparing intervention groups at the endpoint of the study, an effect was observed on ACR when comparing the change results obtained at 6-weeks and 10-weeks post-surgery (Fig 4.4.7). ACR measurement at 6-weeks (Fig 4.4.6 A) took place prior to the animals receiving their first intervention dose. No significant differences between the intervention groups were detected at this time, although the group due to begin receiving anti-miR-214 had a trend towards having a higher average. Comparing at the 10-week time-point (Fig 4.4.6 B), the intervention groups again were not significantly different. However, when the change between 6 and 10-weeks within each group was compared (Fig 4.4.7), significant increases in ACR were detected in both the PBS and control anti-miR groups, but not in the group which received anti-miR-214. This suggests anti-miR-214 may inhibit or slow the progression of renal dysfunction once dosing is initiated.

Halting the progressive increase in ACR may be of great benefit clinically, especially if synergistic effects were observed with current pharmacological interventions. However, it should be noted that the effect of inhibited ACR increase appears to have had a weak effect on the overall outcomes of this study, meaning it may be irrelevant to the other measured parameters or simply a spurious result. A longer follow-up study would allow this potential effect on ACR progression to be confirmed over a longer period of time, and may also allow sufficient time for a measurable effect on the parameters investigated in this study to appear.

In evaluating a potential CKD therapeutic intervention, direct renal effects are only part of the picture. CKD and cardiovascular disease are well-known to be closely related,[388] and risk of adverse cardiovascular events is known to increase as GFR declines.[389] The interaction between miR-214 and cardiovascular disease is complex, with increased miR-214 found to be beneficial or deleterious depending on the underlying pathology.[272] As knockdown of miR-214-3p in the heart appeared to be

efficient (Fig 4.5.1), the consequences of this in a model of CKD known to be deleterious to the cardiovascular system are particularly important.

No significant differences between the anti-miR-214 group and control anti-miR or PBS groups were found in cardiac fibrosis, cardiac function (via ejection fraction), blood pressure, or in measures of cardiac hypertrophy. Although the anti-miR-214 group did have a higher average cardiac collagen expression than the other groups (Fig 4.5.2) due to some outlier animals with large patches of cardiac fibrosis present, this was not statistically significant. These data suggest anti-miR-214 is not deleterious or beneficial in the heart when cardiorenal syndrome secondary to chronic renal insufficiency is present. However, due to the results obtained in relation to cardiac fibrosis, it may be prudent to confirm this with a larger study (statistically powered to detected this) or with a longer study to assess how the cardiovascular parameters are affected over a longer period of time.

Conclusion:

In vitro analysis carried out while on placement at Regulus Therapeutics suggested the anti-miR-214 compound provided successfully inhibited miR-214-3p expression, while the control anti-miR had no inhibitory affect. 6-weeks post-STNx was chosen as the time-point to initiate intervention based on increased renal collagen and miR-214-3p expression. STNx successfully modelled CKD at 10-weeks post-surgery, as evidenced by increased renal collagen expression, increased miR-214-3p expression, increased urinary ACRs, increased serum creatinine, urea and phosphate, along with cardiac hypertrophy and hypertension. Anti-miR-214, control anti-miR, and PBS were compared as interventions in STNx, with no significant differences between the groups on any renal or cardiovascular parameter measured (bar miR-214-3p expression). Potential explanations for this lack of efficacy include the anti-miR not reaching the appropriate cell types in sufficient concentrations to de-repress miR-214-3p targets, the timing at which intervention was initiated, the length of the study, or that miR-214-3p expression level does not impact any of the measured parameters (in conflict with previous studies in the UUO model). Follow-up studies would be required to help understand the reason for the lack of efficacy observed in this study.

Chapter Five

Identifying and Investigating Cell Population-Specific Gene and miRNA Regulation in the Uninjured, Injured, and Recovering Kidney

5.1: Introduction

In this chapter, results are presented from the reversible UUO (rUUO) model of renal injury and recovery. This is a novel mouse model which allows the investigation of resolution of renal injury caused by the widely-used and well-characterised UUO[81] model of renal fibrosis. The rUUO model was first described in 2005 by Cochrane *et al*[172], in which the ureter was clamped for 10-days before being released to allow the injury to reverse. However, as fibrosis is often observed in the ureter at the site of clamping,[161] an alternate method was used for reversal, which involves surgical re-implantation of the ligated ureter into the bladder, as first described in 2008 by Tapmeier *et al.*[173] The exact surgical methods used were as published By Hesketh *et al* (2014).[161] Here, the UUO was carried out for 7 days, thus preventing urine from flowing into the bladder, resulting in rapid development of renal fibrosis.[81,160,319] Mice were then subjected to a second surgery in which the obstruction was removed and the ureter was re-implanted into the bladder, thus allowing urine to flow into the bladder and resolution of renal injury over time.

Examining individual cell populations can be advantageous over examining bulk renal cortex. The renal cortex contains multiple highly specialised cell types, with unique roles to play in renal fibrosis.[106,115,116,150,390–392] However, more than 50% of the mRNA in the renal cortex comes from the proximal tubular epithelial cells (PTECs).[393] Therefore, the isolation of individual cell populations enhances the ability to detect cell population-specific differential gene expression and pathways which may otherwise be obfuscated. This is also relevant to the investigation of miRNAs and miR-214-3p specifically, as miR-214-3p has been demonstrated to have vastly diverging (and even opposing) roles in different cell types.[248,272,276,282,286,297,298,306,394,395]

FACS was used to sort, from the renal cortex, four cell populations implicated as having significant roles in the pathogenesis of renal fibrosis: proximal tubular epithelial cells (PTECs),[115,145,390] endothelial cells,[154,155,158] macrophages,[125,138,396,397] and fibroblast-like cells.[111,331,398,399]

In order to sort these cell types specifically, a flow cytometry antibody panel was designed. CD45 is a cell surface receptor present on all cells of hematopoietic origin.[400,401] PTECs,[402] endothelial cells[403] and fibroblasts[404] were expected to be CD45 negative, while macrophages were expected to be CD45 positive.[405,406] Lotus tetragonolobus lectin (LTL) functions as a marker of proximal tubular epithelial cells by binding at the brush boarder.[407–409] CD31, also known as platelet/endothelial cell adhesion molecule-1 (PECAM-1), is a cell surface antigen present on endothelial cells and cells of hematopoietic origin.[410] Endothelial cells were identified as CD31 positive and CD45 negative.[410] F4/80 is a cell surface glycoprotein which is considered one of the most specific markers for murine macrophages.[411] Renal F4/80^{hi} cells are kidney-resident macrophages which were derived from the yolk-sac and foetal liver during embryonic development.[405,412] The term "F4/80" in this chapter refers to F4/80^{hi} CD45^{+} cells. CD45^{-} Pdgfrβ^{+} cells were also sorted in this study. Pdgfrβ is used as a surrogate marker for myofibroblasts and their fibroblast and pericyte precursors, due to a lack of a specific cell surface marker.[404] Pdgfrβ is expressed on all myofibroblasts[111] but can also be expressed on fibroblasts, pericytes, mesenchymal stem cells, mesenchymal cells, vascular smooth muscle cells, macrophages, and glomerular mesangial cells.[404,413]

Hypothesis:

miR-214-3p is differentially regulated in specific renal populations to promote a pro-fibrotic phenotype in renal injury.

Aims:

1. Identify cell population-specific regulation of miR-214-3p expression in renal injury and recovery.
2. Characterise the gene expression profiles of four cell populations in renal injury and recovery from injury.
3. Identify potential cell population-specific miR-214-3p pro-fibrotic mechanisms and/or target genes.

5.2: Gene and miRNA expression in whole (bulk) kidney cortex sequencing

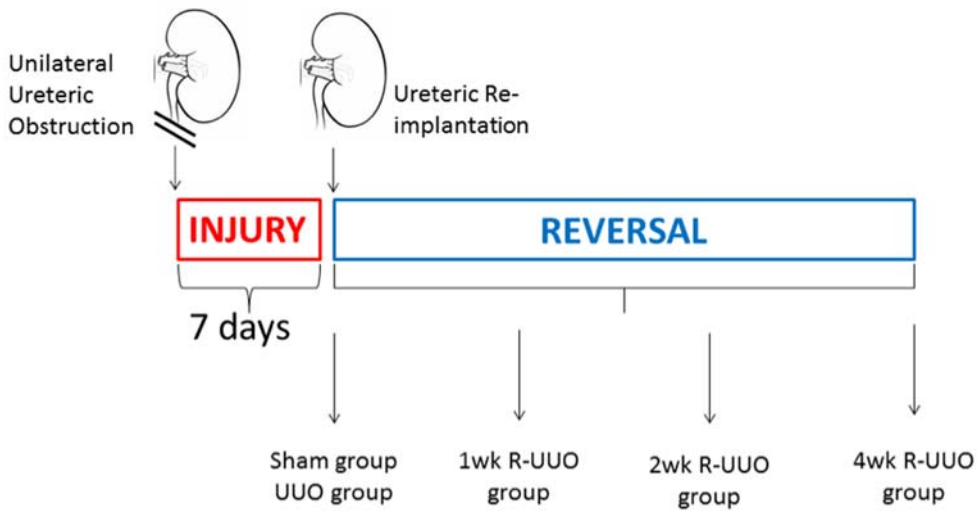

Fig 5.2.1: **Timeline and overview of experimental design**. Five groups were utilised in this study: sham, UUO, rUUO 1-week, rUUO 2-week and rUUO 4-week. All groups (bar sham) were subjected to UUO for 7 days, with sham and UUO groups being culled at this time. The remaining three rUUO groups were subjected to reversal of UUO surgery at this time, thus removing the ureteric obstruction and allowing injury to begin to resolve. rUUO groups were sacrificed at 1, 2 and 4-weeks post-rUUO surgery.

6-8-week old, male C57 black mice were assigned to one of five groups: sham, UUO, rUUO 1-week, rUUO 2-week, or rUUO 4-week. n = 4 per group. RNA was extracted from whole kidney cortex and sent for RNA-sequencing by Genewiz. Poly-A pulldown was used for library preparation for gene expression and libraries for small RNA-sequencing were also prepared. 150 base-pair paired-end reads were used for gene expression analysis. FastQC was used for initial quality control, reads were mapped to the mm10 transcriptome using RSEM[313] and Bowtie2, while DESeq2 was used for differential gene expression analysis.

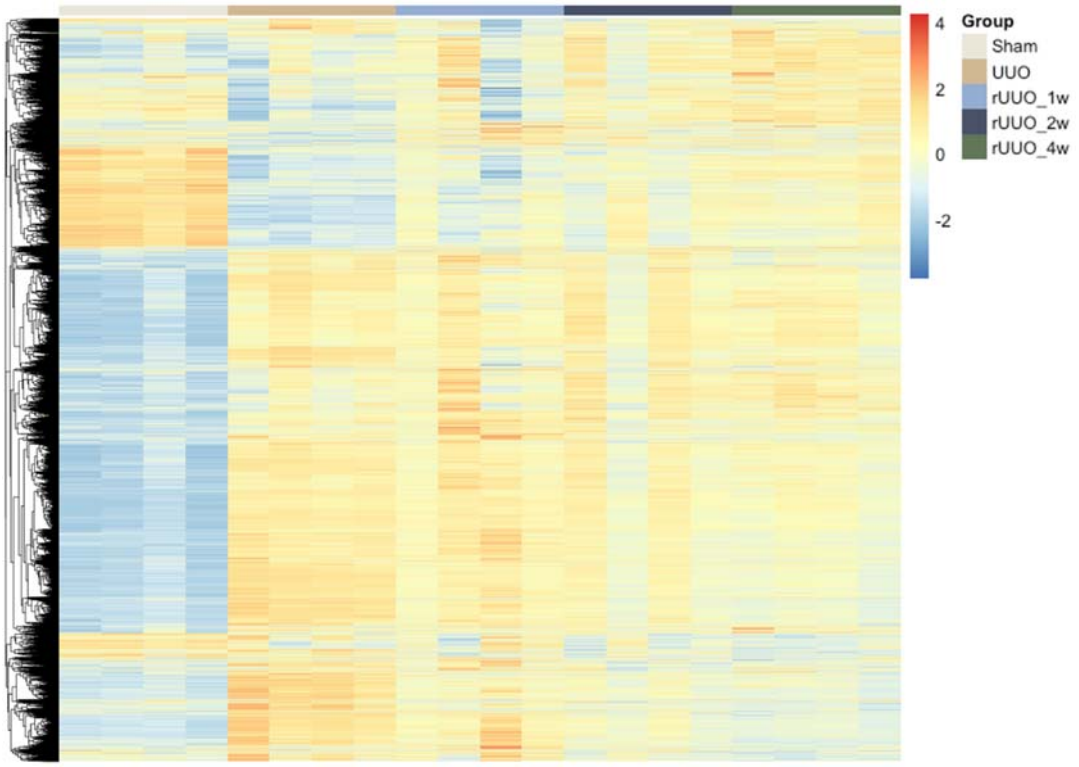

Fig 5.2.2: **Gene expression heatmap in whole kidney cortex**. Heatmap was created using Pheatmap R package. Rows were clustered via unsupervised hierarchical clustering. Sham: n=4, UUO: n=4, rUUO 1-week: n=4, rUUO 2-week: n=4, rUUO 4-week: n=4.

In order to visualise the unsupervised clustering of gene expression data obtained from bulk renal cortex sequencing, a heatmap was generated using Pheatmap R package (Fig 5.2.2). This heatmap summarises the differential gene expression detected. In a clearly observable trend, a large portion of genes in the sham group were of relatively low expression, with increased expression of these genes frequently occurring in UUO.

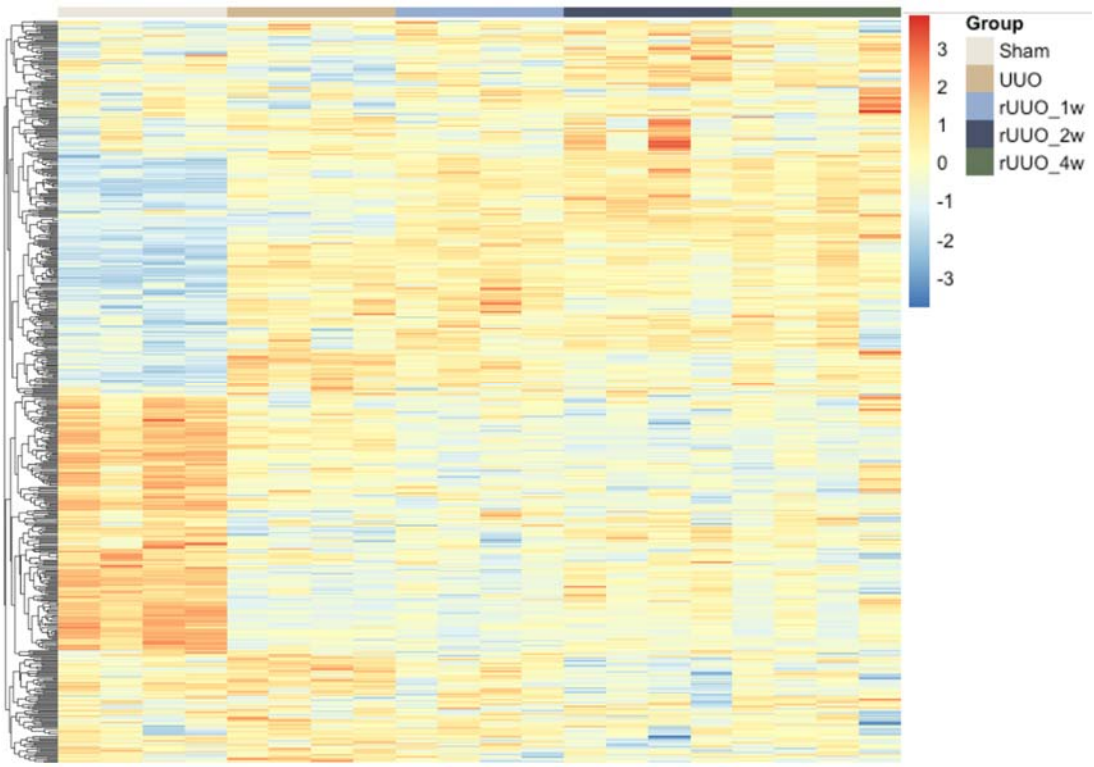

Fig 5.2.3: **miRNA expression heatmap in whole kidney cortex.** Heatmap was created using Pheatmap R package. Rows were clustered via unsupervised hierarchical clustering. Sham: n=4, UUO: n=4, rUUO 1-week: n=4, rUUO 2-week: n=4, rUUO 4-week: n=4.

Similarly, in order to visualise the unsupervised clustering of miRNA expression data obtained from bulk renal cortex sequencing, a heatmap was again generated using Pheatmap R package (Fig 5.2.3). This heatmap summarises the differential miRNA expression detected. Unlike the gene expression data (Fig 5.2.2), a trend for the occurrence of low expression miRNAs was not clearly observable in the sham group.

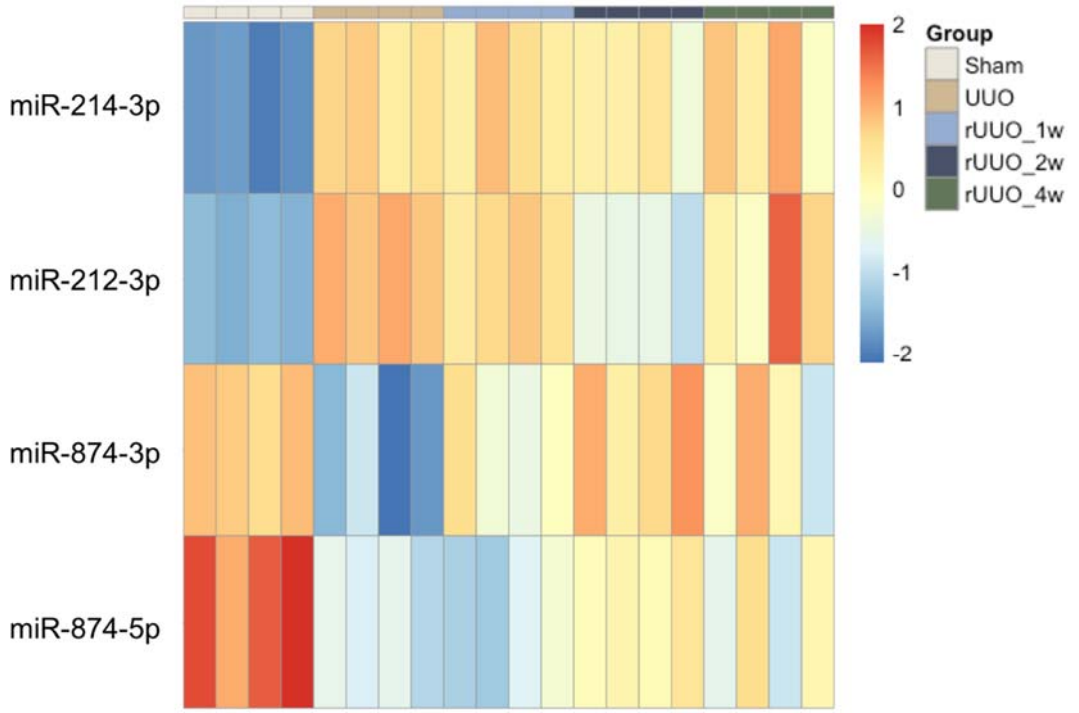

Fig 5.2.4: **Heatmap of miR-214-3p and miRNA selected from bulk sequencing for further validation**. Heatmap was created from whole kidney cortex small RNA sequencing counts, using Pheatmap R package. Sham: n=4, UUO: n=4, rUUO 1-week: n=4, rUUO 2-week: n=4, rUUO 4-week: n=4.

In the bulk renal cortex sequencing, as expect, miR-214-3p was found to be increased (2.13 log2-fold, adjusted p-value: 2.23E-09) from sham to UUO, with no significant change in expression in any of the three rUUO timepoints in comparison to UUO (Fig 5.2.4). In order to further validate the mapping of the small RNA-sequencing and to explore the reproducibility of these results in another model of renal injury (STNx), three miRNAs were manually selected from the bulk miRNA sequencing. These miRNAs were selected on the basis of expression profile (fold-changes between the groups) and expression level. miR-212-3p increased significantly between sham and UUO, then decreased in expression during reversal of injury. miR-874-3p and miR-874-5p had the opposite expression profile, where expression decreased significantly between sham and UUO, then increased during reversal. This expression was validated via qRT-PCR in the samples that the RNA-sequencing was carried out on (Fig 5.2.5). In addition, the dysregulation of these miRNAs was assessed using the

progressive STNx model described in 3.1 whole kidney RNA (Fig 5.2.6). Expression in STNx diverged significantly, with miR-874-3p and miR-874-5p not found to be significantly different from sham expression, however, upregulation of miR-212-3p expression was observed (3.02-fold) but to a lesser extent than in UUO (5.19-fold).

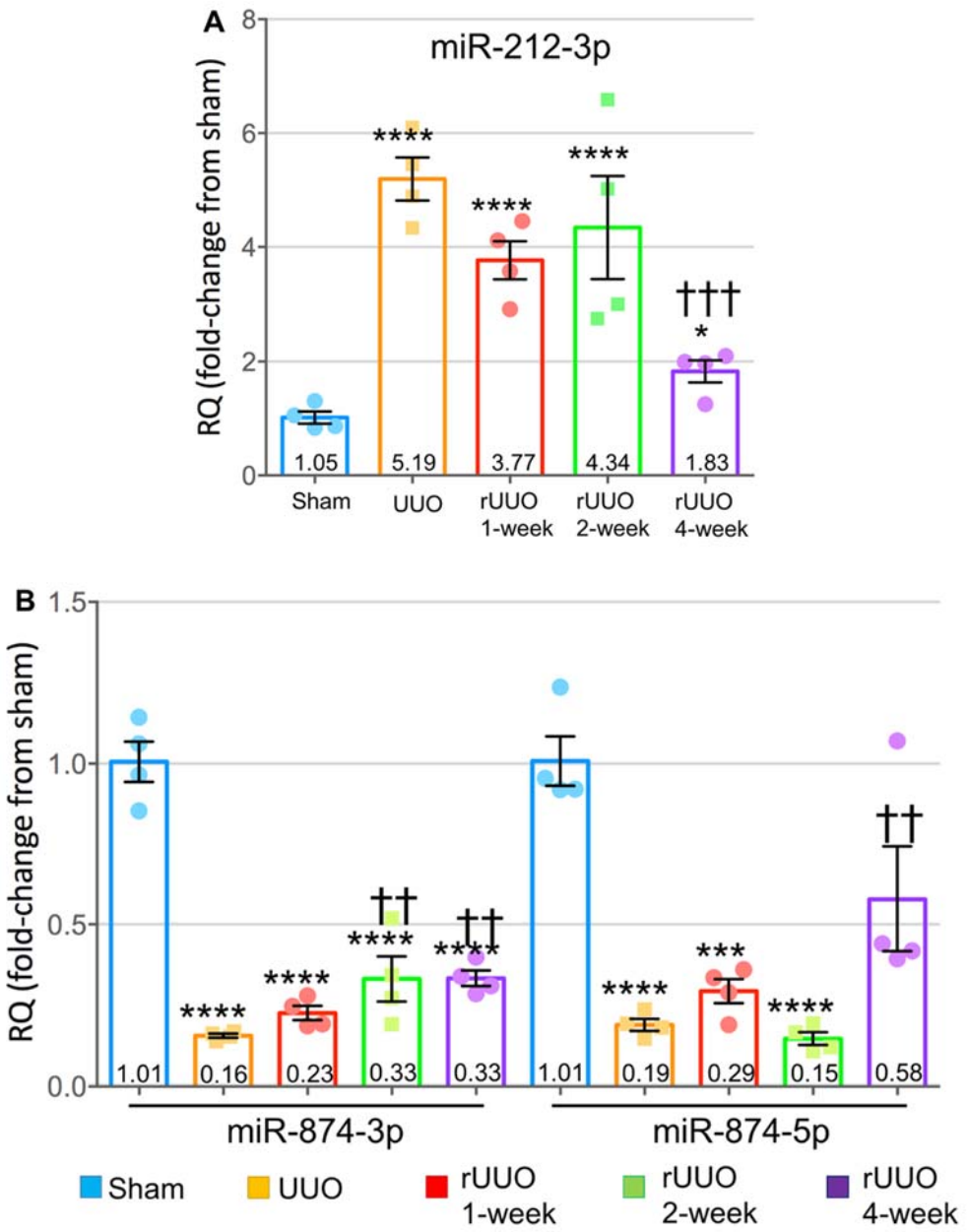

Fig 5.2.5: **Validation of small RNA-seq data via qRT-PCR**. A = miR-212-3p, B = miR-874-3p and miR-874-5p. miRNA expression was assessed via qRT-PCR in RNA from the same samples which RNA-sequencing was carried out on. Taqman probes were used. miRNA expression was normalised to housekeeper U6. Plotted as mean ± SEM. One-way ANOVA with Tukey's multiple comparison test was used for statistical analysis. * = $p<0.05$ vs sham, *** = $p<0.001$ vs sham, **** = $p<0.0001$ vs sham, †† = $p<0.01$ vs UUO, ††† = $p<0.001$ vs UUO. Sham: n=4, UUO: n=4, rUUO 1-week: n=4, rUUO 2-week: n=4, rUUO 4-week: n=4.

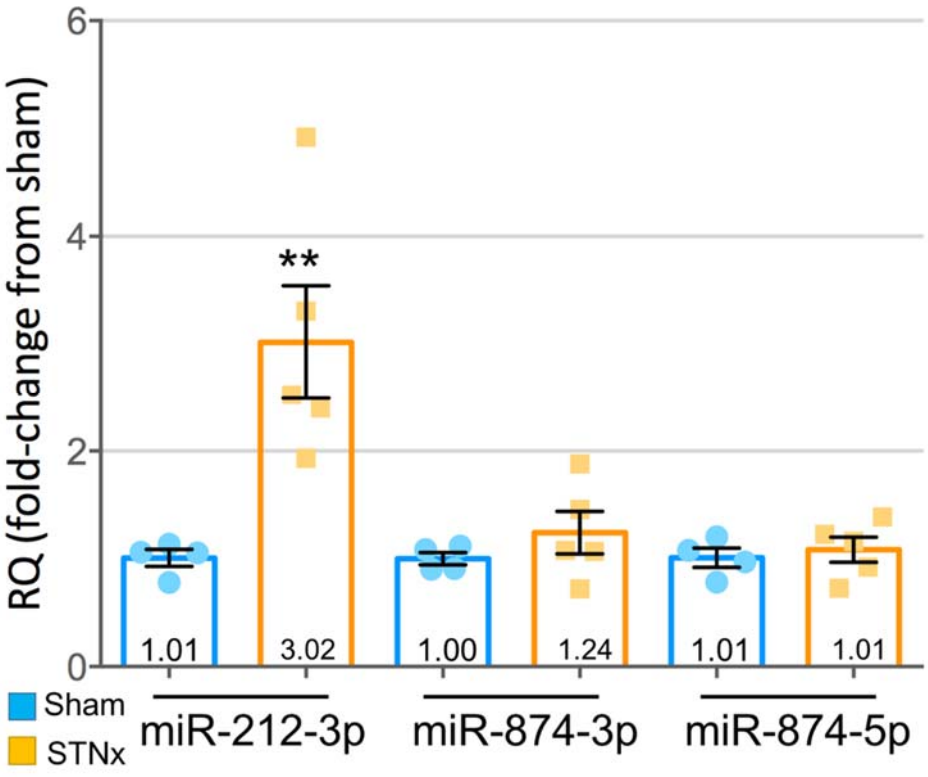

Fig 5.2.6: **Expression of selected miRNA in STNx whole kidney**. miRNA expression was assessed via qRT-PCR with specific Taqman probes. miRNA expression was normalised to housekeeper U6. Plotted as mean ± SEM. Student's T-test (unpaired, two-tailed) was used for statistical analysis. ** = $p<0.01$ vs sham. Sham: n=4, STNx: n=5.

5.3: Gene expression in individual cell populations FACS-sorted from renal cortex

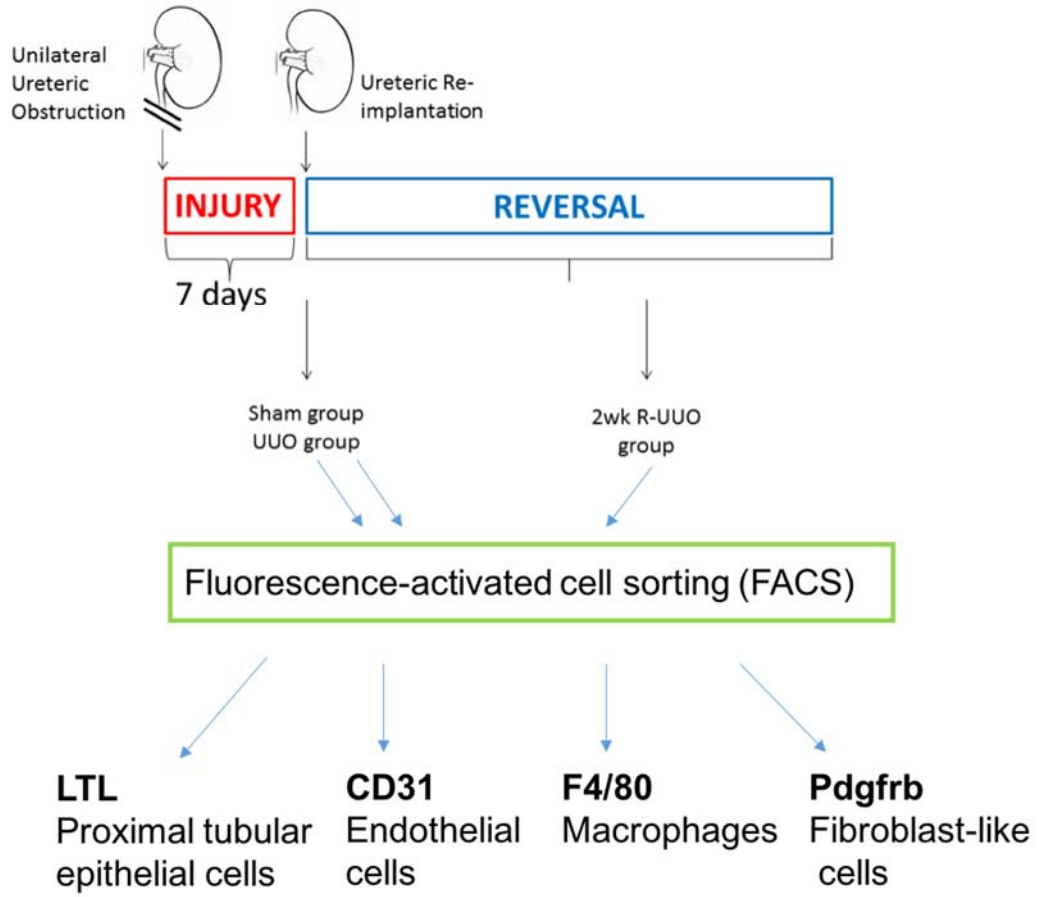

Fig 5.3.1: **Overview of experimental design**. FACS was carried out on sham, UUO and rUUO 2-week groups, sorting LTL, CD31, F4/80 and Pdgfrβ cells from whole renal cortex.

In order to explore cell population-specific differential gene regulation and expression, individual cell populations were isolated from the renal cortex via FACS, RNA was extracted and sent for RNA-sequencing (Genewiz, Poly-A pulldown, 150 base-pair paired-end reads). FastQC was used for initial quality control, reads were mapped to the mm10 transcriptome using RSEM[313] and Bowtie2, while DESeq2 was used for differential gene expression analysis.

One rUUO timepoint (2-weeks post-reversal) was selected for sequencing in this experiment, as this was the initial reversal timepoint in the bulk sequencing where dynamic and significant changes occurred in, for example Kim-1, myeloid cell infiltration, and collagen expression. Therefore, rUUO 2-week was hypothesised to be the optimal timepoint to observe differential regulation of genes, pathways and miRNAs involved with the recovery from renal injury.

Group n numbers were as follows: LTL sham: n=4, LTL UUO: n=4, LTL rUUO: n=3, CD31 sham: n=4, CD31 UUO: n=4, CD31 rUUO: n=4, F4/80 sham: n=4, F4/80 UUO: n=4, F4/80 rUUO: n=4. Pdgfrβ sham: n=4, Pdgfrβ UUO: n=4, Pdgfrβ rUUO: n=4.

Genes which had an average expression of <1 FPKM across all the samples were excluded from all analysis. After initial analysis, expression of genes which are specific to a cell type other than the cell types isolated in this study were observed and were thought to be due to contamination during FACS. To alleviate this contamination, lists of genes found to be markers of a number of renal cell types by Park *et al* (2018)[315] were obtained. Using these lists, marker genes for the following cell types were removed from expression data for all four cell types: loop of Henle, distal convoluted tubule, collecting duct (CD) principal cell, CD intercalated cell, CD transient cell. In addition to this, proximal tubular cell markers were removed from CD31, F4/80 and Pdgfrβ data.

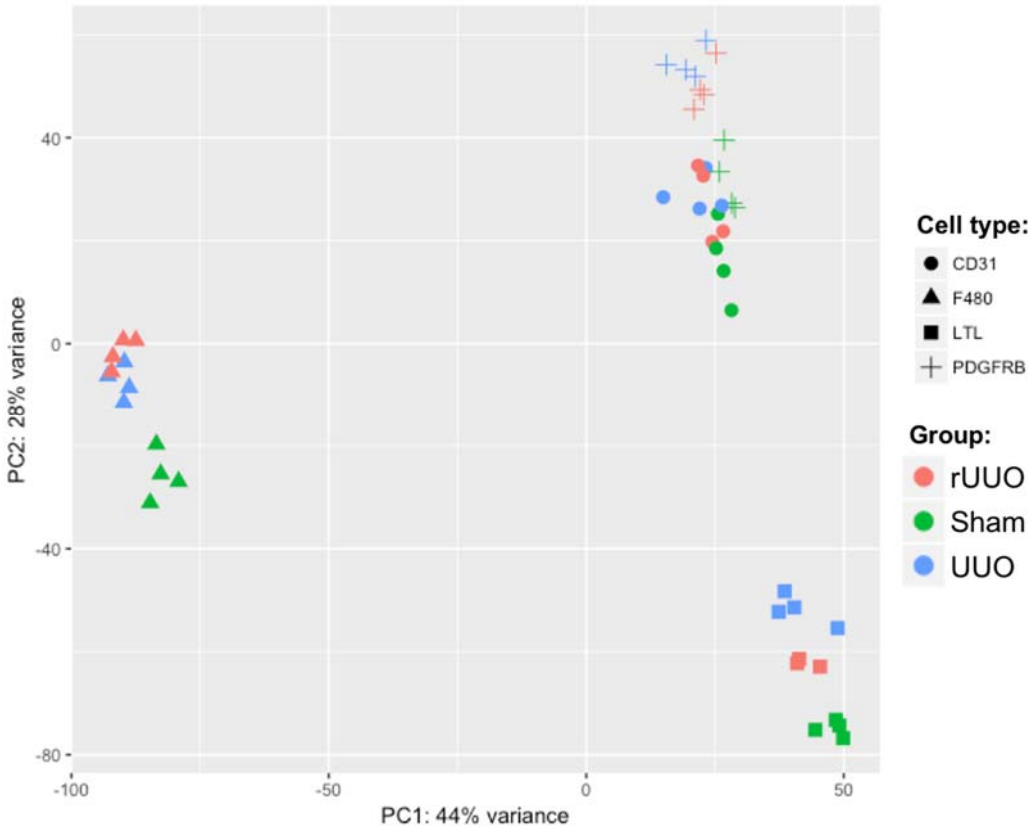

Fig 5.3.2: **Principle component analysis (PCA) for gene expression in individual cell populations.** PCA carried out with the top 1000 genes from each sample. Shapes indicate cell type and colour indicates group. Created using DESeq2 and ggplot2 R packages.

Regularised log (rlog) transformation was performed to transform raw count data to Log2 scale, producing a variance-stabilising effect and normalising between samples for library size. Stabilising variance between samples in this way was carried out to aid visual detection of outlier samples in the data.

All populations were observed to be discrete, especially LTL and F4/80, although Pdgfrβ sham samples were observed to be in close proximity to some of the CD31 samples. Clear separation between the sham and UUO groups was observable for each cell type. Separation between UUO and rUUO groups was most clearly observable in LTL, with separation less distinct in F4/80 and Pdgfrβ, while CD31 appeared to have little separation.

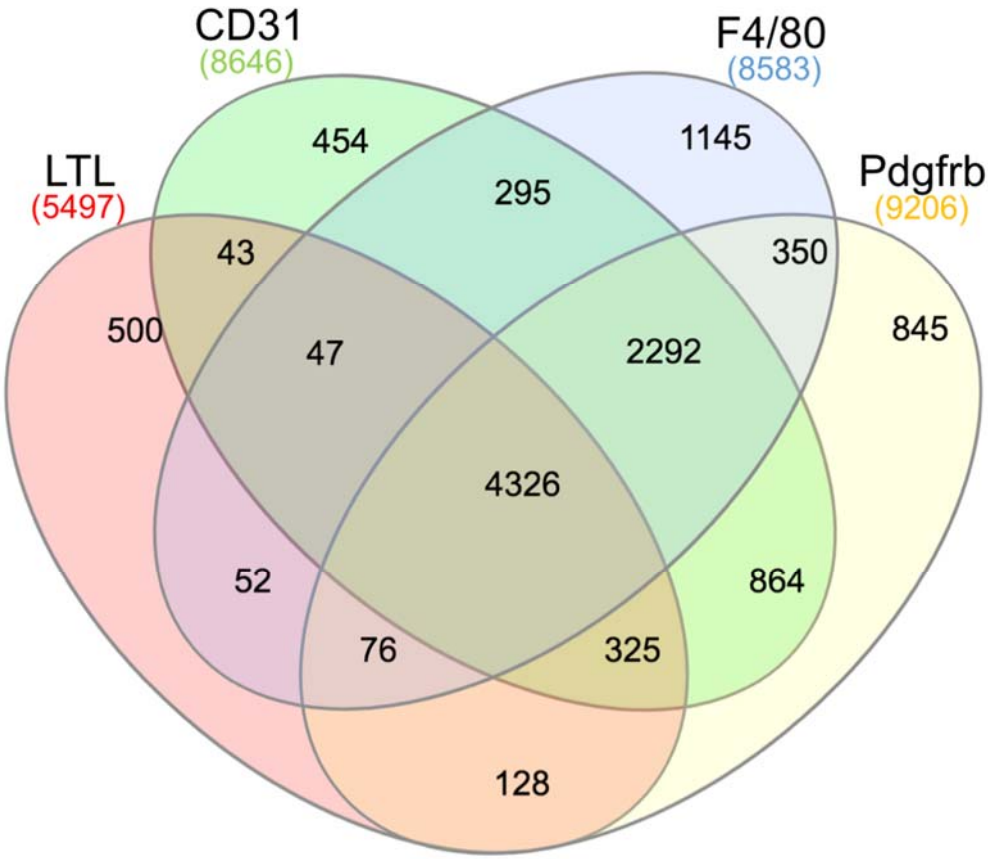

Fig 5.3.3: **Analysis of gene expression between the four cell types in sham.** Venn-diagram showing number of unique and overlapping genes between cell type at sham. Genes with <2 FPKM average expression in the sham group of each cell type were excluded. Number in brackets under the cell type label = total number of genes in this cell type with an expression of ≥ 2 FPKM. Created using InteractiveVenn.[414]

To assess the differences and similarities between the four cell types in uninjured tissue, a Venn diagram (Fig 5.3.3) was created using gene expression (FPKM) in sham samples. F4/80 was found to have the highest number of unique genes at sham.

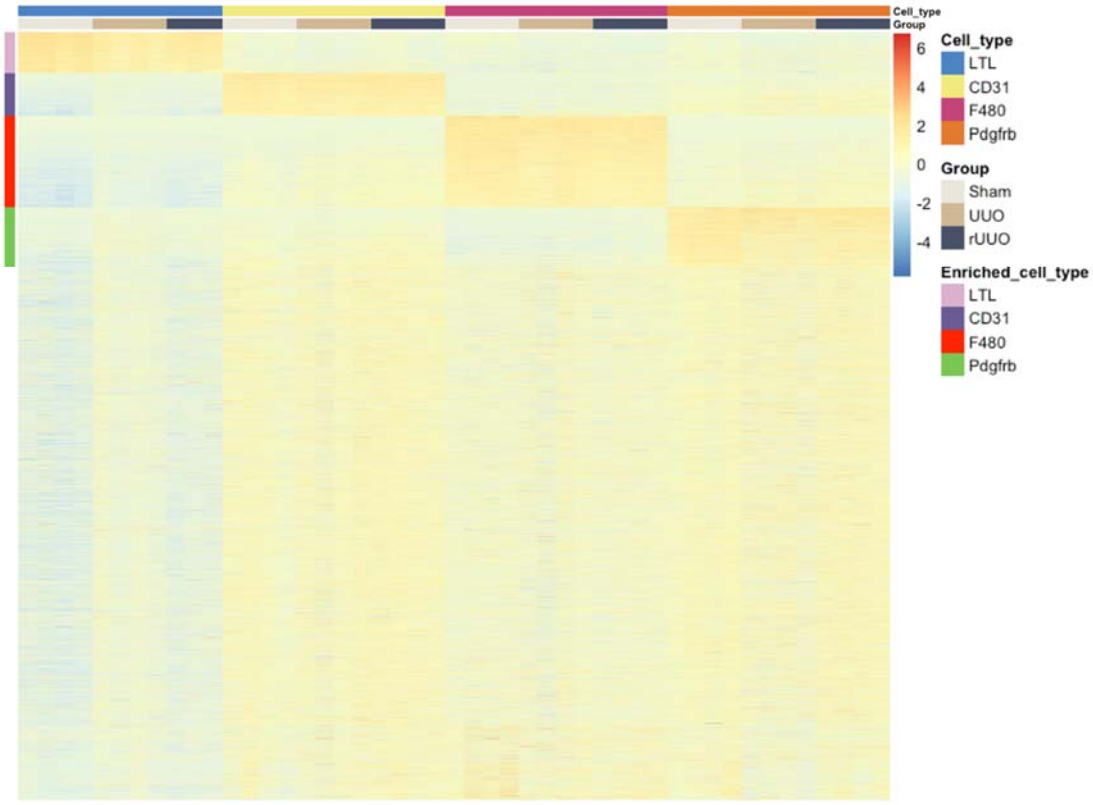

Fig 5.3.4: **Enriched genes at sham from each cell type.** MGFR R package[316] was used to identify enriched genes at sham in each of the four cell types. These genes were grouped together on a heatmap of all gene expression in this study. Heatmap was created using Pheatmap R package.

To better understand the differences in transcriptional profile between the four cell types, genes enriched in each cell type at sham were identified using the MGFR R package. These genes were grouped together on a heatmap of all gene expression data in the FACS sorted kidney cortex population data (section 5.3 data)(Fig 5.3.4). F4/80 was again found to have the highest number of enriched genes at sham. Expression of genes enriched at sham was found to, in general, remain high in UUO and rUUO groups of the same cell type, and remain low in UUO and rUUO groups in other cell types.

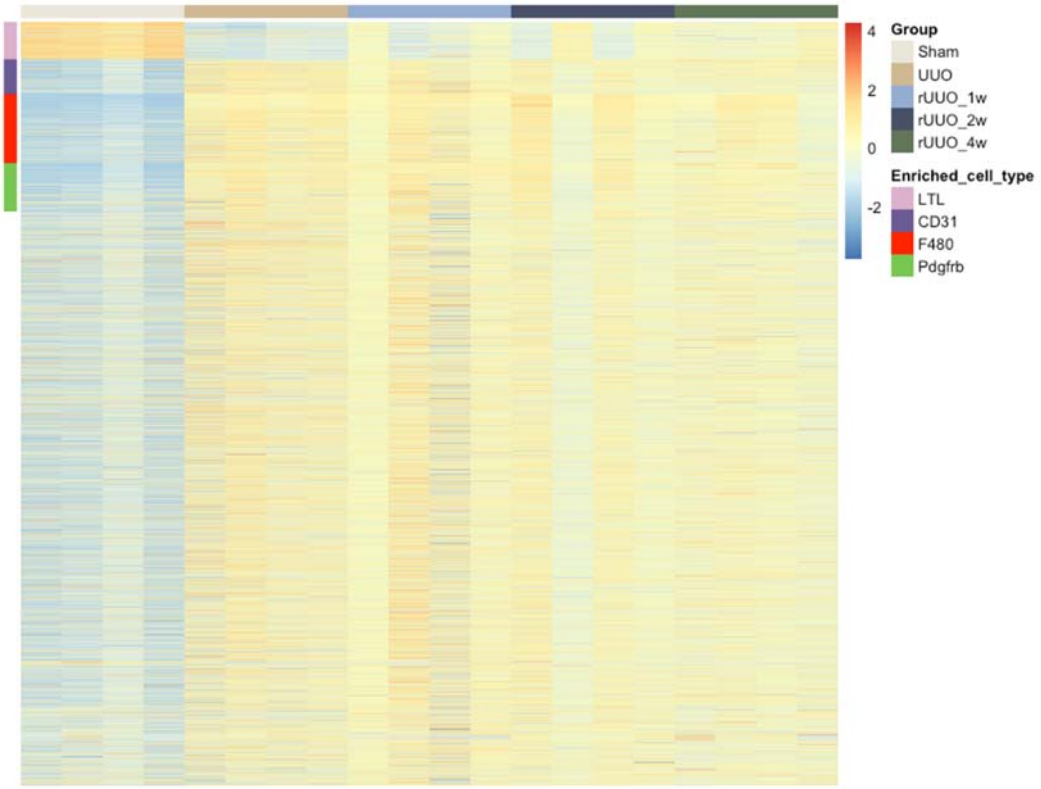

Fig 5.3.5: **Enriched genes at sham from each cell type overlaid on gene expression heatmap from whole kidney cortex sequencing (section 5.2).** MGFR R package was used to identify enriched genes at sham in each of the four cell types in the FACS sequencing data from section 5.3. These genes were grouped together on a heatmap of all gene expression in the whole kidney cortex sequencing from section 5.2. Heatmap was created using Pheatmap R package.

To assess how genes found to be enriched in uninjured conditions (sham) in each of the four cell types compares to whole kidney cortex RNA-sequencing (section 5.2, Fig 5.2.2), these genes were grouped together on a heatmap of gene expression from whole kidney cortex sequencing. In the whole kidney cortex data (Fig 5.3.5), genes found to be enriched in LTL cells at sham were overwhelmingly high in expression in uninjured conditions (sham), then expression dropped dramatically in UUO before expression was clearly observed to be increased again at 4-weeks post-rUUO. In contrast to LTL, genes found to be enriched at sham in each of the other three cell types had mostly low expression in uninjured conditions (sham) in the bulk renal cortex sequencing data and dramatically increased in expression in UUO.

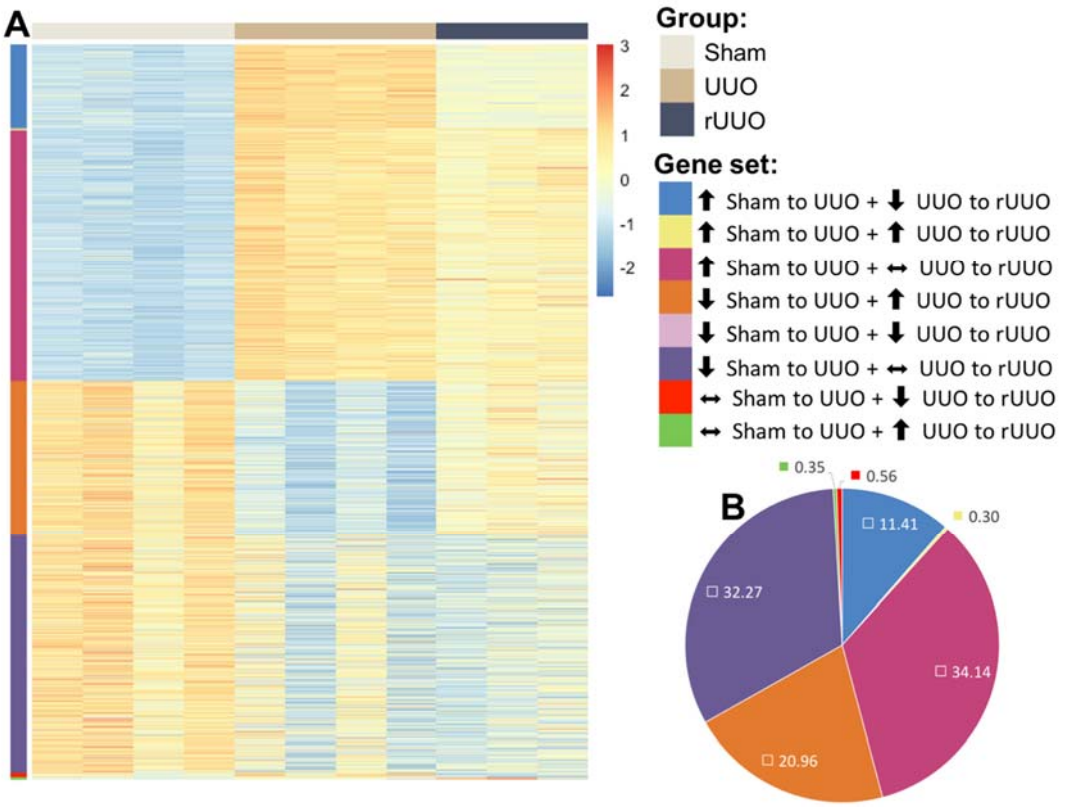

Fig 5.3.6: **Gene expression profile in LTL cell population.** A = Heatmap annotated by gene set, made using pheatmap R package. B = Pie chart of percentage of the total gene expression each gene set accounts for. Genes which were not differentially regulated between sham and UUO, or UUO and rUUO, were excluded (n = 6681). Gene sets were defined based on fold-changes and adjusted p-value (p-adj) values calculated using DESeq2. ⬆ = positive fold-change and p-adj <0.05. ⬇ = negative fold-change and p-adj <0.05. ↔ = p-adj >0.05. n = 1980 genes total.

Proximal tubular cells make up the most significant proportion of cell types in the kidney.[393] Differentially regulated genes in the LTL population were categorised into one of eight gene sets, based on the pattern of gene expression change detected for each gene (Fig 5.3.6). 66.41% of genes were found to either increase or decrease from sham to UUO, then remain unchanged in expression from UUO to rUUO. Therefore, these genes were not sensitive to reversal of UUO injury, at least by 2-weeks post-reversal. In contrast, 32.37% of genes were found to either increase or decrease in expression from sham to UUO, before (at least partially) reversing this

change in rUUO. Therefore, these genes were responsive to both injury and reversal of injury. Only 0.91% of genes were found to have no change from sham to UUO, then significantly increase or decrease in rUUO. Therefore, these genes are reversal-specific.

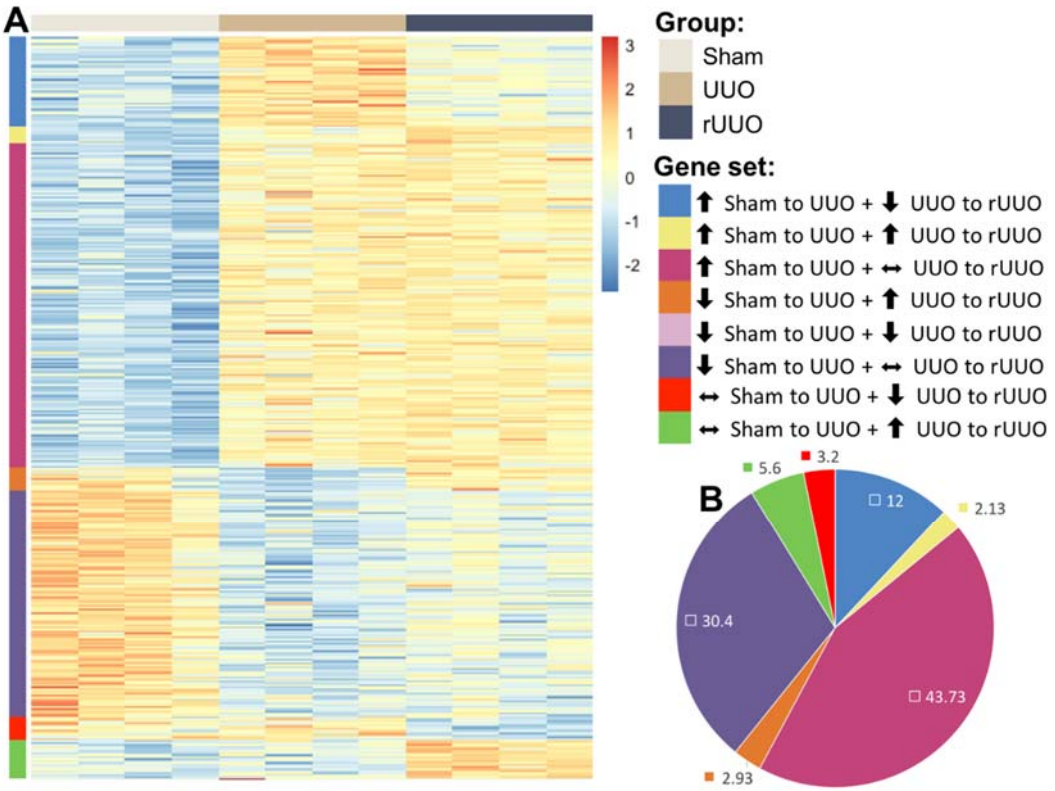

Fig 5.3.7: **Gene expression profile in CD31 cell population.** A = Heatmap annotated by gene set, made using pheatmap R package. B = Pie chart of percentage of the total gene expression each gene set accounts for. Genes which were not differentially regulated between sham and UUO, or UUO and rUUO, were excluded (n = 10975). Gene sets were defined based on fold-changes and adjusted p-value (p-adj) values calculated using DESeq2. ↑ = positive fold-change and p-adj <0.05. ↓ = negative fold-change and p-adj <0.05. ↔ = p-adj >0.05. n = 375 genes total.

Within the CD31 population, when differentially regulated genes were categorised into one of eight gene sets based on the pattern of gene expression change detected for each gene (Fig 5.3.7), 74.13% of genes were found to either increase or decrease from sham to UUO, then remain unchanged in expression from UUO to rUUO which

was higher than that observed in the proximal tubule cells. In contrast, 14.93% of genes were found to either increase or decrease in expression from sham to UUO, before (at least partially) reversing this change in rUUO (i.e. were responsive to both injury and reversal of injury). The endothelial cell compartment appear to have a significant proportion of the reversal-specific genes; 8.8%. The feature of the CD31 population was the low total number of genes which changed in response to UUO or rUUO (n=375), in contrast to the LTL, F4/80 and Pdgfrβ populations which had 1980, 860 and 2630 genes here respectively.

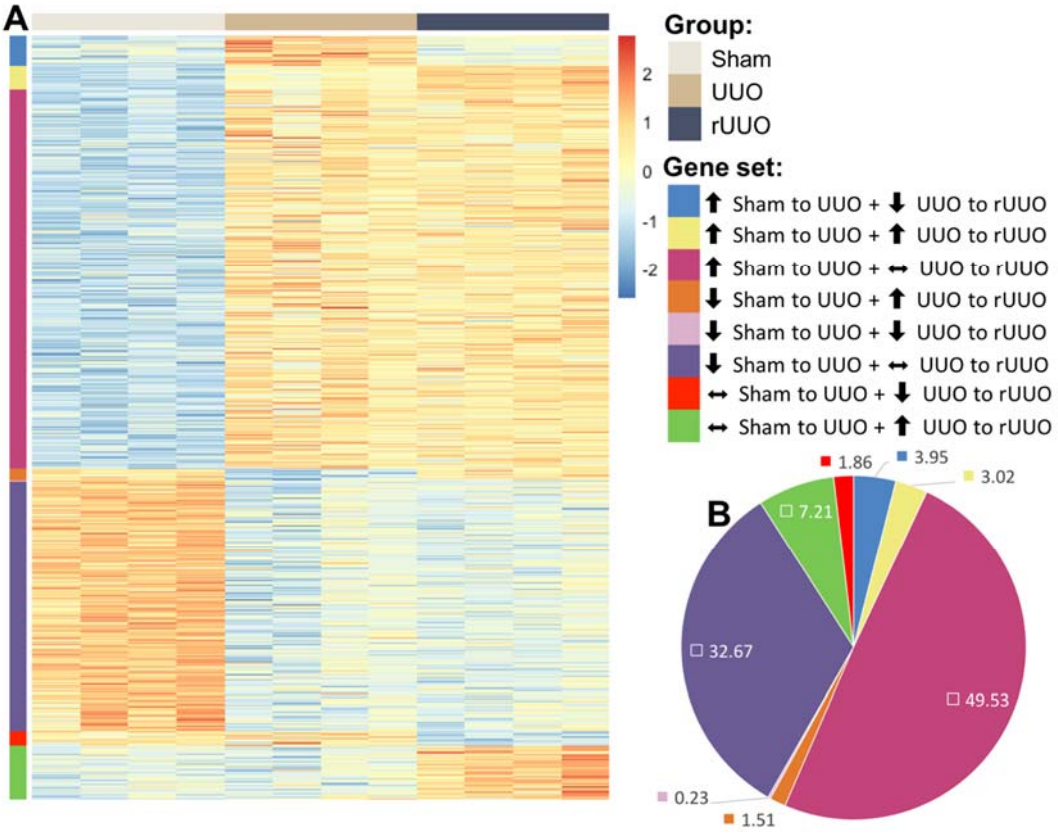

Fig 5.3.8: **Gene expression profile in the F4/80 cell population.** A = Heatmap annotated by gene set, made using pheatmap R package. B = Pie chart of percentage of the total gene expression each gene set accounts for. Genes which were not differentially regulated between sham and UUO, or UUO and rUUO, were excluded (n = 9682). Gene sets were defined based on fold-changes and adjusted p-value (p-adj) values calculated using DESeq2. ⬆ = positive fold-change and p-adj <0.05. ⬇ = negative fold-change and p-adj <0.05. ↔ = p-adj >0.05. n = 860 genes total.

Patterns of differentially regulated genes observed in the F4/80 population (Fig 5.3.8) were similar to that of the CD31 population, with a relatively high portion of injury but not reversal-sensitive genes (82.2%), a low portion of injury and reversal-sensitive genes (5.46%), as well as a high portion of reversal-specific genes (9.07%). This presents an interesting dichotomy in the F4/80 population with respect to the impact of injury resolution on gene expression. That is, the vast majority of F4/80 genes which were differentially regulated by injury do not even partially regress towards their original expression level within the first two weeks of recovery from injury

(5.46%), while a higher portion of genes were not affected by injury, but instead responded specifically to the activation of injury resolution (9.07%). This may represent active participation by the F4/80^{hi} macrophages in both the fibrogenic and regenerative processes which initiate at different timepoints during the rUUO time-course.

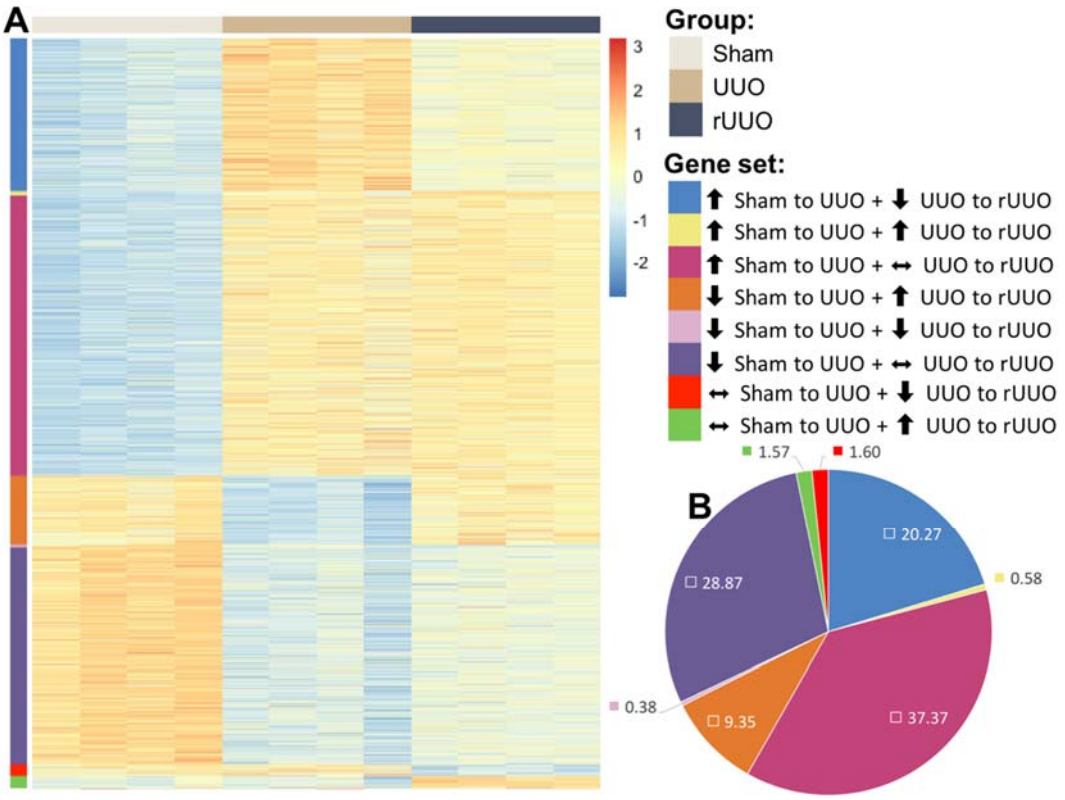

Fig 5.3.9: **Gene expression profile in the Pdgfrβ cell population.** A = Heatmap annotated by gene set, made using pheatmap R package. B = Pie chart of percentage of the total gene expression each gene set accounts for. Genes which were not differentially regulated between sham and UUO, or UUO and rUUO, were excluded (n = 7536). Gene sets were defined based on fold-changes and adjusted p-value (p-adj) values calculated using DESeq2. ⬆ = positive fold-change and p-adj <0.05. ⬇ = negative fold-change and p-adj <0.05. ↔ = p-adj >0.05. n = 2630 genes total.

Differentially regulated genes in the Pdgfrβ population were also categorised into one of eight gene sets, based on the pattern of gene expression change detected for

each gene (Fig 5.3.9). 66.24% of genes were identified to be responsive to injury but not to reversal of injury, 29.62% of genes were regulated injury and this regulation at least partially reverted in reversal of injury, and just 3.17% genes were reversal-specific. Pdgfrβ^{+} was the population with the highest total number of differentially regulated genes (n = 2630).

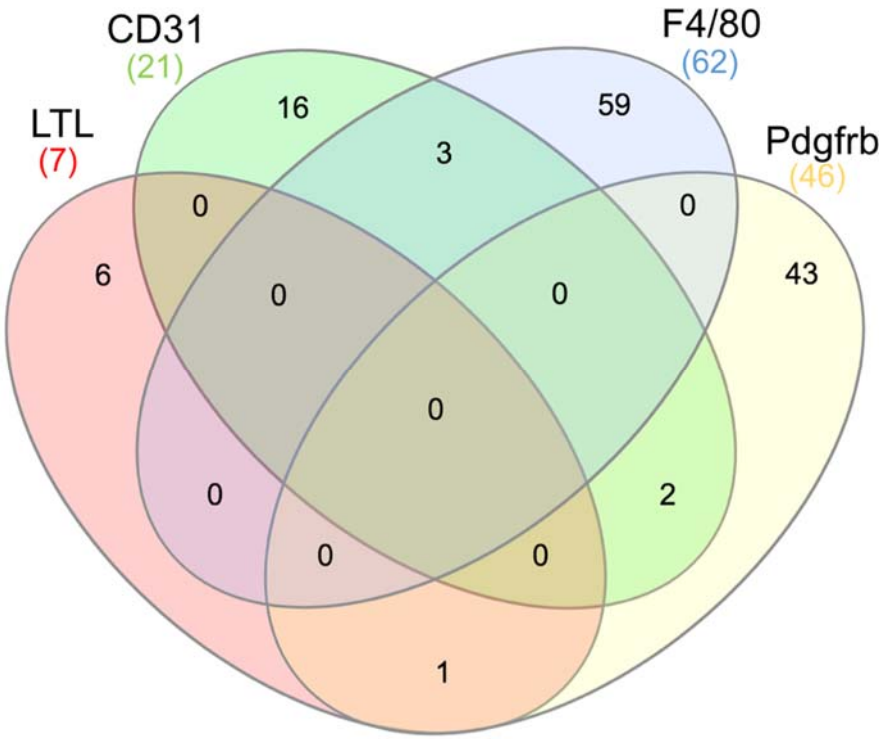

Fig 5.3.10: **Occurrence and overlap of reversal-specific upregulated genes in each cell type.** Genes included are those which do not significantly change in expression between sham and UUO, but then significantly increase in expression between UUO and rUUO. Created using InteractiveVenn.[414]

Identification of significantly increased reversal-specific genes in each of the four cell populations revealed very few genes (n = 6) were present in more than one cell population (Fig 5.3.10), indicating reversal-specific differential gene expression was mostly unique to each population. LTL and CD31 had relatively few reversal-specific genes (n = 7 and 21 respectively), while F4/80 and Pdgfrβ had higher counts (n= 62 and 46 respectively).

5.4: miRNA expression in individual cell populations FACS-sorted from renal cortex

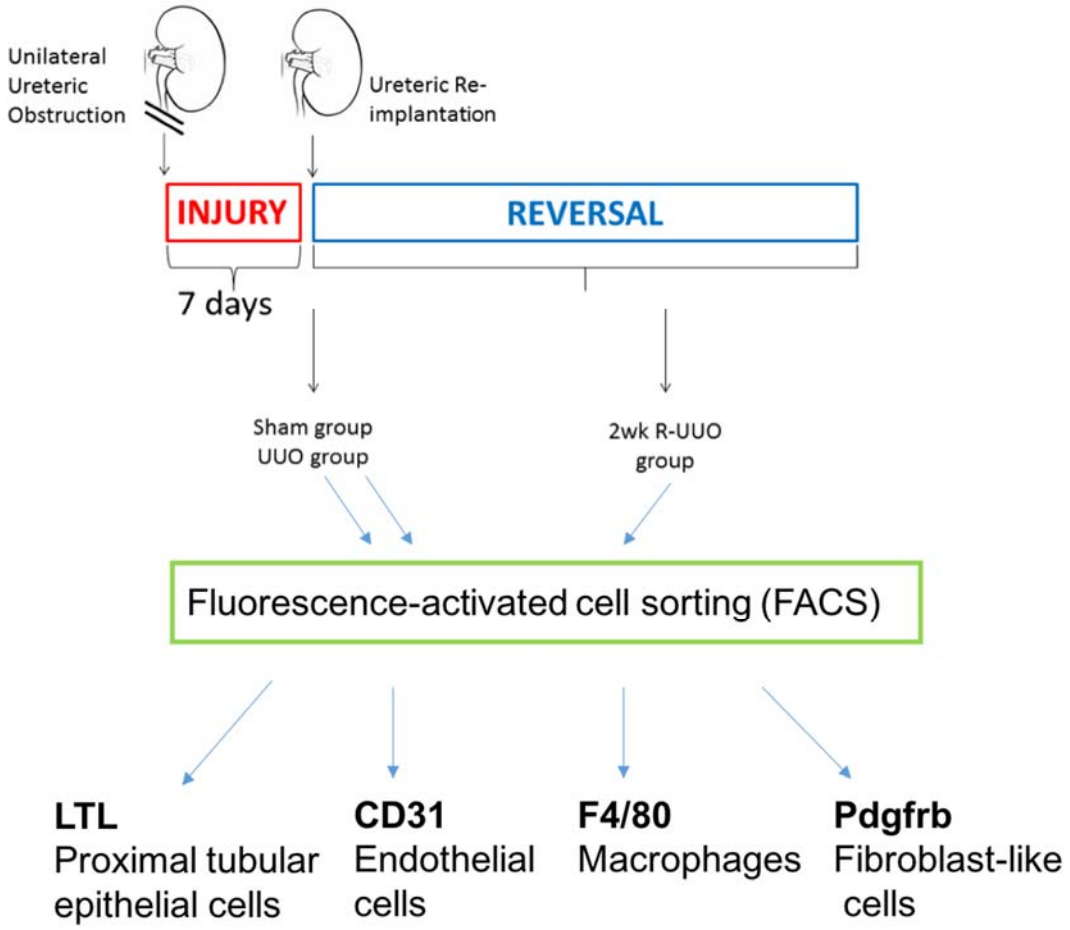

Fig 5.4.1: **Overview of experimental design**. FACS was carried out on sham, UUO and rUUO 2-week groups, sorting LTL, CD31, F4/80 and Pdgfrβ cells from whole renal cortex.

As cell population-specific gene expression was profiled in rUUO, a repeat experiment was carried out to profile cell population-specific miRNA expression. Cell type and pathological context has been shown to be of critical importance in miR-214-3p mechanisms,[248,272,276,282,286,297,298,306,394,395] therefore, uncovering its cell population-specific regulation may provide novel insights into its pathogenic mechanisms in renal fibrosis.

Methods of cell sorting were identical to section 5.3. Samples were sent for RNA-sequencing for small RNA were different to those in section 5.3. Library preparation, sequencing and initial quality control (adaptor trimming) was carried out by Genewiz. Mapping of reads to the mm10 transcriptome and generation of raw read counts was carried out using Shortstack.[314] DESeq2 was used for differential expression statistical analysis, generating log2 fold-changes and adjusted p-values for each gene between each of the groups.

To illustrate the pattern of miRNA expression changes that occurred between the three groups in each cell type, each differentially expressed miRNA was placed into a "miRNA set" based on its pattern of expression (Figs 5.4.2-5.4.5).

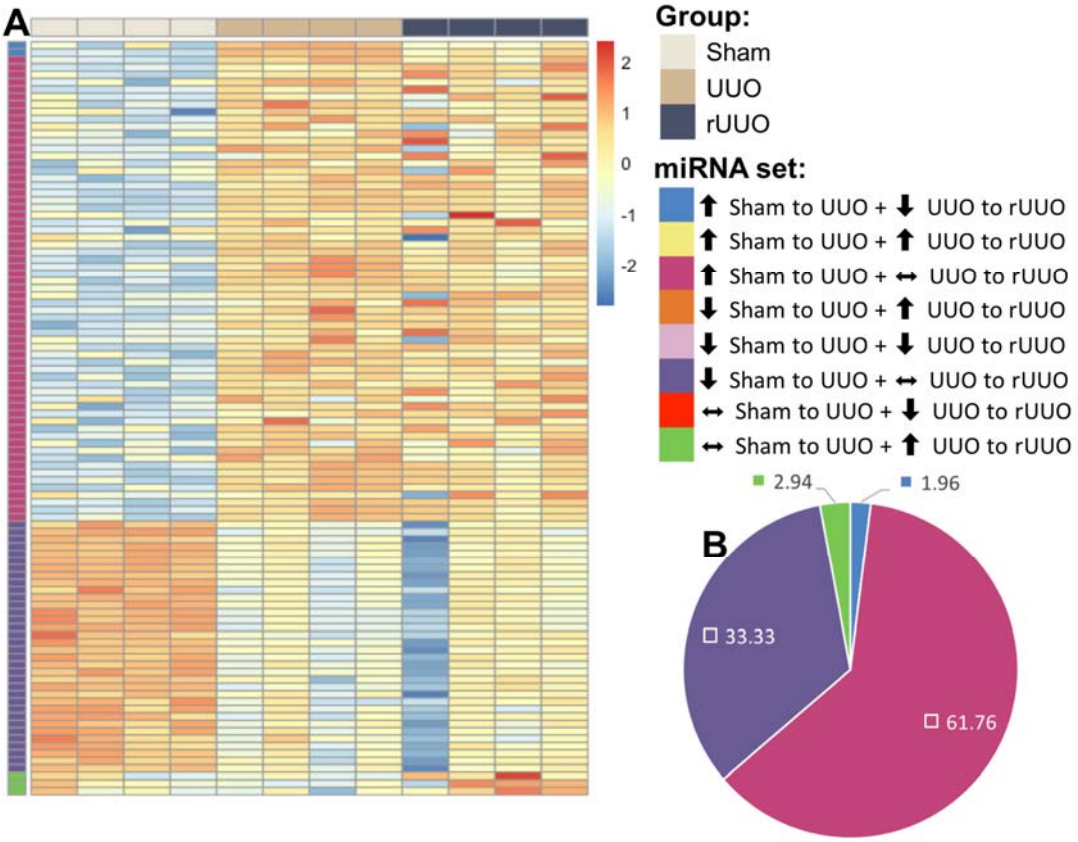

Fig 5.4.2: **miRNA expression profile in the LTL cell population.** A = Heatmap annotated by miRNA set, made using pheatmap R package. B = Pie chart of percentage of the total miRNA expression each miRNA set accounts for. miRNAs which were not differentially regulated between sham and UUO, or UUO and rUUO, were excluded (n = 173). miRNA sets were defined based on fold-changes and adjusted p-value (p-adj) values calculated using DESeq2. ↑ = positive fold-change and p-adj <0.05. ↓ = negative fold-change and p-adj <0.05. ↔ = p-adj >0.05. n = 102 miRNAs total.

In the LTL population (Fig 5.4.2), 95.09% of miRNAs were significantly increased or decreased in expression between sham and UUO, then remain unchanged in expression from UUO to rUUO. Therefore, these miRNAs were not sensitive to reversal of UUO injury, at least by 2-weeks post-reversal. In contrast, 4.9% of miRNAs were found to either increase or decrease in expression from sham to UUO, before (at least partially) reversing this change in rUUO. Therefore, these miRNAs were responsive to both injury and reversal of injury. No reversal-specific miRNAs (miRNAs

with no expression change from sham to UUO, then significantly increase or decrease in rUUO) were detected in the LTL cell population. Overall, this suggests UUO perturbed miRNA expression in the LTL population, which was largely not even partially resolved by 2-weeks post-reversal of injury.

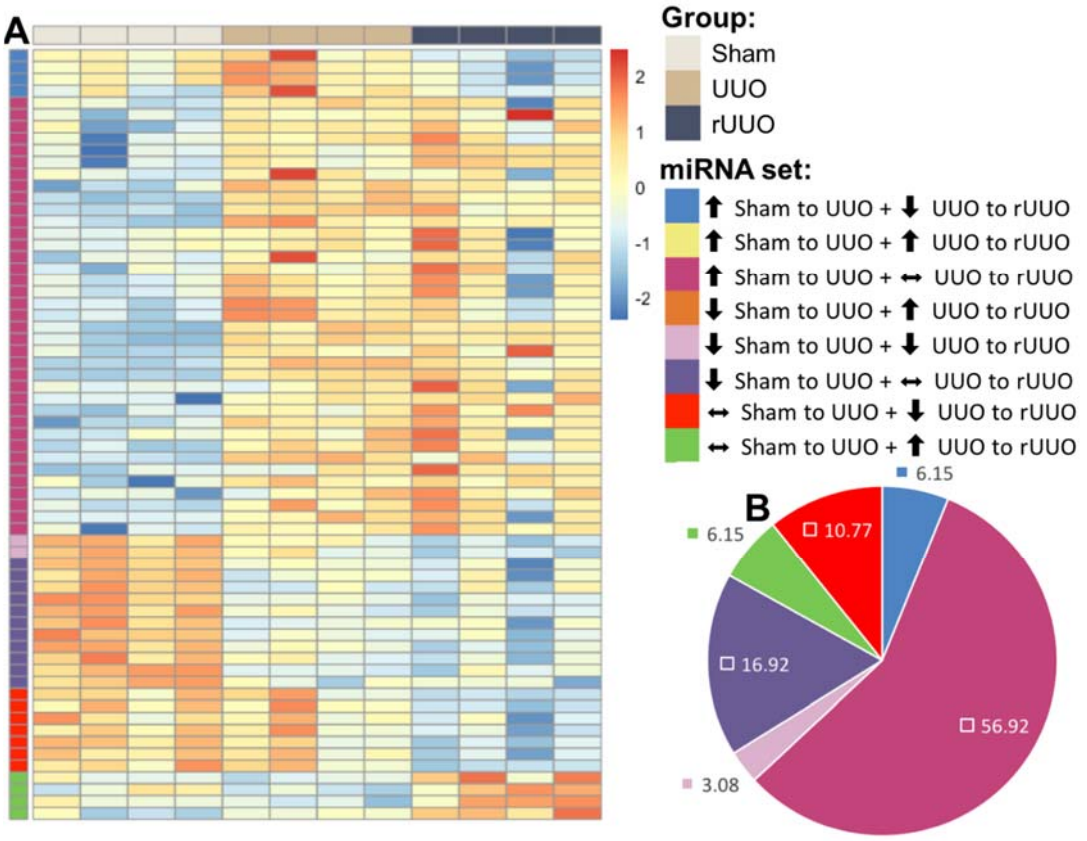

Fig 5.4.3: **miRNA expression profile in the CD31 cell population.** A = Heatmap annotated by miRNA set, made using pheatmap R package. B = Pie chart of percentage of the total miRNA expression each miRNA set accounts for. miRNAs which were not differentially regulated between sham and UUO, or UUO and rUUO, were excluded (n = 168). miRNA sets were defined based on fold-changes and adjusted p-value (p-adj) values calculated using DESeq2. ↑ = positive fold-change and p-adj <0.05. ↓ = negative fold-change and p-adj <0.05. ↔ = p-adj >0.05. n = 65 miRNAs total.

In the $CD31^{+}$ population (Fig 5.4.3), a lower portion of miRNAs were sensitive to injury only (73.84%), but the portion of miRNAs which were sensitive to both injury and

reversal of injury was also low (6.15%). However, a relatively large portion reversal-specific miRNAs were detected (16.92%), indicating miRNA-responsiveness to injury resolution may be a feature of renal endothelial cells. Similarly to the gene expression data, the $CD31^{+}$ population had the lowest number of differentially regulated miRNAs (n = 65) out of the four cell populations investigated, indicating these cells are the least responsive to UUO injury and resolution overall.

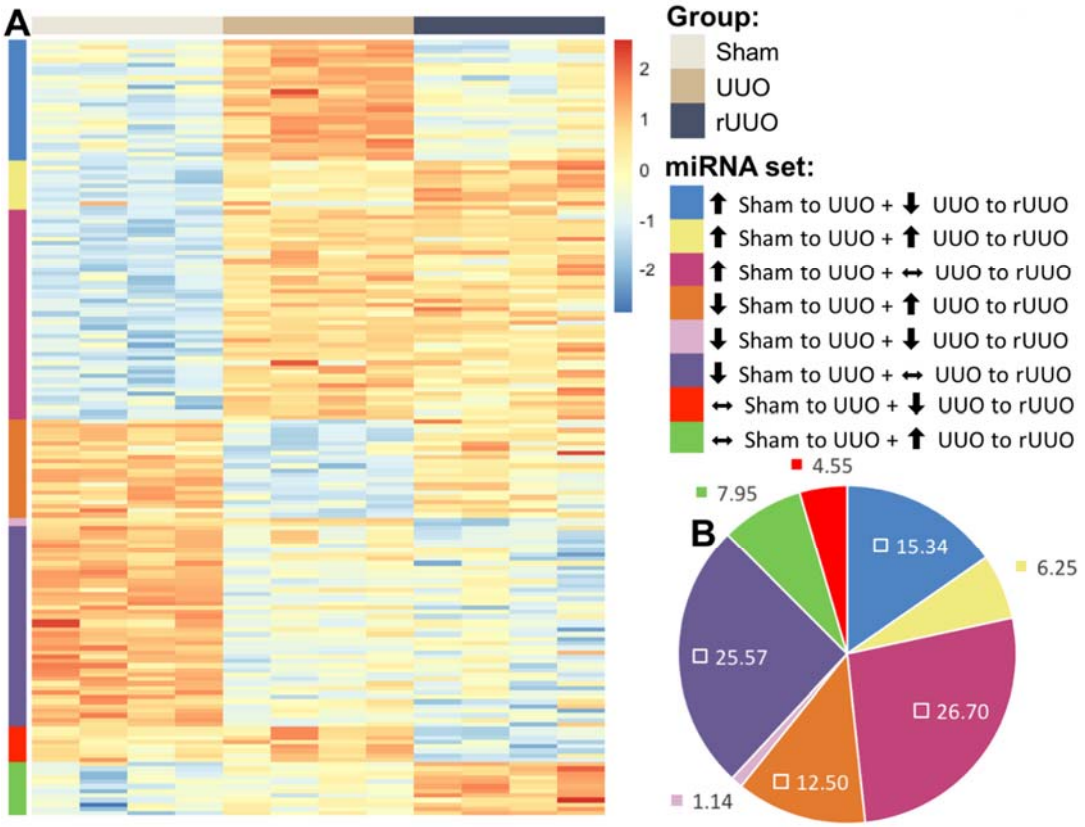

Fig 5.4.4: **miRNA expression profile in the F4/80 cell population.** A = Heatmap annotated by miRNA set, made using pheatmap R package. B = Pie chart of percentage of the total miRNA expression each miRNA set accounts for. miRNAs which were not differentially regulated between sham and UUO, or UUO and rUUO, were excluded (n = 187). miRNA sets were defined based on fold-changes and adjusted p-value (p-adj) values calculated using DESeq2. ↑ = positive fold-change and p-adj <0.05. ↓ = negative fold-change and p-adj <0.05. ↔ = p-adj >0.05. n = 176 miRNAs total.

The F4/80^{hi} population (Fig 5.4.4) was found to have the most diverse and responsive miRNA profile out of the four cell populations, with 52.27% of miRNAs sensitive to injury only, 27.84% of miRNAs dysregulated by injury were (at least partially) restored in rUUO, and 12.5% of miRNAs found to be reversal-specific. In addition, 7.39% of miRNAs here were found to have the uncommon characteristic of increasing or decreasing sequentially in both UUO and rUUO.

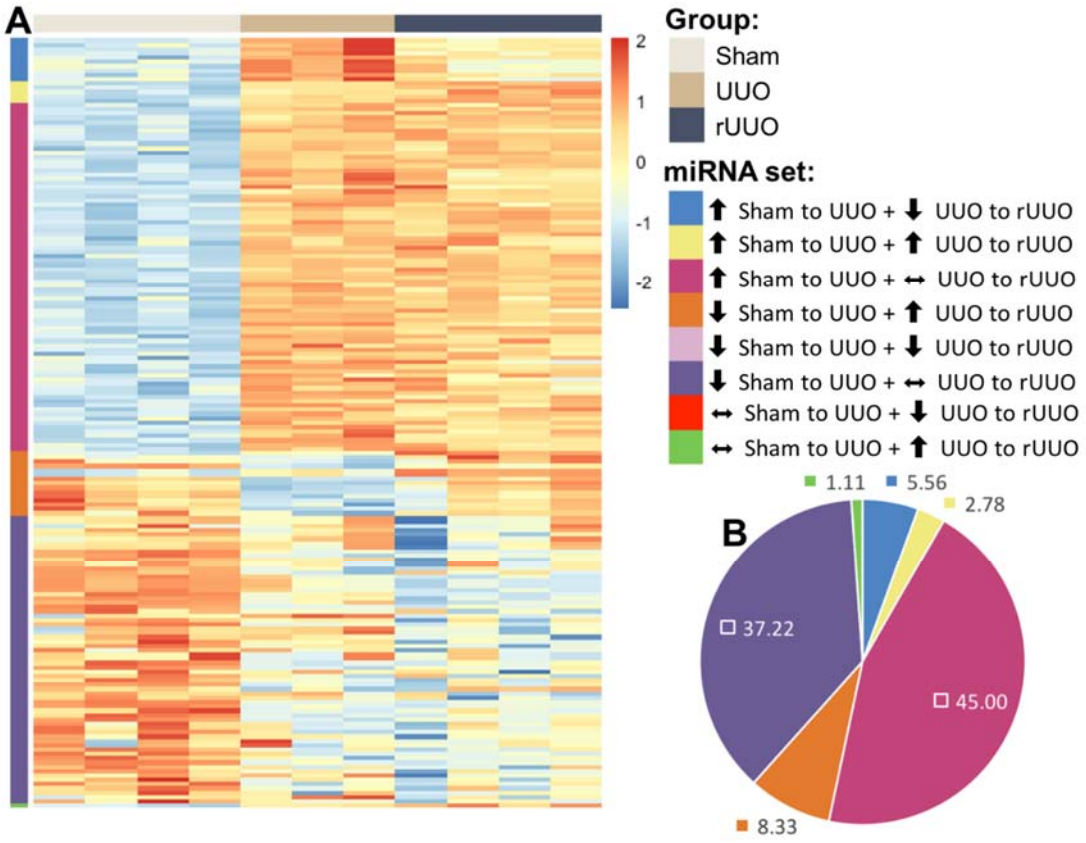

Fig 5.4.5: **miRNA expression profile in the Pdgfrβ cell population.** A = Heatmap annotated by miRNA set, made using pheatmap R package. B = Pie chart of percentage of the total miRNA expression each miRNA set accounts for. miRNAs which were not differentially regulated between sham and UUO, or UUO and rUUO, were excluded (n = 126). miRNA sets were defined based on fold-changes and adjusted p-value (p-adj) values calculated using DESeq2. ⬆ = positive fold-change and p-adj <0.05. ⬇ = negative fold-change and p-adj <0.05. ↔ = p-adj >0.05. n = 180 miRNAs total.

In the Pdgfrβ population (Fig 5.4.5), 82.22% of miRNAs were found to be sensitive to injury only, while 13.89% miRNAs dysregulated by injury were found to be (at least partially) restored in rUUO. Similarly to the Pdgfrβ gene expression data, comparatively little evidence for a reversal-specific response was found, with just 1.11% of miRNAs categorised as reversal-specific.

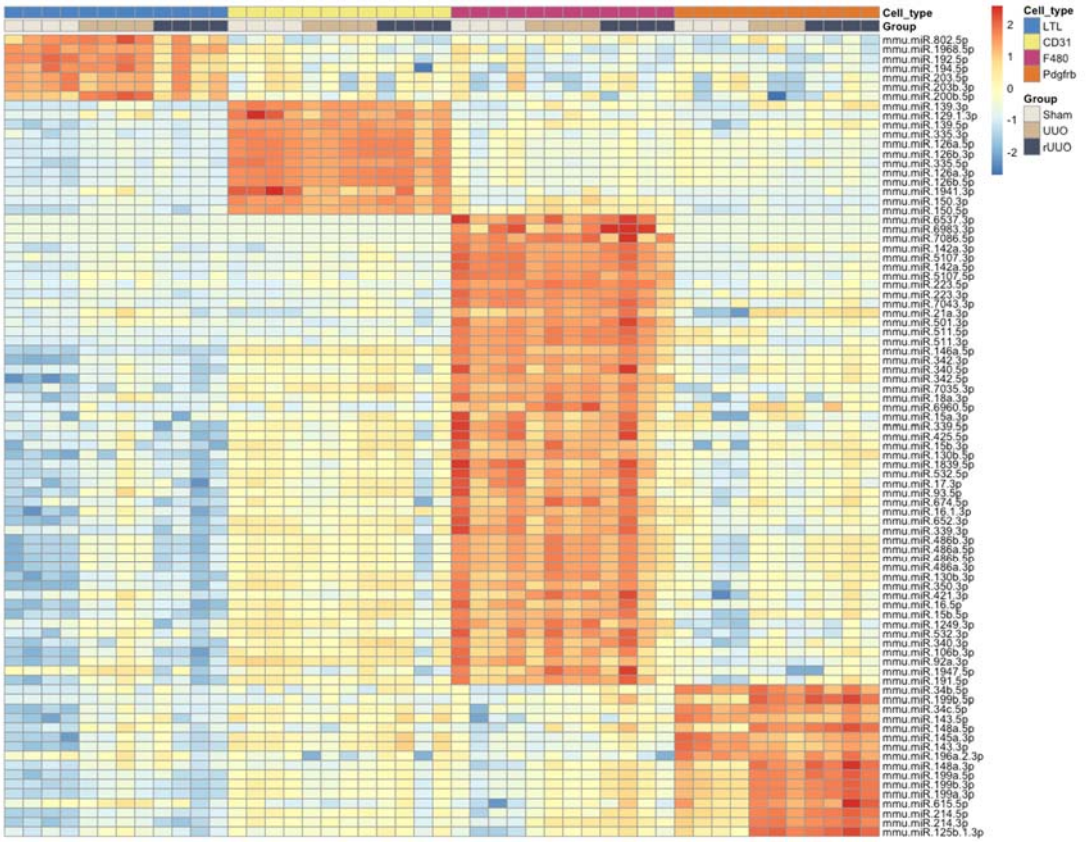

Fig 5.4.6: **Heatmap of miRNA enrichment in each of the 4 cell types.** Enrichment detected using MGFR R package.[316] Only miRNAs which were enriched in a cell type at sham, UUO and rUUO groups were included. Heatmap was created using Pheatmap R package.

To assess if the expression of any given miRNA was significantly associated with one cell population in particular, the MGFR (Marker Gene Finder in RNA-seq data) R package[316] was used to detect miRNAs which were enriched (high expression) in each cell type. Only miRNAs which were significantly enriched in a given cell type at sham, UUO and rUUO were included. LTL was observed to have 7 enriched miRNAs, CD31 had 12, F4/80 had 48, while Pdgfrβ had 16. miR-214-3p (the focus of this thesis), miR-

214-5p, as well as miR-199a-3p and miR-199a-5p (expressed in the same polycistronic transcript as miR-214) were enriched in the Pdgfrβ population. miR-199b-3p and miR-199b-5p, which have identical mature sequences to miR-199a-3p/5p but originate from a separate chromosomal location,[415] were also enriched in the Pdgfrβ population.

Table 5.4.7: **miRNA enrichment in each of the 4 cell types**.

LTL	CD31	F4/80	Pdgfrβ
miR-802-5p	miR-139-3p	miR-6537-3p	miR-34b-5p
miR-1968-5p	miR-129-1-3p	miR-6983-3p	miR-199b-5p
miR-192-5p	miR-139-5p	miR-7086-5p	miR-34c-5p
miR-194-5p	miR-335-3p	miR-142a-3p	miR-143-5p
miR-203-5p	miR-126a-5p	miR-5107-3p	miR-148a-5p
miR-203b-3p	miR-126b-3p	miR-142a-5p	miR-145a-3p
miR-200b-5p	miR-335-5p	miR-5107-5p	miR-143-3p
	miR-126a-3p	miR-223-5p	miR-196a-2-3p
	miR-126b-5p	miR-223-3p	miR-148a-3p
	miR-1941-3p	miR-7043-3p	miR-199a-5p
	miR-150-3p	miR-21a-3p	miR-199b-3p
	miR-150-5p	miR-501-3p	miR-199a-3p
		miR-511-5p	miR-615-5p
		miR-511-3p	miR-214-5p
		miR-146a-5p	miR-214-3p
		miR-342-3p	miR-125b-1-3p
		miR-340-5p	
		miR-342-5p	
		miR-7035-3p	
		miR-18a-3p	
		miR-6960-5p	
		miR-15a-3p	
		miR-339-5p	
		miR-425-5p	
		miR-15b-3p	
		miR-130b-5p	
		miR-1839-5p	
		miR-532-5p	
		miR-17-3p	
		miR-93-5p	
		miR-674-5p	
		miR-16-1-3p	
		miR-652-3p	
		miR-339-3p	
		miR-486b-3p	

		miR-486a-5p miR-486b-5p miR-486a-3p miR-130b-3p miR-350-3p miR-421-3p miR-16-5p miR-15b-5p miR-1249-3p miR-532-3p miR-340-3p miR-106b-3p miR-92a-3p miR-1947-5p miR-191-5p	

	Sham v UUO		UUO v rUUO		Average CPM		
	Log2 FC	**p-adj**	**Log2 FC**	**p-adj**	**Sham**	**UUO**	**rUUO**
LTL							
miR-214-3p	1.33	0.09	-0.52	0.85	3.5	6.6	4.9
CD31							
miR-214-3p	-0.01	0.99	0.55	0.41	7.3	6.5	4.0
F4/80							
miR-214-3p	3.75	2.18E-32	-0.03	0.91	3.8	58.6	50.2
Pdgfrβ							
miR-214-3p	2.88	6.98E-73	-0.29	0.43	47.3	562.8	387.8

Table 5.4.8: **Fold-change and expression of miR-214-3p.** FC = fold-change. P-adj = adjusted p-value. CPM = counts per million reads. Log2FC and p-adjusted values were generated using DESeq2 R package. Green text denotes significant changes.

miR-214-3p expression was found to increase significantly from sham to UUO in F4/80^{hi} macrophages (3.75 log2-fold) and in Pdgfrβ^{+} population (2.88 log2-fold), with no significant change in expression between UUO and rUUO. Despite the large fold-change increase in miR-214-3p expression in F4/80^{hi} macrophages, miR-214-3p expression (in CPM) remained relatively low in comparison to Pdgfrβ. miR-214-3p

was not found to be differentially regulated in LTL or $CD31^+$ cell populations between any timepoints.

As miR-214-3p expression was observed to increase in the $F4/80^{hi}$ and $Pdgfr\beta^+$ cell populations in UUO, the ischemia reperfusion injury (IRI) model was used to assess if the same differential expression occurs in a separate model of renal fibrosis. Mice were subjected to 18-minute unilateral IRI and sacrificed at 2, 7 and 21-days post-IRI. LTL^+ (Fig 5.4.9), $F4/80^{hi}$ (Fig 5.4.10), and $Pdgfr\beta^+$ (Fig 5.4.11) cell populations were FACS sorted from renal cortex and miR-214-3p expression was assessed in each. A comparison of miR-214-3p expression between each cell population at each timepoint was also carried out (Fig 5.4.12). FACS sorting methods and gating strategy were identical to those previously described. The number of animals in each surgical group was as follows; Sham: n=9, IRI 2d: n=4, IRI 7d: n=3, IRI 21d = 4. The following samples were excluded from analysis due to the RNA yield obtained being too low to carry out reverse-transcription reactions: LTL IRI 2d (n=1), F4/80 sham (n=1), Pdgfrβ IRI 2d (n=1).

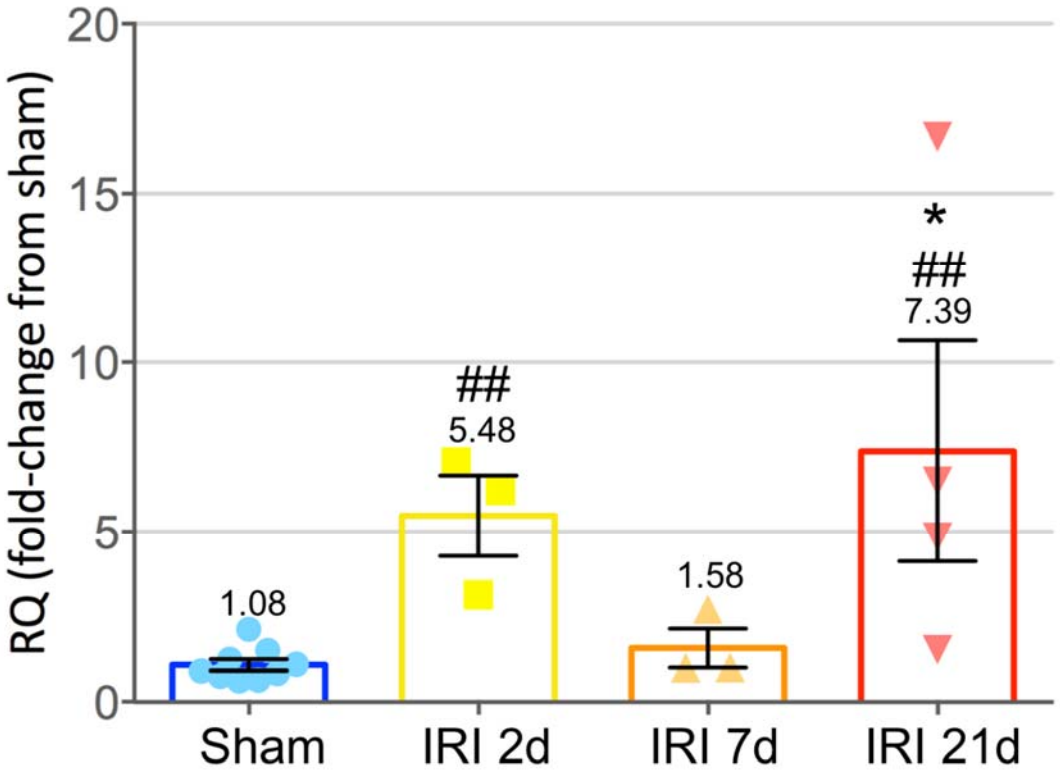

Fig 5.4.9: **miR-214-3p expression in renal proximal tubular epithelial (LTL+) cells FACS sorted from mice subjected to 18-minute unilateral ischemia reperfusion injury (IRI).** 2d = 2-days post-IRI, 7d = 7-days post-IRI, 21d = 21-days post-IRI. miR-214-3p expression was assessed via qRT-PCR using specific Taqman probe. miR-214-3p expression was normalised to housekeeper u6. Plotted as mean ± SEM. One-way ANOVA with Tukey's multiple comparison test was used for statistical analysis. ## = $P < 0.01$ vs sham. * = $P < 0.05$ vs IRI 7d. Sham: n=9, IRI 2d: n=3, IRI 7d: n=3, IRI 21d: n=4.

In the proximal tubular epithelial (LTL^+) population (Fig 5.4.9), miR-214-3p expression was significantly increased at IRI 2d and IRI 21d in comparison to sham, but not at IRI 7d. miR-214-3p expression was significantly increased from IRI 7d to IRI 21d.

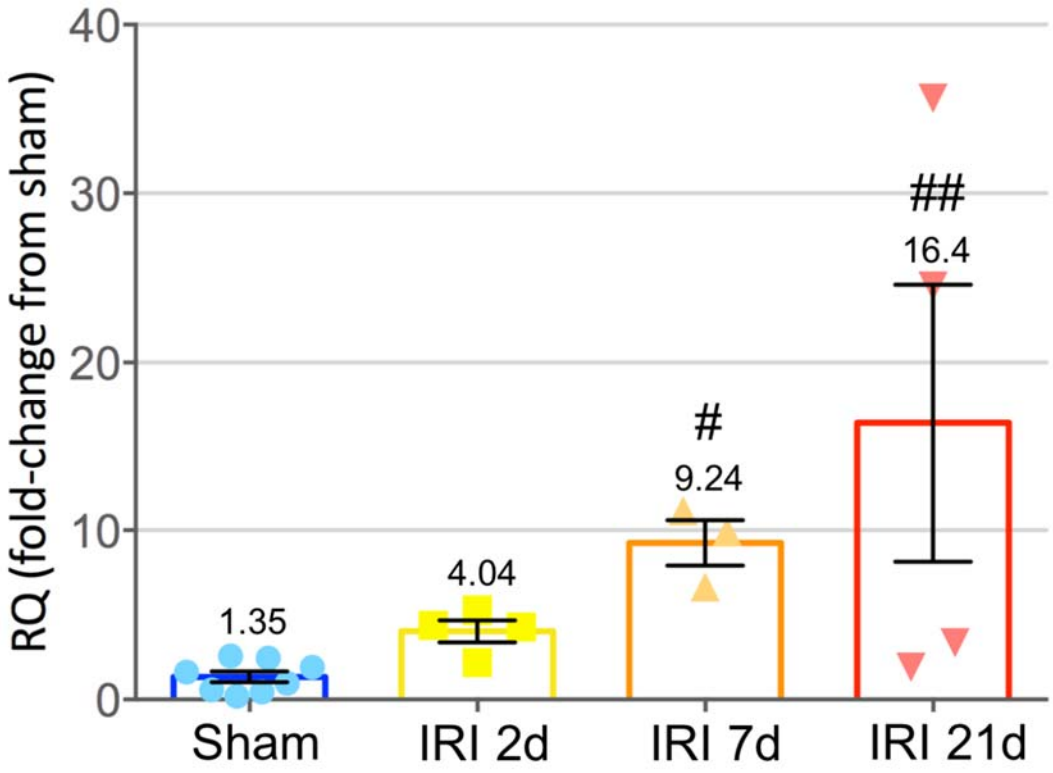

Fig 5.4.10: **miR-214-3p expression in F4/80hi (tissue resident) macrophages FACS sorted from mice subjected to 18-minute unilateral ischemia reperfusion (IRI).** 2d = 2-days post-IRI, 7d = 7-days post-IRI, 21d = 21-days post-IRI. miR-214-3p expression was assessed via qRT-PCR using specific Taqman probe. miR-214-3p expression was normalised to housekeeper U6. Plotted as mean ± SEM. One-way ANOVA with Tukey's multiple comparison test was used for statistical analysis. ## = $P < 0.01$ vs sham. * = $P < 0.05$ vs IRI 7d. Sham: n=8, IRI 2d: n=4, IRI 7d: n=3, IRI 21d: n=4.

In the F4/80^{hi} macrophage population (Fig 5.4.10), miR-214-3p expression was significantly increased at IRI 7d and IRI 21d compared to sham, but not at IRI 2d. No significant change in expression was detected between IRI 7d and IRI 21d.

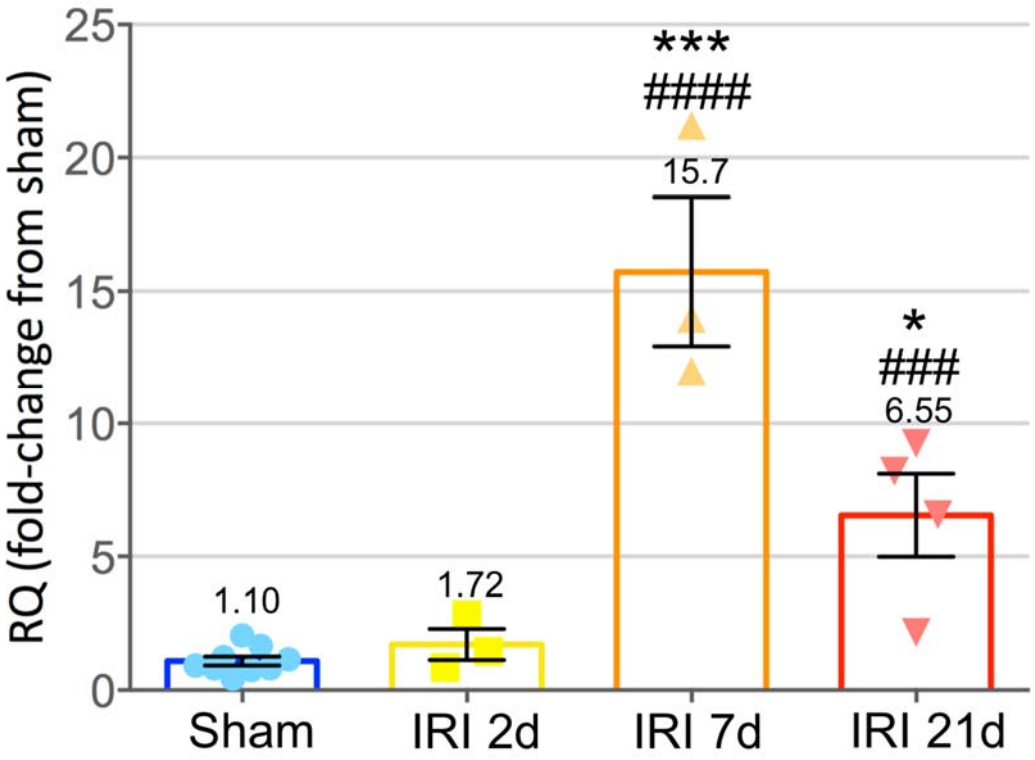

Fig 5.4.11: **miR-214-3p expression in Pdgfrβ+ cells FACS sorted from mice subjected to 18-minute unilateral ischemia reperfusion injury (IRI) .** 2d = 2-days post-IRI, 7d = 7-days post-IRI, 21d = 21-days post-IRI. miR-214-3p expression was assessed via qRT-PCR using specific Taqman probe. miR-214-3p expression was normalised to housekeeper U6. Plotted as mean ± SEM. One-way ANOVA with Tukey's multiple comparison test was used for statistical analysis. ### = $P < 0.001$ vs sham, #### = $P < 0.0001$ vs sham. * = $P < 0.05$ vs IRI 2d, *** = $P < 0.001$ vs IRI 2d. Sham: n=9, IRI 2d: n=3, IRI 7d: n=3, IRI 21d: n=4.

In the Pdgfrβ+ population, miR-214-3p expression was found to be significantly increased at IRI 7d and IRI 21d in comparison to sham, but not at IRI 2d (Fig 5.4.11). Expression was not significantly different between IRI 7d and IRI 21d groups.

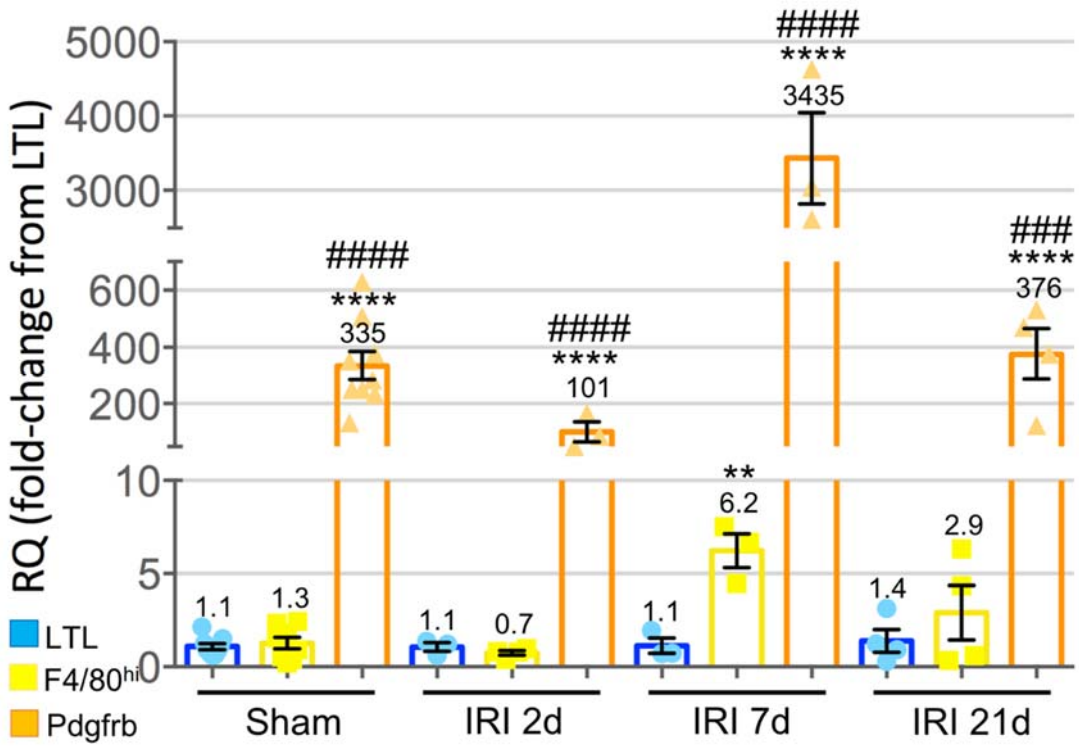

Fig 5.4.12: **Comparison of miR-214-3p expression in three cell populations FACS sorted from mice subjected to 18-minute unilateral ischemia reperfusion injury (IRI) .** 2d = 2-days post-IRI, 7d = 7-days post-IRI, 21d = 21-days post-IRI. miR-214-3p expression was assessed via qRT-PCR using specific Taqman probe. miR-214-3p expression was normalised to housekeeper U6. Plotted as mean ± SEM. One-way ANOVA with Tukey's multiple comparison test was used for statistical analysis, carried out separately at each timepoint. ** = P < 0.01 vs LTL, **** = P < 0.0001 vs LTL, ### = P < 0.001 vs F4/80, #### = P < 0.0001 vs F4/80. Sham: LTL n=9, F4/80 n=8, Pdgfrβ n=9. IRI 2d: LTL n=3, F4/80 n=4, Pdgfrβ n=3. IRI 7d: LTL n=3, F4/80 n=3, Pdgfrβ n=3. IRI 21d: LTL n=4, F4/80 n=4, Pdgfrβ n=4.

At sham and each post-IRI timepoint, miR-214-3p expression was significantly higher in Pdgfrβ^{+} cells in comparison to the LTL and F4/80^{hi} cell populations (Fig 5.4.12). At IRI 7d, miR-214-3p expression was significantly higher in F4/80^{hi} cells than LTL cells, but this was not observed at any other timepoint. Expression was normalised to LTL for the purposes of graphing, with LTL being chosen as it had the lowest miR-214-3p expression of the three cell types at most timepoints.

As miR-214-3p was found to be enriched in the Pdgfrβ population, this data was investigated to identify potential miR-214-3p direct target genes. miR-214-3p expression was found to significantly increase in the Pdgfrβ population from sham to UUO, with no significant change in expression between UUO and rUUO (table 5.4.8). Therefore, Pdgfrβ genes which decreased significantly between sham to UUO and remained repressed in rUUO (Pdgfrβ_DNu_NSr) were assessed as potential miR-214-3p targets via the MultimiR R package. Genes which were predicted by at least 4 of the 8 potential databases were considered potential miR-214-3p targets. 18 genes which matched these criteria were identified (table 5.4.13). A literature search was carried out for each of these 18 genes, in order to generate a hypothesis relating to how their differential regulation may be relevant to the Pdgfrβ population in UUO. A gene expression cut-off of 20 FPKM was implemented, resulting in n=9 genes with expression lower than the cut-off being excluded from further analysis (Pgf (placental growth factor), Baz2a (bromodomain adjacent to zinc finger domain 2A), Atxn1l (ataxin 1 like), Igdcc3 (immunoglobulin superfamily DCC subclass member 3), Nrxn3 (neurexin 3), Pik3cb (phosphatidylinositol-4,5-bisphosphate 3-kinase catalytic subunit beta), Plxna2 (plexin A2), Pptc7 (PTC7 protein phosphatase homolog), and Sema4d (Semaphorin 4D)). Two genes were excluded from further analysis due to a lack of mechanistic publications (Ahdc1 (AT hook, DNA binding motif, containing 1) and Rcsd1 (RCSD domain containing 1)). Myo18a (myosin XVIIIA) was excluded from further analysis as it was unclear as to how differential regulation of this gene may be involved in the Pdgfrβ population in renal fibrosis and has never been investigated as a miR-214-3p target.

		Sham v UUO		UUO v rUUO		Average FPKM		
Gene	**Pred. #**	**Log2 FC**	**p-adj**	**Log2 FC**	**p-adj**	**Sham**	**UUO**	**rUUO**
Myo18a	7	-2.31	1.87E-15	0.64	0.17	28.3	5.4	7.9
Qk	7	-0.44	0.009	0.0004	1.00	46.1	33.5	38.8
Ahdc1	6	-0.80	0.005	0.25	0.69	21.4	8.4	14.7
Pgf	6	-1.56	0.005	-0.79	0.63	12.1	3.6	2.5
Sept4	6	-2.88	6.28E-13	0.18	0.88	142.3	18.5	24.7
Baz2a	5	-1.24	1.43E-09	0.55	0.09	18.3	8.4	13.8
Ppm1a	5	-0.63	0.01	0.05	0.94	44.5	29.2	33.3
Atxn1l	4	-0.84	0.0002	-0.02	0.97	18.3	11.5	12.4
Igdcc3	4	-10.2	5.41E-18	5.94	0.09	6.2	0.0	0.3
Mef2c	4	-1.14	2.37E-06	0.01	0.98	53.1	20.4	20.4
Nrxn3	4	-3.19	3.82E-08	-0.77	0.72	6.5	0.9	0.4
Pik3cb	4	-1.43	0.03	0.39	0.81	1.6	0.6	0.9
Plxna2	4	-1.16	0.009	0.05	0.97	9.2	3.9	4.6
Pptc7	4	-0.94	0.01	0.21	0.82	6.5	3.2	4.3
Rcsd1	4	-2.59	2.97E-11	1.10	0.06	36.1	5.6	15.6
Rybp	4	-0.90	0.001	0.44	0.35	26.0	12.7	19.7
Sema4d	4	-1.10	0.006	-0.20	0.89	3.3	1.3	2.0
Smg7	4	-0.72	0.0009	0.08	0.89	48.3	27.3	29.9

Table 5.4.13: **Predicted miR-214-3p target genes in Pdgfrβ cell population in rUUO gene expression sequencing**. Gene = gene symbol. Pred. # = number of databases which predict mouse miR-214-3p binding. Log2 FC = log2 fold-change. P-adj = adjusted p-value. Log2 FC and p-adj were obtained from DESeq2. FPKMs were generated by RSEM. Genes selected for further validation were highlighted in green.

6 potential miR-214-3p target genes were selected for further validation via qRT-PCR (Fig 5.4.14 and Fig 5.4.15) in cDNA synthesised from matched samples which were previously sent for RNA sequencing. These were: Qk (Quaking), Sept4 (Septin4), Ppm1a (Protein Phosphatase Magnesium Dependent 1A), Mef2c (Myocyte Enhancer Factor 2C), Rybp (RING1 and YY1 Binding Protein), and Smg7 (SMG7 Nonsense Mediated mRNA Decay Factor).

qRT-PCR was used to validate the expression of selected miR-214-3p targets in Pdgfrβ^+ cell population (Figs 5.4.14 and 5.4.15). Out of the six genes assessed, two were found to be significantly down-regulated from sham to UUO via qRT-PCR (Sept4 and Smg7). Sept4 is a member of the Septin family of proteins which were initially found to play a role in cytokinesis, but subsequent investigation revealed them to be involved in a wide variety of cellular processes,[416] with Sept4 in particular being linked to the promotion of apoptosis.[416–419] Smg7 is involved in nonsense-mediated decay of mRNA transcripts,[420] as well in telomere maintenance and apoptosis.[421,422]

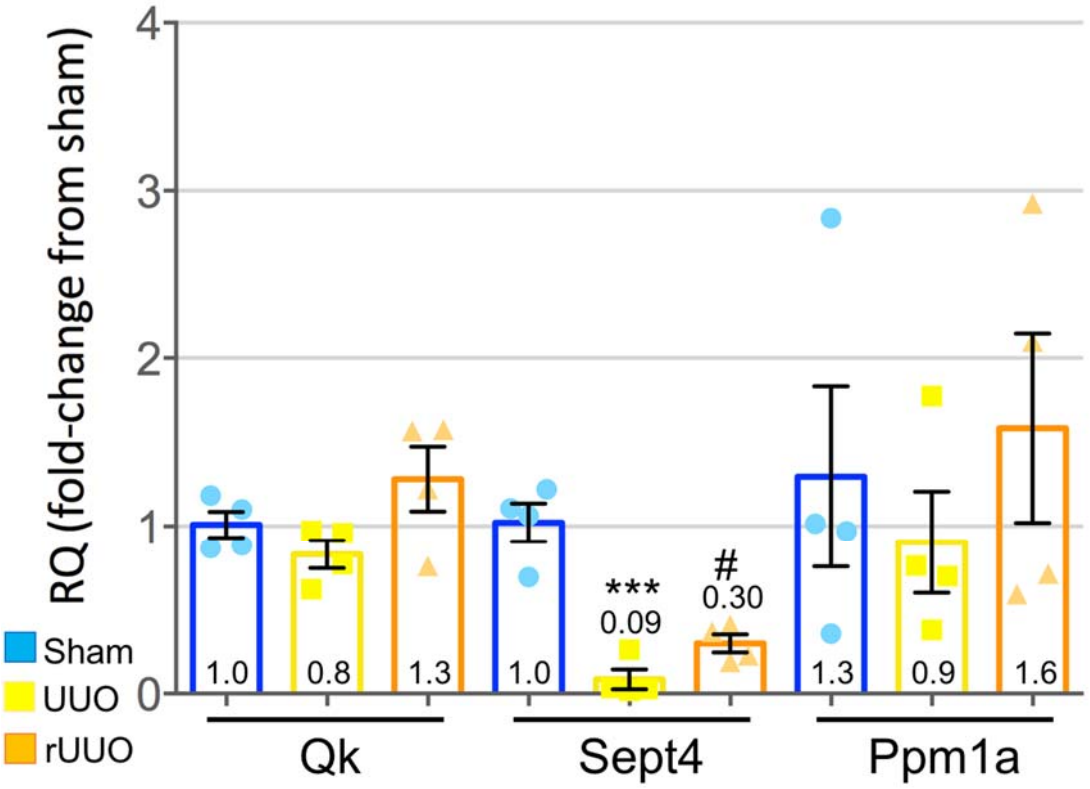

Fig 5.4.14: **Validation of selected miR-214-3p targets via qRT-PCR.** Gene expression was assessed via qRT-PCR using specific Taqman probes. Gene expression was normalised to housekeeper Gapdh (glyceraldehyde-3-phosphate dehydrogenase). Plotted as mean ± SEM. One-way ANOVA with Tukey's multiple comparison test was used for statistical analysis. *** = $P < 0.001$ vs sham, # = $P < 0.05$ vs UUO. Sham: n=4, UUO: n=4, rUUO: n=4.

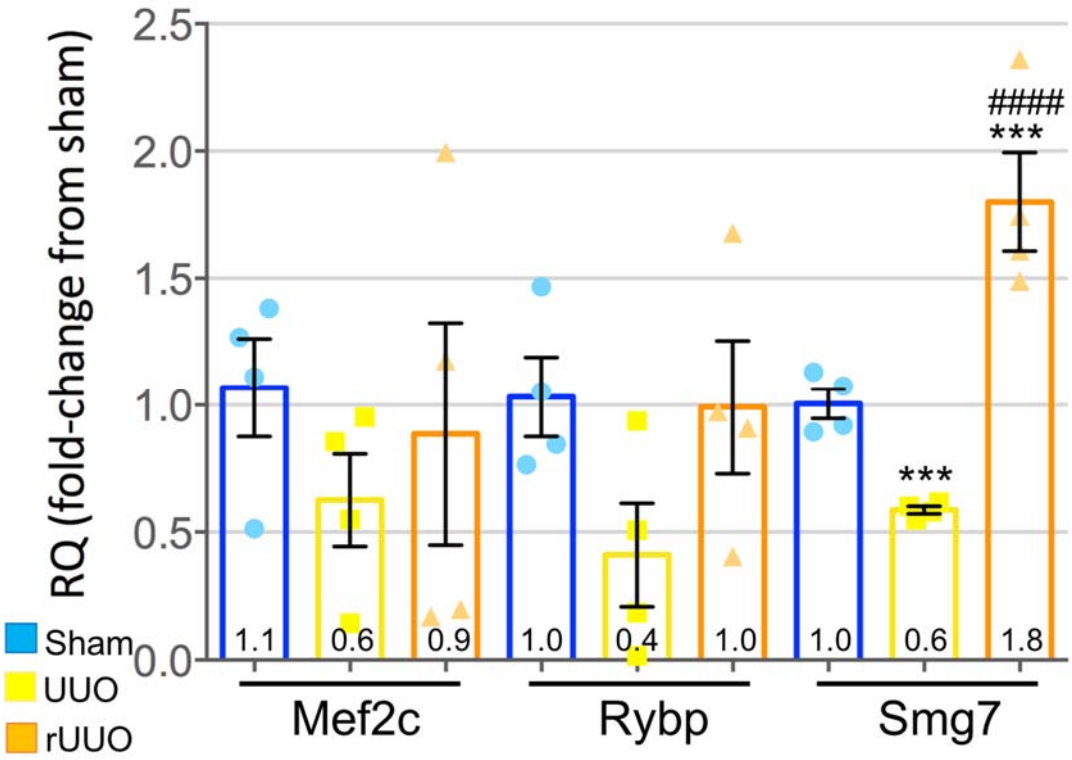

Fig 5.4.15: **Validation of selected miR-214-3p targets via qRT-PCR.** Gene expression was assessed via qRT-PCR using specific Taqman probes. Gene expression was normalised to housekeeper Gapdh. Plotted as mean ± SEM. One-way ANOVA with Tukey's multiple comparison test was used for statistical analysis. *** = $P < 0.001$ vs sham, #### = $P < 0.0001$ vs UUO. Sham: n=4, UUO: n=4, rUUO: n=4.

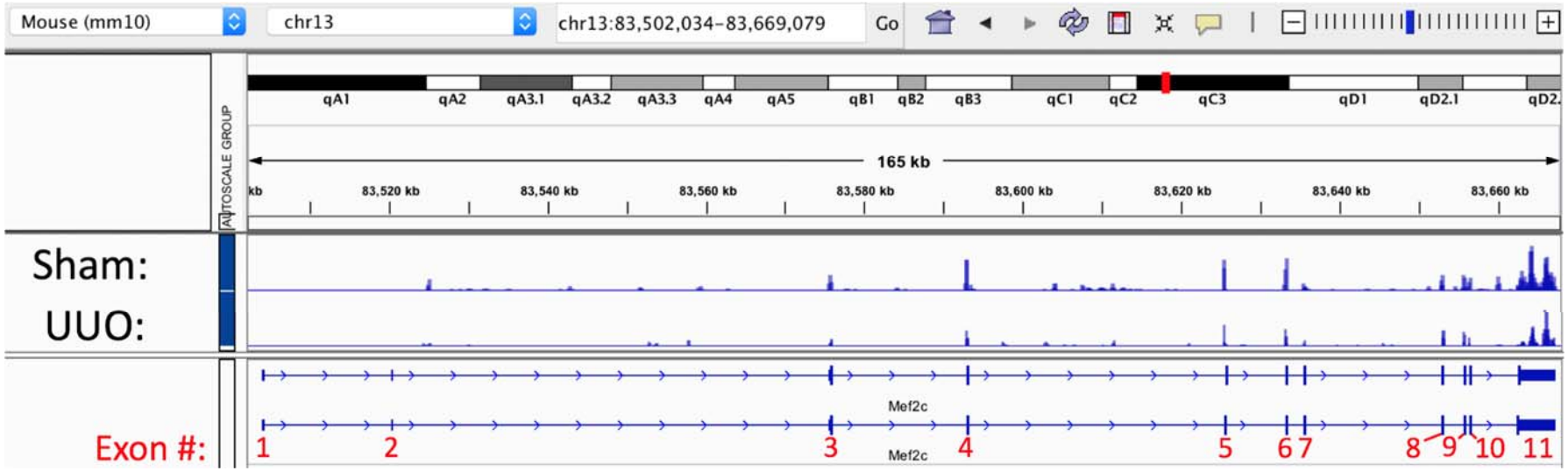

Fig 5.4.16: **View of Pdgfrβ+ cell population reads mapping to the Mef2c gene in the mm10 genome**. Reads were aligned using STAR, prepared for visualisation using BigWig, and visualised using IGV (integrative Genomics Viewer) browser. Individual sham and UUO samples were overlaid into one track each.

As Mef2c is a validated miR-214-3p target,[277,278] further investigation into why significant differential regulation of Mef2c was detected in the Pdgfrβ^{+} population from sham to UUO via RNA sequencing but not via qRT-PCR was carried out. Here, the read mapping profile of the RNA sequencing data was visualised in the IGV browser (Fig 5.4.16). The qRT-PCR probe used amplified the exon-exon boundary between exons 8-9. However, the most dramatic reductions in reads from sham to UUO appeared to occur in exons 3, 4, 5 and 6. This indicates the Mef2c Taqman probe used may not amplify the splice variants (or enough relevant variants) of the Mef2c gene which are large contributors to the overall differential regulation of the Mef2c gene as observed via RNA sequencing.

As the Pdgfrβ population was identified as a population of mechanistic interest in relation to miR-214 in renal fibrosis, the influence of miR-214 inhibition on Pdgfrβ expression was assessed. RNA from Denby *et al* (2014)[261] was used here, as anti-miR-214 was used to knockdown miR-214-3p expression in the UUO model in this study, resulting in an 87% reduction in renal fibrosis in comparison to control anti-miR. In this publication the source of the miR-214-3p expression was not identified nor was the number of fibroblasts present. Therefore, the expression of Pdgfrβ was used as a surrogate for myofibroblast number.

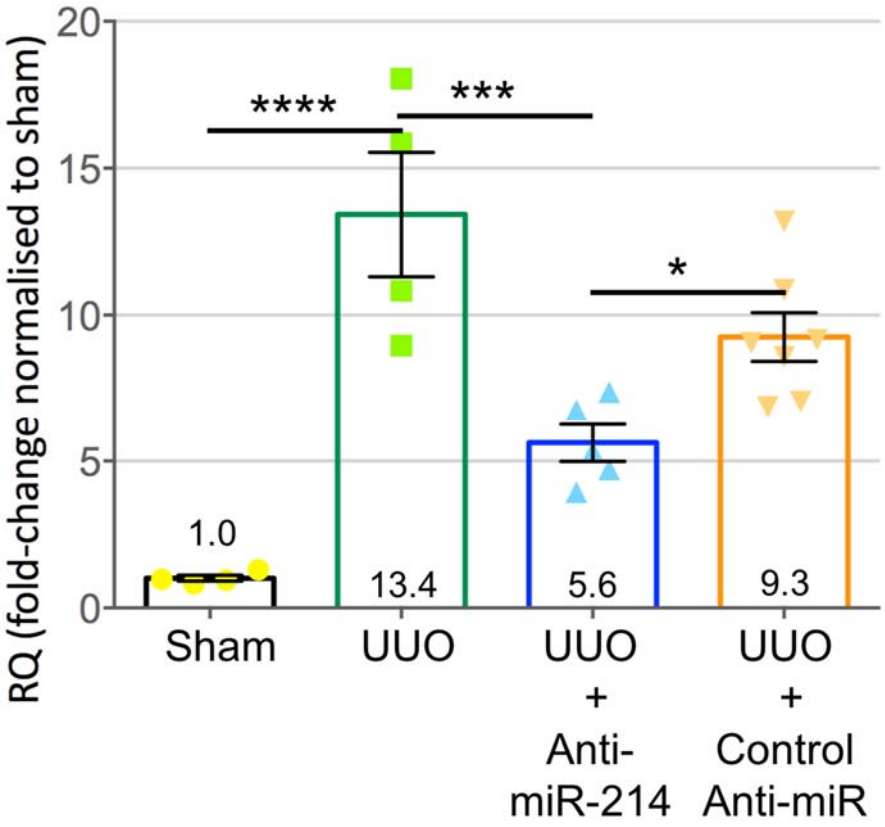

Fig 5.4.17: **Pdgfrβ gene expression in Denby et al (2014) UUO anti-miR-214 study.** Quantitative real-time PCR (qRT-PCR) was carried out with specific Taqman probe, normalised to housekeeper Gapdh. Sham: n=4, UUO: n=4, Anti-miR-214: n=5, Ctrl anti-miR: n=7. Plotted as mean ± SEM. Statistical analysis: Sham and UUO compared via student's t-test (unpaired, two-tailed). UUO, anti-miR-214 and control anti-miR groups compared via one-way ANOVA with Tukey multiple comparison test. * = $P < 0.05$, *** = $P < 0.001$, **** = $P < 0.0001$.

It was found that Pdgfrβ expression increases 13.4-fold ± 2.1 SEM from sham in UUO, and was not significantly different in control anti-miR compared to UUO (Fig 5.4.17). Significantly reduced Pdgfrβ expression was detected in the anti-miR-214-treated group, in comparison to both the control anti-miR group and UUO with no intervention group. This suggests a lower number of fibroblasts were present in UUO kidneys treated with anti-miR-214.

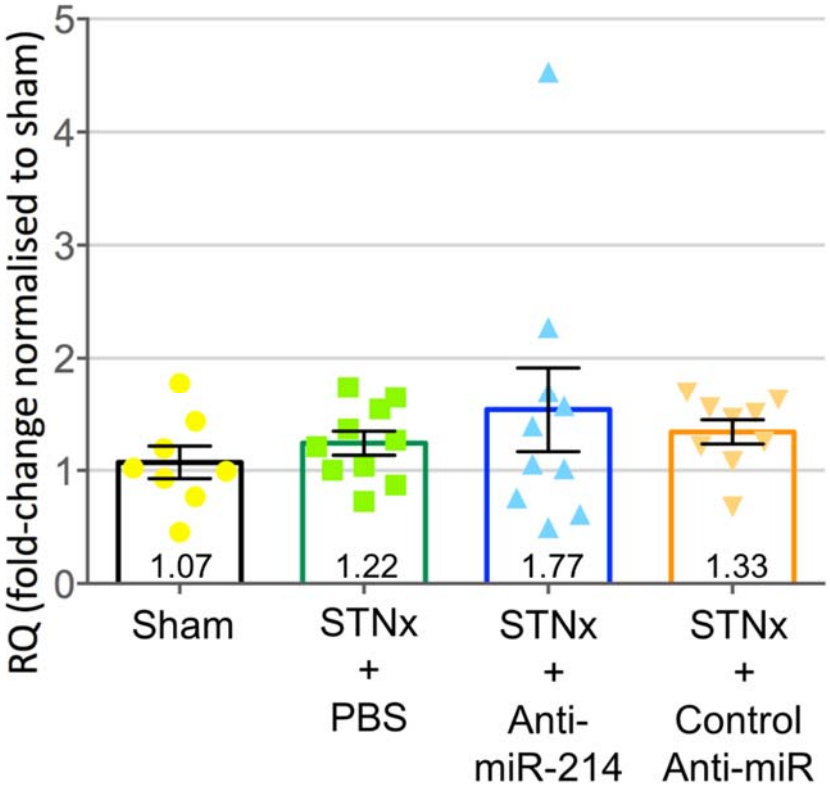

Fig 5.4.18: **Pdgfrβ gene expression in STNx anti-miR-214 study.** Quantitative real-time PCR (qRT-PCR) was carried out with specific Taqman probe, normalised to housekeeper Ppia. Sham: n=8, PBS: n=10, Anti-miR-214: n=10, Ctrl anti-miR: n=9. Plotted as mean ± SEM. Statistical analysis: Sham and PBS compared via student's t-test (unpaired, two-tailed). PBS, anti-miR-214 and control anti-miR groups compared via one-way ANOVA with Tukey multiple comparison test.

As we had previously administered an anti-miR-214 compound in the STNx model (Chapter 4) and had now found that miR-214-3p was significantly expressed in the Pdgfrβ^{+} population in UUO, the expression of Pdgfrβ was assessed in STNx (Fig 5.4.18). Here, no significant increase or change in Pdgfrβ expression was detected in any group. As this was surprising, Pdgfrβ was then assessed in the kidneys from the STNx characterisation study presented in chapter 3 (Fig 5.4.19). Here, a small but statistically significant increase in Pdgfrβ expression was observed in the STNx group (1.37-fold ± 0.21 SEM). However, this was still a much lower magnitude increase than what was observed in UUO (13.4-fold ± 2.1 SEM) and may reflect the difference between a slowly progressive chronic kidney disease and an acute model of injury.

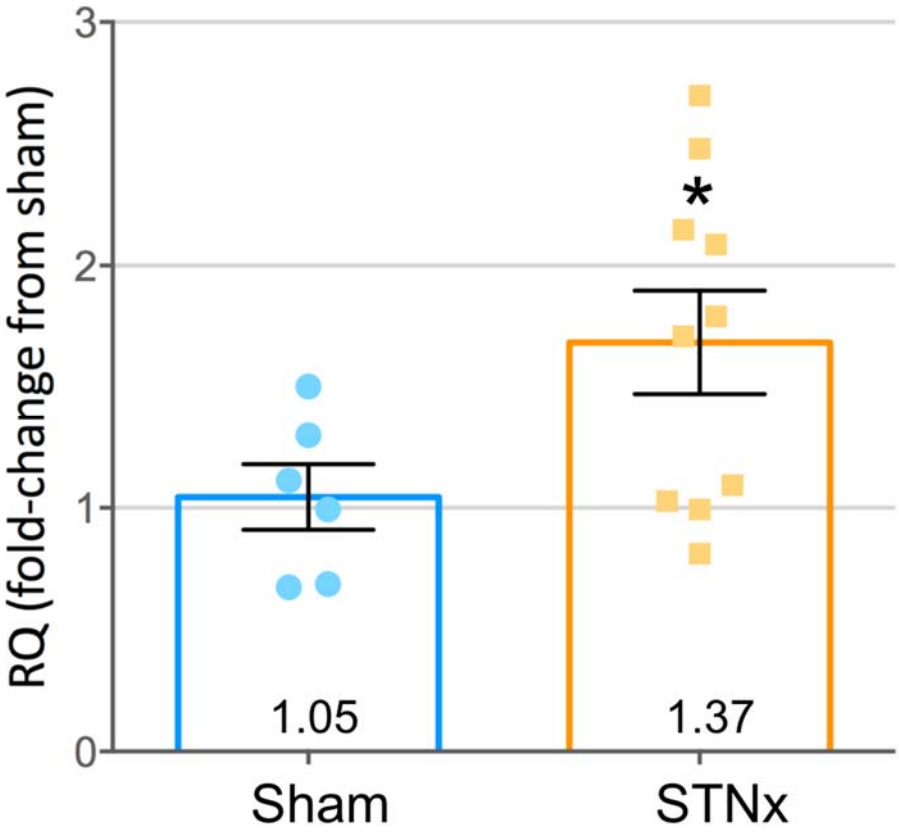

Fig 5.4.19: **Pdgfrβ gene expression in STNx characterisation study (chapter 3).** Quantitative real-time PCR (qRT-PCR) was carried out with specific Taqman probe, normalised to housekeeper Ppia. Sham: n=6, STNx: n=10. Plotted as mean ± SEM. Sham and STNx compared via student's t-test (unpaired, two-tailed). * = $P < 0.05$ vs sham.

As we had previously administered an anti-miR-214 compound in the STNx model (Chapter 4) and had now found that miR-214-3p was significantly expressed in the Pdgfrβ^{+} population in UUO, the expression of Pdgfrβ was assessed (Fig 5.4.18). Here, no significant increase or change in Pdgfrβ expression was detected in any group. As this was surprising, Pdgfrβ was then assessed in the kidneys from the STNx characterisation study presented in chapter 3 (Fig 5.4.19). Here, a small but statistically significant increase in Pdgfrβ expression was observed in the STNx group (1.37-fold ± 0.21 SEM). However, this was a much lower magnitude increase than what was observed in UUO (13.4-fold ± 2.1 SEM) and may reflect the difference between a slowly progressive chronic kidney disease and an acute model of injury.

5.5: Discussion

Initially, RNA sequencing for gene and small RNA expression was carried out on bulk renal cortical tissue of mice in one of five surgical groups. These groups consisted of mice subjected to sham, 7-day UUO, and 7-day UUO followed by reversal of injury for 1-week (rUUO 1-week), 2-weeks (rUUO 2-week) or 4-weeks (rUUO 4-week). The surgical methods used were as published in Hesketh *et al* (2014).[161]

Three miRNAs were selected from the bulk small RNA sequencing for validation of the read mapping via qRT-PCR (Fig 5.2.4) and then to assess if these miRNAs were differentially regulated in other mouse models (Fig 5.2.5 AB, Fig 5.2.6). miR-212-3p was selected as its expression profile suggested it was responsive to renal injury and reversal of renal injury (i.e., its expression dramatically increased between sham and UUO, then steadily decreased during the reversal phase). miR-874-5p and miR-874-3p were selected as their expression profile was the opposite to miR-212-3p (i.e., decreased expression between sham and UUO, then gradual increase in expression during reversal). Although qRT-PCR analysis indicated the mapping of the small RNA sequencing reads was accurate in the rUUO study, not all these miRNAs followed the same pattern of expression in STNx. miR-212-3p was also up-regulated in whole kidney cortex 10-weeks post-STNx, but to a lesser magnitude than in UUO, while miR-874-3p and miR-874-5p expression was not significantly affected by STNx. This suggest that although UUO may be a useful tool for the discovery of miRNAs (or genes) of interest within the realm of renal fibrosis, further validation of these results should take place in alternate models.

The kidney is composed of an array of distinct cell populations, which in turn have distinct roles to play in normal kidney homeostasis and disease.[315] Therefore, to better understand how gene expression in certain cell populations of interest changes in response to UUO and reversal of injury, FACS was used to sort four cell types with key roles in renal fibrosis, from which RNA sequencing was performed.

These cell types were: LTL (proximal tubular epithelial cells),[140,143,145,423] CD31 (endothelial cells),[155,157–159] F4/80^{hi} (tissue-resident) macrophages,[122,397,405,406,424] and Pdgfrβ^{+} cells (fibroblast-like cells).[116,118,120,398,425,426]

Another reason to sort out cell populations of interest instead of relying on bulk renal cortex sequencing is to eliminate, or greatly reduce, the effect a change in number of certain cell types between experimental groups has on detected differential gene expression. More specifically, following UUO, significant autophagy and apoptosis occurs in the tubular cells, leading to a significant reduction in the number of tubular cells.[427] As it has been estimated that more than half of the mRNA in kidney comes from the proximal tubular cells,[393] tubular atrophy caused by UUO may have significant consequences for the overall gene expression profile. At the same time, macrophage infiltration and accumulation of myofibroblasts occurs.[407] Together, these complicate the interpretation of single-gene expression fold-changes between sham and UUO samples. For example, it may be difficult to determine if a gene observed to be down-regulated in whole kidney cortex between sham and UUO is due to injury-driven down-regulation or simply due to a loss of the cell population (such as tubular epithelial cells) which it was expressed in. This may also apply in situations where a therapeutic intervention may alter the number of various cell populations, for example a therapeutic may inhibit proximal tubular epithelial cell apoptosis or inhibit myofibroblast proliferation.

The RNA sequencing data generated was used to better understand the impact on gene expression data that assessment via bulk renal cortex sequencing has in comparison to sequencing FACS-isolated cell populations. Here, the MGFR R package[316] was used to identify genes (at sham) which were enriched (high-expression) in each of the four sorted cell populations. When these genes were grouped together on a heatmap of all the gene expression data from the FACS rUUO study (Fig 5.3.4), a clear trend for these sham-enriched genes to remain highly expressed in the UUO and rUUO (2-week) groups was observable. However, when

these genes were grouped together on a heatmap of all the gene expression data from the bulk renal cortex sequencing experiment (Fig 5.3.5), the expression of these genes varies drastically different between the different experimental groups. LTL-enriched genes were found highly expressed in the bulk data sham group, before a large expression decrease in expression in UUO and what appeared to be some increased expression again by rUUO week 4 as the kidney repaired. CD31, F4/80 and Pdgfrβ-enriched genes generally show a reversed pattern to LTL-enriched genes in the bulk data, where expression was generally low in the sham group and increased noticeably in UUO. Again, as these genes generally remained high in expression in UUO and rUUO in these individual cell populations when sorted, this suggests these expression changes observed in the bulk data were largely due to changes in cell number rather than differential gene expression in cells in response to injury. This highlights the importance of isolating cell populations of interest in the kidney when using *in vivo* models of renal fibrosis, in order to obtain accurate differential gene expression data. This may also be important when carrying out mechanistic investigation of potential therapeutic interventions which may themselves cause alterations in the number of various cell populations in the kidney. This is again compounded by the fact that the different renal cell types have been observed to respond to renal injury in differing and unique ways, activating drastically different (and sometimes opposing) pathways,[83,84,107,115,428] making it of critical importance to understand the cellular source of differential gene expression.

The four cell populations, and the three groups within each cell population appeared to separate well on PCA (Fig 5.3.1) and a number of genes were found to be uniquely expressed at >2 FPKM in each cell type at sham (Fig 5.3.3). Interestingly, less transcriptomic diversity was observed in LTL cells, with 5497 genes >2 FPKM in expression here, compared to an average of 8811 genes >2 FPKM in expression in the other three cell types. F4/80^{hi} macrophages were observed to have the highest percentage of uniquely expressed genes (13.3%), with LTL, CD31 and Pdgfrβ having 9.1%, 5.3% and 9.2% respectively. This introduces a common theme in this dataset

as a whole, with F4/80 seemingly being the most discreet cell population on a number of metrics, which may be unsurprising given these are the only immune cell population being examined.[397,429]

To better categorise the changes in gene expression observed in each cell population in across the sham, UUO and rUUO groups, each gene in each cell population was assigned to one of nine gene sets. One example of a gene set is: genes which significantly increase in expression between sham and UUO, then significantly decreases between UUO and rUUO (UPu_DNr). Nomenclature used is "[X]u_[X]r", with X being either UP (significantly increased), DN (significantly down) or NS (not significantly changed), u = between sham and UUO, and r = between UUO and rUUO.

Using this gene set system, genes which were responsive or unresponsive to injury (UUO), as well as genes which were responsive or unresponsive to reversal of that injury (by 2-weeks post-reversal - rUUO), were identified in each of the four cell populations. Renal injury and reversal resulted in differential gene expression being observable in each of the four cell types. However, the LTL^+ and $Pdgfr\beta^+$ populations were found to contain a much lower number of genes which were unresponsive to either injury or reversal of injury (remained unchanged in expression in each of the three groups (sham/UUO/rUUO), indicating the transcriptome of these cell populations was more responsive to the experimental conditions.

Regulation of gene expression in LTL^+ and $Pdgfr\beta^+$ populations in response to reversal of renal injury also appeared to be more dynamic than in the other populations, with 32.37% (n = 641 genes) and 29.62% (n = 868) of differentially regulated genes (respectively) responding to both 7-day UUO injury and 2-week reversal of that injury (Figs 5.3.6 and 5.3.9). This is in contrast to the $CD31^+$ and $F4/80^{hi}$ populations, with 14.93% (n = 56) and 5.46% (n = 47) of genes with this expression profile observed (Figs 5.3.7 and 5.3.8). Taken together, these data implicate the LTL^+ and $Pdgfr\beta^+$

populations as being the renal cell populations which are most affected by injury and reversal of injury within these experimental conditions.

A small number of reversal-specific genes were detected for each cell type (Fig 5.3.10). These were genes which did not change in expression between sham and UUO, but then significantly increased between UUO and rUUO. Very little overlap in these genes was found between the four cell types, indicating reversal/reparative/regenerative pathways are relatively specific to each cell population. F4/80 and Pdgfrβ had the most reversal-specific genes (62 and 46 respectively), but by percentage of total genes, endothelial cells and F4/80^{hi} macrophages were more enriched for reversal-specific genes.

A separate run of the rUUO model was conducted and the same four cell populations were again sorted out and sent for RNA sequencing, this time for small RNA sequencing to assess miRNA expression (section 5.4). miRNA expression in each cell type was categorised into miRNA sets (analogous to "gene sets" in section 5.3). Interestingly, miRNA expression patterns generally did not closely align with the gene expression patterns. For example, 95.09% of LTL miRNAs were responsive to injury but not reversal of injury (Fig 5.4.2), whereas only 66.42% of genes shared this expression pattern (Fig 5.3.6). A similar trend was observed in the Pdgfrβ^{+} population, with 82.22% of miRNAs being responsive to injury but not reversal (Fig 5.4.5), in comparison to 66.24% of genes (Fig 5.3.9). This suggests the dysregulation of miRNA expression caused by injury to these cell populations is more likely to persist for a longer period of time after the source of the injury is relieved than dysregulated gene expression. As miRNAs have been shown to be regulators and promoters of a variety of pathologies, including fibrosis,[217,221,300,430,431] persistent dysregulation of pathogenic miRNAs despite the removal of the initial source of damage may be function as an inhibitory mechanism in the recovery and return to homeostasis. miR-214-3p is an example of a miRNA with such an expression pattern. Bulk renal cortex sequencing indicates miR-214-3p expression increased significantly in UUO, where it

remained unchanged in rUUO 1, 2, and 4-week groups (Fig 5.2.4). This is also observable in cell populations where miR-214-3p expression increased in UUO (F4/80^{hi} and Pdgfrβ^{+}), with no significant change in expression by rUUO 2-weeks (table 5.4.8). In this way, it may be possible that miR-214-3p is involved in regulating pathways which promote a persistent fibrosis phenotype.

Enrichment of miRNA expression was detected in each cell population using the MGFR R package (Fig 5.4.6). Here, miR-214-3p was found to be enriched in the Pdgfrβ cell population in comparison to the other three populations, indicating this population may be of mechanistic interest in relation to miR-214-3p. miR-214-5p and miR-199-3p/5p (expressed on the same polycistronic transcript) were also found to be enriched here. Differential expression analysis via DESeq2 indicated that miR-214-3p expression was significantly increased in the Pdgfrβ population from sham to UUO, with no significant difference between UUO and rUUO (table 5.4.8). Expression was also significantly increased in the F4/80^{hi} population, although expression was low relative to Pdgfrβ (table 5.4.8). Therefore, the Pdgfrβ gene set DNu_NSr was examined to identify potential miR-214-3p target genes, as these genes were observed to have the opposite pattern of expression to miR-214-3p (table 5.4.13). Here, 6 potential target genes were identified: Qk (Quaking), Sept4 (Septin4), Ppm1a (Protein Phosphatase Magnesium Dependent 1A), Mef2c (Myocyte Enhancer Factor 2C), Rybp (RING1 and YY1 Binding Protein), and Smg7 (SMG7 Nonsense Mediated mRNA Decay Factor).

Of the 6 potential miR-214-3p target genes in the Pdgfrβ population, 2 have previously been described in publications as miR-214-3p target genes: Qk[236,249,251,288] and Mef2c.[251,277,278] Additionally, Smg7 expression has been noted to be responsive to miR-214 in myocytes.[432]

Myofibroblast apoptosis is a critical mechanism for the resolution of the wound healing process.[433] In organ fibrosis, myofibroblast expression is persistent, as they acquire an apoptosis-resistant phenotype.[433] A number of Pdgfrβ potential miR-214-3p target genes have been described as having pro-apoptotic properties; such as Qk,[434] Sept4,[416,435,436] Ppma1,[437–439] Rybp,[440–442] and Smg7.[421,422]

When the expression of 6 potential miR-214-3p target genes was attempted to be validated via qRT-PCR, only 2 (Sept4 and Smg7) successfully validated (were significantly down-regulated from sham to UUO). It is worth noting that the cDNA used here was generated by adding 776 picograms of RNA per reaction and pre-amplified prior to being used for qRT-PCR. Due to low RNA yield, only 560 picograms of RNA from one sample from the Pdgfrβ sham group could be loaded into the reaction. This is quite low input in comparison to the usual 1000 nanograms of RNA that is typically added per cDNA synthesis reaction according to the standard protocol used in our lab.

Sept4 is localised to the mitochondrial outer membrane.[416,435] Pro-apoptotic stimuli trigger its (caspase-independent) release into the cytosol, where it functions as pro-apoptotic factor through the inhibition of XIAP (X-linked inhibitor of apoptosis proteins) which in-turn leads to caspase activation.[416,435] Sept4 release is a very early event in the initiation of the mitochondrial apoptosis pathway, occurring before mitochondrial outer membrane permeability (MOMP) and release of pro-apoptotic mitochondrial factors such as cytochrome C and SMAC/Diablo.[418] Sept4 release initially induces XIAP degradation, which in-turn causes caspase activation to a low and non-lethal extent, thus reducing the threshold for the occurrence of apoptosis.[418] Sustained apoptotic stimuli can then result in increased caspase activity to a level which is sufficient to trigger MOMP, thus initiating the non-reversible amplified phase of apoptosis.[418] Sept4 may also facilitate apoptosis via promoting the interaction between Bcl2 (B cell leukemia/lymphoma 2) and XIAP, thus promoting Bcl2 (a key antiapoptotic factor which inhibits MOMP) down-regulation.[443] These

mechanisms may be of particular relevance to myofibroblasts. Myofibroblasts activated under mechanical stress (such as that which occurs in organ fibrosis), while resistant to apoptosis are also "primed" for responsiveness to apoptotic stimuli via MOMP in the event of a reduction in mechanical stress.[444] In this way, Sept4 inhibition by miR-214-3p may control and inhibit responsiveness to the induction of apoptosis in the myofibroblasts. Sept4 has also been shown to promote TGFβ-induced apoptosis via nuclear translocation in response to TGFβ signalling.[445] As TGFβ is a critical mediator of renal fibrosis and myofibroblast activation,[85,86,112] inhibition of Sept4 by miR-214-3p may reduce TGFβ-mediated apoptotic priming in these cells. Sept4 also regulates apoptosis and self-renewal capacity in intestinal stem cells,[417] hair-follicle stem cells,[419] hematopoietic stem cells,[446] and cancer stem cells.[447] Sept4 knockout mice were found to have drastically improved wound-healing and regenerative capacity.[419] In this way, miR-214-3p may also promote the proliferation and self-renewal capacity of progenitor cell populations in the kidney, thus contributing to the pool of available myofibroblast progenitor cells, such as the Gli1+ perivascular mesenchymal stem cells shown to expand dramatically and contribute ~45% of myofibroblasts in the injured kidney.[119]

Smg7 is an mRNA surveillance factor which is involved in nonsense-mediated mRNA decay (NMD), a process by which mRNA with premature stop codons are degraded.[420,422] Non-NMD functions of Smg7 have also been described, such as the maintenance of telomere integrity in the regulation of the response to DNA damage via regulating p53 protein stability.[422,448] Smg7 expression level has been found to be responsive to miR-214-3p expression in myocytes.[432] Decreased Smg7 has been found to be promote the pathogenesis of systemic lupus erythematosus.[449] Smg7 has been identified as a pro-apoptotic mediator in certain contexts,[421] although the authors suggested regulation of p53 protein stability and cellular localisation to be a potential mechanism through which Smg7 mediates this effect. Smg7 has been found to form a complex with the catalytic subunit of protein phosphatase 2A (PP2Ac).[450,451] PP2A protein has been found to be down-regulated in myofibroblasts cardiac[452] and

lung[453] fibrosis, as well as in scleroderma fibroblasts,[454] thus promoting activation and proliferation of fibroblasts in these contexts. Smg7 expression was significantly reduced from sham to UUO in the Pdgfrβ population via qRT-PCR, as the RNA sequencing data indicated. Smg7 has been hypothesised to have a role in fibroblast activation in renal fibrosis,[455] but this requires further study to validate.

Both Sept4 and Smg7 would need to undergo additional steps to validate miR-214-3p binding, such as the use of 3'UTR luciferase constructs, as at present only a negative correlation with miR-214-3p expression has been observed.

Qk is an RNA-binding protein which has been demonstrated to be a direct miR-214-3p target gene in multiple contexts.[236,249,251,288] miR-214 has been reported to inhibit Qk expression in order to modulate the differentiation of multiple cell types, such as promoting the differentiation of neural progenitor cells in cerebral cortex development,[249] promoting neuronal dendritic morphogenesis,[236] and promoting vascular smooth muscle cell differentiation from embryonic stem cells.[251] However, a role for Qk in the differentiation of fibroblasts, myofibroblasts or pericytes has not been explored in any published literature. Qk has previously been demonstrated to be a master-regulator of circular RNA (circRNA) biogenesis,[456,457] however, circRNA expression unfortunately could not be assessed using the RNA-sequencing data generated due to the poly-A-pulldown method of library generation used. Three protein-coding isoforms of Qk exist,[434] with Qki-7 being found to be a potent inducer of apoptosis in a fibroblast cell line and in primary rat oligodendrocyte cultures.[434]

RSEM, the program used to map the RNA sequencing reads to the mouse (mm10) transcriptome, had assigned the majority of the reads from the Qk gene to a nonsense-mediated decay isoform (average 65.5% ± 1.7 in sham, 80.4% ± 8.4 in UUO) and the remaining reads to Qki-7 (average 34.5% ± 1.7 in sham, 19.6% ± 8.4 in UUO). The Qk Taqman probe used amplified the junction between exons 4 and 5, a junction which is shared between all protein-coding isoforms of Qk and the nonsense-

mediated decay biotype isoform. Therefore, it is unclear as to why Qk expression was not significantly down-regulated from sham to UUO via qRT-PCR (Fig 5.4.14), but was significantly down-regulated in the RNA sequencing dataset. It is possible the fold-change observed via RNA sequencing (-0.44 log2-fold) may have been too modest to be detected as statistically significant via qRT-PCR, especially considering the low-input of RNA in the cDNA reaction.

Mef2c is a transcription factor with a notable role in the development of multiple cell types, including cardiac and skeletal muscle, vascular endothelium, neural crest, lymphocytes, and bone.[458] miR-214-3p has been reported to inhibit Mef2c to inhibit angiotensin-II mediated cardiomyocyte hypertrophy[277] and promote smooth muscle cell phenotype switching in pulmonary arterial hypertension.[278] Overexpression of Mef2c has been demonstrated to promote the reprogramming of fibroblasts into cardiomyocytes (with Gata4 (GATA binding protein 4) and Tbx5 (T-box binding protein 5))[459,460] or smooth muscle cells (with Myocd (myocardin) and Gata6 (GATA binding protein 6)),[461] and therefore Mef2c repression may be important in maintaining fibroblast phenotype. Mef2c has also been proposed to have an inhibitory effect on fibroblast cell cycle progression.[462] Mef2c expression was not found the be significantly reduced from sham to UUO via qRT-PCR (Fig 5.4.15). Variability within groups was again an issue in statistical analysis of Mef2c expression via qRT-PCR. Interestingly, the most dramatic reduction in Mef2c expression occurred in exons 3, 4, 5, and 6, with a much less obvious change in read counts occurring in exons 8-9 (where the Taqman probe was designed to amplify)(Fig 5.4.16). A number of isoforms are produced from the Mef2c gene, with a total of 31 splice variants described in Ensembl. As the exon 8-9 junction is present in only 7 of these isoforms, it is possible the Taqman probe did not amplify the isoforms which were major determinants of the loss of Mef2c expression from sham to UUO in the RNA sequencing data.

Many of the potential miR-214-3p target genes identified in the Pdgfrβ+ population had notable roles in regulating apoptosis and proliferation, therefore, reduced Pdgfrβ expression would be hypothesised to be observed when miR-214-3p is inhibited in the context of renal fibrosis. To explore this hypothesis, samples from the Denby *et al* (2014)[261] study were probed for Pdgfrβ expression. This study was chosen as it demonstrated an 87% reduction in renal fibrosis (UUO) with anti-miR-214 in comparison to control anti-miR. Pdgfrβ expression was found to increase significantly from sham to UUO, with the UUO + anti-miR-214 group having significantly reduced Pdgfrβ expression in comparison to both the UUO and UUO + control anti-miR groups (Fig 5.4.17). This demonstrates anti-miR-214 had a measurable effect on Pdgfrβ expression, which suggests a reduction in the Pdgfrβ$^+$ cell population occurred. However, this does not necessarily mean anti-miR-214 had a direct impact on this population, as, for example, reduced tubular injury with anti-miR-214 may lead to less Pdgfrβ$^+$ cell proliferation.[139] As such, further studies on direct effects of miR-214-3p on renal myofibroblasts (and myofibroblast precursors) are warranted to differentiate between these and secondary effects via interactions with other cell types. This may be of particular relevance to understanding miR-214-3p's deleterious mechanisms in renal fibrosis, as the data generated demonstrates miR-214-3p is highly enriched in the Pdgfrβ$^+$ population in the kidney and a dramatic increase in expression occurs here in response to UUO and IRI-induced renal fibrosis

In contrast to the Denby *et al* (2014) study,[261] Pdgfrβ expression was not significantly increased at 10-weeks post-STNx or altered by anti-miR-214 administration (Fig 5.4.18). This suggests Pdgfrβ$^+$ cell population-dependant pro-fibrotic mechanisms of miR-214-3p were not active in the STNx anti-miR-214 study. In contrast to the STNx anti-miR-214 study, Pdgfrβ expression was found to be significantly increased from sham to STNx in the STNx characterisation study presented in chapter 3 (5.4.19), suggesting the lack of Pdgfrβ expression increase is not common to the STNx model in general. Increased Pdgfrβ expression at the mRNA and protein levels has previously

been described to be a feature of traditional subtotal nephrectomy methods in rats.[463]

miR-214-3p cell-population-specific regulation was also examined in another model of renal fibrosis, 18-minute unilateral ischemia reperfusion injury (IRI)(Figs 5.4.9 to 5.4.12). This was carried out to ensure the patterns of miR-214-3p differential expression in each cell type were not unique to UUO, and therefore were associated with the renal fibrosis phenotype in general. Results obtained in the IRI study LTL population diverge from what was observed in the rUUO study LTL population. No significant changes in miR-214-3p expression occurred in the rUUO study, while a significant increase was detected in the IRI study at 2 and 21-days post-IRI, but not at 7-days post-IRI. This suggests increased miR-214-3p expression initially occurs in the LTL population as an acute response to IRI, returning to baseline expression by 7-days post-injury, but then expression increases again by 21-days post-injury in response to progressive renal injury. Acute miR-214-3p up-regulation in response to IRI-induced hypoxia has previously been suggested to be protective against tubular epithelial cell apoptosis,[266] similarly to the protective effects of miR-214-3p against ischemic/hypoxic cardiac injury,[255,464,465] ischemic/hypoxic myoblast injury,[244] and in a hypoxic model of pulmonary arterial hypertension.[466] This is in contrast to the deleterious and pro-fibrotic properties of miR-214-3p noted with chronic expression in the kidney in renal fibrosis.[246,261] A proximal tubular cell-specific deleterious mechanism has also been described for miR-214-3p in renal fibrosis and CKD models.[267] Together, these data suggest that the regulation of miR-214-3p in response to acute vs chronic renal injury may be associated with predominantly protective or deleterious mechanisms respectively in the proximal tubular epithelial cells. miR-214-3p was not found to be differentially regulated at 7-days post-UUO in the data generated (1.33 log2-fold-change, 0.09 adjusted-p-value), however, the study may have been under-powered to detect this. miR-214-3p expression detected in the IRI F4/80^{hi} and Pdgfrβ^{+} populations more closely matches the differential regulation observed in response to UUO. Similarly to the enrichment analysis carried

out in the rUUO data (Fig 5.4.6), miR-214-3p expression was found to be significantly higher in IRI in the Pdgfrβ^{+} population compared to LTL^{+} and F4/80^{hi} (Fig 5.4.12). This further suggests the Pdgfrβ^{+} population as a site of potential mechanistic interest for miR-214-3p in renal fibrosis.

Conclusion:

The importance of isolating renal cell populations of interest over analysing gene expression on the whole renal cortex level was discussed, with examples provided to demonstrate the differing patterns of differential gene expression obtained from single populations vs whole kidney cortex. The four cell populations sorted from whole kidney cortex were found to be discrete populations, as evidenced by principle component analysis and the unique gene expression patterns at sham and during injury reversal observed in each. miR-214-3p was found to be significantly up-regulated from sham to UUO in F4/80^{hi} macrophages and Pdgfrβ^{+} cells, with expression being enriched in Pdgfrβ^{+} cells at sham, UUO and rUUO. This was confirmed using an IRI model of renal fibrosis, suggesting the regulation of miR-214-3p in these cell types is associated with the fibrosis phenotype in general rather than UUO specifically. Therefore, the Pdgfrβ^{+} cell population was selected as the most promising site of mechanistic interest for miR-214-3p in renal fibrosis. Bioinformatic analysis revealed several predicted miR-214-3p target genes, the differential expression of which are the inverse of miR-214-3p. Literature search revealed many of these genes were found to be pro-apoptotic and/or anti-proliferative. Pdgfrβ expression was assessed in two prior studies in which anti-miR-214 was administered in the context of renal fibrosis and potential implications for this on anti-miR-214 efficacy highlighted.

Chapter Six

General Discussion

6.1: STNx as a model of chronic kidney disease

Subtotal nephrectomy is a longstanding *in vivo* model of CKD, with a history of successful translation of results to clinical practice.[102,177,188–191] Historically most commonly performed on rats, but more recently adapted for use in mice,[177,180,181] subtotal nephrectomy produces a CKD phenotype over the course of several weeks.[181] This allows the measurement of a wide variety of clinically-relevant parameters, such as renal fibrosis, serum and urine markers of renal dysfunction, as well as hypertension and cardiac dysfunction.[186,467,468] Therefore, subtotal nephrectomy can be a powerful platform for the preclinical investigation of candidate therapeutic interventions in CKD. However, subtotal nephrectomy comes with considerable downsides in comparison to other models of renal fibrosis or CKD, in relation to animal welfare, the lengthy duration of studies and time spent performing surgery.

Traditionally, subtotal nephrectomy was performed as two separate surgeries, with surgery on each kidney taking place 1-2 weeks apart.[81,177] STNx, initially characterised in chapter 3, was developed to mitigate these downsides. The main adaptation STNx made to traditional methods was that it was carried out in a single surgical procedure, thus eliminating the need for multiple surgical procedures to be carried out on each mouse. Therefore, the hypothesis was STNx allows for *in vivo* modelling of CKD in a single-surgery with improved animal welfare. STNx was characterised in chapter 3 before being used as a platform to investigate miR-214 as a therapeutic target in CKD in chapter 4.

Mortality rates associated with the use of traditional subtotal nephrectomy methods in mice are substantial, with reports as high 43%[196] and >50%[326] in published literature. Aside from animal welfare concerns, a high mortality rate necessitates more animals be subjected to the procedure to achieve results which are of adequate statistical power. UK legislation pertaining to the use of animals for scientific research

requires both animal use and suffering be minimised, adhering to 3Rs guidelines.[469] The 3Rs are Replacement (to use non-*in-vivo* research methods), Reduction (to minimise the number of animals used), and Refinement (to minimise animal suffering and improve welfare).

Across the two STNx studies which took place in a mouse strain which was sensitive to developing CKD in response to renal mass reduction (129S2/SV), presented in chapters 3 and 4, positive outcomes in terms of animal welfare were well-supported. Animal welfare and body condition scoring sheets were used to monitor animal welfare throughout the studies, as well as animal weight being recorded on a weekly basis. No significant difference in bodyweight was detected between sham and STNx groups at any timepoint post-surgery. As bodyweight is an important indicator of overall health in mice, this was a positive outcome in terms of animal welfare.[311] This result is in contrast to many traditional subtotal nephrectomy method mouse studies, where reduced bodyweight was observed in comparison to sham,[194,320,470] suggesting STNx is associated with better animal welfare in comparison to traditional methods.

In chapter 3, a mortality rate of 7.69% was observed in mice subjected to STNx, while 6.25% was observed in chapter 4. Therefore, a total mortality rate of 6.67% was observed after a total of 45 surgeries carried out across two independent studies. This mortality rate allowed for a lower number of animals to be subjected to STNx in order to achieve adequate statistical power at the end of the study to assess key endpoints such as renal fibrosis. STNx surgical methods detailed in this thesis have been demonstrated to be associated with a reduced mortality rate compared to traditional methods, thus fulfilling the "Reduction" and "Refinement" arms of the 3Rs guidelines.

Cardiac hypertrophy is the most commonly diagnosed cardiovascular abnormality in CKD patients, as well as being the strongest independent predictor of cardiovascular disease-related mortality in this patient population.[68–73] Cardiac structure and

function were investigated in the STNx model in this thesis, with evidence of cardiac hypertrophy in the results as detailed in Chapter 3, and further dissected through the use of echocardiography at both 6 and 10-weeks post-surgery in Chapter 4. Here, cardiac hypertrophy was evident at 10-weeks, but not 6-weeks, post-STNx, without cardiac function (ejection fraction) being affected. Hypertension was also observed at 10-weeks post-STNx. Heart weight (normalised to tibia length) at sacrifice was very consistent between the two studies (0.091 in chapter 3 vs 0.092 in chapter 4). These results indicate cardiac hypertrophy to be a clear feature of STNx by 10-weeks post-surgery, but a longer time-course may be required to observe cardiac functional abnormalities. Therefore, STNx models this important aspect of CKD, providing a platform for its investigation and preclinical evaluation of novel therapeutics.

Renal fibrosis (determined histologically) is a key indicator of CKD severity and prognosis.[80] Increased fibrosis was observed histologically in both chapter 3 and 4 studies to a similar degree. The data obtained from the two STNx model runs was may suggest less myofibroblast activation was observed in the chapter 4 study than the chapter 3 study. When Pdgfrβ expression was assessed in chapter 5, expression was found to be significantly increased in STNx in the chapter 3 study but not in the chapter 4 study. Pdgfrβ functions as a myofibroblast marker due to it being expressed on all myofibroblasts, although it is also expressed on a variety of other cell types.[372,398] The lack of Pdgfrβ and Acta2 expression increase in the chapter 4 study, as well as lower magnitude of collagen gene expression increases, together suggest a less myofibroblast activation took place in the chapter 4 study. Interestingly, this correlated with a lower magnitude miR-214-3p expression increase in the chapter 4 study (3.58-fold in chapter 3 vs 2.2-fold in chapter 4).

Reproducibility of results obtained in subtotal nephrectomy is a notable drawback to the model.[177] However, for most of the parameters measured in both of these studies, including urinary ACR, the results are quite similar between the chapter 3 and chapter 4 studies. The portion of total renal mass removed in the two studies is also similar,

but slightly more renal mass was removed in the chapter 3 study (68% ± 1.8 SEM) than the chapter 4 study (64.1% ± 1.7 SEM). It may be possible that this difference may have resulted in a less-severe phenotype in the chapter 4 study, although this difference was not statistically significant via an unpaired, two-tailed t-test ($p = 0.14$). For future studies using the STNx model, it may be prudent to ensure the portion of the total renal mass removed is closer to the 68% mark, and that this remain as consistent as possible between all the animals to reduce variability of results observed within a group. However, as mentioned, some variability of results is an issue inherent to the subtotal nephrectomy model, regardless of the method used to induce it, and relatively speaking, the results aside from renal molecular markers of fibrosis suggest STNx is overall quite a consistent iteration of subtotal nephrectomy.

Therefore, the adaptions made to traditional subtotal nephrectomy methods in STNx allowed for the induction of subtotal nephrectomy-mediated modelling of chronic kidney disease, in a single-surgery with reduced mortality rate. This allowed for saving time and costs associated with surgery, reducing the total amount of time the mice spent on-procedure, and through reduced mortality rate, reduced the number of animals required to undergo surgery to supply sufficient statistical power.

6.2: miR-214-3p inhibition as a therapeutic intervention in CKD

miR-214 inhibition has been demonstrated to have a significant anti-fibrotic effect in the kidneys of mice subjected to UUO, with an 87% reduction in fibrosis in animals administered anti-miR-214 in comparison to control anti-miR.[261] However, due to the limitations of the UUO model used, clinically-relevant correlates of renal function, as well as cardiorenal effects, could not be assessed. The hypothesis was anti-miR-214 is an effective therapeutic in CKD. To investigate this hypothesis, an anti-miR-214 oligonucleotide compound was administered in the STNx model (detailed in chapter 4). The STNx model was used as it permits the measurement of clinically-relevant markers of renal function, produces renal fibrosis and cardiovascular dysfunction, as well as subtotal nephrectomy methods having a history of successful translation of results to clinical practice. The chronic nature of the STNx model also allowed the potential to initiate administration the anti-miR-214 compound at a stage where some renal fibrosis and dysfunction were already present, as well as when miR-214 expression had already increased in response to renal injury.

Prior to initiation of STNx studies, the anti-miR-214 and control anti-miR oligonucleotide compounds provided by Regulus Therapeutics were investigated *in vitro* to uncover details such as capacity for binding miR-214-3p and efficacy in reducing pro-fibrotic gene expression. A dose-response curve for miR-214-3p inhibition was uncovered for anti-miR-214, while control anti-miR did not appear to inhibit miR-214-3p, suggesting both the active compound and control were suitable for use in further studies. Next, an *in vitro* model of renal fibrosis was produced by stimulating a rat renal fibroblast cell line (NRK49F) with TGFβ1. Here, anti-miR-214, but not control anti-miR, appeared to ameliorate the pro-fibrotic gene expression induced in this cell line by TGFβ, thus suggesting anti-miR-214 could inhibit miR-214-3p expression to an extent that produced an anti-fibrotic effect under these conditions. Therefore, the compounds were deemed suitable to progress to *in vivo* study.

One aim of the STNx anti-miR-214 study was to exploit the chronic nature of the STNx model and administer the compound as a therapeutic intervention at a timepoint when some renal dysfunction and fibrosis were already present in the kidney. This was to allow a more realistic modelling of the clinical scenario where an anti-miR-214-based therapeutic would be deployed, as CKD is typically only diagnosed when a significant decline in renal function and renal fibrosis are already present. 6-weeks post-surgery was investigated and deemed to be a suitable timepoint for intervention, as increased total collagen (via histology), urinary ACR, and miR-214-3p expression were all found to be increased here. From this timepoint, mice were dosed twice per week (subcutaneous, 25 mg/kg) until sacrifice at 10-weeks post-surgery.

A large number of parameters were measured, such as urinary ACR at 6 and 10-weeks post-surgery; echocardiography at 6 and 10-weeks post-surgery; serum creatinine, urea and phosphate at 10-weeks; total collagen expression (histology) in the kidney and heart at 10-weeks; pro-fibrotic gene and miR-214-3p expression in the kidney and heart at 10-weeks; blood pressure at 10-weeks; and heart weight at 10-weeks. Disappointingly, anti-miR-214 did not significantly ameliorate the CKD phenotype induced by STNx in almost all the measured parameters, including renal fibrosis. miR-214-3p expression was found to be significantly reduced in the kidney and heart tissue in the anti-miR-214 group. In contrast to the STNx + PBS and STNx + control anti-miR groups, a significant increase in ACRs from 6 to 10-weeks post-surgery was not observed in the STNx + anti-miR-214 group, which may be indicative that miR-214 inhibition inhibits the progressive decline in renal function caused by STNx.

Given the dramatic reduction in renal fibrosis observed with anti-miR-214 inhibition in the UUO model, the lack of efficacy in STNx was surprising and, of course, begs the question of why. There are a number of potential contributing factors at play here, such as differences between the UUO and STNx model, the timing of the initiation of anti-miR-214 intervention, the possibility of anti-miR-214 not reaching the

appropriate cellular compartments, and a potential lack of sufficient myofibroblast activation in that particular run of the STNx model.

Differences in model aetiology is arguably the more straightforward explanation for why anti-miR-214 was such an effective anti-fibrotic in the UUO model but not in the STNx model. The process by which each of these models result in activation of the "final common pathway" of renal fibrosis is actually quite different.

In UUO, the primary injury is to the proximal tubular epithelial cells (PTECs), which occurs through an initial substantial increase in intratubular pressure,[168] followed by hypoxia due to decreased renal blood flow and capillary rarefaction (which is associated with endothelial cell activation).[168,169] These factors triggers PTECS to undergo apoptosis or de-differentiate and arrest in the G2/M phase of the cell cycle, acquiring a secretory phenotype.[146,160] These injured PTECs and endothelial cells secrete a variety of inflammatory and pro-fibrotic factors, resulting in macrophage infiltration and increased myofibroblast accumulation in the tubulointerstitial space, resulting in renal fibrosis.[160,168] The UUO is quite a fast-paced model, with significant renal fibrosis being present by 7-days post-surgery.

In contrast to UUO, progressive renal injury in the STNx model (or any model driven by a significant reduction in renal mass/nephron number) likely stems from the glomerulus. Here, the significant decline in nephron number elicits a compensatory response from the remaining nephrons, in an effort to maintain overall GFR. Increased intraglomerular hypertension (and nephron hypertrophy) result in a hyperfiltrative phenotype, dramatically increasing single-nephron GFR.[183,185] However, over time, intraglomerular hypertension becomes one of the main pathogenic triggers in this model,[183] as the glomerular injury is transferred to the tubulointerstitium through a number of potential mechanisms. Over time, this results in tubular degeneration, inducing local inflammation with macrophage infiltration and the appearance of collagen-producing myofibroblasts.[183] Increased "leakiness"

of the glomerular basement membrane to proteins (such as albumin) can amplify these processes by triggering PTEC dysfunction in response to increased reabsorption of these filtered proteins.[185] Therefore, it may be possible that miR-214-3p was involved in promoting pro-fibrotic processes which were more (or only) relevant in UUO.

The timepoint post-surgery chosen to initiate anti-miR-214 inhibition may have also been a contributing factor to lack of efficacy observed. The biggest challenge in evaluating this issue is the fact that a study was not carried out with anti-miR-214 being administered from before the surgery was carried out. Therefore, it is difficult to discern if the lack of efficacy is due to the timepoint when administration was initiated or other factors, such as if anti-miR-214 has efficacy in the model in general. Although renal fibrosis (via histology) appeared to be somewhat increased in the 6-week STNx study in chapter 4, this was not significantly different at 10-weeks ($p = 0.3$ via unpaired, two-tailed t-test). Therefore, in order for anti-miR-214 to have demonstrated efficacy here, it would have had to induce a reduction in fibrosis within the ~4-weeks it was being administered, which may have been a high bar to set. However, collagen gene expression was not significantly increased at 6-weeks, but was significantly increased at 10-weeks, and anti-miR-214 did not affect this increase, thus raising questions of efficacy in affecting fibrosis in this model.

The only parameter which seemed to be impacted by anti-miR-214 (aside from miR-214-3p expression) was that ACR increase between 6 and 10-weeks was not observed in animals administered anti-miR-214, in comparison to the significant increase in the STNx + PBS and STNx + control anti-miR groups during this timeframe. This suggests anti-miR-214 may have halted the progression of renal dysfunction in these animals. Albuminuria in the STNx model is linked to glomerular dysfunction and leakiness of the glomerular basement membrane, processes upstream of the tubular degeneration and tubulointerstitial fibrosis which occur in this model. Therefore, it may be possible that earlier intervention with anti-miR-214 may have been more

efficacious, as at an earlier stage less tubular degeneration may have occurred. As such, preventing or inhibiting further tubular degeneration at an earlier timepoint may have been able to have a larger impact on the overall phenotype induced by the model. Similarly, allowing the model to run longer than 10-weeks (with anti-miR-214 administration beginning at 6-weeks) may enhance the ability to assess the long-term impact of miR-214 inhibition in an already compromised kidney, thus allowing to assessment of inhibition of renal injury progression as a potential mechanism.

In terms of evaluating the potential for clinical deployment, the potential for adverse-effects is an important consideration. In fact, for miR-214 inhibition in CKD, the potential for side-effects may be particularly serious in relation to the cardiovascular system. miR-214 has been shown to both promote and inhibit cardiac fibrosis in animal models.[272] Cardiac fibrosis was assessed in the STNx anti-miR-214 study and was found to not be significantly different in the anti-miR-214 group to the control anti-miR or PBS groups. However, 3 out of the 11 animals in the anti-miR-214 group were found to have a very high fibrosis score. It may be a coincidence that STNx animals which happened to develop a high amount of cardiac fibrosis occurred more frequently in the anti-miR-214 group (compared 1 in the control anti-miR group). It may also form a trend which this study was under-powered statistically to detect, and/or suggest animals in the anti-miR-214 group may be more prone to develop cardiac fibrosis if allowed to stay on-procedure for longer than 10-weeks.

miR-214 has also been reported to have contrasting roles in cardiac hypertrophy, either promoting or inhibiting it depending on the model used.[272–276] miR-214 expression is reduced in the hearts of patients with cardiac hypertrophy.[272,277] Given that cardiac hypertrophy is the most commonly diagnosed cardiac condition in CKD patients and is the strongest independent predictor of adverse cardiovascular events,[68–73] it may be crucial for the long-term safety of CKD patients that miR-214 inhibition does not promote further cardiac hypertrophy. As no significant impact of anti-miR-214 on cardiac weight was detected in STNx, this is somewhat reassuring

for the prospect of future administration to CKD patients. However, as STNx may not model the exact pathophysiology which underlies cardiac hypertrophy in all CKD patients, notably, for example, in patients who have CKD secondarily to cardiovascular disease, these results may not be representative of the CKD cohort overall. Regular assessment of cardiovascular structure and function would be required in the early clinical trial phases to monitor for potential adverse cardiovascular side-effects.

Insights derived from RNA sequencing in the kidney (chapter 5) provide additional information about miR-214 in the context of renal fibrosis. Initially, bulk renal cortex small RNA sequencing revealed miR-214-3p is up-regulated significantly in 7-day UUO, consistent with previous reports.[261,303] miR-214-3p expression was then unaffected by reversal of the UUO injury and did not significantly decrease at 1, 2 or 4-weeks post-reversal. The observation that miR-214-3p remains elevated in the repairing kidney is interesting, possibly resulting in persistent repression of genes or pathways which initially functioned to promote fibrosis despite the overall renal phenotype observed during that time being regenerative. This suggests miR-214-3p may act to counteract the regenerative processes in the kidney and promote renal fibrosis or other pathological processes long-term. Therefore, inhibition of miR-214-3p may provide a break in the promotion of these pathological processes, which may be relevant in clinical CKD.

The rUUO model was then used again, with four renal cell populations with central roles in renal fibrosis isolated using FACS and RNA sequencing for gene and miRNA expression carried out. These were: LTL^{+} proximal tubular epithelial cells (PTECs), $CD31^{+}$ endothelial cells, $F4/80^{hi}$ macrophages, and $Pdgfr\beta^{+}$ (fibroblast-like) cells. This data may aid the investigation of cell population-specific miR-214-3p pro-fibrotic pathways.

As the kidney is home to highly-specialised cell populations, each of the four cell populations isolated may have genes and miRNAs which are enriched (high-expression) in one of these populations compared to the others. Cell population-enriched genes were identified for each cell population in the uninjured (sham) kidney group. These were genes which were highly expressed in one of the cell populations (based on expression observed in sham only), while being lowly expressed in the other three cell populations. A strong and clearly observable trend for these genes to remain static (high) in expression in the UUO and rUUO groups of their enriched cell population was present. These cell population-specific enriched genes were then identified in the bulk renal cortex sequencing gene expression data, where, in contrast to the sorted cell population data, dramatic changes in expression of these genes occurred from sham to UUO. LTL enriched genes were highly expressed in the sham group of the bulk sequencing data, with a large drop in expression occurring in the UUO group. CD31, F4/80 and Pdgfrβ-enriched genes were lowly expressed in the sham group of the bulk sequencing data, with a clear increase in expression occurring in the UUO group. As the PTECs constitute a large portion of the renal cortex, it appears their apoptosis caused by UUO results in highly expressed PTEC genes to be detected as significantly down-regulated. However, the expression of these genes actually remains unchanged in the PTECs themselves. The change in PTEC cell number also appears to have a large influence on the other three cell populations assessed, with significant increases in the expression of their enriched genes being detectable in the bulk renal cortex from sham to UUO, while the expression of these genes actually remains stable in the individual cell populations.

These data demonstrate the potential pitfalls in generating accurate differential gene expression data from bulk kidney cortex in the UUO model, thus highlighting the importance of investigating individual cell populations. This also has interesting implications for situations where a therapeutic intervention may inhibit PTEC apoptosis and inhibit myofibroblast or macrophage accumulation, as this data

suggests it can be difficult to decipher changes in cell number vs true differential gene expression from bulk kidney cortex.

For each cell population, each differentially regulated gene was assigned into one of eight gene sets based on the pattern of differential expression observed within that cell population. This process was then repeated for miRNA expression data.

Cell population-specific analysis then significant increases in miR-214-3p expression in F4/80^{hi} macrophages and Pdgfrβ^{+} cells from sham to UUO, but not in CD31^{+} endothelial cells or LTL^{+} proximal tubular epithelial cells, although the study was likely underpowered to detect increased miR-214-3p expression in the LTL^{+} population. The Pdgfrβ^{+} population was found to be significantly enriched for miR-214-3p expression in sham, UUO and rUUO groups. Although miR-214-3p expression was significantly increased in F4/80^{hi} macrophages, overall expression level detected was relatively low.

miR-214-3p expression was then assessed in LTL^{+}, F4/80^{hi}, and Pdgfrβ^{+} cells FACS-isolated from renal cortex at 2, 7, and 21-days post-18-minute unilateral IRI. This was carried out to ensure differential miR-214-3p regulation in these cell types was associated with renal fibrosis in general, as opposed to being a UUO-specific anomaly. Here, miR-214-3p expression was found to significantly increase at 7 and 21-days post-IRI in the F4/80^{hi} and Pdgfrβ^{+} populations, thus confirming the differential regulation observed in UUO. Interestingly, miR-214-3p was significantly up-regulated at 2 and 21-days post-IRI in the LTL^{+} population, but not at 7-days, indicating a biphasic response to acute vs chronic injury here. Compared to LTL^{+}, the population with the lowest miR-214-3p expression at most timepoints, expression in the Pdgfrβ^{+} population was observed to be increased by between 100 to 3435-fold. miR-214-3p expression in the F4/80^{hi} population was only found to be significantly higher than LTL^{+} at one timepoint (7-days post-IRI).

Due to the enrichment of miR-214-3p expression in the Pdgfrβ^{+} population in two *in vivo* models of renal fibrosis, as well as large increases in miR-214-3p expression in this population in injury, further mechanistic investigation was focused on this population.

Genes which were found to have the opposite pattern of regulation to that of miR-214-3p in the Pdgfrβ^{+} population were screened for miR-214-3p binding sites. After genes predicted to be miR-214-3p targets by >4 databases and lowly expressed genes were excluded, a literature search was conducted to identify potential mechanisms these genes may be involved in in the Pdgfrβ^{+} population in UUO. Two genes (Qk[236,249] and Mef2c[277,278]) were found to be validated miR-214-3p target genes in biological contexts other than renal injury. Qk,[434] Sept4,[416,435,436] Ppma1,[437–439] Rybp,[440–442] and Smg7[421,422] were found to have pro-apoptotic properties. However, when the expression of these genes was assessed via qRT-PCR in matched samples to those sent for RNA sequencing, only Sept4 and Smg7 were found to be significantly down-regulated from sham to UUO in the Pdgfrβ^{+} population.

The data generated in the rUUO and IRI models clearly suggests Pdgfrβ^{+} to be a site of potential mechanistic interest for miR-214-3p, as expression is significantly enriched in this population. Early-stage investigation of potential target genes here suggests inhibition of apoptosis to be a potential mechanism. To assess this hypothesis, Pdgfrβ expression was assessed via qRT-PCR in RNA from the UUO anti-miR-214 study published by Denby *et al* (2014)[261] and was found to increase 13.4-fold (from sham) in UUO, with anti-miR-214 significantly reducing this expression in comparison to both UUO and UUO + control anti-miR groups. However, as myofibroblast accumulation occurs in response to renal injury, notably PTEC injury,[115] the reduction in Pdgfrβ expression may indicate anti-miR-214 inhibited renal injury rather than reduced myofibroblast cell number through, for example, promoting apoptosis or reducing proliferation in these cell types directly. Further study would certainly be required to differentiate if this was a direct or indirect effect, or to

determine the relative contribution of direct and indirect effects here. Regardless, this suggests a reduction in myofibroblast number was associated with the anti-fibrotic effect of anti-miR-214 in UUO.

This may have implications for why the anti-miR-214 in the STNx intervention study did not demonstrate efficacy. When Pdgfrβ expression was assessed in the STNx anti-miR-214 study, no significant increase was observed in STNx in comparison to sham, with anti-miR-214 also having no influence on expression. Acta2 (α-SMA), a myofibroblast marker,[333,471,472] was also not found to increase from sham to STNx in this study, with anti-miR-214 not having a significant impact on expression. These data suggest that significant myofibroblast accumulation did not occur by 10-weeks post-STNx, which in-turn indicates that any pro-fibrotic mechanism of miR-214-3p related to myofibroblast accumulation was not active in this study. Therefore, the inhibition pro-fibrotic pathways by anti-miR-214 which occurred in the UUO study may not have been possible in the STNx study, as they may not have been activated by the STNx model to a detectable extent. However, lack of activation of these pathways did not appear to be common feature of STNx, as Acta2 and Pdgfrβ were found to be significantly increased at 10-weeks post-STNx in the chapter 3 study (as well as larger increases in collagen gene and miR-214-3p expression). Increased Acta2 and Pdgfrβ have long been noted as features of subtotal nephrectomy in rats.[463] Therefore, for future STNx experiments involving anti-miR-214, it would be important to ensure at least 68% of the total renal mass is removed during each surgery (as was carried out in the chapter 3 study), as this appears to be the optimal amount of renal mass to remove. Alternatively, if the study were allowed to continue for a longer period of time, these Pdgfrβ-dependant pro-fibrotic pathways may have been active.

Despite the enrichment for miR-214-3p expression in the Pdgfrβ^{+} population, the PTECs cannot be ignored as a potentially important (or even primary) site where miR-214 promotes renal fibrosis. As detailed by Bai *et al* (2019),[267] miR-214 is enriched in the mitochondria of PTECs, where its expression increases in response a range of pro-

fibrotic stimuli, including TGFβ1, albumin, and hypoxia. It was proposed that miR-214-3p promotes tubular mitochondrial dysfunction and apoptosis. The authors also showed that PTEC-specific conditional knockout of miR-214 resulted in dramatically lower renal fibrosis in the UUO and IRI models, with lower tubular injury, tubular apoptosis, and pro-inflammatory cytokine production. A comparison between the reduction in renal fibrosis observed in UUO in tubular-specific miR-214 knockout vs global miR-214 knockout would have been interesting, as it would allow an assessment of the contribution of miR-214-3p in the PTECs vs other renal cell populations to renal fibrosis overall.

PTEC injury and tubular apoptosis are thought to precede the accumulation of myofibroblasts in both the UUO[146,160,168,169] and STNx models.[183,185,463] Therefore, PTEC-specific mechanisms could potentially be sufficient to explain the anti-fibrotic efficacy and reduction in Pdgfrβ expression in the anti-miR-214 in the Denby *et al* (2014) study. PTEC-specific mechanisms may also underlie or contribute to the lack of efficacy observed in the STNx anti-miR-214 study, if tubular damage was insufficient to cause a large accumulation of myofibroblasts.

6.3: Future directions

In evaluating the future of anti-miR-214 as a therapeutic in CKD, further anti-miR-214 intervention studies in the STNx model may prove useful. Prior to such studies taking place, it may be prudent to first carry out optimisation studies to determine the appropriate dose of anti-miR-214 compound to be administered in the STNx model, as well as ensuring the anti-miR compound is successfully delivered to the appropriate cell types (particularly PTECs and fibroblasts) in STNx. As this process was not carried out prior to the STNx anti-miR-214 study detailed in this thesis, questions of whether anti-miR-214 was delivered to the appropriate cell types in sufficient concentrations remain unanswered.

Building on observations from the previous STNx anti-miR-214 study, initiating the administration of anti-miR-214 before the STNx surgery takes place would first allow a baseline assessment of the potential efficacy of anti-miR-214 in this model. After this is established (assuming positive results in relation to renal fibrosis and/or function are obtained), anti-miR-214 intervention studies could take place. These would stand to assess the potential for anti-miR-214 to ameliorate the STNx-induced CKD phenotype (in terms of renal fibrosis, renal function, or cardiac parameters) when administered after these are already present. As intervention in CKD typically is only initiated after significant renal impairment already exists, these intervention studies may prove to be insightful in evaluating the potential of anti-miR-214 for future clinical deployment.

Longer-term STNx studies may also be useful. All deaths which occurred animals subjected to STNx occurred within the first 3 weeks, an effect which has been noted with traditional subtotal nephrectomy methods in mice up to 13-weeks post-surgery.[326] Little to no decrease in welfare as measured by the animal welfare and body condition scoring methods detailed in this thesis was typically recorded by 10-weeks post-surgery. Together, these indicate longer STNx studies are likely to be possible without significant mortality occurring. Longer studies may enhance our ability to detect the impact of chronic anti-miR-214 administration. This would allow studies such as initiation of anti-miR-214 administration in later-stage STNx with severe fibrosis and renal dysfunction, or enhance our ability to assess the potential cardiac side-effects of long-term anti-miR-214 administration in CKD.

Conclusion:

A single-surgery, mouse subtotal nephrectomy model (STNx) was characterised in terms of animal welfare, renal fibrosis, renal functional parameters and cardiovascular parameters. The STNx model was found to recapitulate many features of CKD observed in the clinic, such as increased urinary ACR; increased serum creatinine, urea, and phosphate; renal fibrosis; cardiac hypertrophy; and hypertension. The STNx model was then used to assess the potential efficacy of anti-miR-214 when administered in situation where renal fibrosis and dysfunction were already present. Anti-miR-214 was not found to be efficacious in ameliorating the CKD phenotype induced by STNx, despite inhibiting the expression of miR-214-3p, with the exception of halting ACR increase between 6 and 10-weeks post-surgery. Multiple potential contributing factors to this lack of efficacy were discussed, such as the timepoint where anti-miR-214 administration was initiated and the activation of cell population-specific mechanisms by STNx. The rUUO model was used to assess cell population-specific miR-214-3p expression and potential mechanisms. Pdgfrβ^+ cells were identified to be the primary population of mechanistic interest for miR-214-3p, as expression was highly enriched here and increased dramatically with renal injury. Potential miR-214-3p target genes in this population were identified, with potential roles in regulating apoptosis in the Pdgfrβ^+ population hypothesised.

Appendix 1

Origional research article:

Front. Physiol., 15 November 2019 | https://doi.org/10.3389/fphys.2019.01365

Refining the Mouse Subtotal Nephrectomy in Male 129S2/SV Mice for Consistent Modeling of Progressive Kidney Disease With Renal Inflammation and Cardiac Dysfunction.

James O'Sullivan[1], Sarah Louise Finnie[1], Oliver Teenan[1], Carolynn Cairns[1], Andrew Boyd[1], Matthew A. Bailey[1], Adrian Thomson, Jeremy Hughes[2], Cécile Bénézech[1], Bryan Ronald Conway[1] and Laura Denby[1]

[1]Centre for Cardiovascular Science, Queen's Medical Research Centre, The University of Edinburgh, Edinburgh, United Kingdom

[2]Centre for Inflammation, Queen's Medical Research Centre, The University of Edinburgh, Edinburgh, United Kingdom

Abstract:

Chronic kidney disease (CKD) is prevalent worldwide and is associated with significant co-morbidities including cardiovascular disease (CVD). Traditionally, the subtotal nephrectomy (remnant kidney) experimental model has been performed in rats to model progressive renal disease. The model experimentally mimics CKD by reducing nephron number, resulting in renal insufficiency. Presently, there is a lack of translation of pre-clinical findings into successful clinical results. The pre-clinical nephrology field would benefit from reproducible progressive renal disease models in mice in order to avail of more widely available transgenics and experimental tools to dissect mechanisms of disease. Here we evaluate if a simplified single step subtotal nephrectomy (STNx) model performed in the 129S2/SV mouse can recapitulate the renal and cardiac changes observed in patients with CKD in a reproducible and robust way. The single step STNx surgery was well-tolerated and resulted in clinically

relevant outcomes including hypertension, increased urinary albumin:creatinine ratio, and significantly increased serum creatinine, phosphate and urea. STNx mice developed significant left ventricular hypertrophy without reduced ejection fraction or cardiac fibrosis. Analysis of intra-renal inflammation revealed persistent recruitment of Ly6C^{hi} monocytes transitioning to pro-fibrotic inflammatory macrophages in STNx kidneys. Unlike 129S2/SV mice, C57BL/6 mice exhibited renal fibrosis without proteinuria, renal dysfunction, or cardiac pathology. Therefore, the 129S2/SV genetic background is susceptible to induction of progressive proteinuric renal disease and cardiac hypertrophy using our refined, single-step flank STNx method. This reproducible model could be used to study the systemic pathophysiological changes induced by CKD in the kidney and the heart, intra-renal inflammation and for testing new therapies for CKD.

Introduction:

Chronic kidney disease (CKD) is increasing in prevalence (Eckardt et al., 2013) and is a significant public health problem due to its associated economic burden (Kerr et al., 2012). Multiple clinical etiologies result in CKD with hypertension and diabetes being the leading causes (Horowitz et al., 2015; Alicic et al., 2017; Obrador and Levin, 2019). CKD progression is staged via estimated glomerular filtration rate (eGFR) and urinary albumin-creatinine ratio (ACR) (Stevens and Levin, 2013). Patients with CKD are at increased risk of cardiovascular disease (CVD) and this risk increases as renal function declines. Once patients reach end-stage kidney disease (ESKD) requiring dialysis or transplantation, the risk of CVD is 10–30x that of the general population with cardiovascular events accounting for almost 50% of deaths in CKD patients (Di et al., 2015).

The common end-pathway of progressive CKD is the deposition of fibrotic scar tissue that replaces the functional renal parenchyma in the form of tubulointerstitial fibrosis and glomerulosclerosis. The underlying mechanisms of fibrosis remain incompletely understood as it is a complex process involving a diverse array of cell types and molecular pathways, with cross-talk between cell types being evident

(Gewin et al., 2017). These cell types include fibroblasts, tubular epithelial cells, macrophages, endothelial cells, dendritic cells, and lymphocytes (Boor et al., 2010). For example, fibroblasts differentiate into myofibroblasts, proliferate, and deposit extracellular matrix components (Mack and Yanagita, 2015). The sources of myofibroblasts within the injured kidney have been the subject of intense study, perivascular Gli^{+} progenitor cells have been suggested to be particularly important (Kramann et al., 2015). Another notable feature of CKD is tubular atrophy and loss of tubular epithelial cells (Venkatachalam et al., 2015; Schelling, 2016; Webster et al., 2017). The renal tubule has long been thought of as a target of renal injury, however it may also function as a propagator of injury as tubular cells may undergo cell-cycle arrest, de-differentiation, and acquire a pro-secretory phenotype (Gewin, 2018). Cytokines secreted by tubular cells may act as paracrine factors to promote the production of collagenous matrix by surrounding myofibroblasts (Gewin, 2018).

Subtotal nephrectomy, or 5/6 nephrectomy, is used as a rodent model of progressive CKD (Yang et al., 2010). Historically, the subtotal nephrectomy model was performed in rats, although it has more recently been conducted in mice (Ma and Fogo, 2003; Kennedy et al., 2008; Siedlecki et al., 2009; Yang et al., 2010; Gava et al., 2012; Oosterhuis et al., 2017). The effectiveness of STNx to produce experimental-CKD in mice has been found to vary depending on the strain of mouse used (Leelahavanichkul et al., 2010), with C57BL/6 mice being more resistant (Kren and Hostetter, 1999; Ma and Fogo, 2003; Leelahavanichkul et al., 2010) and SV129/CD1 mice being permissive (Ma and Fogo, 2003; Kennedy et al., 2008; Siedlecki et al., 2009; Leelahavanichkul et al., 2010). However, the results in mice have been inconsistent and there is a lack of technical information about how the model was performed, any power calculation data, mortality rates, information on post-surgery animal welfare and whether the ARRIVE guidelines were followed. This lack of standardization in the model in mice likely contributes to the inconsistencies reported (Chatzimanouil et al., 2018).

We sought with this paper to standardize the STNx model in mice, to improve animal welfare standards and define the renal and cardiac effects to enable consistent modeling of the pathophysiological changes induced during progressive CKD

Materials and Methods:

Single Step Flank Subtotal Nephrectomy Model

The refined STNx model involves a single anesthetic and surgery (~40 min), performed via flank incisions that result in improved animal condition scores, reduced mortality with reproducible outcomes between studies.

Male 129S2/SV mice were obtained from Envigo and used when 6–8 weeks old (weighing 24.7 ± 0.37 g SEM). Male Gli1 × Ai14 mice on a C57BL/6 genetic background were used at 9 ± 3 weeks old (weighing 31.9 ± 1.1 g SEM). Mice were group-housed and provided with *ad lib* access to water and fed with Rm1 standard chow (Special Diets Services) with the following content 0.25% Na, 0.67% K, 0.38% Cl. Mice were also given environmental enrichment. A 12-h light–dark cycle was maintained. During the study, mice were weighed weekly and had their condition recorded. ARRIVE guidelines were adhered to at all times. Only male mice were selected as unlike in other organs, notable sex difference in myeloid cells, including macrophages have been documented in the kidney (Bain et al., 2016).

Animals were randomized to receive sham or subtotal nephrectomy surgery (STNx) using a random number generator website[1]. Prior to surgery, mice had a timed overnight urine sample collected (single housed metabolic cage), blood sample taken (superficial vein) and blood pressure measured (tail cuff). Immediately prior to surgery, mice were weighed and a total of four studies including two pilot studies were performed.

Surgery was performed in a sterile surgical environment using inhalational isoflurane for anesthesia. Once anesthetised, the mouse was shaved and received perioperative s.c. analgesia.

The mouse was initially placed on the left lateral side and an incision was made on the flank over the right kidney. The right kidney was located and carefully maneuvred

out of the incision site. The adrenal gland was carefully blunt dissected away from the kidney to avoid adrenalectomy. The right renal pedicle was clamped and a nephrectomy performed. The vascular clamp was removed, the renal bed checked for signs of bleeding and the abdominal wall sutured closed and skin clips applied to close the outer skin incision.

The left kidney was then located and adrenal gland blunt-dissected away. The renal artery and vein were isolated and clamped ensuring ischemic time was less than 5 min. Renal poles (approximately 2/3 renal mass) were then surgically removed and spongostan applied. The vascular clamp was released and once hemostasis had been achieved, the kidney was placed back into the abdomen and the incisions closed. For sham surgery, animals were prepared the same way, had bilateral flank incisions and both kidneys isolated and manipulated.

At the end of surgery, mice were immediately placed in a fresh cage with littermates in a hotbox at 28°C, where they remained for 7 days. During this time, the mice were checked three times daily and scored using bespoke animal condition scoring sheets (Supplementary Table 1). After this time the mice were weighed, skin clips removed and placed in a regular animal holding room and maintained under normal conditions.

For quality control purposes, the weight of kidney removed was calculated to estimate how much residual kidney was left (with the caveat that the kidneys have a small mismatch in weights). The weight of the whole right kidney was measured and compared to the weight of the two pole sections of kidney removed from the left kidney. In order to maintain consistency in this model we ensured that the percentage remaining was as consistent as possible. Residual kidney mass was calculated by the following:

$$\% \text{ left renal mass remaining} = 100 - [(\text{left kidney sections weight}/\text{whole right kidney weight}) * 100]$$

Animals were schedule 1 culled in compliance with United Kingdom Home Office regulations. Upon confirmation of death, blood was obtained via cardiac puncture and the animal perfused with PBS and tibia length recorded. For isolation of serum, blood was allowed to clot and spun down at 3000G for 20 min at 4°C. Organs were

removed and weighed, prior to being cut into predefined sections with sections for RNA and protein snap frozen in liquid nitrogen, while those for histology were placed in 10% formalin for 24-h, before embedding in paraffin to produce FFPE sections. For flow cytometry studies kidney portions were collected in PBS on ice prior to processing.

Histology

Three µM thick FFPE sections were cut and deparaffinized prior to staining with picrosirius red in accordance with manufacturer's guidelines (Abcam, ab150681). Slides were imaged using ZEISS Axio Scan.Z1 Slide Scanner. Quantification of images was carried out using Image-Pro Premier 9.2.

RNA Extraction, Gene and miRNA Expression

Tissue was homogenized using Qiagen TissueLyser II. RNA was extracted from homogenized tissue with the RNeasy Mini Kit (Qiagen 74106) and RNA yields were quantified using NanoDrop 1000 (Thermo Fisher). Reverse transcription was carried out using high-capacity cDNA synthesis kit (Applied Biosystems, 4368814). Quantitative real-time PCR (qRT-PCR) was carried out using specific Taqman gene probes (Table 1).

Gene	Probe/assay ID
Col1a1	Mm00801666_g1
Col3a1	Mm01254476_m1
Col4a1	Mm01210125_m1
Acta2	Mm00725412_s1
Mmp2	Mm00439498_m1
Tgfb1	Mm01178820_m1
Il1b	Mm00434228_m1
Tnf	Mm00443258_m1
Ppia	Mm02342430_g1
Nppa	Mm01255747_g1
Nppb	Mm01255770_g1
Gapdh	Mm99999915_g1
miR-21-5p	000397
miR-214-3p	002306
u6	001973

Table 1. Taqman gene and miRNA expression assays used for qRT-PCR in these studies.

Renal Function Analysis

Timed overnight collections of urine (18 h) were performed at baseline, 6-weeks post-STNx and 10-weeks post-STNx from mice housed singly in metabolic cages. Blood was collected at baseline and at termination. Urine and serum were stored at −20°C prior to analysis by an in-house biochemical analysis service[2].

Mouse urine albumin measurements were determined using a commercial Microalbumin Kit (DiaSys Diagnostics Systems, Germany) adapted for use on a Cobas Mira analyzer (Roche Diagnostics, Ltd., Welwyn Garden City, United Kingdom). The immunoturbidimetric assay was standardized against purified mouse albumin standards (Sigma Chemical, Co., Poole, United Kingdom) with samples diluted in phosphate buffer saline as appropriate. Within run precision was CV < 5% while intra-batch precision was CV < 7.1%.

Urine ion concentration was determined using ion-selective electrodes using the SPOTCHEM™ E-Plate with the SPOTCHEM™ EL Analyzer. Urine osmolality was measured by freezing-point depression on a Micro-Digital i-Osmometer (Type 16M, CamLab, United Kingdom).

Echocardiography for Cardiac Structure and Function

Echocardiography was carried out by University of Edinburgh pre-clinical imaging facility under isoflurane anesthesia at 6 and 10-weeks post-surgery as previously published (Respress and Wehrens, 2010; Gao et al., 2011; Lindsey et al., 2018). A parasternal long-axis view of the heart was used to obtain EKV (ECG-gated Kilohertz Visualization) over one cardiac cycle. Spectral Doppler was carried out in parasternal short-axis view and used to assess mitral valve and blood-flow. Doppler sample volume was placed across the mitral valve for measurement of E (early) and A (late, atrial) wave velocity. Doppler sample volume was placed at mid-left ventricular level to measure isovolumic relaxation (IV RT).

Blood-Pressure Analysis

Systolic blood-pressure was measured via a non-invasive tail-cuff method in a customized machine (Wang et al., 2017). Mice were trained prior to the start of the study. The mice were placed in a hot-box at 32°C for 5–10 min prior to blood-pressure measurement.

Flow Cytometry

Tissue was placed in gentleMACS™ C Tubes with digestion buffer (Collagenase Type II 0.425 mg/mL, Collagenase D 0.625 mg/mL, Dispase 1 mg/mL and DNAse 30 µg/mL) and dissociated using the gentleMACS™ Dissociator. Cellular suspensions were digested at 37°C for 30 min then gentleMACS™ dissociated for a second time. The cellular suspensions were then put through 100, 70, and 40 µM sieves sequentially and red blood lysis performed with Red Blood Cell Lysing Buffer (Sigma). The concentration of the resultant single cell suspension was determined using a cell counter and cells dispensed into 96-well round-bottom plate and incubated with appropriate rat anti-mouse antibodies (Table 2). Unstained samples, compensation beads for each antibody, FMO samples and cell suspensions were run on the six laser LSR Fortessa cell analyzer (BD Biosciences) using DAPI to determine live cells. Data was analyzed using FlowJo software.

Antibody	Clone/flurochrome/final concentration
Live	DAPI/1:1000
CD45	30-F11/APC or BV650/1:100
F4/80	BM8/Pe-Cy7/1:200
MHCII	M5/114.15.2/APC-Cy7/1:400
Ly6G	1A8/e450/1:200
Ly6C	HK1.4/AF700/1:200
CD11b	M1_70/PE Dazzle/1:1000
CD11c	N418/BV605/1:100
CD206	MR5D3/APC/1:200

Table 2. Antibodies utilized in flow cytometry.

Statistical Analysis

A pilot study was performed using Col1a1 gene expression as the outcome measure. Power calculations derived from the pilot study determined that *n* = 9 mice in each group were required to ensure sufficient power (95%) to detect a 30% difference of in Col1a1 expression at a 5% level of significance. To account for mortality at 9% (combined anesthetic and model mortality), *n* = 10 mice/group was employed. For C57BL/6 study the results are from a pilot study performed on group size *n* = 6.

All data was assessed for normal distribution using the D'Agostino-Pearson normality test. Comparisons between two, normally-distributed, data points were carried out via Student's *t*-test. Comparisons between two unpaired, non-normally distributed data points were carried out via Mann–Whitney test. All data generated was subjected to Grubbs outlier test, outliers were removed from analysis. ACR at 6 and 10-weeks post-surgery (Figure 1D) was assessed for statistical significance via two-way ANOVA for repeat measures with Sidak's multiple comparison test. Gene and miRNA expression at 6 and 10-weeks post-surgery (Figures 2D,E) were compared via ordinary two-way ANOVA with Tukey's multiple comparison test.

Results:

Effect of One-Step Flank STNx on Renal Function

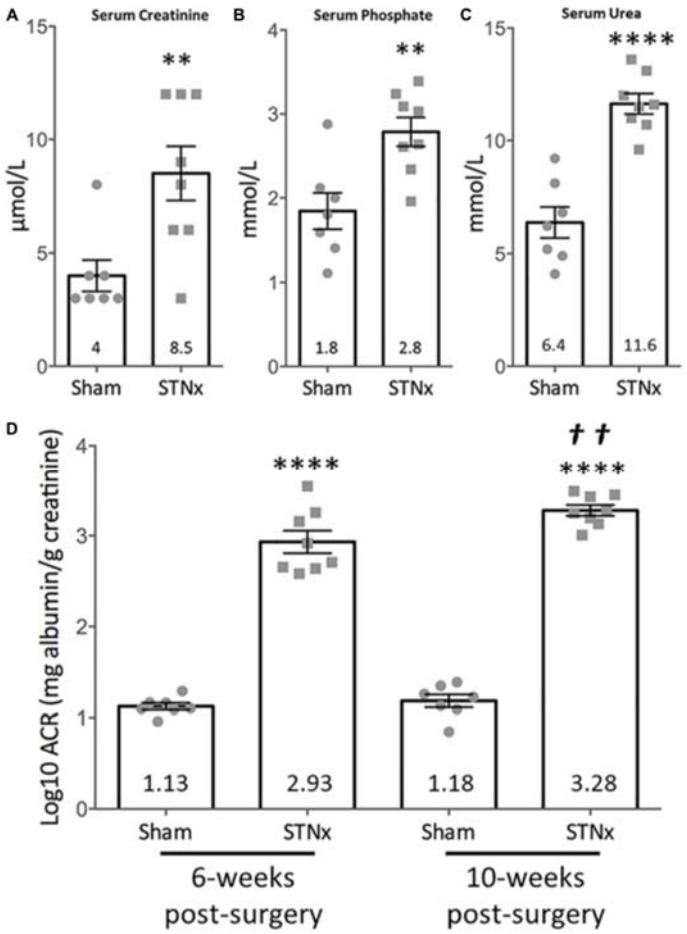

Figure 1. Effect of single-step subtotal nephrectomy on renal function. 129S2/SV mice were subjected to flank single-step STNx or sham surgery and were culled 10-weeks post-surgery. Urine and blood at 10-weeks post-STNx or sham surgery was analyzed for renal function parameters. **(A)** Serum creatinine, **(B)** phosphate, **(C)** urea. Sham: n = 7, STNx: n = 8. Student's t-test was used for statistical analysis. $^{**}P \leq 0.01$, $^{****}P \leq 0.0001$. Plotted as mean ± SEM. **(D)** Urinary albumin:creatinine ratios (log10) were calculated from timed overnight (18 h) collections from animals 6 and 10-weeks post-surgery. Sham: n = 7, STNx: n = 8. All comparisons made via two-way ANOVA for repeat measures, with Sidak's multiple comparisons test. $^{****}P \leq 0.0001$ vs. sham (of same timepoint), $^{††}P \leq 0.01$ vs. STNx 6-week. Plotted as mean ± SEM.

We utilized initially male 129S2/SV mice because they have been shown to be sensitive to developing renal dysfunction in previous studies. Following our refined single step flank subtotal nephrectomy (STNx) procedure there was no significant difference in body weight between the sham and STNx animals during the 10-week study run (Supplementary Figure 1A). The use of a single surgery procedure was well-tolerated. In total across four studies (pilot and full studies), 53 male 129S2/SV mice aged 7–10 weeks (weights 24.7 ± 0.37 g SEM) and 10 male Gli1 × Ai14 mice on a C57BL/6 genetic background aged 9 ± 3 weeks (weights 31.9 ± 1.1 g SEM) were subjected to STNx or sham surgery. There was an overall model failure rate of 9% (5% mortality, 2% anesthetic death, and 2% early termination rate due to deteriorating animal body condition scoring). Group housing the mice post-surgery resulted in improved animal condition scores and faster recovery compared to single housing (Supplementary Figure 1B). Animal stress peaked day 3 post-surgery as assessed by body condition score for single and grouped house, which may suggest analgesia up to day 2 post-surgery may be warranted (Supplementary Figure 1B). Across the studies the mean percentage of residual left kidney mass was 32.9 ± 0.98% SEM (Supplementary Figure 1C).

Initially we examined the effect of the STNx performed on 129S2/SV male mice on renal excretory function and proteinuria as patients with CKD have increased serum creatinine (Jha et al., 2013; Levey et al., 2014; Hill et al., 2016), urea (Jörres et al., 2004; Almeras and Argilés, 2009; Lau and Vaziri, 2016; Vanholder et al., 2018), and phosphate (Martin and González, 2011; Felsenfeld et al., 2015; Ritter and Slatopolsky, 2016; Vervloet et al., 2017) levels as well as proteinuria. Biochemical analysis of blood samples from mice 10-weeks post-STNx consistently revealed significant increases in serum creatinine (9.29 vs. 4 µmol/l) (Figure 1A), phosphate (2.74 vs. 1.84 mmol/L) (Figure 1B) and urea (11.62 vs. 6.35 mmol/L) (Figure 1C) compared to sham operated mice indicating a reduction of renal excretion. Total urinary albumin excretion was significantly increased 123-fold in STNx mice compared to controls (Table 3). STNx mice had a significant increase in urinary albumin:creatinine ratio (ACR) at 6 and 10-weeks post-surgery, with ACR significantly increasing from 6 to 10-weeks post-

surgery indicating progressive proteinuria (Figure 1D). Renal sodium excretion was not significantly different between STNx and sham operated mice at both 6-weeks (174 ± 24 vs. 121 ± 26 µmol/18 h) and 10-weeks (167 ± 20 vs. 132 ± 24 µmol/18 h; Table 3). Chloride excretion was also not different between groups at 6-weeks (372 ± 38 vs. 290 ± 61 µmol/18 h) and 10-weeks (255 ± 21 vs. 271 ± 25 µmol/18 h; Table 3). Potassium excretion was significantly different between groups, reflecting an increase in excretion in STNX mice at 6-weeks (380 ± 32 vs. 260 ± 45 µmol/18 h, P = 0.019); potassium excretion was not different between groups at 10-weeks (234 ± 15 vs. 218 ± 28 µmol/18 h; Table 3). Urine osmolarity was also measured with no significant difference at 6-weeks between sham and STNx groups (1272.7 vs. 1157.5 mOsm) but by 10-weeks post-STNx there was significantly lower osmolarity compared with sham animals (Table 3).

Urine parameters	Sham (10-weeks)	STNx (10-weeks)
Na excretion	131.94 ± 24 µM/18 h	166.77 ± 20 µM/18 h
K excretion	271.78 ± 28 µM/18 h	164.45 ± 21 µM/18 h
Cl excretion	270.84 ± 25 µM/18 h	225.75 ± 11 µM/18 h
Total albumin	3.39 ± 0.48 µg/18 h	418.16 ± 89 µg/18 h ***
Osmolality	1347 ± 89 mOsm	914.5 ± 63 mOsm ***

*Ion excretion, total albumin and osmolality was measured in 18 h-timed urine collection from mice 10-weeks post-surgery or age-matched sham mice. ***$P < 0.001$ unpaired t-test.*

Table 3. Urine parameters measured in male 129S2/SV mice 10-weeks post-STNx.

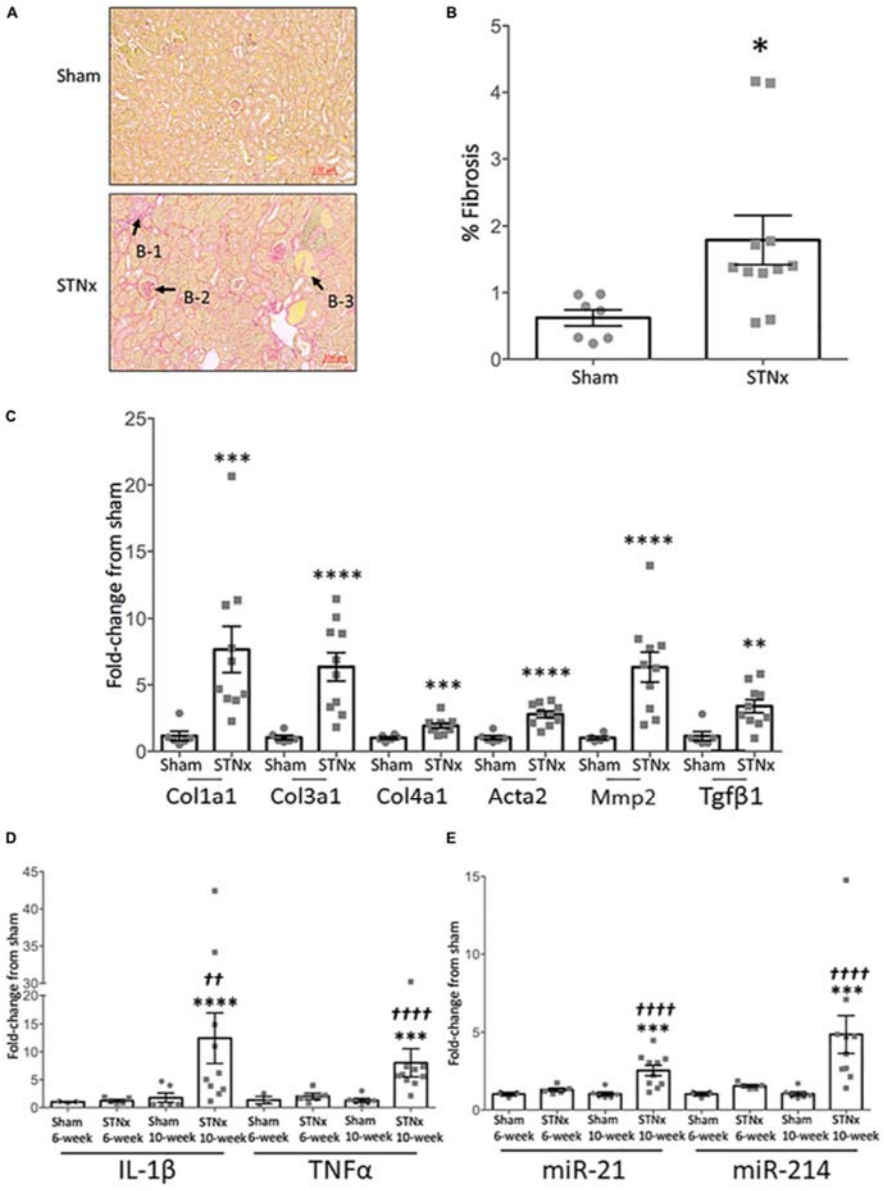

Figure 2. Single-step subtotal nephrectomy induces significant renal fibrosis. 129S2/SV mice were subjected to flank single-step STNx or sham surgery and were culled 10-weeks post-surgery. At sacrifice kidney sections were snap frozen for RNA analysis and to prepare FFPE 3 µM sections. **(A)** Picrosirius red staining for total collagen in kidneys. Exemplar images are provided at 5x magnification, scale bar 100 µM. B-1 = Tubulointerstitial fibrosis, B-2 = glomerulosclerosis, B-3 = tubular dilation. **(B)** Quantification of fibrosis (% PSR staining). Sham: *n* = 7, STNx: *n* = 11. Student's *t*-test was used for statistical analysis. $^{*}P < 0.05$. Plotted as mean ± SEM. **(C)** Pro-fibrotic gene expression in whole kidney tissue was determined by quantitative real-time PCR (qRT-PCR) carried out with specific Taqman probes for

each gene, normalized to housekeeper Ppia. Sham: *n* = 6, STNx: *n* = 10. Col1a1 was found to have non-parametric distribution, therefore Mann–Whitney test was used, Student's *t*-test was used for other genes. $^{****}P < 0.0001$, $^{***}P < 0.001$, $^{**}P < 0.01$. Plotted as RQ mean ± SEM. **(D)** Inflammatory gene expression in whole kidney tissue at 6 and 10-weeks post-surgery was determined by quantitative real-time PCR (qRT-PCR) carried out with specific Taqman probes for each gene, normalized to housekeeper Ppia. Sham 6-week: *n* = 3, STNx 6-week: *n* = 5, Sham 10-week: *n* = 6, STNx 10-week: *n* = 10. All comparisons made via an ordinary two-way ANOVA with Tukey's multiple comparisons test. $^{***}P < 0.001$ vs. sham (of same timepoint), $^{****}P < 0.0001$ vs. sham (of same timepoint), $^{††}P < 0.01$ vs. STNx 6-week, † † $^{††}P < 0.0001$ vs. STNx 6-week. Plotted as mean ± SEM. **(E)** Renal fibrosis-associated miRNA expression in whole kidney tissue at 6 and 10-weeks post-surgery was determined by quantitative real-time PCR (qRT-PCR) carried out with specific Taqman probes for each miRNA, normalized to housekeeper U6. Sham 6-week: *n* = 3, STNx 6-week: *n* = 5, Sham 10-week: *n* = 6, STNx 10-week: *n* = 10. All comparisons made via an ordinary two-way ANOVA with Tukey's multiple comparisons test. $^{***}P < 0.001$ vs. sham (of same timepoint), † † †† $P < 0.0001$ vs. STNx 6-week. Plotted as mean ± SEM.

Renal fibrosis remains one of the best histological markers of progressive kidney disease (Ito et al., 2004; Hewitson, 2009; Hewitson et al., 2017). At 10-weeks post-STNx, renal fibrosis as measured by picrosirius red staining was increased 3.4-fold (increasing from 0.62 ± 0.12% in sham kidneys to 2.11 ± 0.37% in STNx kidneys) (Figures 2A,B). Evidence of tubulointerstitial fibrosis and glomerulosclerosis was observed along with tubular dilation (Figure 2A). 6-weeks post-STNx surgery, when ACR was already increased, there were no significant pro-fibrotic gene expression changes (Supplementary Figure 2). However, by 10-weeks post-STNx surgery, gene expression analysis revealed significant increases in the expression of pro-fibrotic genes (*Col1a1, Col3a1, Col4a1, Acta2, Mmp2, Tgf*β*1*) (Figure 2C). When gene expression of pro-inflammatory genes (*Il1*β and *Tnf*α) were examined there was no difference in expression compared to sham animals at 6 weeks but a significant

increase from 6 to 10-weeks post-STNx (Figure 2D). We have previously reported that miR-21 and miR-214 are consistently elevated in the kidney following injury (Denby et al., 2011), however, these miRs have not been assessed in progressive renal dysfunction induced by STNx in 129S2/SV mice. We found that the pro-fibrotic miRNA miR-214-3p (Denby et al., 2014; Bai et al., 2019) was significantly upregulated 6-weeks post-STNx surgery (Figure 2E), prior to pro-fibrotic gene expression changes, with no change in the pro-fibrotic miRNA miR-21-5p expression (Denby et al., 2011; Chau et al., 2012; Gomez et al., 2015; Hennino et al., 2016). At 10-weeks post-STNx surgery, miR-21-5p was significantly upregulated 2.4-fold and miR-214-3p remained significantly elevated with a 3.5-fold higher expression compared to sham kidneys (Figure 2E). Significant increases in miR-214-3p and miR-21-5p expression were detected in the kidneys of STNx group animals between the 6 and 10-week post-surgery timepoints (Figure 2E).

Effect of One-Step Flank STNx on Intra-Renal Inflammation

As we observed an increase in pro-inflammatory gene expression markers 10-weeks post-STNx, we sought to further characterize the nature of the inflammatory cells in kidneys from mice that underwent STNx. Analysis by flow cytometry (gating strategy provided in Supplementary Figure 3A) revealed that at 10-weeks post-STNx there was a significant increase in the proportion of cells in the kidney that expressed $CD45^+$ compared to sham kidneys (2.23% STNx vs. 0.96% Sham, Figures 3A,B and Supplementary Figure 3B). Similarly, a significant increase in $CD45^+$ cells was also observed in the hearts of animals subjected to STNx (Supplementary Figure 3C). Further analysis of the $CD45^+$ population in the kidney revealed no significant difference in the proportion of $CD45^+$ inflammatory cells constituted by neutrophils (7.9% STNx vs. 4.5% Sham; Figure 3C), $CD11b^+$ $F4/80^{lo}$ macrophages (monocyte derived), or $CD11b^+$ $F4/80^{hi}$ macrophages (resident population) (Figures 3D,E). However, further subset analysis of the $CD11b^+$ $F4/80^{lo}$ population revealed a clear waterfall effect in the STNx kidneys with $Ly6C^{hi}$ monocytes transitioning to $Ly6C^{lo}$ $MHCII^+$ macrophages, an effect which was absent in the sham kidney (Figure

3F). Furthermore, the percentage of CD45^{+} CD11b^{+} F4/80^{lo} Ly6C^{hi} cells was significantly increased in the STNx kidneys (Figure 3G). Analysis of the CD11b^{+} F4/80^{hi} resident macrophages population revealed that there was significantly increased expression of CD206 in these resident macrophages in the STNx kidneys (Figure 3H).

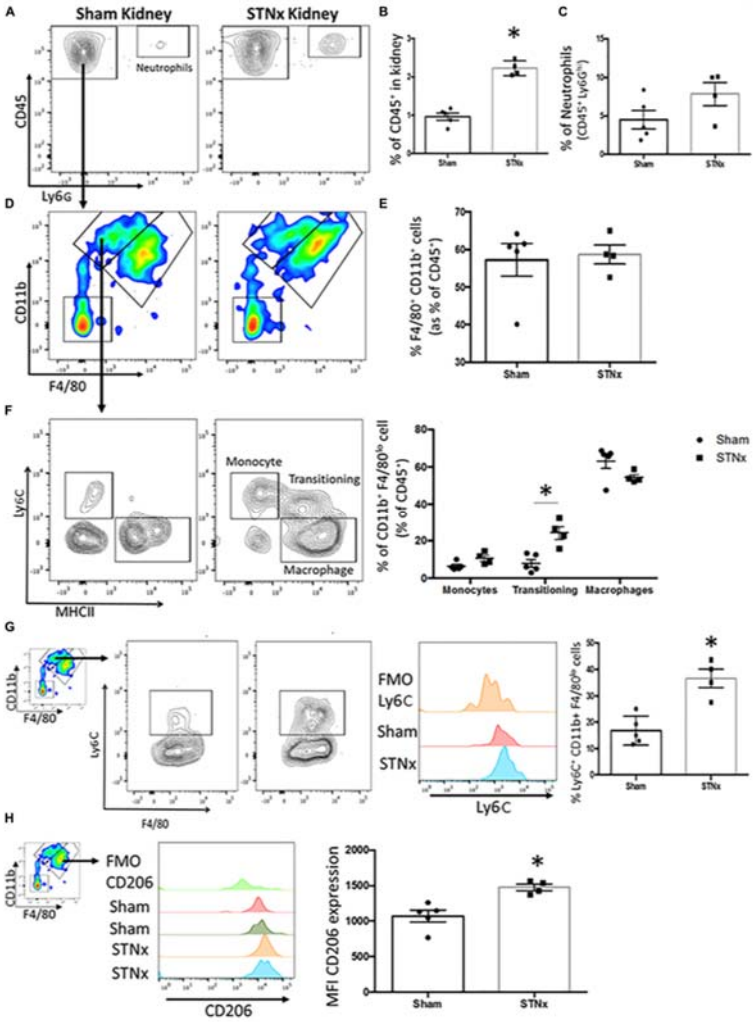

Figure 3. Analysis of inflammatory infiltrate in the STNx kidney. 129S2/SV mice were subjected to flank single-step STNx or sham surgery and were culled 10-weeks post-surgery. At sacrifice *n* = 5 Sham and *n* = 4 STNx kidneys were perfused and kidneys digested for flow cytometry and analyzed on the 6L Fortessa Flow Analyzer. **(A)** Plot of CD45^{+} cells and neutrophils (CD45 + Ly6G^{hi}) in kidney. **(B)** Quantification of the percentage of total cells that express CD45^{+} in the kidney. **(C)** Quantification of Neutrophils (CD45^{+} Ly6G^{hi}) in the kidney. **(D)** Analysis of

$CD45^+$ $Ly6G^-$ $CD11b^+$ $F4/80^+$ population in the kidney. **(E)** Quantification of $CD45^+$ $Ly6G^-$ $CD11b^+$ $F4/80^+$ population in the kidney. **(F)** Subset analysis and quantification of $CD45^+$ $Ly6G^-$ $CD11b^+$ $F4/80^{lo}$ population into monocytes ($Ly6C^{hi}$ $MHCII^-$), transitioning monocyte-macrophages and macrophages ($Ly6C^-$ $MHCII^+$). **(G)** Expression and quantification of the proportion of $CD45^+$ $Ly6G^-$ $CD11b^+$ $F4/80^{lo}$ that express Ly6C. **(H)** Analysis and quantification of CD206 expression in the resident macrophage population $CD45^+$ $Ly6G^-$ $CD11b^+$ $F4/80^{hi}$. $N = 5$ Sham $N = 4$ STNx statistical analysis by Mann–Whitney test $^*P < 0.05$.

Effect of One-Step Flank STNx on Vascular and Cardiac Parameters

We next determined the effect of the STNx surgery on vascular and cardiac function in the 129S2/SV mice we had measured renal excretory function and proteinuria. We determined systolic blood pressure using tail vein plethysmograph in trained conscious mice at baseline, at 6-weeks post-surgery and at study end. The mean systolic blood pressure at 6-weeks was not significantly different in STNx mice compared with sham animals, but was significantly increased from 115 ± 2.6 mmHg in sham animals to 153.1 ± 4.6 mmHg in STNx animals 10-weeks post-STNx surgery (Figure 4A). The STNx mice also had significantly increased heart mass compared to sham animals at 10-weeks post-STNx surgery (Figure 4B). Therefore, we sought to determine the effects of the progressive loss of renal function induced by our one-step STNx surgery in the 129S2/SV mice on cardiac function as measured by echocardiography (ECHO) carried out at baseline, 6- and 10-weeks post-surgery (Figure 4C and Table 4). No significant differences in percentage ejection fraction were detected, although there was a trend for a reduction 10-weeks post-STNx. At 6-weeks, changes were detected in % fractional area change (FAC) and area change, indicating that adaption had begun to occur at this point (Table 4), but no statistical difference was detected in heart weight (data not shown). By 10-weeks, STNx animals had increased cardiac wall thickness (0.88 ± 0.02 to 1.05 ± 0.04 mm) and left-ventricle mass (182.7 ± 9.06 to 234.6 ± 17.75 mm) compared with sham animals (Table 4),

which mirrored the increased heart weights measured at 10-weeks post-STNx (Figure 4B). Doppler imaging performed on the mitral valve revealed a significantly increased left ventricle isovolumetric relaxation time (IV RT) at 10-weeks post-STNx, but not 6-weeks post-STNx, suggesting STNx induced renal dysfunction may lead to diastolic dysfunction over time (Lindsey et al., 2018; Schnelle et al., 2018). As ECHO analysis suggested cardiac hypertrophy and diastolic dysfunction had occurred, cardiac fibrosis was assessed histologically. At 10-weeks post-STNx there was no significant increase in total collagen deposition in the heart (Figures 4D,E). At 6-weeks post-STNx, no change in expression for fibrillar collagen genes *Col1a1* and *Col3a1* was observed (Figure 4F), however *Col3a1* expression was significantly increased at 10-weeks compared with sham animals (Figure 4G). There was significantly higher expression of the cardiac hypertrophy markers ANP (Nppa) and BNP (Nppb) in the STNx compared with sham animals at 6-weeks with ANP remaining increased a 10-weeks (Figures 4F,G).

	6-weeks post-surgery		10-weeks post-surgery	
	Sham	**STNx**	**Sham**	**STNx**
EKV:	*n* = 8	*n* = 10	*n* = 8	*n* = 10
Ejection fraction (%)	59.1 ± 1.5	48.8 ± 4.4	54.4 ± 4	45.9 ± 2.8
Fractional area change (%)	40.5 ± 0.8	32.2 ± 3.3 *	37.2 ± 3.2	29.8 ± 2.3
Area change (mm^2)	9.21 ± 0.8	7.21 ± 0.64 *	8.73 ± 0.86	6.91 ± 0.34 †
Cardiac wall thickness (mm)	0.92 ± 0.03	1.02 ± 0.04	0.88 ± 0.02	1.04 ± 0.04 ††
LV mass (mg)	189.1 ± 10.7	215.8 ± 16.3	182.7 ± 9.1	234.6 ± 17.7 †
Mitral valve spectral doppler:	*n* = 8	*n* = 9	*n* = 8	*n* = 9
E wave (mm/s)	770 ± 27.4	650 ± 41.7*	747 ± 25.6	663 ± 38.9
A wave (mm/s)	457 ± 24.5	479 ± 44.3	443 ± 39.9	471 ± 45.5
LV IV RT	24.5 ± 1.24	28.2 ± 1.75	24.1 ± 0.82	28.6 ± 1.38 †

*Echocardiography measurements were obtained under isoflurane anesthesia at 6 and 10-week post-STNx or sham surgery. Sham: n = 8, STNx: n = 10. Student's t-test was used for statistical analysis of difference between sham and STNx groups at 6 or 10-weeks post-surgery. *P ≤ 0.05 at 6-weeks vs. sham. †P ≤ 0.05, ††P ≤ 0.01 at 10-weeks vs. sham.*

Table 4. Cardiac echocardiography measurements in STNX and Sham animals at 6 and 10-weeks post-surgery.

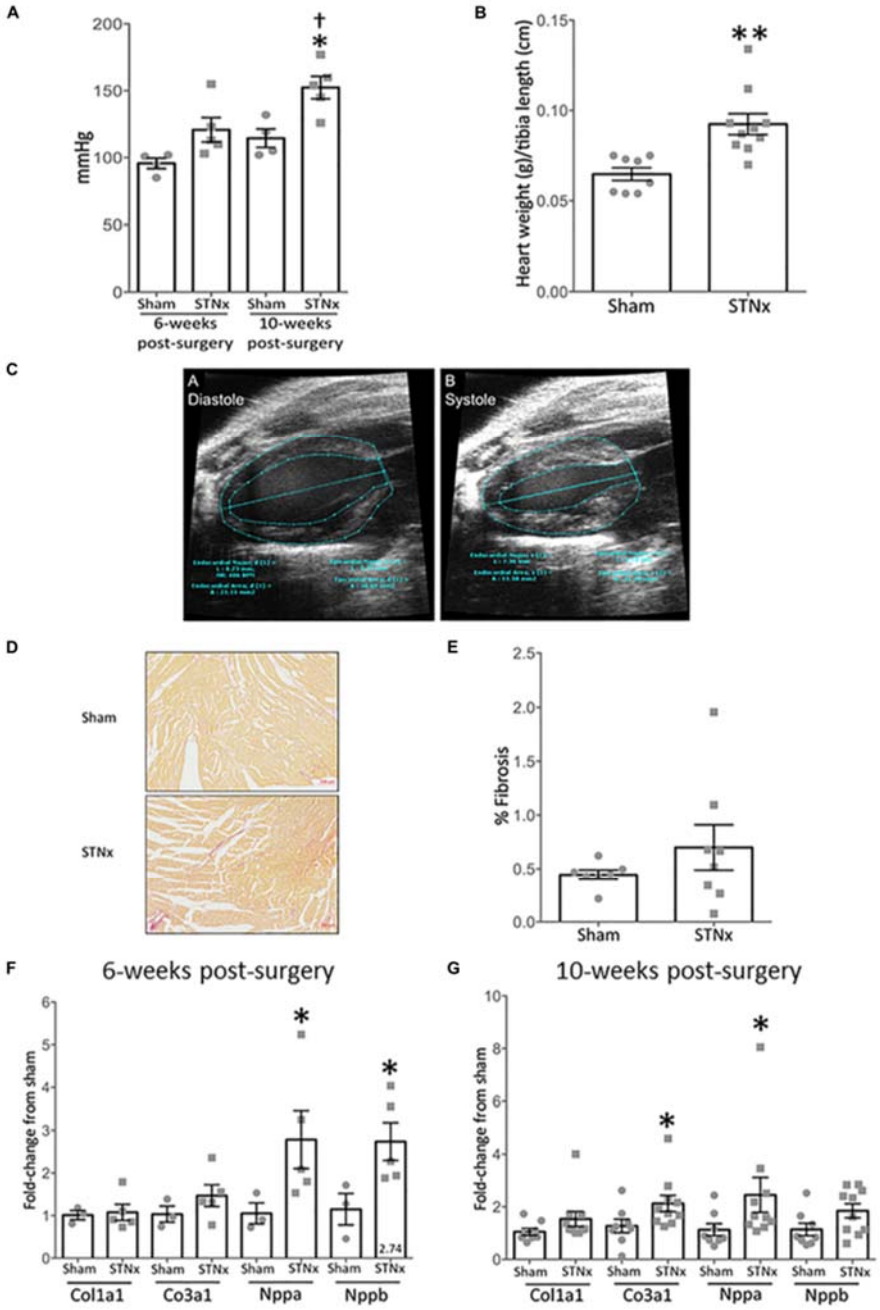

Figure 4. Single-step flank STNx induces cardiac dysfunction and hypertrophy but not cardiac fibrosis. 129S2/SV mice were subjected to flank single-step STNx or sham surgery and were culled 10-weeks post-surgery. At sacrifice heart sections were taken and snap frozen for RNA analysis and to prepare FFPE 3 µM sections. **(A)** Systolic blood pressure was measured via tail cuff at 6 and 10-weeks post-surgery. Sham: n = 4, STNx: n = 5. One way-ANOVA with Tukey's multiple comparison test, all compared to sham. $^{*}P \leq 0.05$, $^{\dagger}P < 0.05$ vs. STNx at 6 weeks. Plotted as mean ± SEM. **(B)** Heart weight at cull normalized to tibia length. Sham: n =

7, STNx: *n* = 11. Student's *t*-test was used for statistical analysis. $^{**}P \leq 0.01$. Plotted as mean ± SEM. **(C)** Exemplar images of the analysis of EKV echocardiography via VisualSonics software. A = diastole, B = systole. Trace lines were drawn along the epicardial and endocardial borders at both end systole and end diastole. Left ventricle (LV) major axes were also traced at end systole and end diastole by drawing a line from the LV apex endocardium or LV apex epicardium, to the mitral valve line. **(D)** Picrosirius red stain for total collagen in hearts. Exemplar images are provided at 5x magnification. **(E)** Quantification of fibrosis (% PSR staining) carried out via Image-Pro Plus 7. Sham: *n* = 7, STNx: *n* = 8. Student's *t*-test was used for statistical analysis. Plotted as mean ± SEM. **(F)** Gene expression in whole heart tissue was assessed 6 weeks post-STNx using quantitative real-time PCR (qRT-PCR) using specific Taqman probes for each gene, normalized to housekeeper Gapdh. Sham: *n* = 3, STNx: *n* = 5. Student's *t*-test was used for statistical analysis. $^{*}P \leq 0.05$. Plotted as mean ± SEM. **(G)** Gene expression in whole heart tissue 10-weeks post-STNx or sham surgery was assessed using quantitative real-time PCR (qRT-PCR) using specific Taqman probes for each gene, normalized to housekeeper Gapdh. Sham: *n* = 8, STNx: *n* = 10. Col1a1, Col3a1, and Nppa expression were determined to have non-parametric distribution. Mann–Whitney test was used for statistical analysis on Col1a1, Col3a1 and Nppa, Student's *t*-test was used on Nppb. $^{*}P \leq 0.05$. Plotted as mean ± SEM.

To demonstrate consistent outputs from the STNx model presented in this manuscript, two independent studies were compared in male 129S2/SV mice run 1.5 years apart (Figure 5). Between the two studies there were no significant differences in the amount of renal fibrosis detected, the increase in ACRs induced, amount of LVH (measured by heart weight:normalized to tibia) or gene expression of collagen 1 in renal tissue (Figure 5).

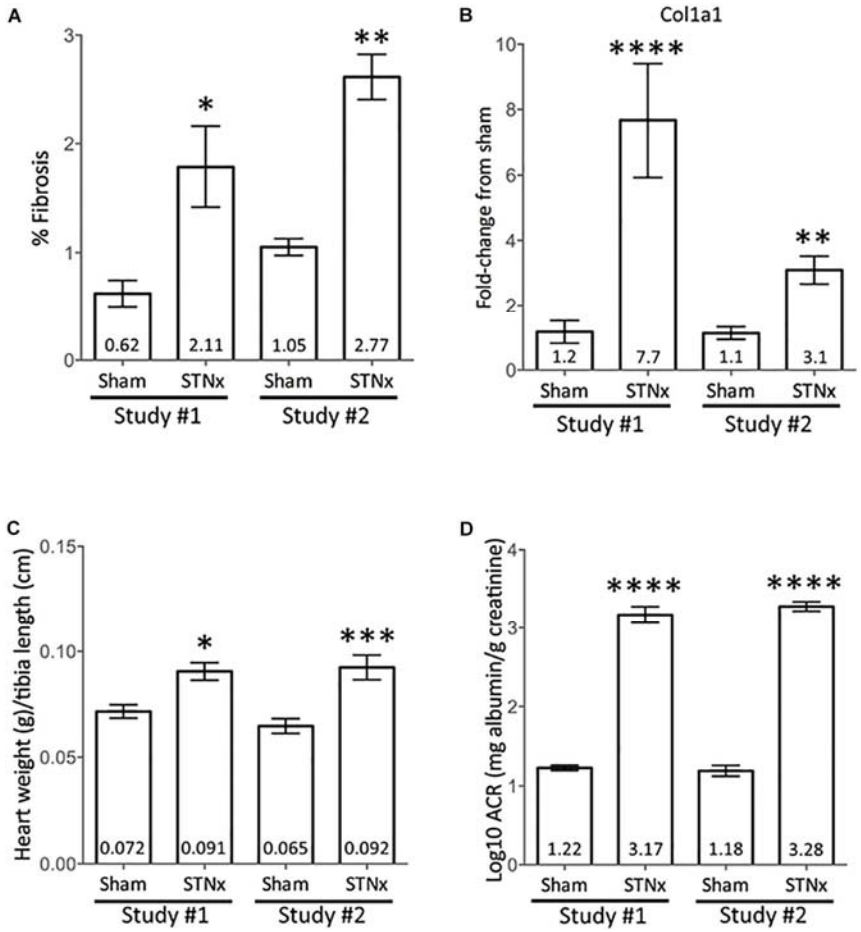

Figure 5. Comparison between independent STNx studies conducted in male 129S2/SV mice. Male 129S2/SV mice (bought from Envigo) were subjected to STNx in two separate studies, 1.5 years apart (Study 1 – March 2017; Study 2 – September 2018). Plotted as mean ± SEM. **(A)** Quantification of picrosirius red stain for total renal collagen, via Image-Pro Plus. Study #1 Sham: *n* = 7, study #1 STNx: *n* = 11, Study #2 Sham: *n* = 7, study #2 STNx: *n* = 6. **(B)** Renal Col1a1 gene expression at 10-weeks post-surgery. Study #1 Sham: *n* = 6, study #1 STNx: *n* = 10, Study #2 Sham: *n* = 8, study #2 STNx: *n* = 10. **(C)** Heart weight normalized to tibia length at cull, 10-weeks post-surgery. Study #1 Sham: *n* = 7, study #1 STNx: *n* = 11, Study #2 Sham: *n* = 8, study #2 STNx: *n* = 10. **(D)** Log10 albumin:creatinine ratio (ACR) at 10-weeks post-surgery. Study #1 Sham: *n* = 7, Study #1 STNx: *n* = 11, Study #2 Sham: *n* = 7, study #2 STNx: *n* = 8. Statistical analysis carried out via ordinary one-way ANOVA with Tukey's multiple comparisons test. $^{*}P < 0.05$ vs. sham (same study), $^{**}P < 0.01$, $^{***}P < 0.001$, $^{****}P < 0.0001$.

Effect of Genetic Background on One-Step Flank STNx Induced Renal and Cardiac Dysfunction

Subtotal nephrectomy is known to be a strain-dependent model, with C57BL/6 mice being resistant to developing fibrosis (Ma and Fogo, 2003; Leelahavanichkul et al., 2010). However, this strain is commonly used as a background for the production of transgenic animals. To assess how the single step STNx performs in this genetic background, a Gli1 reporter mouse (Gli1 × Ai14) on a C57BL/6 background was used. An increase in total collagen expression (sham: 0.81 ± 0.03%, STNx: 2.57 ± 0.42%) along with histological hallmarks of renal fibrosis (tubulointerstitial fibrosis and glomerulosclerosis) was observed (Supplementary Figures 4A,B), as well as a significant increase in pro-fibrotic genes and inflammatory genes (Supplementary Figure 4C). However, the urinary ACRs of STNx animals were not different to sham at 6 or 10-weeks post-surgery (Supplementary Figure 4D) and there was no increase in heart weight observed (Supplementary Figure 4E).

Discussion:

Clinically, CKD is characterized by worsening excretory function with or without proteinuria and renal biopsies typically show glomerulosclerosis, tubulointerstitial fibrosis, and inflammatory cell infiltrates. In addition, CKD is associated with the development of CVD, characterized by hypertension and cardiac and vascular dysfunction. Therefore, we set out to establish if a one-step flank STNx performed in male 129S2/SV mice could model these clinical CKD parameters in a consistent and robust manner.

Urinary albumin to creatinine ratio (ACR) is an important prognostic indicator for progression of renal disease (Feldman et al., 2014; Vassalotti et al., 2016), and cardiovascular events (Waheed et al., 2012). Furthermore, regression of albuminuria is associated with improved renal outcomes (Perkins et al., 2007) and hence represents a therapeutic target in CKD patients (Heerspink and Gansevoort, 2015). Hence, the significantly increased ACR in STNx mice compared to sham operated mice represents an important clinically-relevant readout for testing novel therapeutics in

this model. Indeed, this was a key readout used to demonstrate the efficacy of ACE inhibition in seminal studies in the rat subtotal nephrectomy model (Meyer et al., 1985; Anderson et al., 1986), which represents one of the few therapies that have been successfully translated from rodent models to human CKD. Urinary excretion of sodium, chloride and potassium were largely comparable between sham-operated and STNx mice at both time points. Although GFR was not directly measured here, the major reduction in filtration following STNx would significantly reduce the filtered load for sodium, chloride and potassium and our data indicate a proportionate decline tubular reabsorption. Thus, over this time course, the renal tubule adapted to maintain electrolyte excretion and preserve balance. The STNx group showed a progressive decline in urine osmolarity, indicating a reduced concentrating capacity in the remnant kidney.

Male 129S2/SV mice subjected to the refined one-step STNx developed increased serum creatinine, BUN and phosphate which are important clinical manifestations of renal disease. There was approximately a twofold increase in both creatinine and urea by 10-weeks post-STNx, however, the coefficient of variation (CV) for urea was only 11.1% compared to 39.8% for creatinine suggesting that serum urea measurements are more reliable as kidney injury markers in rodents. In this context, it would be interesting to measure some newer markers of renal function such as Cystatin C (Song et al., 2009) to further validate this model of progressive renal dysfunction in mice. The increase in serum phosphate is important as hyperphosphatemia is observed in late-stage CKD and is a driver of secondary hyperparathyroidism (Locatelli et al., 2002), mineral bone disorder and vascular calcification (Felsenfeld et al., 2015). Hyperphosphatemia is also thought to contribute to cardiac hypertrophy and calcification of heart valves and conduction system (Di et al., 2015).

The serum urea levels recorded in the mice following the single step flank STNx procedure were significantly increased compared to age matched sham controls, however, these levels are lower than those observed in some other studies which might suggest this surgery resulted in less tissue being taken and a less severe renal

dysfunction being induced which resulted in less mortality. The lack of a statistical difference in body weight appears to support this too. There are very few studies that document the amount of tissue taken beyond those studies that showed the relationship between renal function and the amount of tissue removed (Rambausek et al., 1985). In our studies in male SV129/SV mice, when on average 32.9% of left renal tissue remained, all mice developed renal dysfunction with significant alterations in renal excretory function and proteinuria. Importantly, the low mortality rate in this STNx model means animals survived to pre-defined study end-points which maintained statistical power in the studies.

The relationship between CKD and hypertension is bidirectional. CKD is known to cause hypertension and hypertension is a known risk factor for CKD (Gosmanova and Kovesdy, 2016). 86% of CKD patients have hypertension (Gosmanova and Kovesdy, 2016). Blood pressure lowering strategies have been shown to decrease progression of kidney disease and all-cause mortality in patients with CKD (Peters et al., 2017). At 10-weeks post-STNx, a significant increase in systolic blood pressure was detected using tail vein plethysmograph. This was in agreement with several other studies (Kennedy et al., 2008; Leelahavanichkul et al., 2010; Gava et al., 2012). However, this is contrast to subtotal nephrectomy two-step models run in 129SV and FVB mice, where no change in blood pressure was observed (Siedlecki et al., 2009; Dilauro et al., 2010). Interestingly, sham mice from the 129SV study had higher systolic blood pressures than recorded in our study (129 ± 4 mmHg; Siedlecki et al., 2009 sham versus 115 ± 2.6 mmHg sham operated in our study). The mice in this study were trained prior to blood pressure measurements to ensure the results were not affected by stress of the procedure, potentially explaining the lower conscious blood pressures obtained. However, the diet of the mice differing between studies could also explain these effects as increased dietary NaCl is known to aggravate hypertension. Similarly, group housing of the animals may also have affected our results, as this is a less stressful environment for the animals that may have led to our sham animals having lower systolic blood pressure.

The refined single-step flank STNx performed on 129S2/SV mice results in significant renal fibrosis, accompanied by histological hallmarks tubulointerstitial fibrosis (TIF) and glomerulosclerosis (GS) by 10-weeks post-surgery. Both TIF and GS are observed in CKD patients (Nakagawa et al., 2015), with TIF being an important predictor of disease progression (Nath, 1992). Increases in three collagen genes mirror what can be seen histologically. *Col1a1* and *Col3a1* encode fibrillar collagens (Delella et al., 2017) which are important extracellular matrix components (Nakagawa and Duffield, 2013). *Col4a1* is an important basement membrane component (Jones et al., 2016), suggesting possible basement membrane expansion in STNx kidneys. *Acta2* encodes α-smooth muscle actin, a marker of activated myofibroblasts, which increase in number in renal fibrosis (Bernard et al., 2014) and secrete excess extracellular matrix components (Bernard et al., 2014). The increased expression of miR-21 and miR-214 is of interest given the pro-fibrotic role these miRNAs are known to have in the kidney (Denby et al., 2014). Importantly, miR-21 and miR-214 have also been shown to be up-regulated in the kidneys of patients with CKD, indicating that the STNx model mimics the mechanisms that promote fibrosis in human disease (Lv et al., 2018). Taken together, increased expression of these genes and miRNAs in the kidney suggests a pro-fibrotic environment is present in the kidneys of mice subjected to STNx on both the histological and molecular level.

Gene expression of the cardiac hypertrophy marker ANP (Kerkelä et al., 2015; Riaz et al., 2015) was increased in hearts at both 6 and 10-weeks post-STNx whilst BNP (Kerkelä et al., 2015) was only significantly increased at 6-weeks. This coupled with the increased heart weight detected at 10-weeks post-STNx and increased average cardiac wall thickness and left-ventricular mass detected by ECHO at 10-weeks post-STNx suggests significant hypertrophy had taken place, although cardiac fibrosis had not manifested at the histological level at this time-point. However, no significant change in these measures was detected at 6-weeks post-STNx, indicating the development of this cardiac hypertrophy in the STNx model is time dependent. Prolonged isovolumic relaxation time (IV RT) was observed at 10-weeks post-STNx (but not at 6-weeks), indicating diastolic dysfunction is present in these mice via

impairment of myocardial relaxation (Schnelle et al., 2018). No significant decrease in ejection fraction was observed, indicating that adaptive measures taken by the heart to overcome the increased stress have been successful up until 10-weeks post-STNx. It is likely necessary to extend the timeline of the model past 10-weeks post-surgery in order to observe diastolic dysfunction and fibrosis.

The STNx model has been extensively reviewed from the point of heart-kidney interactions (Bongartz et al., 2012; Hewitson et al., 2015; Liu, 2019). A common comment in reviews of the literature is that in mice this model is highly variable if not uniformly performed and you can get conflicting results depending on the strain. Here we are able to present data which shows that in 129S2/SV male mice you can achieve reproducible physiological readouts using the single step STNx model described, with the added advantage of low mortality and improved animal welfare. The model is amenable to echocardiography studies which allow longitudinal studies of cardiac structure and function. Utilizing the 129S2/SV mouse also allows for the inflammatory cell profile to be examined in detail as multiple validated antibodies are available for mouse unlike rat.

Low grade inflammation is common in CKD patients (Amdur et al., 2016), with patients typically exhibiting elevated CRP, TNFα, and IL-6 levels (Panichi et al., 2001; Lacson and Levin, 2004). Furthermore, macrophage infiltration into the kidney in CKD has been found to correlate with a decline in kidney function (Eardley et al., 2006; Amdur et al., 2016). The analysis of the inflammatory cell content of the STNx mice revealed there is increased $CD45^+$ hematopoietic cell content in the STNx kidney and heart. The STNx model mimics the findings in human CKD of increased inflammation, with flow cytometry data demonstrating persistent $Ly6C^{hi}$ monocyte recruitment to the STNx kidney where they transition into pro-inflammatory macrophages. Previous work has identified a $CD11b^+$ $Ly6C^{hi}$ population to be induced with the onset of renal injury following ischemia reperfusion injury and unilateral ureteric obstruction (Lin et al., 2009; Clements et al., 2016). Importantly, in our study we excluded $Ly6G^+$ neutrophils and found that significantly more $CD45^+$ $Ly6G^-$ $CD11b^+$ $F4/80^{lo}$ cells express Ly6C. This population has been previously

shown to have a pro-inflammatory gene signature (Clements et al., 2016), and promote fibrosis in other organs such as the liver (Ramachandran et al., 2012). Within the $CD45^{+}$ $CD11b^{+}$ $F4/80^{hi}$ resident macrophage population there was a significantly greater expression of CD206 (Mannose receptor 1, Mrc1). This C-type lectin is expressed predominantly by tissue macrophages and is involved in phagocytosis and acts as a scavenger receptor (Taylor et al., 2005). CD206 is classically thought of as an alternatively activated or M2 macrophage marker (Murray et al., 2014). The increase in the Mrc1 expression is confined to the resident macrophage population that may suggest that resident macrophages may play an important role in scavenging of debris and scar tissue. Hence, this STNx model in mice affords an opportunity in future studies to perform detailed mechanistic studies of the role of each immune cell subset in progressive CKD.

A number of refinements to traditional methods of undertaking subtotal nephrectomy were employed in the refined single-step STNx surgery used in this study with a key focus on animal welfare. One of the key differences between the surgical methods presented in this paper and the majority of previously published studies is the use of a single-surgery via flank incisions to perform both the nephrectomy and contralateral partial nephrectomy. Multiple papers have been published where nephrectomy is performed in one surgery, then 1–2 weeks later, resection of the poles or renal artery ligation is performed in a separate surgery (Kren and Hostetter, 1999; Ma and Fogo, 2003; Soler et al., 2008; Windt et al., 2008; Leelahavanichkul et al., 2010; Yang et al., 2010; Babelova et al., 2012; Gava et al., 2012; Li et al., 2012; Purnomo et al., 2013; Hyde et al., 2014; Ucero et al., 2014; Vavrinec et al., 2016; Rosendahl et al., 2018). Reducing the number of surgeries to which the mice are subjected, by performing the single-step STNx surgery has a number of benefits for animal welfare including: the animals undergo anesthesia on one less occasion, the length of time the mice are on-procedure is decreased, and requirement for analgesics is reduced. Our approach also avoids hypertrophy of the remaining kidney or remnant kidney (depending on the surgical order) between surgeries. Renal tissue during this phase could be argued to be in the “regenerative

mode" and thus may be more resistant to the development of fibrosis which would not be present in this refined STNx model. Animal welfare in response to STNx was monitored weekly throughout the study using an animal condition scoring sheet (Supplementary Table 1), which included body condition scoring. A cumulative score of 5 or higher resulted in a mandatory schedule 1 termination of the animal. We found that group housing resulted in improved animal welfare scores, therefore group housing animals is recommended. Decreased weight and body condition score in mice is an important determinant of health status (Foltz and Ullman-Culleré, 1999; Ullman-Culleré and Foltz, 1999; Burkholder et al., 2012) and mice subjected to STNx were found not to differ in weight in comparison to sham animals at any time-point during the 10-weeks between surgery and sacrifice. In studies which use traditional two-step subtotal nephrectomy protocols, most (Leelahavanichkul et al., 2010; Gava et al., 2012; Zeng et al., 2018) but not all (Siedlecki et al., 2009), report a reduction in body weight with subtotal nephrectomized animals compared to sham controls. The lack of a difference in body weight may be due to this model inducing milder progressive renal disease as systolic blood pressure and ACRs were not significantly increased until 6-weeks post-surgery. However, this may also be in part due to improved animal welfare brought about by group housing. This study could have benefited from a side by side comparison with the traditional two-step STNx to fully demonstrate its advantages, however, the mortality rates for this surgery can be high and in a recent study shown to be 60% 4 weeks post-surgery (Tan et al., 2019). Therefore, in the interests of animal welfare it is not appropriate to run such a study. The mortality following subtotal nephrectomy has been poorly reported in the literature, but is often high, for example 43% by 12-weeks post-surgery (Ma and Fogo, 2003). Other studies report no mortality but it is not clear if this included animals that either did not develop significant renal dysfunction or were terminated prematurely due to animal welfare concerns. In our model in total 9% of animals did not complete the study due to a combination of mortality during follow-up (n = 3), exceeding animal welfare scoring limits (n = 2) or failure to recover from anesthetic (n = 2).

These data suggest that the single-step STNx surgery is well-tolerated by the mice, although a small mortality rate needs to be factored into power calculations.

The subtotal nephrectomy is known to be a strain-dependent model. Both the 129S2/SV and CD1 strain have been reported to be permissive to injury (Ma and Fogo, 2003; Kennedy et al., 2008; Siedlecki et al., 2009; Leelahavanichkul et al., 2010). In our 129S2/SV mice no cardiac fibrosis was detected *per se* but on the gene expression level Collagen III was increased by 10-weeks post-surgery. Using the CD1 strain of mice, cardiac fibrosis can be induced with the added insult of additional dietary salt (Fontes et al., 2015) which may be required in this model too. In a pilot study in this genetic background, the refined STNx model resulted in significant renal fibrosis and increased pro-fibrotic gene expression in the kidney which matches that previously observed (Ma and Fogo, 2003). However, there were no functional alterations detectable, e.g., increased ACR or changes in heart weight. This indicates that STNx in C57BL/6 mice may not be the best pre-clinical model to test novel therapies where clinically relevant renal and cardiac outcomes are required. These results mirror the experience of other groups with subtotal nephrectomy in C57BL/6 mice (Ma and Fogo, 2003; Leelahavanichkul et al., 2010), with additional stimuli such as angiotensin II infusion required to produce hard renal outcomes (Leelahavanichkul et al., 2010). The resistance to development of albuminuria in the C57BL/6 mice is well-recognized, albumin overloaded 129S2/SV mice develop abundant albuminuria whereas C57BL/6 show none despite increased serum albumin (Ishola et al., 2006). The significant increase in fibrosis observed, however, suggests that for studies into renal fibrosis, the STNx model could be further utilized to understand the precise pathophysiology of progressive renal fibrosis using genetic knockout mice on the C57BL/6 genetic background.

Summary:

Together, these data provide evidence that conducting the subtotal nephrectomy model with our refined protocol in male 129S2/SV mice results in renal dysfunction,

renal inflammation, and fibrosis with systemic pathologies akin to what is observed in patients.

This model is also suitable for testing new therapies for CKD given its progressive nature, clinically relevant biochemical measurements and cardiac dysfunction. In addition, these therapies can be given with standard therapy of ACEi to examine physiological effects beyond those offered by blood pressure reduction alone.

C57BL/6 mice as previously reported are refractory to proteinuric renal dysfunction, blood pressure and cardiac changes but do develop significant renal fibrotic disease. Therefore, for pathophysiological studies of fibrosis the STNx model in C57BL/6 background may offer some insight when using genetic knockout models on this genetic background.

Data Availability Statement:

All datasets generated for this study are included in the article/Supplementary Material.

Ethics Statement:

The animal study was reviewed and approved by University of Edinburgh Animal Welfare and Ethical Review Board.

Author Contributions:

JO'S contributed to the investigation, analysis, the writing and revising of the original draft of the manuscript. SF contributed to the investigation, analysis, the writing and editing of the original draft of the manuscript. OT and AB contributed to the investigation and analysis. CC contributed to the investigation, analysis, and the editing of the original draft of the manuscript. MB contributed to the analysis and the editing of revised manuscript. AT contributed to the investigation, methodology, and analysis of the study. JH contributed to the conceptualization and methodology of the study. CB contributed to the methodology, analysis, and the writing, the review and the editing of the manuscript. BC contributed to the conceptualization,

methodology, analysis, and the writing, the review and the editing of the manuscript. LD contributed to the funding acquisition, supervision, conceptualization, project administration, methodology, investigation, analysis, the writing, the review and the editing original, and revised draft of the manuscript.

Funding:

This study was funded by Medical Research Scotland 789_Ph.D._2014, Kidney Research UK Fellowships PDF6/2012, SF_001_20181122, and BBSRC Ph.D. studentship BB/R505638/1, and British Heart Foundation Ph.D. studentship FS/15/63/32033 awarded to LD.

Conflict of Interest:

LD is an awardee and JO'S is a recipient of an MRS Ph.D. studentship co-funded by Regulus Therapeutics. Regulus Therapeutics had no input on the studies contained in this manuscript.

The remaining authors declare that the research was conducted in the absence of any commercial or financial relationships that could be construed as a potential conflict of interest.

Acknowledgments:

Thanks to Lorraine Bruce for urine osmolality measurements. Flow cytometry data was generated with support from the QMRI Flow Cytometry and Cell Sorting Facility, University of Edinburgh.

Supplementary Material:

The Supplementary Material for this article can be found online at: https://www.frontiersin.org/articles/10.3389/fphys.2019.01365/full#supplementary-material

Footnotes:

1. ^ http://random.org
2. ^ https://surf.ed.ac.uk/facilities/specialist-assay-service/

References:

Alicic, R. Z., Rooney, M. T., and Tuttle, K. R. (2017). Diabetic kidney disease: challenges, progress, and possibilities. *Clin. J. Am. Soc. Nephrol.* 12, 2032–2045. doi: 10.2215/CJN.11491116

Almeras, C., and Argilés, À (2009). The general picture of uremia. *Semin. Dial.* 22, 329–333. doi: 10.1111/j.1525-139X.2009.00575.x

Amdur, R. L., Feldman, H. I., Gupta, J., Yang, W., Kanetsky, P., Shlipak, M., et al. (2016). Inflammation and progression of CKD: the CRIC study. *Clin. J. Am. Soc. Nephrol.* 11, 1546–1556. doi: 10.2215/CJN.13121215

Anderson, S., Rennke, H. G., and Brenner, B. M. (1986). Therapeutic advantage of converting enzyme inhibitors in arresting progressive renal disease associated with systemic hypertension in the rat. *J. Clin. Invest.* 77, 1993–2000. doi: 10.1172/jci112528

Babelova, A., Avaniadi, D., Jung, O., Fork, C., Beckmann, J., Kosowski, J., et al. (2012). Role of Nox4 in murine models of kidney disease. *Free Radic. Biol. Med.* 53, 842–853. doi: 10.1016/j.freeradbiomed.2012.06.027

Bai, M., Chen, H., Ding, D., Song, R., Lin, J., Zhang, Y. Y., et al. (2019). MicroRNA- 214 promotes chronic kidney disease by disrupting mitochondrial oxidative phosphorylation. *Kidney Int.* 95, 1–16. doi: 10.1016/j.kint.2018.12.028

Bain, C. C., Hawley, C. A., Garner, H., Scott, C. L., Schridde, A., Steers, N. J., et al. (2016). Long-lived self-renewing bone marrow-derived macrophages displace embryo-derived cells to inhabit adult serous cavities. *Nat. Commun.* 7:ncomms11852. doi: 10.1038/ncomms11852

Bernard, M., Dieude, M., Yang, B., Hamelin, K., Underwood, K., and Hebert, M.- J. (2014). Autophagy fosters myofibroblast differentiation through MTORC2 activation and downstream upregulation of CTGF. *Autophagy* 10, 2193–2207. doi: 10.4161/15548627.2014.981786

Bongartz, L. G., Braam, B., Gaillard, C. A., Cramer, M. J., Goldschmeding, R., Verhaar, M. C., et al. (2012). Target organ cross talk in cardiorenal syndrome: animal models. *Am. J. Physiol. Ren. Physiol.* 303, 1253–1263. doi: 10.1152/ajprenal.00392.2012

Boor, P., Ostendorf, T., and Floege, J. (2010). Renal fibrosis: novel insights into mechanisms and therapeutic targets. *Nat. Rev. Nephrol.* 6, 643–656. doi: 10. 1038/nrneph.2010.120

Burkholder, T., Foltz, C., Karlsson, E., Linton, C. G., and Smith, J. M. (2012). Health evaluation of experimental laboratory mice. *Curr. Protoc. Mouse Biol.* 2, 145–165. doi: 10.1002/9780470942390.mo110217

Chatzimanouil, M. K. T., Wilkens, L., and Anders, H.-J. (2018). Quantity and reporting quality of kidney research. *J. Am. Soc. Nephrol.* 30, 13–22. doi: 10. 1681/ASN.2018050515

Chau, B. N., Xin, C., Hartner, J., Ren, S., Castano, A. P., Linn, G., et al. (2012). MicroRNA-21 promotes fibrosis of the kidney by silencing metabolic pathways. *Sci. Transl. Med.* 4:121ra18. doi: 10.1126/scitranslmed.3003205

Clements, M., Gershenovich, M., Chaber, C., Campos-Rivera, J., Du, P., Zhang, M., et al. (2016). Differential Ly6C expression after renal ischemia-reperfusion identifies unique macrophage populations. *J. Am. Soc. Nephrol.* 27, 159–170. doi: 10.1681/ASN.2014111138

Delella, F. K., de Almeida, F. L. A., Nunes, H. C., Rinaldi, J. C., and Felisbino, S. L. (2017). Fibrillar collagen genes are not coordinately upregulated with TGF β1 expression in finasteride-treated prostate. *Cell Biol. Int.* 41, 1214–1222. doi: 10.1002/cbin.10787

Denby, L., Ramdas, V., Lu, R., Conway, B. R., Grant, J. S., Dickinson, B., et al. (2014). MicroRNA-214 antagonism protects against renal fibrosis. *J. Am. Soc. Nephrol.* 25, 65–80. doi: 10.1681/ASN.2013010072

Denby, L., Ramdas, V., McBride, M. W., Wang, J., Robinson, H., McClure, J., et al. (2011). miR-21 and miR-214 are consistently modulated during renal injury in rodent models. *Am. J. Pathol.* 179, 661–672. doi: 10.1016/j.ajpath.2011.04.021

Di, L., Andrew, L., Antonio, H., Santoboni, A., Russo, D., and Ronco, C. (2015). Chronic kidney disease and cardiovascular complications. *Hear. Fail Rev.* 20, 259–272.

Dilauro, M., Zimpelmann, J., Robertson, S. J., Genest, D., and Burns, K. D. (2010). Effect of ACE2 and angiotensin-(1–7) in a mouse model of early chronic kidney disease. *Am J Physiol Ren. Physiol.* 298, F1523–F1532. doi: 10.1152/ajprenal.00426.2009

Eardley, K. S., Zehnder, D., Quinkler, M., Lepenies, J., Bates, R. L., Savage, C. O., et al. (2006). The relationship between albuminuria, MCP-1/CCL2, and interstitial macrophages in chronic kidney disease. *Kidney Int.* 69, 1189–1197. doi: 10.1038/sj.ki.5000212

Eckardt, K., Coresh, J., Devuyst, O., Johnson, R. J., Levey, A. S., and Levin, A. (2013). Evolving importance of kidney disease: from subspecialty to global health burden. *Lancet* 382, 158–169. doi: 10.1016/S0140-6736(13)60439-0

Feldman, H. I., Peralta, C. A., Inker, L. A., Lash, J. P., Fox, C. H., Kurella Tamura, M., et al. (2014). KDOQI US commentary on the 2012 KDIGO clinical practice guideline for the evaluation and management of CKD. *Am. J. Kidney Dis.* 63, 713–735. doi: 10.1053/j.ajkd.2014.01.416

Felsenfeld, A. J., Levine, B. S., and Rodriguez, M. (2015). Pathophysiology of calcium, phosphorus, and magnesium dysregulation in chronic kidney disease. *Semin. Dial.* 28, 564–577. doi: 10.1111/sdi.12411

Foltz, C. J., and Ullman-Culleré, M. (1999). Guidelines for assessing the health and condition of mice. *Lab. Anim.* 28, 28–32.

Fontes, M. S. C., Papazova, D. A., Van Koppen, A., De Jong, S., Korte, S. M., Bongartz, L. G., et al. (2015). Arrhythmogenic remodeling in murine models of deoxycorticosterone acetate-salt-induced and 5/6-subtotal nephrectomy- salt-induced cardiorenal disease. *CardioRenal Med.* 5, 208–218. doi: 10.1159/ 000430475

Gao, S., Ho, D., Vatner, D. E., and Vatner, S. F. (2011). Murine echocardiography. *Curr. Protoc. Mouse Biol.* 1, 71–83. doi: 10.1002/9780470942390.mo100130

Gava, A. L., Freitas, F. P., Balarini, C. M., Vasquez, E. C., and Meyrelles, S. S. (2012). Effects of 5/6 nephrectomy on renal function and blood pressure in mice. *Int. J. Physiol. Pathophysiol. Pharmacol.* 4, 167–173.

Gewin, L., Zent, R., and Pozzi, A. (2017). Progression of chronic kidney disease: too much cellular talk causes damage. *Kidney Int.* 91, 552–560. doi: 10.1016/j. kint.2016.08.025

Gewin, L. S. (2018). Renal fibrosis: primacy of the proximal tubule. *Matrix Biol.* 6, 248–262. doi: 10.1016/j.matbio.2018.02.006

Gomez, I. G., Mackenna, D. A., Johnson, B. G., Kaimal, V., Roach, A. M., Ren, S., et al. (2015). Anti–microRNA-21 oligonucleotides prevent Alport nephropathy progression by stimulating metabolic pathways. *J. Clin. Invest.* 125, 141–156. doi: 10.1172/jci75852

Gosmanova, E. O., and Kovesdy, C. P. (2016). Blood pressure targets in CKD: lessons learned from sprint and previous observational studies. *Curr. Cardiol. Rep.* 18:88. doi: 10.1007/s11886-016-0769-y

Heerspink, H. J. L., and Gansevoort, R. T. (2015). Albuminuria Is an appropriate therapeutic target in patients with CKD: the pro view. *Clin. J. Am. Soc. Nephrol.* 10, 1079–1088. doi: 10.2215/CJN.11511114

Hennino, M.-F., Buob, D., Van der Hauwaert, C., Gnemmi, V., Jomaa, Z., Pottier, N., et al. (2016). miR-21-5p renal expression is associated with fibrosis and renal survival in patients with IgA nephropathy. *Sci. Rep.* 6:27209. doi: 10.1038/ srep27209

Hewitson, T. D. (2009). Renal tubulointerstitial fibrosis: common but never simple. *Am. J. Physiol. Ren. Physiol.* 296, F1239–F1244. doi: 10.1152/ajprenal.90521. 2008

Hewitson, T. D., Holt, S. G., and Smith, E. R. (2015). Animal models to study links between cardiovascular disease and renal failure and their relevance to human pathology. *Front. Immunol.* 6:465. doi: 10.3389/fimmu.2015.00465

Hewitson, T. D., Holt, S. G., and Smith, E. R. (2017). Progression of tubulointerstitial fibrosis and the chronic kidney disease phenotype - role of risk factors and epigenetics. *Front. Pharmacol.* 8:520. doi: 10.3389/fphar.2017.00520

Hill, N. R., Fatoba, S. T., Oke, J. L., Hirst, J. A., O'Callaghan, C. A., Lasserson, D. S., et al. (2016). Global prevalence of chronic kidney disease – a systematic review and meta-analysis. *PLoS One* 6:e0158765. doi: 10.1371/journal.pone.015 8765

Horowitz, B., Miskulin, D., and Zager, P. (2015). Epidemiology of hypertension in CKD. *Adv. Chronic Kidney Dis.* 22, 88–95. doi: 10.1053/j.ackd.2014.09.004

Hyde, G. D., Taylor, R. F., Ashton, N., Borland, S. J., Wu, H. S. G., Gilmore, A. P., et al. (2014). Axl tyrosine kinase protects against tubulo-interstitial apoptosis and progression of renal failure in a murine model of chronic kidney disease and hyperphosphataemia. *PLoS One* 9:e102096. doi: 10.1371/journal.pone.0102096

Ishola, D. A., van der Giezen, D. M., Hahnel, B., Goldschmeding, R., Kriz, W., Koomans, H. A., et al. (2006). In mice, proteinuria and renal inflammatory responses to albumin overload are strain-dependent. *Nephrol. Dial. Transplant.* 21, 591–597. doi: 10.1093/ndt/gfi303

Ito, K., Chen, J., El Chaar, M., Stern, J. M., Seshan, S. V., Khodadadian, J. J., et al. (2004). Renal damage progresses despite improvement of renal function after relief of unilateral ureteral obstruction in adult rats. *Am. J. Physiol. Ren. Physiol.* 287, F1283–F1293.

Jha, V., Garcia-Garcia, G., Iseki, K., Li, Z., Naicker, S., Plattner, B., et al. (2013). Chronic kidney disease: global dimension and perspectives. *Lancet* 382, 260– 272. doi: 10.1016/S0140-6736(13)60687-X

Jones, F. E., Bailey, M. A., Murray, L. S., Lu, Y., Mcneilly, S., Lennon, R., et al. (2016). ER stress and basement membrane defects combine to cause glomerular and tubular renal disease resulting from Col4a1 mutations in mice. *Dis. Model. Mech.* 9, 165–176. doi: 10.1242/dmm.021741

Jörres, A., Lemke, H. D., Henle, T., Descamps-Latscha, B., De Smet, R., Glorieux, G., et al. (2004). Review on uremic toxins: classification, concentration, and interindividual variability. *Kidney Int.* 63, 1934–1943. doi: 10.1046/j.1523-1755. 2003.00924.x

Kennedy, D. J., Elkareh, J., Shidyak, A., Shapiro, A. P., Smaili, S., Mutgi, K., et al. (2008). Partial nephrectomy as a model for uremic cardiomyopathy in the mouse. *Am. J. Physiol. Ren. Physiol.* 294, F450–F454.

Kerkelä, R., Ulvila, J., and Magga, J. (2015). Natriuretic peptides in the regulation of cardiovascular physiology and metabolic events. *J. Am. Heart Assoc.* 4, 1–13.

Kerr, M., Bray, B., Medcalf, J., O'Donoghue, D. J., and Matthews, B. (2012). Estimating the financial cost of chronic kidney disease to the NHS in England. *Nephrol. Dial. Transplant.* 27(Suppl. 3):iii73-80. doi: 10.1093/ndt/gfs269

Kramann, R., Schneider, R. K., Dirocco, D. P., Machado, F., Fleig, S., Bondzie, P. A., et al. (2015). Perivascular Gli1+ progenitors are key contributors to injury- induced organ fibrosis. *Cell Stem Cell* 16, 51–66. doi: 10.1016/j.stem.2014.11.004

Kren, S., and Hostetter, T. H. (1999). The course of the remnant kidney model in mice. *Kidney Int.* 56, 333–337. doi: 10.1046/j.1523-1755.1999.00527.x

Lacson, E., and Levin, N. (2004). C-reactive protein and end-stage renal disease. *Semin. Dial.* 17, 438–448.

Lau, W. L., and Vaziri, N. D. (2016). Urea, a true uremic toxin: the empire strikes back. *Clin. Sci.* 131, 3–12. doi: 10.1042/cs20160203

Leelahavanichkul, A., Yan, Q., Hu, X., Eisner, C., Huang, Y., Chen, R., et al. (2010). Angiotensin II overcomes strain-dependent resistance of rapid CKD progression in a new remnant kidney mouse model. *Kidney Int.* 78, 1136–1153. doi: 10.1038/ki.2010.287

Levey, A. S., Inker, L. A., and Coresh, J. (2014). GFR estimation: from physiology to public health. *Am. J. Kidney Dis.* 63, 820–834. doi: 10.1053/j.ajkd.2013.12.006

Li, K. L., He, Y. N., Chen, J., Zhan, J., Li, Z. H., and Zhao, L. (2012). P53 negatively regulates the osteogenic differentiation of vascular smooth muscle cells in mice with chronic kidney disease. *Cardiovasc. J. Afr.* 23, e1–e9. doi: 10.5830/CVJA- 2011-069

Lin, G. H. Y., Sedgmen, B. J., Moraes, T. J., Snell, L. M., Topham, D. J., and Watts, T. H. (2009). Endogenous 4-1BB ligand plays a critical role in protection from influenza-induced disease. *J. Immunol.* 182, 934–947. doi: 10.4049/jimmunol. 182.2.934

Lindsey, M. L., Kassiri, Z., Virag, J. A. I., de Castro Brás, L. E., and Scherrer-Crosbie, M. (2018). Guidelines for measuring cardiac physiology in mice. *Am. J. Physiol. Circ. Physiol.* 314, H733–H752. doi: 10.1152/ajpheart.00339.2017

Liu, S. (2019). Heart-kidney interactions: mechanistic insights from animal models. *Am. J. Physiol. Ren. Physiol.* 316, F974–F985. doi: 10.1152/ajprenal.00624.2017

Locatelli, F., Cannata-Andia, J. B., Drueke, T. B., Horl, W. H., Fouque, D., Heimburger, O., et al. (2002). Management of disturbances of calcium and phosphate metabolism in chronic renal insufficiency, with emphasis on the control of hyperphosphataemia. *Nephrol. Dial. Transplant.* 17, 723–731. doi: 10.1093/ndt/17.5.723

Lv, W., Fan, F., Wang, Y., Gonzalez-Fernandez, E., Wang, C., Yang, L., et al. (2018). Therapeutic potential of microRNAs for the treatment of renal fibrosis and CKD. *Physiol. Genom.* 50, 20–34. doi: 10.1152/physiolgenomics.00039.2017

Ma, L.-J., and Fogo, A. B. (2003). Model of robust induction of glomerulosclerosis in mice: importance of genetic background. *Kidney Int.* 64, 350–355. doi: 10.1046/j.1523- 1755.2003.00058.x

Mack, M., and Yanagita, M. (2015). Origin of myofibroblasts and cellular events triggering fibrosis. *Kidney Int.* 87, 297–307. doi: 10.1038/ki.2014.287

Martin, K. J., and González, E. A. (2011). Prevention and control of phosphate retention/ hyperphosphatemia in CKD-MBD: what is normal, when to start, and how to treat? *Clin. J. Am. Soc. Nephrol.* 6, 440–446. doi: 10.2215/CJN. 05130610

Meyer, T. W., Anderson, S., Rennke, H. G., and Brenner, B. M. (1985). Converting enzyme inhibitor therapy limits progressive glomerular injury in rats with renal insufficiency. *Am. J. Med.* 79, 31–36. doi: 10.1016/0002-9343(85)90077-4

Murray, P. J., Allen, J. E., Biswas, S. K., Fisher, E. A., Gilroy, D. W., Goerdt, S., et al. (2014). Macrophage activation and polarization: nomenclature and experimental guidelines. *Immunity* 41, 14–20. doi: 10.1016/j.immuni.2014. 06.008

Nakagawa, N., and Duffield, J. S. (2013). Myofibroblasts in fibrotic kidneys. *Curr. Pathobiol. Rep.* 1, 189–198. doi: 10.1007/s40139-013-0025-8

Nakagawa, S., Nishihara, K., Miyata, H., Shinke, H., Tomita, E., Kajiwara, M., et al. (2015). Molecular markers of tubulointerstitial fibrosis and tubular cell damage in patients with chronic kidney disease. *PLoS One* 10:e0136994. doi: 10.1371/journal.pone.0136994

Nath, K. A. (1992). Tubulointerstitial changes as a major determinant in the progression of renal damage. *Am. J. Kidney Dis.* 20, 1–17. doi: 10.1016/s0272- 6386(12)80312- x

Obrador, G. T., and Levin, A. (2019). CKD hotspots: challenges and areas of opportunity. *Semin. Nephrol.* 39, 308–314. doi: 10.1016/j.semnephrol.2019. 02.009

Oosterhuis, N. R., Papazova, D. A., Gremmels, H., Joles, J. A., and Verhaar, M. C. (2017). T-cells contribute to hypertension but not to renal injury in mice with subtotal nephrectomy. *BMC Nephrol.* 18:153. doi: 10.1186/s12882-017-0555-0

Panichi, V., Migliori, M., De Pietro, S., Taccola, D., Bianchi, A. M., Norpoth, M., et al. (2001). C reactive protein in patients with chronic renal diseases. *Ren. Fail.* 23, 551–562. doi: 10.1081/jdi-100104737

Perkins, B. A., Ficociello, L. H., Ostrander, B. E., Silva, K. H., Weinberg, J., Warram, J. H., et al. (2007). Microalbuminuria and the risk for early progressive renal function decline in type 1 diabetes. *J. Am. Soc. Nephrol.* 18, 1353–1361. doi: 10.1681/asn.2006080872

Peters, R., Staessen, J. A., Cheung, A. K., Beckett, N., Nadkarni, G. N., Mant, J., et al. (2017). Association between more intensive vs less intensive blood pressure lowering and risk of mortality in chronic kidney disease stages 3 to 5. *JAMA Intern. Med.* 177:1498. doi: 10.1001/jamainternmed.2017.4377

Purnomo, E., Emoto, N., Nugrahaningsih, D. A. A., Nakayama, K., Yagi, K., Heiden, S., et al. (2013). Glycosaminoglycan overproduction in the aorta increases aortic calcification in murine chronic kidney disease. *J. Am. Heart Assoc.* 2, 1–18. doi: 10.1161/JAHA.113.000405

Ramachandran, P., Pellicoro, A., Vernon, M. A., Boulter, L., Aucott, R. L., Ali, A., et al. (2012). Differential Ly-6C expression identifies the recruited macrophage phenotype, which orchestrates the regression of murine liver fibrosis. *Proc. Natl. Acad. Sci. U.S.A.* 109, E3186–E3195. doi: 10.1073/pnas.1119964109

Rambausek, M., Ritz, E., Mall, G., Mehls, O., and Katus, H. (1985). Myocardial hypertrophy in rats with renal insufficiency. *Kidney Int.* 28, 775–782. doi: 10. 1038/ki.1985.197

Respress, J. L., and Wehrens, X. H. T. (2010). Transthoracic echocardiography in mice. *J. Vis. Exp.* 39:1738. doi: 10.3791/1738

Riaz, N., Wolden, S. L., Gelblum, D. Y., and Eric, J. (2015). Atrial natriuretic peptide in cardiovascular biology and disease (NPPA). *Gene* 569, 1–6. doi: 10.1016/j.gene.2015.06.029

Ritter, C. S., and Slatopolsky, E. (2016). Phosphate toxicity in CKD: the killer among us. *Clin. J. Am. Soc. Nephrol.* 11, 1088–1100. doi: 10.2215/CJN.11901115

Rosendahl, A., Kabiri, R., Bode, M., Cai, A., Klinge, S., Ehmke, H., et al. (2018). Adaptive immunity and IL-17A are not involved in the progression of chronic kidney disease after 5/6 nephrectomy in mice. *Br. J. Pharmacol.* 176, 2002–2014. doi: 10.1111/bph.14509

Schelling, J. R. (2016). Tubular atrophy in the pathogenesis of chronic kidney disease progression. *Pediatr. Nephrol.* 31, 693–706. doi: 10.1007/s00467-015- 3169- 4

Schnelle, M., Catibog, N., Zhang, M., Nabeebaccus, A. A., Anderson, G., Richards, D. A., et al. (2018). Echocardiographic evaluation of diastolic function in mouse models of heart disease. *J. Mol. Cell. Cardiol.* 114, 20–28. doi: 10.1016/j.yjmcc. 2017.10.006

Siedlecki, A. M., Jin, X., and Muslin, A. J. (2009). Uremic cardiac hypertrophy is reversed by rapamycin but not by lowering of blood pressure. *Kidney Int.* 75, 800–808. doi: 10.1038/ki.2008.690

Soler, M. J., Wysocki, J., and Batlle, D. (2008). Angiotensin-converting enzyme 2 and the kidney. *Exp. Physiol.* 93, 549–556.

Song, S., Meyer, M., Türk, T. R., Wilde, B., Feldkamp, T., Assert, R., et al. (2009). Serum cystatin C in mouse models: a reliable and precise marker for renal function and superior to serum creatinine. *Nephrol. Dial. Transplant.* 24, 1157–1161. doi: 10.1093/ndt/gfn626

Stevens, P. E., and Levin, A. (2013). Evaluation and management of chronic kidney disease: synopsis of the kidney disease: improving global outcomes 2012 clinical practice guideline. *Ann. Intern. Med.* 158, 825–830. doi: 10.7326/0003-4819- 158- 11- 201306040- 00007

Tan, R. Z., Zhong, X., Li, J. C., Zhang, Y. W., Yan, Y., Liao, Y., et al. (2019). An optimized 5/6 nephrectomy mouse model based on unilateral kidney ligation and its application in renal fibrosis research. *Ren. Fail.* 41, 555–566. doi: 10. 1080/0886022X.2019.1627220

Taylor, P. R., Martinez-Pomares, L., Stacey, M., Lin, H.-H., Brown, G. D., and Gordon, S. (2005). Macrophage receptors and immune recognition. *Annu. Rev. Immunol.* 23, 901–944. doi: 10.1146/annurev.immunol.23.021704.115816

Ucero, A. C., Benito-Martin, A., Izquierdo, M. C., Sanchez-Niño, M. D., Sanz, A. B., Ramos, A. M., et al. (2014). Unilateral ureteral obstruction: beyond obstruction. *Int. Urol. Nephrol.* 46, 765–776. doi: 10.1007/s11255-013-0520-1

Ullman-Culleré, M. H., and Foltz, C. J. (1999). Body condition scoring: a rapid and accurate method for assessing health status in mice. *Lab. Anim. Sci.* 49, 319–323.

Vanholder, R., Gryp, T., and Glorieux, G. (2018). Urea and chronic kidney disease: the comeback of the century? (in uraemia research). *Nephrol. Dial. Transplant.* 33, 4–12. doi: 10.1093/ndt/gfx039

Vassalotti, J. A., Centor, R., Turner, B. J., Greer, R. C., Choi, M., and Sequist, T. D. (2016). Practical approach to detection and management of chronic kidney disease for the primary care clinician. *Am. J. Med.* 129:153-162.e7. doi: 10.1016/j.amjmed.2015.08.025

Vavrinec, P., Buikema, H., Vettoretti, S., Deelman, L. E., De Zeeuw, D., Henning, R. H., et al. (2016). Renal endothelial function is associated with the anti- proteinuric effect of ACE inhibition in 5/6 nephrectomized rats. *Am. J. Physiol. Physiol.* 310, F1047–F1053. doi: 10.1152/ajprenal.00325.2015

Venkatachalam, M. A., Weinberg, J. M., Kriz, W., and Bidani, A. K. (2015). Failed tubule recovery, AKI-CKD transition, and kidney disease progression. *J. Am. Soc. Nephrol.* 26, 1765–1776. doi: 10.1681/ASN.2015010006

Vervloet, M. G., Sezer, S., Massy, Z. A., Johansson, L., Cozzolino, M., and Fouque, D. (2017). The role of phosphate in kidney disease. *Nat. Rev. Nephrol.* 13, 27–38. doi: 10.1038/nrneph.2016.164

Waheed, S., Matsushita, K., Sang, Y., Hoogeveen, R., Ballantyne, C., Coresh, J., et al. (2012). Combined association of albuminuria and cystatin C-based estimated GFR with mortality, coronary heart disease, and heart failure outcomes: the atherosclerosis risk in communities (ARIC) study. *Am. J. Kidney Dis.* 60, 207–216. doi: 10.1053/j.ajkd.2012.03.011

Wang, Y., Thatcher, S. E., and Cassis, L. (2017). Measuring blood pressure using a noninvasive tail cuff method in mice. *Methods Mol. Biol.* 1614, 69–73. doi: 10.1007/978- 1- 4939- 7030- 8_6

Webster, A. C., Nagler, E. V., Morton, R. L., and Masson, P. (2017). Chronic kidney disease. *Lancet* 389, 1238–1252. doi: 10.1016/S0140-6736(16) 32064-5

Windt, W. A. K. M., van Dokkum, R. P. E., Kluppel, C. A., Jeronimus-Stratingh, C. M., Hut, F., de Zeeuw, D., et al. (2008). Therapeutic resistance to angiotensin converting enzyme (ACE) inhibition is related to pharmacodynamic and - kinetic factors in 5/6 nephrectomized rats. *Eur. J. Pharmacol.* 580, 231–240. doi: 10.1016/j.ejphar.2007.10.060

Yang, H.-C., Zuo, Y., and Fogo, A. B. (2010). Models of chronic kidney disease. *Drug Discov. Today Dis. Model.* 7, 13–19.

Zeng, L., Mathew, A. V., Byun, J., Atkins, K. B., Brosius, F. C., and Pennathur, S. (2018). Myeloperoxidase-derived oxidants damage artery wall proteins in an animal model of chronic kidney disease–accelerated atherosclerosis. *J. Biol. Chem.* 293, 7238–7249. doi: 10.1074/jbc.ra117.000559

General appearance:	Score
Normal	0
Slightly unkempt	1
Moderate piloerection	2
Marked piloerection (staring coat)	3
Slightly hunched	1
Markedly hunched	3
Weight and BC score:	**Score**
Normal - < 5% loss and/or BC3	0
Body wt. 5-10% loss and/or BC3/2	1
Body wt. 10-15% loss and/or BC2	2
Body wt. 15-20% loss and/or BC2/1	4
Body wt. ≥ 20% loss and/or BC1	5
Clinical signs:	**Score**
Soft stools	2
Laboured respiration	2
Dull, pale eyes	1
Semi-closed eyes	2
Less inquisitive than normal	1
Little interaction with peers	3
Totally "uninterested"/cold to the touch	5
Tremors/convulsions	5
Marked dehydration (skin pinch test)	4

Supplementary Table 1: Animal condition scoring criteria for STNx. A cumulative score of 5 for any individual mouse results in a mandatory schedule 1 cull for health reasons. BC = body condition score based on weight, with BC1 being emaciated and BC5 being obese.

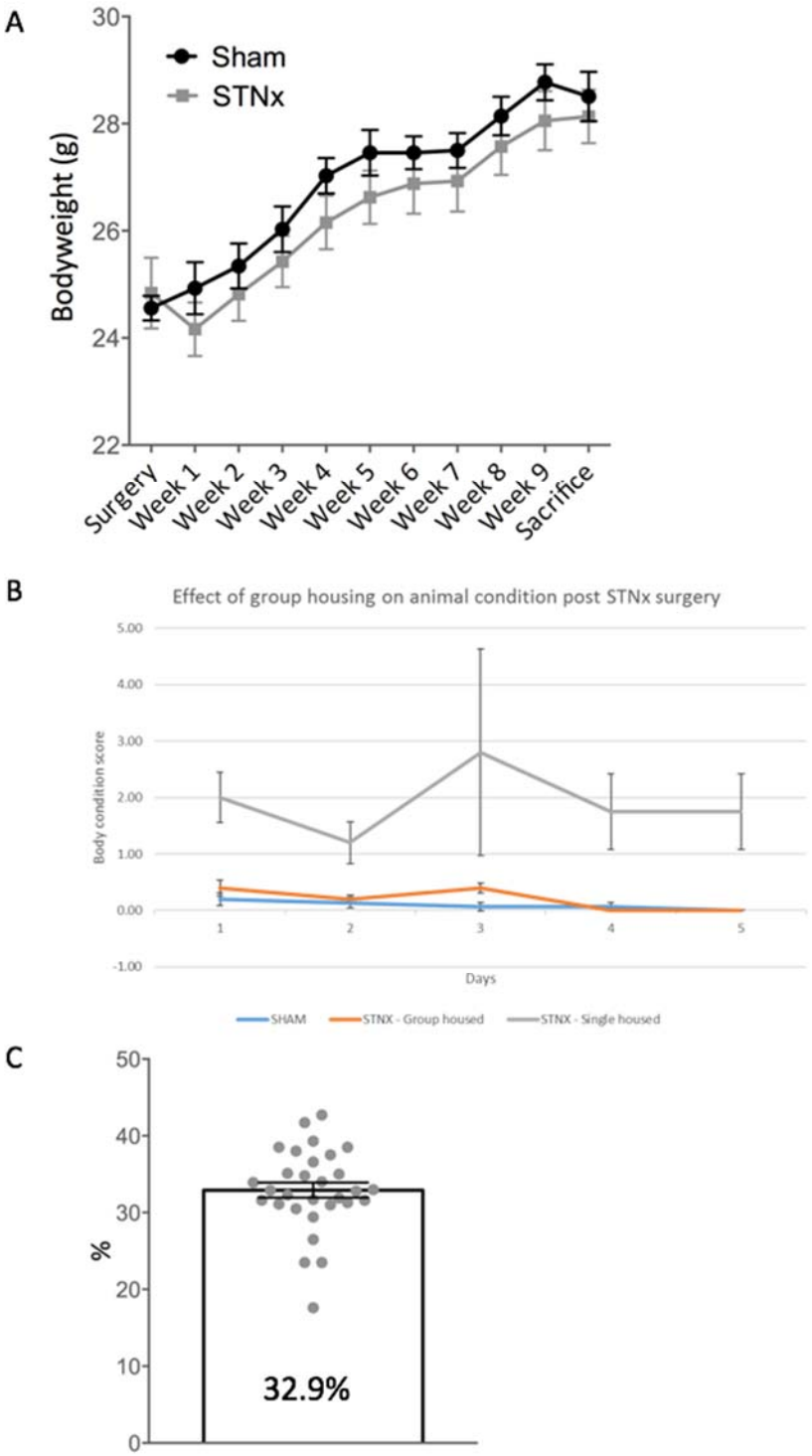

Supplementary Figure 1: Effect of single step flank subtotal nephrectomy on 129S2/SV animal condition. 129S2/SV mice had single-step flank STNX performed and were group housed unless indicated for the length of the study. A) Bodyweights of mice subjected to subtotal nephrectomy (STNx) or sham surgery were measured weekly to determine the effect of STNx on animal condition. Sham: n=7, STNx: n=11.

Statistical analysis was carried out (comparing sham vs STNx at each time-point) with correction for multiple comparisons via Holm-Sidak method. Plotted as mean ± SEM. B) Body condition was scored Day 1-5 post surgery. Analgesia was administered peri-operatively and day 1 post surgery. Sham: n=15, Group housed STNx: n=5, Single housed STNx n=5. C) The percentage of left kidney renal mass remaining following STNx surgery, across multiple experiments. Plotted as mean ± SEM. n=30.

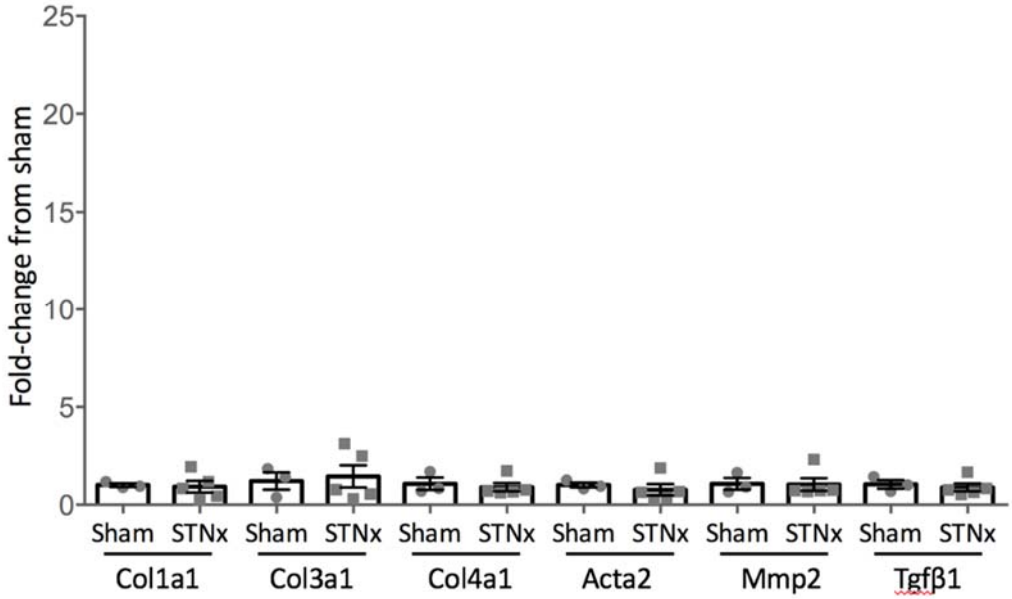

Supplementary Figure 2: Analysis of pro-fibrotic gene expression 6 weeks post single-step subtotal nephrectomy. 129S2/SV mice were subjected to flank single-step STNx or sham surgery and were culled 6-weeks post-surgery. Pro-fibrotic gene expression in whole kidney tissue was determined by quantitative real-time PCR (qRT-PCR) carried out with specific Taqman probes for each gene, normalised to housekeeper Ppia. Sham: n=3, STNx: n=5. Student's t-test was used for statistical analysis.

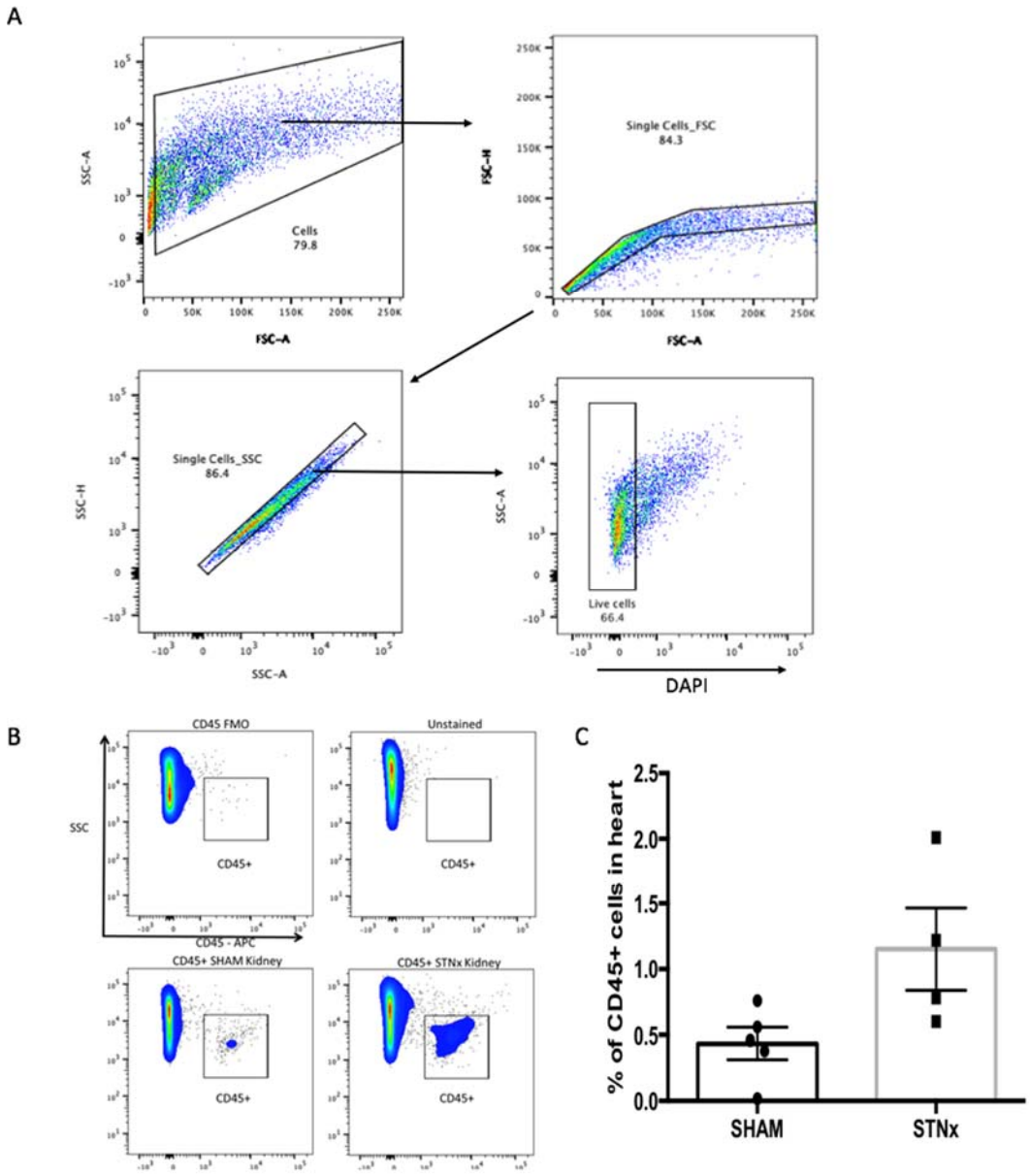

Supplementary Figure 3: Flow cytometry gating strategy and inflammatory infiltration into kidney following STNx surgery. A) Gating strategy utilised in flow cytometry analysis to determine live single cell population. B) SV129/S2 mice subjected to Sham or STNx surgery. Animals were culled 10 weeks post surgery, perfused and kidney placed into FACS buffer. Kidneys were digested and incubated with specific antibodies and analysed. Sham: n=5, STNx n=4 B) Example analysis of $CD45^+$ positive cells in the kidney following Sham or STNx surgery C) Quantification of $CD45^+$ positive cells in the heart Sham: n=5, STNx: n=4

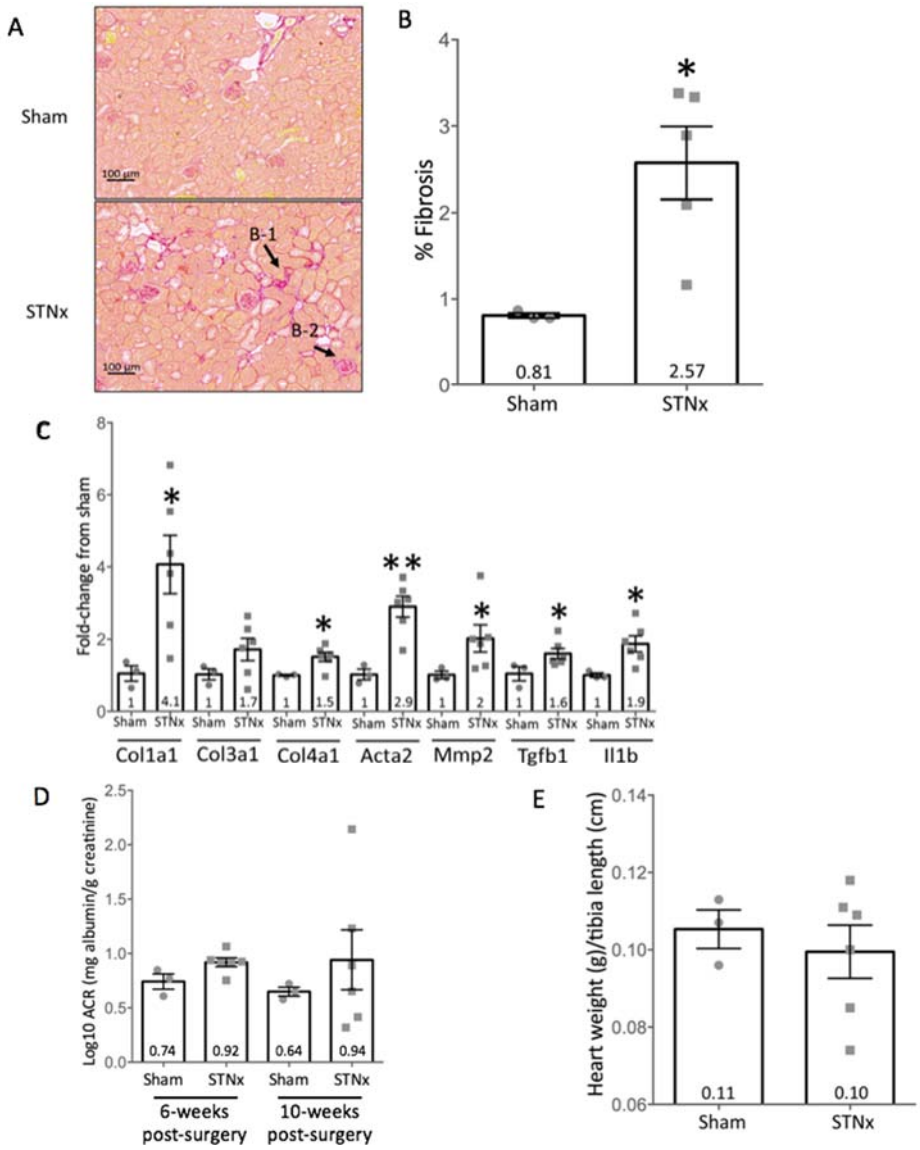

Supplementary Figure 4: Single-step flank STNx in C57 black background mice induces renal fibrosis without proteinuric disease. Gli1 reporter mice (Gli1 x Ai14 on a C57BL/6 background) were subjected to flank single-step STNx or sham surgery and were culled 10-weeks later. A) Picrosirius red staining for total collagen in kidneys. Exemplar images are provided at 5x magnification. B-1 = Tubulointerstitial fibrosis, B-2 = glomerulosclerosis. B) Quantification of picrosirius red staining carried out via Image-Pro Plus 7. Sham: n=3, STNx: n=5. Student's t-test was used for statistical analysis. * = $P \leq 0.05$. Plotted as mean ± SEM. n=1 STNx animal was excluded due to tissue section being too low quality to accurately quantify collagen. C) Pro-fibrotic gene expression in whole kidney using specific Taqman probes for each gene, normalised to housekeeper Ppia. Sham: n=3, STNx: n=5. Student's t-test was used for

statistical analysis. * = P ≤ 0.05, ** = P ≤ 0.01, *** = P ≤ 0.001. Plotted as mean ± SEM. D) Urinary albumin:creatinine ratio in mice 6 and 10-weeks post-STNx or sham surgery. Urine was collected overnight via metabolic cages from animals 6 and 10-weeks post-surgery. Albumin and creatinine content was determined via in-house biochemical analysis service. Sham: n=3, STNx: n=6. One-way ANOVA with Tukey's multiple comparison test was used for statistical analysis. Plotted as mean ± SEM. E) Heart weight at cull normalised to tibia length. Sham: n=3, STNx: n=6. Student's t-test was used for statistical analysis. Plotted as mean ± SEM.

Bibliography

1. Douglas Eaton, Pooler John, V. A. J. *Vander's Renal Physiology, 7th edition*. (2009).
2. Muir, W. W. Factors Influencing Analgesic Drug Selection, Dose, and Routes of Drug Administration. in *Handbook of Veterinary Pain Management: Third Edition* 302–334 (2014). doi:10.1016/B978-0-323-08935-7.00015-6.
3. Klaassen, C. D., Liu, J., Goyer, R. A. & Waalkes, M. P. *Casarett and Doull's Toxicology*. *The Basic Science of Poison* vol. 12 (2008).
4. Hill, N. R. *et al.* Global Prevalence of Chronic Kidney Disease – A Systematic Review and Meta-Analysis. *PLoS One* **11**, (2016).
5. Jha, V. *et al.* Chronic kidney disease: Global dimension and perspectives. *Lancet* **382**, 260–272 (2013).
6. McCulloch, C. E. *et al.* Trends in Prevalence of Chronic Kidney Disease in the United States. *Ann. Intern. Med.* **165**, 473 (2016).
7. Eckardt, K. *et al.* Evolving importance of kidney disease: from subspecialty to global health burden. *Lancet* **382**, 158–169 (2013).
8. Christensen, K., Doblhammer, G., Rau, R. & Vaupel, J. W. Ageing populations: the challenges ahead. *Lancet* **374**, 1196–1208 (2009).
9. Wang, H. *et al.* Global, regional, and national life expectancy, all-cause mortality, and cause-specific mortality for 249 causes of death, 1980–2015: a systematic analysis for the Global Burden of Disease Study 2015. *Lancet* **388**, 1459–1544 (2016).
10. Feldman, H. I. *et al.* KDOQI US Commentary on the 2012 KDIGO Clinical Practice Guideline for the Evaluation and Management of CKD. *Am. J. Kidney Dis.* **63**, 713–735 (2014).
11. Kanda, H. *et al.* Perioperative Management of Patients With End-Stage Renal Disease. *J. Cardiothorac. Vasc. Anesth.* **31**, 2251–2267 (2017).
12. Ballew, S. H. & Matsushita, K. Cardiovascular Risk Prediction in CKD. *Semin. Nephrol.* **38**, 208–216 (2018).
13. Kerr, M., Bray, B., Medcalf, J., O'Donoghue, D. J. & Matthews, B. Estimating the financial cost of chronic kidney disease to the NHS in England. *Nephrol. Dial. Transplant* **27 Suppl 3**, iii73-80 (2012).
14. Wang, X. & Garrett, M. R. Nephron number, hypertension, and CKD: physiological and genetic insight from humans and animal models. *Physiol. Genomics* **49**, 180–192 (2017).
15. Pasala, S. & Carmody, J. B. How to use… serum creatinine, cystatin C and GFR. *Arch. Dis. Child. Educ. Pract. Ed.* **102**, 37–43 (2017).
16. Soveri, I. *et al.* Measuring GFR: A systematic review. *Am. J. Kidney Dis.* **64**, 411–424 (2014).
17. Levey, A. S. Serum Creatinine as an Index of Renal Function: New Insights into Old Concepts. *CLIN. CHEM.* **38**, 1933–1953 (1992).
18. Levey, A. S., Inker, L. A. & Coresh, J. GFR estimation: From physiology to public health. *Am. J. Kidney Dis.* **63**, 820–834 (2014).

19. Shardlow, A. *et al.* The clinical utility and cost impact of cystatin C measurement in the diagnosis and management of chronic kidney disease: A primary care cohort study. *PLoS Med.* **14**, 1–18 (2017).
20. Herget-Rosenthal, S., Bökenkamp, A. & Hofmann, W. How to estimate GFR-serum creatinine, serum cystatin C or equations? *Clin. Biochem.* **40**, 153–161 (2007).
21. Mussap, M. *et al.* Cystatin C is a more sensitive marker than creatinine for the estimation of GFR in type 2 diabetic patients. *Kidney Int.* **61**, 1453–1461 (2002).
22. Hoek, F. J., Kemperman, F. A. W. & Krediet, R. T. A comparison between cystatin C, plasma creatinine and the Cockcroft and Gault formula for the estimation of glomerular filtration rate. *Nephrol. Dial. Transplant.* **18**, 2024–2031 (2003).
23. Wilkie, M. *et al.* Serum cystatin C measured by automated immunoassay: A more sensitive marker of changes in GFR than serum creatinine. *Kidney Int.* **47**, 312–318 (2007).
24. Peralta, C. A. *et al.* Detection of chronic kidney disease with creatinine, cystatin c, and urine albumin-to-creatinine ratio and association with progression to end-stage renal disease and mortality. *JAMA - J. Am. Med. Assoc.* **305**, 1545–1552 (2011).
25. Fraser, S. D., Roderick, P. J. & Taal, M. W. Where now for proteinuria testing in chronic kidney disease?: Good evidence can clarify a potentially confusing message. *Br. J. Gen. Pract.* **66**, 215–217 (2016).
26. Matsushita, K. *et al.* Estimated glomerular filtration rate and albuminuria for prediction of cardiovascular outcomes: A collaborative meta-analysis of individual participant data. *Lancet Diabetes Endocrinol.* **3**, 514–525 (2015).
27. Nauta, F. L. *et al.* Glomerular and tubular damage markers in individuals with progressive albuminuria. *Clin. J. Am. Soc. Nephrol.* **8**, 1106–1114 (2013).
28. He, X. M. & Carter, D. C. Atomic structure and chemistry of human serum albumin. *Nature* **358**, 932–935 (1992).
29. Gorriz, J. L. & Martinez-Castelao, A. Proteinuria: Detection and role in native renal disease progression. *Transplant. Rev.* **26**, 3–13 (2012).
30. Remuzzi, G. & Bertani, T. Is glomerulosclerosis a consequence of altered glomerular permeability to macromolecules? *Kidney Int.* **38**, 384–394 (1990).
31. Abbate, M., Zoja, C. & Remuzzi, G. How Does Proteinuria Cause Progressive Renal Damage? *J. Am. Soc. Nephrol.* **17**, 2974–2984 (2006).
32. Heerspink, H. J. L. & Gansevoort, R. T. Albuminuria Is an appropriate therapeutic target in patients with CKD: The pro view. *Clin. J. Am. Soc. Nephrol.* **10**, 1079–1088 (2015).
33. Agrawal, S., Guess, A. J., Chanley, M. A. & Smoyer, W. E. Albumin-induced podocyte injury and protection are associated with regulation of COX-2. *Kidney Int.* **86**, 1150–1160 (2014).
34. Dickson, L. E., Wagner, M. C., Sandoval, R. M. & Molitoris, B. A. The Proximal Tubule and Albuminuria: Really! *J. Am. Soc. Nephrol.* **25**, 443–453 (2014).
35. Birn, H. & Christensen, E. I. Renal albumin absorption in physiology and pathology. *Kidney Int.* **69**, 440–449 (2006).

36. Wang, Y., Rangan, G. K., Tay, Y.-C., Wang, Y. & Harris, D. C. H. Induction of monocyte chemoattractant protein-1 by albumin is mediated by nuclear factor κB in proximal tubule cells. *J. Am. Soc. Nephrol.* **10**, 1204–1213 (1999).
37. Habibi, J. *et al.* Albumin Activation of NAD(P)H Oxidase Activity Is Mediated via Rac1 in Proximal Tubule Cells. *Am. J. Nephrol.* **27**, 15–23 (2007).
38. Zoja, C. *et al.* Proximal tubular cell synthesis and secretion of endothelin-1 on challenge with albumin and other proteins. *Am. J. Kidney Dis.* **26**, 934–941 (1995).
39. Yard, B. A., Chorianopoulos, E., Herr, D. & Van Der Woude, F. J. Regulation of endothelin-1 and transforming growth factor-β1 production in cultured proximal tubular cells by albumin and heparan sulphate glycosaminoglycans. *Nephrol. Dial. Transplant.* **16**, 1769–1775 (2001).
40. Drumm, K., Bauer, B., Freudinger, R. & Gekle, M. Albumin Induces NF-κB Expression in Human Proximal Tubule-Derived Cells (IHKE-1). *Cell Physiol Biochem* **12**, 187–196 (2002).
41. Tang, S. *et al.* Albumin stimulates interleukin-8 expression in proximal tubular epithelial cells in vitro and in vivo Find the latest version : Albumin stimulates interleukin-8 expression in proximal tubular epithelial cells in vitro and in vivo. *J Clin Invest* **111**, 515–527 (2003).
42. Mao, W. *et al.* Albumin Stimulates the Accumulation of Extracellular Matrix in Renal Tubular Epithelial Cells. *Am. J. Nephrol.* **24**, 14–19 (2003).
43. Eddy, A. A. Proteinuria and interstitial injury. *Nephrol Dial Transpl.* **19**, 277–281 (2004).
44. Vervloet, M. G. *et al.* The role of phosphate in kidney disease. *Nat Rev Nephrol* vol. 13 27–38 (2017).
45. Felsenfeld, A. J., Levine, B. S. & Rodriguez, M. Pathophysiology of Calcium, Phosphorus, and Magnesium Dysregulation in Chronic Kidney Disease. *Semin. Dial.* **28**, 564–577 (2015).
46. Martin, K. J. & González, E. A. Prevention and control of phosphate retention/ hyperphosphatemia in CKD-MBD: What is normal, when to start, and how to treat? *Clin J Am Soc Nephrol* vol. 6 440–446 (2011).
47. Giachelli, C. M. Vascular calcification mechanisms. *Journal of the American Society of Nephrology* vol. 15 2959–2964 (2004).
48. Di Marco, G. S. *et al.* High phosphate directly affects endothelial function by downregulating annexin II. *Kidney Int.* **83**, 213–222 (2013).
49. Saleh, F. N., Schirmer, H., Sundsfjord, J. & Jorde, R. Parathyroid hormone and left ventricular hypertrophy. *Eur. Heart J.* **24**, 2054–2060 (2003).
50. Vanholder, R., Gryp, T. & Glorieux, G. Urea and chronic kidney disease: The comeback of the century? (in uraemia research). *Nephrol. Dial. Transplant.* **33**, 4–12 (2018).
51. Almeras, C. & Argilés, À. The general picture of uremia. *Semin. Dial.* **22**, 329–333 (2009).
52. Lau, W. L. & Vaziri, N. D. Urea, a true uremic toxin: the empire strikes back. *Clin. Sci.* **131**, 3–12 (2016).
53. Cohen, D. M., Gullans, S. R. & Chin, W. W. Urea inducibility of egr-1 in murine

inner medullary collecting duct cells is mediated by the serum response element and adjacent Ets motifs. *J. Biol. Chem.* **271**, 12903–12908 (1996).
54. Cohen, D. M. Urea-associated oxidative stress and Gadd153/CHOP induction. *Am J Physiol* **276**, F786-93 (1999).
55. D'Apolito, M. *et al.* Urea-induced ROS generation causes insulin resistance in mice with chronic renal failure. *J. Clin. Invest.* **120**, 203–213 (2010).
56. Trécherel, E. *et al.* Upregulation of BAD, a pro-apoptotic protein of the BCL2 family, in vascular smooth muscle cells exposed to uremic conditions. *Biochem. Biophys. Res. Commun.* **417**, 479–483 (2012).
57. Vaziri, N. D., Yuan, J. & Norris, K. Role of urea in intestinal barrier dysfunction and dysruption of epithelial tight junction in CKD. *Am. J. Nephrol.* **37**, 1–6 (2014).
58. D'Apolito, M. *et al.* Urea-induced ROS cause endothelial dysfunction in chronic renal failure. *Atherosclerosis* **239**, 393–400 (2015).
59. Manning Fox, J. E. *et al.* Urea impairs β cell glycolysis and insulin secretion in chronic kidney disease. *J. Clin. Invest.* **126**, 3598–3612 (2016).
60. House, A. A., Haapio, M., Lassus, J., Bellomo, R. & Ronco, C. Therapeutic strategies for heart failure in cardiorenal syndromes. *Am. J. Kidney Dis.* **56**, 759–773 (2010).
61. Umanath, K. & Emani, S. Getting to the Heart of the Matter: Review of Treatment of Cardiorenal Syndrome. *Adv. Chronic Kidney Dis.* **24**, 261–266 (2017).
62. Rangaswami, J. *et al. Cardiorenal Syndrome: Classification, Pathophysiology, Diagnosis, and Treatment Strategies: A Scientific Statement From the American Heart Association*. *Circulation* vol. 139 (2019).
63. Schrier, R. W. Cardiorenal versus renocardiac syndrome: is there a difference? *Nat. Clin. Pract. Nephrol.* **3**, 637–637 (2007).
64. Takahama, H. & Kitakaze, M. Pathophysiology of cardiorenal syndrome in patients with heart failure: potential therapeutic targets. *Am. J. Physiol. Circ. Physiol.* **313**, H715–H721 (2017).
65. Weiner, D. E. *et al.* Chronic Kidney Disease as a Risk Factor for Cardiovascular Disease and All-Cause Mortality: A Pooled Analysis of Community-Based Studies. *J. Am. Soc. Nephrol.* **15**, 1307–1315 (2004).
66. Di, L. *et al.* Chronic kidney disease and Cardiovascular complications. *Hear. Fail Rev* **20**, 259–272 (2015).
67. Chitturi, C. & Novak, J. E. Diuretics in the Management of Cardiorenal Syndrome. *Adv. Chronic Kidney Dis.* **25**, 425–433 (2018).
68. Zoccali, C. *et al.* Prognostic Value of Echocardiographic Indicators of Left Ventricular Systolic Function in Asymptomatic Dialysis Patients. *J. Am. Soc. Nephrol.* **15**, 1029–1037 (2004).
69. Middleton, R. J. Left ventricular hypertrophy in the renal patient. *J. Am. Soc. Nephrol.* **12**, 1079–1084 (2001).
70. Shlipak, M. G. *et al.* Cardiovascular Mortality Risk in Chronic Kidney Disease. *Jama* **293**, 1737 (2005).
71. Di Lullo, L., Gorini, A., Russo, D., Santoboni, A. & Ronco, C. Left Ventricular

Hypertrophy in Chronic Kidney Disease Patients: From Pathophysiology to Treatment. *CardioRenal Med.* **5**, 254–266 (2015).
72. London, G. M. *et al.* Alterations of left ventricular hypertrophy in and survival of patients receiving hemodialysis: follow-up of an interventional study. *J. Am. Soc. Nephrol.* **12**, 2759–67 (2001).
73. Grabner, A. & Faul, C. The role of fibroblast growth factor 23 and Klotho in uremic cardiomyopathy. *Curr. Opin. Nephrol. Hypertens.* **25**, 314–324 (2016).
74. McCullough, P. A. Why is chronic kidney disease the 'spoiler' for cardiovascular outcomes? *J. Am. Coll. Cardiol.* **41**, 725–728 (2003).
75. Suresh, H., B.S., A., Moger, V. & Swamy, M. Cardiorenal syndrome type 4: A study of cardiovascular diseases in chronic kidney disease. *Indian Heart J.* **69**, 11–16 (2017).
76. Bülow, R. D. & Boor, P. Extracellular Matrix in Kidney Fibrosis: More Than Just a Scaffold. *J. Histochem. Cytochem.* (2019) doi:10.1369/0022155419849388.
77. Hewitson, T. D., Holt, S. G. & Smith, E. R. Progression of tubulointerstitial fibrosis and the chronic kidney disease phenotype - Role of risk factors and epigenetics. *Front. Pharmacol.* **8**, 1–8 (2017).
78. Hewitson, T. D. Renal tubulointerstitial fibrosis: common but never simple. *Am J Physiol Ren. Physiol* **296**, F1239–F1244 (2009).
79. Genovese, F., Manresa, A. A., Leeming, D. J., Karsdal, M. A. & Boor, P. The extracellular matrix in the kidney: A source of novel non-invasive biomarkers of kidney fibrosis? *Fibrogenes. Tissue Repair* **7**, 1–14 (2014).
80. Nath, K. A. Tubulointerstitial Changes as a Major Determinant in the Progression of Renal Damage. *Am. J. Kidney Dis.* **20**, 1–17 (1992).
81. Nogueira, A., Pires, M. J. & Oliveira, P. A. Pathophysiological Mechanisms of Renal Fibrosis: A Review of Animal Models and Therapeutic Strategies. *In Vivo (Brooklyn).* **31**, 1–22 (2017).
82. Johnson, R. J. Mechanisms of Progressive Glomerulosclerosis and Tubulointerstitial Fibrosis. *Front. Nephrol.* **2**, 307–312 (1998).
83. Zeisberg, M. & Neilson, E. G. Mechanisms of tubulointerstitial fibrosis. *J. Am. Soc. Nephrol.* **21**, 1819–34 (2010).
84. Gewin, L., Zent, R. & Pozzi, A. Progression of chronic kidney disease: too much cellular talk causes damage. *Kidney Int.* **91**, 552–560 (2017).
85. Sureshbabu, A., Muhsin, S. A. & Choi, M. E. TGF-β signaling in the kidney: profibrotic and protective effects. *Am. J. Physiol. Physiol.* **310**, F596–F606 (2016).
86. Meng, X.-M., Tang, P. M.-K., Li, J. & Lan, H. Y. TGF-β/Smad signaling in renal fibrosis. *Front. Physiol.* **6**, 82 (2015).
87. Shi, M. *et al.* Latent TGF-β structure and activation. *Nature* **474**, 343–351 (2011).
88. Horiguchi, M., Ota, M. & Rifkin, D. B. Matrix control of transforming growth factor-β function. *J. Biochem.* **152**, 321–329 (2012).
89. Munger, J. S. *et al.* The integrin αvβ6 binds and activates latent TGFβ1: A mechanism for regulating pulmonary inflammation and fibrosis. *Cell* **96**, 319–328 (1999).

90. Qin, Y. & Ivan, S. Cell surface-localized matrix metalloproteinase-9 proteolytically activates TGF-β and promotes tumor invasion and angiogenesis. *Genes Dev.* **14**, 163–176 (2000).
91. Taipale, J., Miyazono, K., Heldin, C. H. & Keski-Oja, J. Latent transforming growth factor-β1 associates to fibroblast extracellular matrix via latent TGF-β binding protein. *J. Cell Biol.* **124**, 171–181 (1994).
92. Barcellos-Hoff, M. H. & Dix, T. A. Redox-mediated activation of latent transforming growth factor-beta 1. *Mol. Endocrinol.* **10**, 1077–1083 (2014).
93. Wipff, P. J. & Hinz, B. Integrins and the activation of latent transforming growth factor β1 - An intimate relationship. *Eur. J. Cell Biol.* **87**, 601–615 (2008).
94. Shi, Y. & Massagué, J. Mechanisms of TGF-Signaling from Cell Membrane to the Nucleus have been observed in both TGF-family receptors and the Smad proteins. The TGF-type II receptor is inacti-vated by mutation in most human gastrointestinal can. *Cell* **113**, 685–700 (2003).
95. Chen, S. J. *et al.* Stimulation of type I collagen transcription in human skin fibroblasts by TGF-β: Involvement of Smad 3. *J. Invest. Dermatol.* **112**, 49–57 (1999).
96. Verrecchia, F. *et al.* Smad3/AP-1 interactions control transcriptional responses to TGF-β in a promoter-specific manner. *Oncogene* **20**, 3332–3340 (2001).
97. Meng, X.-M., Chung, A. C. K. & Lan, H. Y. Role of the TGF-β/BMP-7/Smad pathways in renal diseases. *Clin. Sci.* **124**, 243–254 (2012).
98. Sparks, M. A., Crowley, S. D., Gurley, S. B., Mirotsou, M. & Coffman, T. M. Classical Renin-Angiotensin system in kidney physiology. *Compr. Physiol.* **4**, 1201–28 (2014).
99. Nishimura, H. *Renin-angiotensin system in vertebrates : phylogenetic view of structure and function*. *Anatomical Science International* vol. 92 (Springer Japan, 2017).
100. Mezzano, S. A., Ruiz-Ortega, M. & Egido, J. Angiotensin II and renal fibrosis. *Hypertens. (Dallas, Tex. 1979)* **38**, 635–8 (2001).
101. Xu, Z. *et al.* Angiotensin II induces kidney inflammatory injury and fibrosis through binding to myeloid differentiation protein-2 (MD2). *Sci. Rep.* **7**, 1–11 (2017).
102. Georgianos, P. I. & Agarwal, R. Revisiting RAAS blockade in CKD with newer potassium-binding drugs. *Kidney Int.* **93**, 325–334 (2018).
103. Lv, W., Booz, G. W., Wang, Y., Fan, F. & Roman, R. J. Inflammation and renal fibrosis: Recent developments on key signaling molecules as potential therapeutic targets. *Eur. J. Pharmacol.* **820**, 65–76 (2018).
104. Klahr, S. & Morrissey, J. J. The role of vasoactive compounds, growth factors and cytokines in the progression of renal disease. *Kidney Int.* **57**, 7–14 (2004).
105. Quiroga, B. Present and Future in the Treatment of Diabetic Kidney Disease. *J. Diabetes Res.* 1–13 (2015).
106. Eddy, A. A. Overview of the cellular and molecular basis of kidney fibrosis. *Kidney Int. Suppl.* **4**, 2–8 (2014).
107. Pakshir, P. & Hinz, B. The big five in fibrosis: Macrophages, myofibroblasts, matrix, mechanics, and miscommunication. *Matrix Biol.* **68–69**, 81–93 (2018).

108. Glasser, S. W. *et al.* Mechanisms of Lung Fibrosis Resolution. *Am. J. Pathol.* **186**, 1066–1077 (2016).
109. Hinz, B. Myofibroblasts. *Exp. Eye Res.* **142**, 56–70 (2015).
110. Djudjaj, S. & Boor, P. Cellular and molecular mechanisms of kidney fibrosis. *Mol. Aspects Med.* **65**, 16–36 (2019).
111. Humphreys, B. D. Mechanisms of Renal Fibrosis. *Annu. Rev. Physiol.* **80**, 309–326 (2018).
112. Gerarduzzi, C. & Di Battista, J. A. Myofibroblast repair mechanisms post-inflammatory response: a fibrotic perspective. *Inflamm. Res.* **66**, 451–465 (2017).
113. Hinz, B. The myofibroblast: Paradigm for a mechanically active cell. *J. Biomech.* **43**, 146–155 (2010).
114. Bechtel, W. *et al.* Methylation determines fibroblast activation and fibrogenesis in the kidney. *Nat. Med.* **16**, 544–550 (2010).
115. Gewin, L. S. Renal fibrosis: Primacy of the proximal tubule. *Matrix Biol.* **68**–**69**, 248–262 (2018).
116. Mack, M. & Yanagita, M. Origin of myofibroblasts and cellular events triggering fibrosis. *Kidney Int.* **87**, 297–307 (2015).
117. Asada, N. *et al.* Dysfunction of fibroblasts of extrarenal origin underlies renal fibrosis and renal anemia in mice. *J. Clin. Invest.* **121**, 3981–3990 (2011).
118. Humphreys, B. D. *et al.* Fate tracing reveals the pericyte and not epithelial origin of myofibroblasts in kidney fibrosis. *Am. J. Pathol.* **176**, 85–97 (2010).
119. Kramann, R. *et al.* Perivascular Gli1+ progenitors are key contributors to injury-induced organ fibrosis. *Cell Stem Cell* **16**, 51–66 (2015).
120. Kramann, R., Wongboonsin, J., Chang-Panesso, M., Machado, F. G. & Humphreys, B. D. Gli1 + Pericyte Loss Induces Capillary Rarefaction and Proximal Tubular Injury. *J. Am. Soc. Nephrol.* **28**, 776–784 (2017).
121. Lebleu, V. S. *et al.* Origin and function of myofibroblasts in kidney fibrosis. *Nat. Med.* **19**, 1047–1053 (2013).
122. Tang, P. M. K., Nikolic-Paterson, D. J. & Lan, H. Y. Macrophages: versatile players in renal inflammation and fibrosis. *Nat. Rev. Nephrol.* **15**, 144–158 (2019).
123. Isbel, N. M. *et al.* Tubules are the major site of M-CSF production in experimental kidney disease: Correlation with local macrophage proliferation. *Kidney Int.* **60**, 614–625 (2001).
124. Isbel, N. M., Nikolic-Paterson, D. J., Hill, P. A., Dowling, J. & Atkins, R. C. Local macrophage proliferation correlates with increased renal M-CSF expression in human glomerulonephritis. *Nephrol. Dial. Transplant.* **16**, 1638–1647 (2001).
125. Pan, B., Liu, G., Jiang, Z. & Zheng, D. Regulation of renal fibrosis by macrophage polarization. *Cell. Physiol. Biochem.* **35**, 1062–1069 (2015).
126. Jose, M. D., Le Meur, Y., Atkins, R. C. & Chadban, S. J. Blockade of macrophage colony-stimulating factor reduces macrophage proliferation and accumulation in renal allograft rejection. *Am. J. Transplant.* **3**, 294–300 (2003).
127. Le Meur, Y. *et al.* Macrophage accumulation at a site of renal inflammation is dependent on the M-CSF/c-fms pathway. *J Leukoc Biol* **72**, 530–537 (2002).

128. Lim, A. K. H. *et al.* Antibody blockade of c-fms suppresses the progression of inflammation and injury in early diabetic nephropathy in obese db/db mice. *Diabetologia* **52**, 1669–1679 (2009).
129. Haller, H., Bertram, A., Nadrowitz, F. & Menne, J. Monocyte chemoattractant protein-1 and the kidney. *Curr. Opin. Nephrol. Hypertens.* **25**, 42–49 (2016).
130. Li, L. The chemokine receptors CCR2 and CX3CR1 mediate monocyte/ macrophage trafficking in kidney ischemia–reperfusion injury. *Kidney Int.* **74**, 736-7401526–1537 (2008).
131. Awad, A. S. Macrophage-derived Tumor Necrosis Factor-α mediates diabetic renal injury. *Kidney Int.* **88**, 722–733 (2015).
132. Lan, H. Y., Nikolic-Paterson, D. J., Zarama, M., Vannice, J. L. & Atkins, R. C. Suppression of experimental crescentic glomerulonephritis by the interleukin-1 receptor antagonist. *Kidney Int.* **43**, 479–485 (1993).
133. Lee, S. *et al.* Distinct Macrophage Phenotypes Contribute to Kidney Injury and Repair. *J. Am. Soc. Nephrol.* **22**, 317–326 (2011).
134. Zhang, M. Z. *et al.* IL-4/IL-13–mediated polarization of renal macrophages/dendritic cells to an M2a phenotype is essential for recovery from acute kidney injury. *Kidney Int.* **91**, 375–386 (2017).
135. Klessens, C. Q. F. *et al.* Macrophages in diabetic nephropathy in patients with type 2 diabetes. *Nephrol. Dial. Transplant.* **32**, 1322–1329 (2017).
136. Ikezumi, Y. *et al.* Identification of alternatively activated macrophages in new-onset paediatric and adult immunoglobulin A nephropathy: Potential role in mesangial matrix expansion. *Histopathology* **58**, 198–210 (2011).
137. Ikezumi, Y. *et al.* Alternatively activated macrophages in the pathogenesis of chronic kidney allograft injury. *Pediatr. Nephrol.* **30**, 1007–1017 (2015).
138. Kim, M. G. *et al.* The role of M2 macrophages in the progression of chronic kidney disease following acute kidney injury. *PLoS One* **10**, 1–17 (2015).
139. Liu, B. C., Tang, T. T., Lv, L. L. & Lan, H. Y. Renal tubule injury: a driving force toward chronic kidney disease. *Kidney Int.* **93**, 568–579 (2018).
140. Chevalier, R. L. The proximal tubule is the primary target of injury and progression of kidney disease: role of the glomerulotubular junction. *Am. J. Physiol. Renal Physiol.* **311**, F145-61 (2016).
141. Cristofori, P., Zanetti, E., Fregona, D., Piaia, A. & Trevisan, A. Renal proximal tubule segment-specific nephrotoxicity: An overview on biomarkers and histopathology. *Toxicol. Pathol.* **35**, 270–275 (2007).
142. Kalakeche, R. *et al.* Endotoxin Uptake by S1 Proximal Tubular Segment Causes Oxidative Stress in the Downstream S2 Segment. *J. Am. Soc. Nephrol.* **22**, 1505–1516 (2011).
143. Takaori, K. *et al.* Severity and Frequency of Proximal Tubule Injury Determines Renal Prognosis. *J. Am. Soc. Nephrol.* **27**, 2393–2406 (2016).
144. Thadhani, R. Acute Renal Failure. *N. Engl. J. Med.* **334**, 1448–1460 (1996).
145. Bonventre, J. V. Primary proximal tubule injury leads to epithelial cell cycle arrest, fibrosis, vascular rarefaction, and glomerulosclerosis. *Kidney Int. Suppl.* **4**, 39–44 (2014).
146. Yang, L., Besschetnova, T. Y., Brooks, C. R., Shah, J. V. & Bonventre, J. V.

Epithelial cell cycle arrest in G2/M mediates kidney fibrosis after injury. *Nat. Med.* **16**, 535–543 (2010).
147. Kang, H. M. *et al.* Defective fatty acid oxidation in renal tubular epithelial cells plays a key role in kidney fibrosis development. *Nat. Med.* **21**, 37–46 (2015).
148. Susztak, K., Ciccone, E., McCue, P., Sharma, K. & Böttinger, E. P. Multiple metabolic hits converge on CD36 as novel mediator of tubular epithelial apoptosis in diabetic nephropathy. *PLoS Med.* **2**, 0152–0161 (2005).
149. Tran, M. *et al.* PGC-1α promotes recovery after acute kidney injury during systemic inflammation in mice. *J Clin iInvest* **121**, 4003–4014 (2011).
150. Jourde-Chiche, N. *et al.* Endothelium structure and function in kidney health and disease. *Nat. Rev. Nephrol.* **15**, 87–108 (2019).
151. Verma, S. K. & Molitoris, B. A. Renal Endothelial Injury and Microvascular Dysfunction in Acute Kidney Injury. *Semin. Nephrol.* **35**, 96–107 (2015).
152. Miner, J. H. The glomerular basement membrane. *Exp. Cell Res.* **318**, 973–978 (2012).
153. Ballermann, B. J. & Obeidat, M. Tipping the balance from angiogenesis to fibrosis in CKD. *Kidney Int. Suppl.* **4**, 45–52 (2014).
154. Tanaka, S., Tanaka, T. & Nangaku, M. Hypoxia and Dysregulated Angiogenesis in Kidney Disease. *Kidney Dis.* **1**, 80–89 (2015).
155. Lipphardt, M. *et al.* The third path of tubulointerstitial fibrosis: aberrant endothelial secretome. *Kidney Int.* **92**, 558–568 (2017).
156. Rafii, S., Butler, J. M. & Ding, B. Sen. Angiocrine functions of organ-specific endothelial cells. *Nature* **529**, 316–325 (2016).
157. Bábíčková, J. *et al.* Regardless of etiology, progressive renal disease causes ultrastructural and functional alterations of peritubular capillaries. *Kidney Int.* **91**, 70–85 (2017).
158. Kida, Y., Tchao, B. N. & Yamaguchi, I. Peritubular capillary rarefaction: A new therapeutic target in chronic kidney disease. *Pediatr. Nephrol.* **29**, 333–342 (2014).
159. Afsar, B. *et al.* Capillary rarefaction from the kidney point of view. *Clin. Kidney J.* **11**, 295–301 (2018).
160. Ucero, A. C. *et al.* Unilateral ureteral obstruction: Beyond obstruction. *Int. Urol. Nephrol.* **46**, 765–776 (2014).
161. Hesketh, E. E. *et al.* A Murine Model of Irreversible and Reversible Unilateral Ureteric Obstruction. *J. Vis. Exp.* 1–6 (2014) doi:10.3791/52559.
162. Ucero, A. C. *et al.* TNF-related weak inducer of apoptosis (TWEAK) promotes kidney fibrosis and Ras-dependent proliferation of cultured renal fibroblast. *Biochim. Biophys. Acta - Mol. Basis Dis.* **1832**, 1744–1755 (2013).
163. Chevalier, R. L., Forbes, M. S. & Thornhill, B. A. Ureteral obstruction as a model of renal interstitial fibrosis and obstructive nephropathy. *Kidney Int.* **75**, 1145–1152 (2009).
164. Yang, M. *et al.* Role of sirolimus in renal tubular apoptosis in response to unilateral ureteral obstruction. *Int. J. Med. Sci.* **15**, 1433–1442 (2018).
165. Vaughan, E. D., Marion, D., Poppas, D. P. & Felsen, D. Pathophysiology of unilateral ureteral obstruction: Studies from Charlottesville to New York. *J.*

Urol. **172**, 2563–2569 (2004).
166. Arendshorst, W. J., Finn, W. F. & Gottschalk, C. W. Nephron stop flow pressure response to obstruction for 24 hours in the rat kidney. *J. Clin. Invest.* **53**, 1497–1500 (1974).
167. Klahr, S. & Morrissey, J. Obstructive nephropathy and renal fibrosis. *Am. J. Physiol. Physiol.* **283**, F861–F875 (2015).
168. Docherty, N. G., O'Sullivan, O. E., Healy, D. A., Fitzpatrick, J. M. & Watson, R. W. G. Evidence that inhibition of tubular cell apoptosis protects against renal damage and development of fibrosis following ureteric obstruction. *Am. J. Physiol. Physiol.* **290**, F4–F13 (2005).
169. Hotter, G., Palacios, L. & Sola, A. Low O 2 and high CO 2 in LLC-PK1 cells culture mimics renal ischemia-induced apoptosis. *Lab. Investig.* **84**, 213–220 (2004).
170. Eddy, A. A., López-Guisa, J. M., Okamura, D. M. & Yamaguchi, I. Investigating mechanisms of chronic kidney disease in mouse models. *Pediatr. Nephrol.* **27**, 1233–1247 (2012).
171. Li, L., Zepeda-Orozco, D., Black, R. & Lin, F. Autophagy is a component of epithelial cell fate in obstructive uropathy. *Am. J. Pathol.* **176**, 1767–1778 (2010).
172. Cochrane, A. L. *et al.* Renal Structural and Functional Repair in a Mouse Model of Reversal of Ureteral Obstruction. *J. Am. Soc. Nephrol.* **16**, 3623–3630 (2005).
173. Tapmeier, T. T. *et al.* Reimplantation of the ureter after unilateral ureteral obstruction provides a model that allows functional evaluation. *Kidney Int.* **73**, 885–889 (2008).
174. Song, J. *et al.* A modified relief of unilateral ureteral obstruction model. *Ren. Fail.* **41**, 497–506 (2019).
175. Chaabane, W. *et al.* Renal functional decline and glomerulotubular injury are arrested but not restored by release of unilateral ureteral obstruction (UUO). *Am. J. Physiol. Physiol.* **304**, F432–F439 (2012).
176. Puri, T. S. *et al.* Chronic kidney disease induced in mice by reversible unilateral ureteral obstruction is dependent on genetic background. *Am. J. Physiol. Physiol.* **298**, F1024–F1032 (2010).
177. Chow, K. M., Liu, Z. C. & Chang, T. M. S. Animal remnant kidney model of chronic renal failure revisited. *Hong Kong J. Nephrol.* **5**, 57–64 (2003).
178. PEARCE, R. M. The Influence of the Reduction of Kidney Substance upon Nitrogenous Metabolism. *Am. J. Med. Sci.* **137**, 128 (1909).
179. Bradford, J. R. The results following partial Nephrectomy and the influence of the Kidney on Metabolism. *J. Physiol.* **23**, 415–496 (1899).
180. Chanutin, A. Experimental renal insufficiency produced by partial nephrectomy. *Arch Intern Med* **58**, 60–80 (1936).
181. Leelahavanichkul, A. *et al.* Angiotensin II overcomes strain-dependent resistance of rapid CKD progression in a new remnant kidney mouse model. *Kidney Int.* **78**, 1136–1153 (2010).
182. López-Novoa, J. M., Martínez-Salgado, C., Rodríguez-Peña, A. B. & Hernández, F. J. L. Common pathophysiological mechanisms of chronic kidney disease: Therapeutic perspectives. *Pharmacol. Ther.* **128**, 61–81 (2010).

183. Kriz, W. & LeHir, M. Pathways to nephron loss starting from glomerular diseases - Insights from animal models. *Kidney Int.* **67**, 404–419 (2005).
184. Schnaper, H. W. Remnant nephron physiology and the progression of chronic kidney disease. *Pediatr. Nephrol.* **29**, 193–202 (2014).
185. Remuzzi, G. PATHOPHYSIOLOGY OF PROGRESSIVE NEPHROPATHIES. *N. Engl. J. Med.* **339**, 1448–1456 (1998).
186. Kren, S. & Hostetter, T. H. The course of the remnant kidney model in mice. *Kidney Int.* **56**, 333–337 (1999).
187. Wang, Q. *et al.* Blood pressure, cardiac, and renal responses to salt and deoxycorticosterone acetate in mice: Role of renin genes. *J. Am. Soc. Nephrol.* **13**, 1509–1516 (2002).
188. Anderson, S., Rennke, H. G. & Brenner, B. M. Therapeutic advantage of converting enzyme inhibitors in arresting progressive renal disease associated with systemic hypertension in the rat. *J. Clin. Invest.* **77**, 1993–2000 (1986).
189. Dilauro, M., Zimpelmann, J., Robertson, S. J., Genest, D. & Burns, K. D. Effect of ACE2 and angiotensin-(1–7) in a mouse model of early chronic kidney disease. *Am J Physiol Ren. Physiol* **298**, F1523–F1532 (2010).
190. Windt, W. A. K. M. *et al.* Therapeutic resistance to angiotensin converting enzyme (ACE) inhibition is related to pharmacodynamic and -kinetic factors in 5/6 nephrectomized rats. *Eur. J. Pharmacol.* **580**, 231–240 (2008).
191. Meyer, T. W., Anderson, S., Rennke, H. G. & Brenner, B. M. Converting enzyme inhibitor therapy limits progressive glomerular injury in rats with renal insufficiency. *Am. J. Med.* **79**, 31–36 (1985).
192. Siedlecki, A. M., Jin, X. & Muslin, A. J. Uremic cardiac hypertrophy is reversed by rapamycin but not by lowering of blood pressure. *Kidney Int.* **75**, 800–808 (2009).
193. Kennedy, D. J. *et al.* Partial nephrectomy as a model for uremic cardiomyopathy in the mouse. *Am J Physiol Ren. Physiol.* **294**, F450–F454 (2008).
194. Zeng, L. *et al.* Myeloperoxidase-derived oxidants damage artery wall proteins in an animal model of chronic kidney disease–accelerated atherosclerosis. *J. Biol. Chem.* **293**, 7238–7249 (2018).
195. Purnomo, E. *et al.* Glycosaminoglycan overproduction in the aorta increases aortic calcification in murine chronic kidney disease. *J. Am. Heart Assoc.* **2**, 1–18 (2013).
196. Ma, L.-J. & Fogo, A. B. Model of robust induction of glomerulosclerosis in mice : Importance of genetic background. *Kidney Int* **64**, 350–355 (2003).
197. Gava, A. L., Freitas, F. P., Balarini, C. M., Vasquez, E. C. & Meyrelles, S. S. Effects of 5/6 nephrectomy on renal function and blood pressure in mice. *Int. J. Physiol. Pathophysiol. Pharmacol.* **4**, 167–73 (2012).
198. Ortiz, A. *et al.* Translational value of animal models of kidney failure. *Eur. J. Pharmacol.* **759**, 205–220 (2015).
199. Bhaskaran, M. & Mohan, M. MicroRNAs: history, biogenesis, and their evolving role in animal development and disease. *Vet. Pathol.* **51**, 759–74 (2014).
200. Sanjay, S. & Girish, C. Role of miRNA and its potential as a novel diagnostic

biomarker in drug-induced liver injury. *Eur J Clin Pharmacol* **73**, 399–407 (2017).
201. Bekris, L. M. & Leverenz, J. B. The biomarker and therapeutic potential of miRNA in Alzheimer's disease. *Neurodegener Dis Manag* **5**, 61–74 (2015).
202. Mayr, B., Niebauer, J. & Breitenbach-Koller, H. Circulating miRNAs as predictors for morbidity and mortality in coronary artery disease. *Mol. Biol. Rep.* 1–5 (2019) doi:10.1007/s11033-019-04963-9.
203. Nappi, L. & Nichols, C. MicroRNAs as Biomarkers for Germ Cell Tumors. *Urol. Clin. North Am.* **46**, 449–457 (2019).
204. Angelucci, F. *et al.* MicroRNAs in Alzheimer's Disease: Diagnostic Markers or Therapeutic Agents? *Front. Pharmacol.* **10**, 1–9 (2019).
205. Shabaninejad, Z. *et al.* Electrochemical-based biosensors for microRNA detection: Nanotechnology comes into view. *Anal. Biochem.* **581**, 113349 (2019).
206. Ha, M. & Kim, V. N. Regulation of microRNA biogenesis. *Nat. Rev. Mol. Cell Biol.* **15**, 509–524 (2014).
207. Davis-Dusenbery, B. N. & Hata, A. Mechanisms of control of microRNA biogenesis. *Journal of Biochemistry* vol. 148 381–392 (2010).
208. AM, D., BB, T., RH, P., RF, K. & GJ, H. Processing of primary microRNAs by the Microprocessor complex. *Nature* **432**, 231–235 (2004).
209. Lund, E., Güttinger, S., Calado, A., Dahlberg, J. E. & Kutay, U. Nuclear Export of MicroRNA. *Science (80-.).* **303**, 95–98 (2004).
210. Park, J. E. *et al.* Dicer recognizes the 5′ end of RNA for efficient and accurate processing. *Nature* **475**, 201–205 (2011).
211. Daugaard, I. & Hansen, T. B. Biogenesis and Function of Ago-Associated RNAs. *Trends in Genetics* vol. 33 208–219 (2017).
212. Huntzinger, E. & Izaurralde, E. Gene silencing by microRNAs: contributions of translational repression and mRNA decay. *Nat. Rev. Genet.* **12**, 99–110 (2011).
213. Wu, H., Ye, C., Ramirez, D. & Manjunath, N. Alternative processing of primary microRNA transcripts by Drosha generates 5′ end variation of mature microRNA. *PLoS One* **4**, (2009).
214. Kloosterman, W. P. & Plasterk, R. H. A. The Diverse Functions of MicroRNAs in Animal Development and Disease. *Dev. Cell* **11**, 441–450 (2006).
215. Ivey, K. N. *et al.* MicroRNA Regulation of Cell Lineages in Mouse and Human Embryonic Stem Cells. *Cell Stem Cell* **2**, 219–229 (2008).
216. Mathieu, J. Regulation of Stem Cell Populations by microRNAs. *Adv Exp Med Biol* **786**, 329–351 (2013).
217. Ma, L. & Qu, L. The function of MicroRNAs in renal development and pathophysiology. *J. Genet. Genomics* **40**, 143–152 (2013).
218. Mugford, J. W., Sipilä, P., McMahon, J. A. & McMahon, A. P. Osr1 expression demarcates a multi-potent population of intermediate mesoderm that undergoes progressive restriction to an Osr1-dependent nephron progenitor compartment within the mammalian kidney. *Dev. Biol.* **324**, 88–98 (2008).
219. Yeh, M., Oh, C. S., Yoo, J. Y., Kaur, B. & Lee, T. J. Pivotal role of microRNA-138 in human cancers. *Am J Cancer Res* **9**, 1118–1126 (2019).
220. Martinez, B. & Peplow, P. MicroRNAs as biomarkers of diabetic retinopathy

and disease progression. *Neural Regen. Res.* **14**, 1858 (2019).
221. Backes, C., Meese, E. & Keller, A. Specific miRNA Disease Biomarkers in Blood, Serum and Plasma: Challenges and Prospects. *Mol. Diagnosis Ther.* **20**, 509–518 (2016).
222. Paola, E. De, Verdile, V. & Paola, M. Non-coding RNA Research Dysregulation of microRNA metabolism in motor neuron diseases : Novel biomarkers and potential therapeutics. *Non-coding RNA Res.* **4**, 15–22 (2019).
223. Lv, W. *et al.* Therapeutic potential of microRNAs for the treatment of renal fibrosis and CKD. *Physiol. Genomics* **50**, 20–34 (2018).
224. Baker, M. A. *et al.* Tissue-Specific MicroRNA Expression Patterns in Four Types of Kidney Disease. *J. Am. Soc. Nephrol.* **28**, 2985–2992 (2017).
225. Mukhadi, S., Hull, R., Mbita, Z. & Dlamini, Z. The Role of MicroRNAs in Kidney Disease. *Non-Coding RNA* **1**, 192–221 (2015).
226. Ichii, O. & Horino, T. MicroRNAs associated with the development of kidney diseases in humans and animals. *J. Toxicol. Pathol.* **31**, 23–34 (2017).
227. Lorenzen, J. M., Haller, H. & Thum, T. MicroRNAs as mediators and therapeutic targets in chronic kidney disease. *Nat. Rev. Nephrol.* **7**, 286–294 (2011).
228. Hanna, J., Hossain, G. S. & Kocerha, J. The potential for microRNA therapeutics and clinical research. *Front. Genet.* **10**, (2019).
229. Rupaimoole, R. & Slack, F. J. MicroRNA therapeutics: Towards a new era for the management of cancer and other diseases. *Nature Reviews Drug Discovery* vol. 16 203–221 (2017).
230. Gambari, R., Brognara, E., Spandidos, D. A. & Fabbri, E. Targeting oncomiRNAs and mimicking tumor suppressor miRNAs: New trends in the development of miRNA therapeutic strategies in oncology. *Int. J. Oncol.* **49**, 5–32 (2016).
231. Kreth, S., Hübner, M. & Hinske, L. C. MicroRNAs as clinical biomarkers and therapeutic tools in perioperative medicine. *Anesth. Analg.* **126**, 670–681 (2018).
232. Gallant-Behm, C. L. *et al.* A MicroRNA-29 Mimic (Remlarsen) Represses Extracellular Matrix Expression and Fibroplasia in the Skin. *J. Invest. Dermatol.* **139**, 1073–1081 (2019).
233. van Rooij, E. & Kauppinen, S. Development of microRNA therapeutics is coming of age. *EMBO Mol. Med.* **6**, 851–864 (2014).
234. Lee, E. C. *et al.* Discovery and preclinical evaluation of anti-miR-17 oligonucleotide RGLS4326 for the treatment of polycystic kidney disease. *Nat. Commun.* **4148**, 1–14 (2019).
235. Desvignes, T., Contreras, A. & Postlethwait, J. H. Evolution of the miR199-214 cluster and vertebrate skeletal development. *RNA Biol.* **11**, 281–294 (2014).
236. Irie, K., Tsujimura, K., Nakashima, H. & Nakashima, K. MicroRNA-214 promotes dendritic development by targeting the schizophrenia-associated gene quaking (Qki). *J. Biol. Chem.* **291**, 13891–13904 (2016).
237. Savary, G. *et al.* The DNM3OS lncRNA is a reservoir of fibromiRs with major functions in lung fibroblast response to TGF-β and pulmonary fibrogenesis. *Am J Respir Crit Care Med* **200**, 184–198 (2019).
238. Watanabe, T. *et al.* Dnm3os, a non-coding RNA, is required for normal growth

and skeletal development in mice. *Dev. Dyn.* **237**, 3738–3748 (2008).
239. Das, S. *et al.* Diabetes mellitus-induced long noncoding RNA DNM3OS regulates macrophage functions and inflammation via nuclear mechanisms. *Arterioscler. Thromb. Vasc. Biol.* **38**, 1806–1820 (2018).
240. Wang, J. *et al.* MicroRNA-214-3p: A link between autophagy and endothelial cell dysfunction in atherosclerosis. *Acta Physiol.* **222**, 1–11 (2018).
241. Kohnken, R. *et al.* Preclinical Targeting of MicroRNA-214 in Cutaneous T-Cell Lymphoma. *J. Invest. Dermatol.* (2019) doi:10.1016/j.jid.2019.01.033.
242. Liu, Y. *et al.* MicroRNA-214-3p in the Kidney Contributes to the Development of Hypertension. *J. Am. Soc. Nephrol.* **29**, 2518–2528 (2018).
243. Ma, L. *et al.* MicroRNA-214 promotes hepatic stellate cell activation and liver fibrosis by suppressing Sufu expression article. *Cell Death Dis.* **9**, 1–13 (2018).
244. Ghaderi, S. *et al.* DJ1 and microRNA-214 act synergistically to rescue myoblast cells after ischemia/reperfusion injury. *J. Cell. Biochem.* **119**, 7192–7203 (2018).
245. Wu, D., Lu, P., Mi, X. & Miao, J. Exosomal miR-214 from endometrial stromal cells inhibits endometriosis fibrosis. *Mol. Hum. Reprod.* **24**, 357–365 (2018).
246. Liu, M. *et al.* Hypoxia-induced activation of Twist/miR-214/E-cadherin axis promotes renal tubular epithelial cell mesenchymal transition and renal fibrosis. *Biochem. Biophys. Res. Commun.* **495**, 2324–2330 (2018).
247. Wang, X. *et al.* miR-214 targets ATF4 to inhibit bone formation. *Nat. Med.* **19**, 93–100 (2012).
248. Zhao, C. *et al.* miR-214 promotes osteoclastogenesis by targeting pten/pi3k/Akt pathway. *RNA Biol.* **12**, 343–353 (2015).
249. Shu, P. *et al.* MicroRNA-214 modulates neural progenitor cell differentiation by targeting Quaking during cerebral cortex development. *Sci. Rep.* **7**, 1–11 (2017).
250. Juan, A. H., Kumar, R. M., Marx, J. G., Young, R. A. & Sartorelli, V. Mir-214-Dependent Regulation of the Polycomb Protein Ezh2 in Skeletal Muscle and Embryonic Stem Cells. *Mol. Cell* **36**, 61–74 (2009).
251. Wu, Y. & Li, Z. MicroRNA-214 regulates smooth muscle cell differentiation from stem cells by targeting RNA-binding protein QKI. *Oncotarget* **8**, 19866–19878 (2017).
252. Decembrini, S. MicroRNAs couple cell fate and developmental timing in retina. *PNAS* **106**, 21179–21184 (2009).
253. Wu, J. *et al.* MicroRNA-214 Affects Fibroblast Differentiation of Adipose-Derived Mesenchymal Stem Cells by Targeting Mitofusin-2 during Pelvic Floor Dysfunction in SD Rats with Birth Trauma. *Cell. Physiol. Biochem.* **42**, 1870–1887 (2017).
254. Liu, H. *et al.* Dysregulation of microRNA-214 and PTEN contributes to the pathogenesis of hypoxic pulmonary hypertension. *Int. J. COPD* **12**, 1781–1791 (2017).
255. Wang, X. *et al.* MicroRNA-214 protects against hypoxia/reoxygenation induced cell damage and myocardial ischemia/reperfusion injury via suppression of PTEN and Bim1 expression. *Oncotarget* **7**, 86926–86936 (2016).
256. Afzal, T. A. *et al.* NCK associated protein 1 modulated by miRNA-214

determines vascular smooth muscle cell migration, proliferation, and neointima hyperplasia. *J. Am. Heart Assoc.* **5**, (2016).
257. Bucha, S., Mukhopadhyay, D. & Bhattacharyya, N. P. Regulation of mitochondrial morphology and cell cycle by microRNA-214 targeting Mitofusin2. *Biochem. Biophys. Res. Commun.* **465**, 797–802 (2015).
258. Wang, Z., Zhang, J., Duan, Y., Zhang, Q. & Li, G. MicroRNA-214 participates in the neuroprotective effect of Resveratrol via inhibiting a -synuclein expression in MPTP-induced Parkinson ' s disease mouse. *Biomed. Pharmacother.* **74**, 252–256 (2015).
259. Li, K. *et al.* MicroRNA-214 suppresses gluconeogenesis by targeting activating transcriptional factor 4. *J. Biol. Chem.* **290**, 8185–8195 (2015).
260. Duan, Q. *et al.* MicroRNA-214 Is Upregulated in Heart Failure Patients and Suppresses XBP1-Mediated Endothelial Cells Angiogenesis. *J. Cell. Physiol.* **230**, 1964–1973 (2015).
261. Denby, L. *et al.* MicroRNA-214 antagonism protects against renal fibrosis. *J Am Soc Nephrol* **25**, 65–80 (2014).
262. Dong, X., Liu, H., Chen, F., Li, D. & Zhao, Y. MiR-214 Promotes the Alcohol-Induced Oxidative Stress via Down-Regulation of Glutathione Reductase and Cytochrome P450 Oxidoreductase in Liver Cells. *Alcohol. Clin. Exp. Res.* **38**, 68–77 (2014).
263. Jindra, P. T., Bagley, J., Godwin, J. G. & Iacomini, J. Costimulation-Dependent Expression of MicroRNA-214 Increases the Ability of T Cells To Proliferate by Targeting Pten. *J. Immunol.* **185**, 990–997 (2010).
264. Li, L. *et al.* Role of MicroRNA-214–Targeting Phosphatase and Tensin Homolog in Advanced Glycation End Product-Induced Apoptosis Delay in Monocytes. *J. Immunol.* **186**, 2552–2560 (2011).
265. Yin, Y. *et al.* Tumor-secreted miR-214 induces regulatory T cells: A major link between immune evasion and tumor growth. *Cell Res.* **24**, 1164–1180 (2014).
266. Zhu, X., Li, W. & Li, H. miR-214 ameliorates acute kidney injury via targeting DKK3 and activating of Wnt/ β-catenin signaling pathway. *Biol. Res.* **51**, 1–10 (2018).
267. Bai, M. *et al.* MicroRNA-214 promotes chronic kidney disease by disrupting mitochondrial oxidative phosphorylation. *Kidney Int.* **95**, 1–16 (2019).
268. Guo, X., Cheng, M., Ke, W., Wang, Y. & Ji, X. Microrna-214 suppresses propofol-induced neuroapoptosis through activation of phosphoinositide 3-kinase/protein kinase B signaling by targeting phosphatase and tensin homolog expression. *Int. J. Mol. Med.* **42**, 2527–2537 (2018).
269. Wang, X. *et al.* Cross talk between miR-214 and PTEN attenuates glomerular hypertrophy under diabetic conditions. *Sci. Rep.* **6**, 31506 (2016).
270. Du, K. T. *et al.* MiR-214 Regulates the Human Hair Follicle Stem Cell Proliferation and Differentiation by Targeting EZH2 and Wnt/β-Catenin Signaling Way In Vitro. *Tissue Eng. Regen. Med.* **15**, 341–350 (2018).
271. Li, J.-P., Zhuang, H.-T., Xin, M.-Y. & Zhou, Y.-L. MiR-214 inhibits human mesenchymal stem cells differentiating into osteoblasts through targeting β-catenin. *Eur. Rev. Med. Pharmacol. Sci.* **21**, 4777–4783 (2017).

272. Zhao, Y. *et al.* The role of miR-214 in cardiovascular diseases. *Eur. J. Pharmacol.* 0–1 (2017) doi:10.1016/j.ejphar.2017.08.009.
273. Duan, Q. *et al.* MicroRNA regulation of unfolded protein response transcription factor XBP1 in the progression of cardiac hypertrophy and heart failure in vivo. *J. Transl. Med.* **13**, 1–11 (2015).
274. Carrillo, E. D., Sampieri, R., Hernández, A., García, M. C. & Sánchez, J. A. MiR-132 regulates rem expression in cardiomyocytes during long-term β-adrenoceptor agonism. *Cell. Physiol. Biochem.* **36**, 141–154 (2015).
275. Hou, Y. *et al.* Beta-adrenoceptor regulates miRNA expression in rat heart. *Med. Sci. Monit.* **18**, 309–314 (2012).
276. Yang, T. *et al.* MicroRNA-214 provokes cardiac hypertrophy via repression of EZH2. *Biochem. Biophys. Res. Commun.* **436**, 578–584 (2013).
277. Tang, C. M. *et al.* Myocyte-specific enhancer factor 2C: A novel target gene of miR-214-3p in suppressing angiotensin II-induced cardiomyocyte hypertrophy. *Sci. Rep.* **6**, 1–8 (2016).
278. Sahoo, S. *et al.* MEF2C-MYOCD and Leiomodin1 Suppression by miRNA-214 Promotes Smooth Muscle Cell Phenotype Switching in Pulmonary Arterial Hypertension. *PLoS One* **11**, e0153780 (2016).
279. Ge, C. miRNA-214 protects sepsis-induced myocardial injury. *Shock* **50**, 112–118 (2018).
280. Liu, H. T. *et al.* Upregulation of MicroRNA-214 Contributes to the Development of Vascular Remodeling in Hypoxia-induced Pulmonary Hypertension Via Targeting CCNL2. *Sci. Rep.* **6**, 1–11 (2016).
281. Penna, E., Orso, F. & Taverna, D. miR-214 as a Key Hub that Controls Cancer Networks: Small Player, Multiple Functions. *Journal of Investigative Dermatology* vol. 135 960–969 (2015).
282. He, H. *et al.* MiRNA-214: Expression, therapeutic and diagnostic potential in cancer. *Tumori* **101**, 375–383 (2015).
283. Liu, F. *et al.* MiR-214 regulates papillary thyroid carcinoma cell proliferation and metastasis by targeting PSMD10. *Int. J. Mol. Med.* **42**, 3027–3036 (2018).
284. Zhang, Z. C. *et al.* Knockdown of miR-214 promotes apoptosis and inhibits cell proliferation in nasopharyngeal carcinoma. *PLoS One* **9**, (2014).
285. Yang, T.-S. MiR-214 regulate gastric cancer cell proliferation, migration and invasion by targeting PTEN. *Cancer Cell Int.* **13**, (2013).
286. Xia, H., Ooi, L. L. P. J. & Hui, K. M. MiR-214 Targets β-Catenin Pathway to Suppress Invasion, Stem-Like Traits and Recurrence of Human Hepatocellular Carcinoma. *PLoS One* **7**, (2012).
287. Wang, X. *et al.* MiR-214 inhibits cell growth in hepatocellular carcinoma through suppression of β-catenin. *Biochem. Biophys. Res. Commun.* **428**, 525–531 (2012).
288. Shih, T. C. *et al.* MicroRNA-214 downregulation contributes to tumor angiogenesis by inducing secretion of the hepatoma-derived growth factor in human hepatoma. *J. Hepatol.* **57**, 584–591 (2012).
289. Derfoul, A. *et al.* Decreased microRNA-214 levels in breast cancer cells coincides with increased cell proliferation, invasion and accumulation of the

polycomb Ezh2 methyltransferase. *Carcinogenesis* **32**, 1607–1614 (2011).
290. Penna, E. *et al.* MicroRNA-214 contributes to melanoma tumour progression through suppression of TFAP2C. *EMBO J.* **30**, 1990–2007 (2011).
291. Wang, J. M. *et al.* MiR-214 inhibits cell migration, invasion and promotes the drug sensitivity in human cervical cancer by targeting FOXM1. *Am. J. Transl. Res.* **9**, 3541–3557 (2017).
292. Yu, Z. wei *et al.* MicroRNAs contribute to the chemoresistance of cisplatin in tongue squamous cell carcinoma lines. *Oral Oncol.* **46**, 317–322 (2010).
293. Yang, H. *et al.* MicroRNA expression profiling in human ovarian cancer: miR-214 induces cell survival and cisplatin resistance by targeting PTEN. *Cancer Res.* **68**, 425–433 (2008).
294. Song, Y. D., Li, D. D., Guan, Y., Wang, Y. L. & Zheng, J. miR-214 modulates cisplatin sensitivity of osteosarcoma cells through regulation of anaerobic glycolysis. *Cell. Mol. Biol.* **63**, 75–79 (2017).
295. Li, Q.-Q. *et al.* Sulforaphane inhibits cancer stem-like cell properties and cisplatin resistance through miR-214-mediated downregulation of c-MYC in non-small cell lung cancer. *Oncotarget* **8**, 12067–12080 (2017).
296. Phatak, P. *et al.* Overexpression of miR-214-3p in esophageal squamous cancer cells enhances sensitivity to cisplatin by targeting survivin directly and indirectly through CUG-BP1. *Oncogene* **35**, 2087–2097 (2016).
297. Yi, S. J., Li, L. L. & Tu, W. B. MiR-214 negatively regulates proliferation and WNT/β-catenin signaling in breast cancer. *Eur. Rev. Med. Pharmacol. Sci.* **20**, 5148–5154 (2016).
298. Qi, W. *et al.* Targeting the Wnt-Regulatory Protein CTNNBIP1 by microRNA-214 Enhances the Stemness and Self-Renewal of Cancer Stem-Like Cells in Lung Adenocarcinomas. *Stem Cells* **33**, 3423–3436 (2015).
299. Yin, G. *et al.* TWISTing stemness, inflammation and proliferation of epithelial ovarian cancer cells through MIR199A2/214. *Oncogene* **29**, 3545–3553 (2010).
300. Mohamed, R. H. *et al.* Co-regulatory Network of Oncosuppressor miRNAs and Transcription Factors for Pathology of Human Hepatic Cancer Stem Cells (HCSC). *Sci. Rep.* **9**, 1–11 (2019).
301. Shi, D. *et al.* TFAP2A regulates nasopharyngeal carcinoma growth and survival by targeting HIF-1a signaling pathway. *Cancer Prev. Res.* **7**, 266–277 (2014).
302. Gomez, I. G., Nakagawa, N. & Duffield, J. S. MicroRNAs as novel therapeutic targets to treat kidney injury and fibrosis. *Am J Physiol Ren. Physiol* **310**, F931–F944 (2016).
303. Denby, L. *et al.* miR-21 and miR-214 Are Consistently Modulated during Renal Injury in Rodent Models. *Am. J. Pathol.* **179**, 661–672 (2011).
304. Assmann, T. S., Recamonde-Mendoza, M., de Souza, B. M., Bauer, A. C. & Crispim, D. MicroRNAs and diabetic kidney disease: Systematic review and bioinformatic analysis. *Mol. Cell. Endocrinol.* **477**, 90–102 (2018).
305. Argyropoulos, C. *et al.* Urinary MicroRNA Profiling in the Nephropathy of Type 1 Diabetes. *PLoS One* **8**, (2013).
306. Bera, A. *et al.* Reciprocal regulation of miR-214 and PTEN by high glucose regulates renal glomerular mesangial and proximal tubular epithelial cell

hypertrophy and matrix expansion. *Am. J. Physiol. Physiol.* **313**, C430–C447 (2017).
307. Maity, S., Das, F., Ghosh-Choudhury, N., Kasinath, B. S. & Ghosh Choudhury, G. High glucose increases miR-214 to power a feedback loop involving PTEN and the Akt/mTORC1 signaling axis. *FEBS Lett.* 1–12 (2019) doi:10.1002/1873-3468.13505.
308. Rahbari, R., Sheahan, T., Modes, V., Collier, P. & Macfarlane, C. A novel L1 retrotransposon marker for HeLa cell line identification. *Biotechniques* **46**, 277–284 (2009).
309. Masters, J. R. HeLa cells 50 years on: the good, the bad and the ugly. *Nat. Rev. Cancer* **2**, 315–319 (2002).
310. De Larco, J. E. & Todaro, G. J. Epithelioid and fibroblastic rat kidney cell clones: Epidermal growth factor (EGF) receptors and the effect of mouse sarcoma virus transformation. *J. Cell. Physiol.* **94**, 335–342 (1978).
311. Ullman-Culleré, M. H. & Foltz, C. J. Body condition scoring: a rapid and accurate method for assessing health status in mice. *Lab. Anim. Sci.* **49**, 319–23 (1999).
312. Wang, Y., Thatcher, S. E. & Cassis, L. Measuring Blood Pressure Using a Noninvasive Tail Cuff Method in Mice. *Methods Mol Biol* **1614**, 69–73 (2017).
313. Li, B. & Dewey, C. N. RSEM: accurate transcript quantification from RNA-Seq data with or without a reference genome. *BMC Bioinformatics* **12**, 1–16 (2011).
314. Axtell, M. J. ShortStack: Comprehensive annotation and quantification of small RNA genes. *Rna* **19**, 740–751 (2013).
315. Park, J. & Susztak, K. Single-cell transcriptomics of the mouse kidney reveals potential cellular targets of kidney disease. *Science (80-.).* **360**, 758–763 (2018).
316. El Amrani, K., Alanis-Lobato, G., Mah, N., Kurtz, A. & Andrade-Navarro, M. A. Detection of condition-specific marker genes from RNA-seq data with MGFR. *PeerJ* **7**, e6970 (2019).
317. Layton, A. T., Edwards, A. & Vallon, V. Adaptive Changes in GFR, Tubular Morphology and Transport in Subtotal Nephrectomized Kidneys: Modeling and Analysis. *Am. J. Physiol. - Ren. Physiol.* ajprenal.00018.2017 (2017) doi:10.1152/ajprenal.00018.2017.
318. Soler, M. J., Wysocki, J. & Batlle, D. Angiotensin-converting enzyme 2 and the kidney. *Exp. Physiol.* **93**, 549–56 (2008).
319. Yang, H.-C., Zuo, Y. & Fogo, A. B. Models of chronic kidney disease. *Drug Discov Today Dis Model.* **7**, 13–19 (2010).
320. Leelahavanichkul, A. *et al.* Rapid CKD progression in a new mouse kidney remnant model: strain-dependent resistance is overcome by angiotensin II. *Kidney Int.* **78**, 1136–1153 (2010).
321. Hyde, G. D. *et al.* Axl tyrosine kinase protects against tubulo-interstitial apoptosis and progression of renal failure in a murine model of chronic kidney disease and hyperphosphataemia. *PLoS One* **9**, 1–11 (2014).
322. Li, K. L. *et al.* P53 negatively regulates the osteogenic differentiation of vascular smooth muscle cells in mice with chronic kidney disease. *Cardiovasc. J. Afr.* **23**, e1–e9 (2012).
323. Babelova, A. *et al.* Role of Nox4 in murine models of kidney disease. *Free Radic.*

Biol. Med. **53**, 842–853 (2012).
324. Rosendahl, A. *et al.* Adaptive immunity and IL-17A are not involved in the progression of chronic kidney disease after 5/6 nephrectomy in mice. *Br. J. Pharmacol.* (2018) doi:10.1111/bph.14509.
325. Vavrinec, P. *et al.* Renal endothelial function is associated with the anti-proteinuric effect of ACE inhibition in 5/6 nephrectomized rats. *Am. J. Physiol. Physiol.* **310**, F1047–F1053 (2016).
326. Tan, R. Z. *et al.* An optimized 5/6 nephrectomy mouse model based on unilateral kidney ligation and its application in renal fibrosis research. *Ren. Fail.* **41**, 555–566 (2019).
327. Duffield, J. S. Cellular and molecular mechanisms in kidney fibrosis. *J Clin Invest* **124**, (2014).
328. Shimizu, A., Masuda, Y., Ishizaki, M., Sugisaki, Y. & Yamanaka, N. Tubular dilatation in the repair process of ischaemic tubular necrosis. *Virchows Arch.* **425**, 281–290 (2004).
329. Pieters, T. T. *et al.* Histological characteristics of Acute Tubular Injury during Delayed Graft Function predict renal function after renal transplantation. *Physiol. Rep.* **7**, e14000 (2019).
330. Delella, F. K., de Almeida, F. L. A., Nunes, H. C., Rinaldi, J. C. & Felisbino, S. L. Fibrillar collagen genes are not coordinately upregulated with TGF β1 expression in finasteride-treated prostate. *Cell Biol. Int.* **41**, 1214–1222 (2017).
331. Nakagawa, N. & Duffield, J. S. Myofibroblasts in Fibrotic Kidneys. *Curr Pathobiol Rep* **1**, 189–198 (2013).
332. Jones, F. E. *et al.* ER stress and basement membrane defects combine to cause glomerular and tubular renal disease resulting from Col4a1 mutations in mice. *Dis. Model. Mech.* **9**, 165–176 (2016).
333. Bernard, M. *et al.* Autophagy fosters myofibroblast differentiation through MTORC2 activation and downstream upregulation of CTGF. *Autophagy* **10**, 2193–2207 (2014).
334. Mansour, S. G., Puthumana, J., Coca, S. G., Gentry, M. & Parikh, C. R. Biomarkers for the detection of renal fibrosis and prediction of renal outcomes: a systematic review. *BMC Nephrol.* **18**, 1–13 (2017).
335. Giannandrea, M. & Parks, W. C. Diverse functions of matrix metalloproteinases during fibrosis. *Dis. Model. Mech.* **7**, 193–203 (2014).
336. Dejonckheere, E., Vandenbroucke, R. E. & Libert, C. Matrix metalloproteinases as drug targets in ischemia/reperfusion injury. *Drug Discov. Today* **16**, 762–778 (2011).
337. Marti, H. P. *et al.* Renal fibrosis mRNA classifier: Validation in experimental lithium-induced interstitial fibrosis in the rat kidney. *PLoS One* **11**, 1–19 (2016).
338. Steinmann-Niggli, K., Ziswiler, R., Küng, M. & Marti, H. P. Inhibition of matrix metalloproteinases attenuates anti-Thy1.1 nephritis. *J. Am. Soc. Nephrol.* **9**, 397–407 (1998).
339. Harendza, S., Schneider, A., Helmchen, U. & Stahl, R. A. K. Extracellular matrix deposition and cell proliferation in a model of chronic glomerulonephritis in the rat. *Nephrol. Dial. Transplant.* **14**, 2873–2879 (1999).

340. Tveitarås, M. K. *et al.* Matrix metalloproteinase-2 knockout and heterozygote mice are protected from hydronephrosis and kidney fibrosis after unilateral ureteral obstruction. *PLoS One* **10**, 1–13 (2015).
341. Munkert, A. *et al.* Characterization of the transcriptional regulation of the human MT1-MMP gene and association of risk reduction for focal-segmental glomerulosclerosis with two functional promoter SNPs. *Nephrol. Dial. Transplant.* **24**, 735–742 (2009).
342. Lemos, D. R. *et al.* Interleukin-1 β Activates a MYC-Dependent Metabolic Switch in Kidney Stromal Cells Necessary for Progressive Tubulointerstitial Fibrosis . *J. Am. Soc. Nephrol.* **29**, 1690–1705 (2018).
343. Lorenz, G. & Anders, H. Canonical and non-canonical effects of the NLRP3 in flammasome in kidney in flammation and fibrosis. *ndt* **29**, 41–48 (2014).
344. Lichtnekert, J. *et al.* Anti-gbm glomerulonephritis involves il-1 but is independent of nlrp3/asc inflammasome-mediated activation of caspase-1. *PLoS One* **6**, (2011).
345. Martínez-Klimova, E., Aparicio-Trejo, O. E., Tapia, E. & Pedraza-Chaverri, J. Unilateral Ureteral Obstruction as a Model to Investigate Fibrosis-Attenuating Treatments. *Biomolecules* **9**, 141 (2019).
346. Meng, X. M., Nikolic-Paterson, D. J. & Lan, H. Y. TGF-β: The master regulator of fibrosis. *Nat. Rev. Nephrol.* **12**, 325–338 (2016).
347. Chau, B. N. *et al.* MicroRNA-21 Promotes Fibrosis of the Kidney by Silencing Metabolic Pathways. *Sci. Transl. Med.* **4**, 121ra18-121ra18 (2012).
348. Gomez, I. G. *et al.* Anti–microRNA-21 oligonucleotides prevent Alport nephropathy progression by stimulating metabolic pathways. *J Clin Invest* **125**, 141–156 (2015).
349. Winterberg, P. D., Jiang, R., Maxwell, J. T., Wang, B. & Wagner, M. B. Myocardial dysfunction occurs prior to changes in ventricular geometry in mice with chronic kidney disease (CKD). *Physiol. Rep.* **4**, 1–11 (2016).
350. Lin, C. Y. *et al.* CB1 cannabinoid receptor antagonist attenuates left ventricular hypertrophy and Akt-mediated cardiac fibrosis in experimental uremia. *J. Mol. Cell. Cardiol.* **85**, 249–261 (2015).
351. Levin, A. *et al.* Left ventricular mass index increase in early renal disease: Impact of decline in hemoglobin. *Am. J. Kidney Dis.* **34**, 125–134 (1999).
352. Stenvang, J., Petri, A., Lindow, M., Obad, S. & Kauppinen, S. Inhibition of microRNA function by antimiR oligonucleotides. *Silence* **3**, 1 (2012).
353. Krützfeldt, J. *et al.* Silencing of microRNAs in vivo with 'antagomirs'. *Nature* **438**, 685–689 (2005).
354. Meister, G. & Tuschl, T. Sequence-specific inhibition of microRNA- and siRNA-induced RNA silencing. *RNA* **10**, 544–550 (2004).
355. Deleavey, G. F. & Damha, M. J. Designing chemically modified oligonucleotides for targeted gene silencing. *Chem. Biol.* **19**, 937–954 (2012).
356. Halle, B. *et al.* Convection-enhanced delivery of an anti-miR is well-tolerated, preserves anti-miR stability and causes efficient target de-repression: a proof of concept. *J. Neurooncol.* **126**, 47–55 (2016).
357. Fraser, S. D. S. *et al.* Chronic kidney disease, albuminuria and socioeconomic

status in the Health Surveys for England 2009 and 2010. *J. Public Health (Oxf).* **36**, 577–86 (2014).
358. Hundae, A. & McCullough, P. A. Cardiac and renal fibrosis in chronic cardiorenal syndromes. *Nephron - Clin. Pract.* **127**, 106–112 (2014).
359. Di Lullo, L., Gorini, A., Russo, D., Santoboni, A. & Ronco, C. Left Ventricular Hypertrophy in Chronic Kidney Disease Patients: From Pathophysiology to Treatment. *Cardiorenal Med.* **5**, 254–266 (2015).
360. Yin, J. *et al.* Renalase attenuates hypertension, renal injury and cardiac remodelling in rats with subtotal nephrectomy. *J. Cell. Mol. Med.* **20**, 1106–17 (2016).
361. MacArthur Clark, J. The 3Rs in research: A contemporary approach to replacement, reduction and refinement. *Br. J. Nutr.* **120**, S1–S7 (2018).
362. Rysz, J., Gluba-Brzózka, A., Franczyk, B., Jablonowski, Z. & Cialkowska-Rysz, A. Novel biomarkers in the diagnosis of chronic kidney disease and the prediction of its outcome. *Int. J. Mol. Sci.* **18**, (2017).
363. Webster, A. C., Nagler, E. V., Morton, R. L. & Masson, P. Chronic Kidney Disease. *Lancet* **389**, 1238–1252 (2017).
364. Ritter, C. S. & Slatopolsky, E. Phosphate toxicity in CKD: The killer among us. *Clin J Am Soc Nephrol* vol. 11 1088–1100 (2016).
365. Edmonston, D., Morris, J. D. & Middleton, J. P. Working Toward an Improved Understanding of Chronic Cardiorenal Syndrome Type 4. *Adv. Chronic Kidney Dis.* **25**, 454–467 (2018).
366. Hsieh, P. F. *et al.* Elucidation of the therapeutic role of mitochondrial biogenesis transducers NRF-1 in the regulation of renal fibrosis. *Exp. Cell Res.* **349**, 23–31 (2016).
367. Hu, Q., Gao, L., Peng, B. & Liu, X. Baicalin and baicalein attenuate renal fibrosis in vitro via inhibition of the TGF-β1 signaling pathway. *Exp. Ther. Med.* **14**, 3074–3080 (2017).
368. Wang, J. L. *et al.* Antifibrotic role of PGC-1α-siRNA against TGF-β1-induced renal interstitial fibrosis. *Exp. Cell Res.* **370**, 160–167 (2018).
369. Ikezaki, M., Higashimoto, N., Matsumura, K. & Ihara, Y. Hsc70 facilitates TGF-β-induced activation of Smad2/3 in fibroblastic NRK-49F cells. *Biochem. Biophys. Res. Commun.* **477**, 448–453 (2016).
370. Neymeyer, H. *et al.* Activation of annexin A1 signalling in renal fibroblasts exerts antifibrotic effects. *Acta Physiol.* **215**, 144–158 (2015).
371. Hao, S. *et al.* Targeted inhibition of β-catenin/CBP signaling ameliorates renal interstitial fibrosis. *J. Am. Soc. Nephrol.* **22**, 1642–53 (2011).
372. Sun, K.-H., Chang, Y., Reed, N. I. & Sheppard, D. αSMA is an inconsistent marker of fibroblasts responsible for force dependent TGFβ activation or collagen production across multiple models of organ fibrosis. *Am. J. Physiol. Lung Cell. Mol. Physiol.* ajplung.00350.2015 (2016) doi:10.1152/ajplung.00350.2015.
373. Farris, A. B. & Colvin, R. B. Renal interstitial fibrosis: mechanisms and evaluation. *Curr. Opin. Nephrol. Hypertens.* **21**, 289–300 (2012).
374. Lam, S., van der Geest, R. N., Verhagen, N. A. M., Daha, M. R. & van Kooten, C. Secretion of collagen type IV by human renal fibroblasts is increased by high

glucose via a TGF-β-independent pathway. *Nephrol. Dial. Transplant.* **19**, 1694–1701 (2004).
375. Zhang, L. *et al.* Lefty-1 alleviates TGF-β1-induced fibroblast-myofibroblast transdifferentiation in NRK-49F cells. *Drug Des. Devel. Ther.* **9**, 4669–78 (2015).
376. Lu, J. *et al.* Activation of AMPK by metformin inhibits TGF-β-induced collagen production in mouse renal fibroblasts. *Life Sci.* **127**, 59–65 (2015).
377. Lichtenberger, B. M., Mastrogiannaki, M. & Watt, F. M. Epidermal β-catenin activation remodels the dermis via paracrine signalling to distinct fibroblast lineages. *Nat. Commun.* **7**, 10537 (2016).
378. Kissin, E. Y., Lemaire, R., Korn, J. H. & Lafyatis, R. Transforming growth factor β induces fibroblast fibrillin-1 matrix formation. *Arthritis Rheum.* **46**, 3000–3009 (2002).
379. Schaefer, L. *et al.* Decorin-mediated regulation of fibrillin-1 in the kidney involves the insulin-like growth factor-I receptor and mammalian target of rapamycin. *Am. J. Pathol.* **170**, 301–315 (2007).
380. Doliana, R. *et al.* Elastic fiber proteins in the glomerular mesangium in vivo and in cell culture. *Kidney Int.* **58**, 1588–1602 (2003).
381. Gröne, H.-J. *et al.* Regulation of Fibrillin-1 by Biglycan and Decorin Is Important for Tissue Preservation in the Kidney During Pressure-Induced Injury. *Am. J. Pathol.* **165**, 383–396 (2011).
382. Yuan, Q. *et al.* Fluorofenidone attenuates tubulointerstitial fibrosis by inhibiting TGF-β1-induced fibroblast activation. *Am. J. Nephrol.* **34**, 181–194 (2011).
383. Mori, K. *et al.* Role of connective tissue growth factor in profibrotic action of transforming growth factor-β: A potential target for preventing renal fibrosis. *Am. J. Kidney Dis.* **38**, S134–S138 (2008).
384. Phanish, M. K., Winn, S. K. & Dockrell, M. E. C. Connective tissue growth factor-(CTGF, CCN2) - A marker, mediator and therapeutic target for renal fibrosis. *Nephron - Exp. Nephrol.* **114**, 83–92 (2010).
385. Toda, N., Mukoyama, M., Yanagita, M. & Yokoi, H. CTGF in kidney fibrosis and glomerulonephritis. *Inflamm. Regen.* **38**, 1–8 (2018).
386. Gu, X. *et al.* KLF 15 works as an early anti-fibrotic transcriptional regulator in ang II-induced renal fibrosis via down-regulation of CTGF expression. *Kidney Blood Press. Res.* **42**, 999–1012 (2017).
387. Ren, Y. *et al.* The Sirt1 activator, SRT1720, attenuates renal fibrosis by inhibiting CTGF and oxidative stress. *Int. J. Mol. Med.* **39**, 1317–1324 (2017).
388. Liu, M. *et al.* Cardiovascular disease and its relationship with chronic kidney disease. *Eur. Rev. Med. Pharmacol. Sci.* **18**, 2918–26 (2014).
389. McCulloch, C. E., Hsu, C., Fan, D., Chertow, G. M. & Go, A. S. Chronic Kidney Disease and the Risks of Death, Cardiovascular Events, and Hospitalization. *N. Engl. J. Med.* **351**, 1296–1305 (2004).
390. Schnaper, H. W. The Tubulointerstitial Pathophysiology of Progressive Kidney Disease. *Adv. Chronic Kidney Dis.* **24**, 107–116 (2017).
391. Ferenbach, D., Kluth, D. C. & Hughes, J. Inflammatory Cells in Renal Injury and Repair. **27**, 250–259 (2018).

392. Vielhauer, V., Kulkarni, O., Reichel, C. A. & Anders, H.-J. Targeting the recruitment of monocytes and macrophages in renal disease. *Semin. Nephrol.* **30**, 318–33 (2010).
393. Clark, J. Z. *et al.* Cell-Type Selective Markers Represented in Whole-Kidney RNA-Seq Data. *bioRxiv* 348615 (2018) doi:10.1101/348615.
394. Sun, Y. *et al.* MiR-214 is an important regulator of the musculoskeletal metabolism and disease. *J. Cell. Physiol.* **234**, 231–245 (2018).
395. Dong, H. *et al.* MicroRNA-214 exerts a Cardio-protective effect by inhibition of fibrosis. *Anat. Rec.* **299**, 1348–1357 (2016).
396. Vernon, M. A., Mylonas, K. J. & Hughes, J. Macrophages and renal fibrosis. *Semin. Nephrol.* **30**, 302–17 (2010).
397. Huen, S. C. & Cantley, L. G. Macrophages in Renal Injury and Repair. *Annu. Rev. Physiol.* **79**, 449–469 (2017).
398. Ostendorf, T., Boor, P., Van Roeyen, C. R. C. & Floege, J. Platelet-derived growth factors (PDGFs) in glomerular and tubulointerstitial fibrosis. *Kidney Int. Suppl.* **4**, 65–69 (2014).
399. Lin, S.-L., Kisseleva, T., Brenner, D. A. & Duffield, J. S. Pericytes and Perivascular Fibroblasts Are the Primary Source of Collagen-Producing Cells in Obstructive Fibrosis of the Kidney. *Am. J. Pathol.* **173**, 1617–1627 (2008).
400. Shivtiel, S. *et al.* CD45 regulates retention, motility, and numbers of hematopoietic progenitors, and affects osteoclast remodeling of metaphyseal trabecules. *J. Exp. Med.* **205**, 2381–2395 (2008).
401. Hermiston, M. L., Xu, Z. & Weiss, A. CD45: A Critical Regulator of Signaling Thresholds in Immune Cells. *Annu. Rev. Immunol.* **21**, 107–137 (2003).
402. Lin, F., Moran, A. & Igarashi, P. Intrarenal cells, not bone marrow-derived cells, are the major source for regeneration in postischemic kidney. *J. Clin. Invest.* **115**, 1756–1764 (2005).
403. Marcu, R. *et al.* Human Organ-Specific Endothelial Cell Heterogeneity. *iScience* **4**, 20–35 (2018).
404. Boor, P. & Floege, J. The renal (myo-)fibroblast: A heterogeneous group of cells. *Nephrol. Dial. Transplant.* **27**, 3027–3036 (2012).
405. Lever, J. M. *et al.* Resident macrophages reprogram toward a developmental state after acute kidney injury. *JCI Insight* **4**, 1–18 (2019).
406. Munro, D. A. D. & Hughes, J. The origins and functions of tissue-resident macrophages in kidney development. *Front. Physiol.* **8**, 1–13 (2017).
407. Forbes, M. S., Thornhill, B. A. & Chevalier, R. L. Proximal tubular injury and rapid formation of atubular glomeruli in mice with unilateral ureteral obstruction: a new look at an old model. *Am. J. Physiol. Physiol.* **301**, F110–F117 (2011).
408. Hennigar, R. A., Schulte, B. A. & Spicer, S. S. Heterogeneous distribution of glycoconjugates in human kidney tubules. *Anat. Rec.* **211**, 376–390 (1985).
409. Schulte, B. & Spicer, S. Histochemical evaluation of mouse and rat kidneys with lectin-horseradish peroxidase conjugates. *Am. J. Anat.* **168**, 345–362 (1983).
410. Lertkiatmongkol, P. *et al.* Endothelial functions of PECAM-1 (CD31). *Curr Opin Hematol.* **23**, 253–259 (2016).

411. Lin, H.-H. *et al.* The macrophage F4/80 receptor is required for the induction of antigen-specific efferent regulatory T cells in peripheral tolerance. *J. Exp. Med.* **201**, 1615–1625 (2005).
412. Schulz, C. *et al.* A Lineage of Myeloid Cells Independent of Myb and Hematopoietic Stem Cells. *Science (80-.).* **336**, 86–90 (2012).
413. Lindahl, P. *et al.* Paracrine PDGF-B/PDGF-Rβ signaling controls mesangial cell development in kidney glomeruli. *Development* **125**, 3313–3322 (1998).
414. Heberle, H., Meirelles, V. G., da Silva, F. R., Telles, G. P. & Minghim, R. InteractiVenn: A web-based tool for the analysis of sets through Venn diagrams. *BMC Bioinformatics* **16**, 1–7 (2015).
415. Wojcicka, A. *et al.* Next generation sequencing reveals microRNA isoforms in liver cirrhosis and hepatocellular carcinoma. *Int. J. Biochem. Cell Biol.* **53**, 208–217 (2014).
416. Mandel-Gutfreund, Y., Kosti, I. & Larisch, S. ARTS, the unusual septin: Structural and functional aspects. *Biol. Chem.* **392**, 783–790 (2011).
417. Koren, E. *et al.* ARTS mediates apoptosis and regeneration of the intestinal stem cell niche. *Nat. Commun.* **9**, 1–17 (2018).
418. Edison, N. *et al.* The IAP-antagonist ARTS initiates caspase activation upstream of cytochrome C and SMACDiablo. *Cell Death Differ.* **19**, 356–368 (2012).
419. Yaron Fuchs *et al.* Sept4/ARTS Regulates Stem Cell Apoptosis and Skin Regeneration. *Science (80-.).* 286–290 (2013) doi:10.6019/PXD000213.Supplementary.
420. Ottens, F., Boehm, V., Sibley, C. R., Ule, J. & Gehring, N. H. Transcript-specific characteristics determine the contribution of endo- and exonucleolytic decay pathways during the degradation of nonsense-mediated decay substrates. *Rna* **23**, 1224–1236 (2017).
421. Trümbach, D. *et al.* ENCoRE: An efficient software for CRISPR screens identifies new players in extrinsic apoptosis. *BMC Genomics* **18**, 1–13 (2017).
422. Luo, H., Cowen, L., Yu, G., Jiang, W. & Tang, Y. SMG7 is a critical regulator of p53 stability and function in DNA damage stress response. *Cell Discov.* **2**, (2016).
423. Venkatachalam, M. A., Weinberg, J. M., Kriz, W. & Bidani, A. K. Failed Tubule Recovery, AKI-CKD Transition, and Kidney Disease Progression. *J. Am. Soc. Nephrol.* **26**, 1765–1776 (2015).
424. Cao, Q. *et al.* Renal F4/80 + CD11c + Mononuclear Phagocytes Display Phenotypic and Functional Characteristics of Macrophages in Health and in Adriamycin Nephropathy . *J. Am. Soc. Nephrol.* **26**, 349–363 (2015).
425. El Agha, E. *et al.* Mesenchymal Stem Cells in Fibrotic Disease. *Cell Stem Cell* **21**, 166–177 (2017).
426. Floege, J., Eitner, F. & Alpers, C. E. A New Look at Platelet-Derived Growth Factor in Renal Disease. *J. Am. Soc. Nephrol.* **19**, 12–23 (2008).
427. Xu, Y. *et al.* Autophagy and apoptosis in tubular cells following unilateral ureteral obstruction are associated with mitochondrial oxidative stress. *Int. J. Mol. Med.* **31**, 628–636 (2013).
428. Macconi, D., Benigni, A. & Remuzzi, G. *The Onset and Resolution of Renal*

Fibrosis. *Kidney Development, Disease, Repair and Regeneration* (Elsevier Inc., 2015). doi:10.1016/b978-0-12-800102-8.00026-6.
429. Lee, S. A., Noel, S., Sadasivam, M., Hamad, A. R. A. & Rabb, H. Role of Immune Cells in Acute Kidney Injury and Repair. *Nephron* **137**, 282–286 (2017).
430. Melton, D. W., Lei, X., Gelfond, J. A. L. & Shireman, P. K. Dynamic macrophage polarization-specific miRNA patterns reveal increased soluble VEGF receptor 1 by miR-125a-5p inhibition. *Physiol. Genomics* **48**, 345–360 (2016).
431. Bhaskaran, M. & Mohan, M. MicroRNAs: History, Biogenesis, and Their Evolving Role in Animal Development and Disease. *Vet. Pathol.* **51**, 759–774 (2014).
432. Liu, J. *et al.* MicroRNA-214 promotes myogenic differentiation by facilitating exit from mitosis via down-regulation of proto-oncogene N-ras. *J. Biol. Chem.* **285**, 26599–26607 (2010).
433. Horowitz, J. C. & Thannickal, V. J. Mechanisms for the resolution of organ fibrosis. *Physiology* **34**, 43–55 (2019).
434. Pilotte, J., Larocque, D. & Richard, S. Nuclear translocation controlled by alternatively spliced isoforms inactivates the QUAKING apoptotic inducer. *Genes Dev.* **15**, 845–858 (2001).
435. Koren, E. & Fuchs, Y. The ARTS of Cell Death. *J. Cell Death* **12**, 117906601983696 (2019).
436. Gottfried, Y., Rotem, A., Klein, E. & Larisch, S. The pro-apoptotic ARTS/Sept4 protein is significantly reduced in post-mortem brains from schizophrenic patients. *Schizophr. Res.* **96**, 257–266 (2007).
437. Shohat, M., Ben-Meir, D. & Lavi, S. Protein phosphatase magnesium dependent 1A (PPM1A) plays a role in the differentiation and survival processes of nerve cells. *PLoS One* **7**, 1–11 (2012).
438. Mazumdar, A. *et al.* The phosphatase PPM1A inhibits triple negative breast cancer growth by blocking cell cycle progression. *npj Breast Cancer* **5**, 1–11 (2019).
439. Ofek, P., Ben-Meir, D., Kariv-Inbal, Z., Oren, M. & Lavi, S. Cell cycle regulation and p53 activation by protein phosphatase 2Cα. *J. Biol. Chem.* **278**, 14299–14305 (2003).
440. Ma, W. *et al.* Proapoptotic RYBP interacts with FANK1 and induces tumor cell apoptosis through the AP-1 signaling pathway. *Cell. Signal.* **28**, 779–787 (2016).
441. Zheng, L., Schickling, O., Peter, M. E. & Lenardo, M. J. The Death Effector Domain-associated Factor Plays Distinct Regulatory Roles in the Nucleus and Cytoplasm. *J. Biol. Chem.* **276**, 31945–31952 (2001).
442. Chen, D. *et al.* RYBP stabilizes p53 by modulating MDM2. *EMBO Rep.* **10**, 166–172 (2009).
443. Mamriev, D. & Larisch, S. Another one bites the dust; ARTS enables degradation of Bcl-2 by XIAP. *Mol. Cell. Oncol.* **5**, 1–2 (2018).
444. Issa, F. Targeted Apoptosis of Myofibroblasts with the BH3 Mimetic ABT-263 Reverses Established Fibrosis. *Transplantation* **102**, 341 (2018).
445. Larisch, S. *et al.* A novel mitochondrial septin-like protein, ARTS, mediates apoptosis dependent on its P-loop motif. *Nat. Cell Biol.* **2**, 915–921 (2000).

446. García-Fernández, M. *et al.* Sept4/ARTS is required for stem cell apoptosis and tumor suppression. *Genes Dev.* **24**, 2282–2293 (2010).
447. Elhasid, R. & Larisch, S. ARTS-based anticancer therapy: Taking aim at cancer stem cells. *Futur. Oncol.* **7**, 1185–1194 (2011).
448. Han, X. *et al.* Nonsense-mediated mRNA decay: A 'nonsense' pathway makes sense in stem cell biology. *Nucleic Acids Res.* **46**, 1038–1051 (2018).
449. Deng, Y. *et al.* Decreased SMG7 expression associates with lupus-risk variants and elevated antinuclear antibody production. *Ann. Rheum. Dis.* **75**, 2007–2013 (2016).
450. Wilkinson, M. F. The cycle of nonsense. *Mol. Cell* **12**, 1059–1061 (2003).
451. Ohnishi, T. *et al.* Phosphorylation of hUPF1 induces formation of mRNA surveillance complexes containing hSMG-5 and hSMG-7. *Mol. Cell* **12**, 1187–1200 (2003).
452. Hong, J. *et al.* Fibrillar type I collagen enhances the differentiation and proliferation of myofibroblasts by lowering α 2 β 1 integrin expression in cardiac fibrosis. *Biomed Res. Int.* **2017**, 14–16 (2017).
453. Guo, W., Shan, B., Klingsberg, R. C., Qin, X. & Lasky, J. A. Abrogation of TGF-β1-induced fibroblast-myofibroblast differentiation by histone deacetylase inhibition. *Am. J. Physiol. - Lung Cell. Mol. Physiol.* **297**, 864–870 (2009).
454. Samuel, G. H., Bujor, A. M., Nakerakanti, S. S., Hant, F. N. & Trojanowska, M. Autocrine transforming growth factor β signaling regulates extracellular signal-regulated kinase 1/2 phosphorylation via modulation of protein phosphatase 2A expression in scleroderma fibroblasts. *Fibrogenes. Tissue Repair* **3**, 25 (2010).
455. Higgins, S. P. *et al.* TGF-β1/p53 signaling in renal fibrogenesis. *Cell. Signal.* **43**, 1–10 (2018).
456. Conn, S. J. *et al.* The RNA binding protein quaking regulates formation of circRNAs. *Cell* **160**, 1125–1134 (2015).
457. Gupta, S. K. *et al.* Quaking inhibits doxorubicin-mediated cardiotoxicity through regulation of cardiac circular RNA expression. *Circ. Res.* **122**, 246–254 (2018).
458. Dong, C. *et al.* Myocyte enhancer factor 2C and its directly-interacting proteins: A review. *Prog. Biophys. Mol. Biol.* **126**, 22–30 (2017).
459. Abad, M. *et al.* Notch Inhibition Enhances Cardiac Reprogramming by Increasing MEF2C Transcriptional Activity. *Stem Cell Reports* **8**, 548–560 (2017).
460. Ieda, M. *et al.* Direct reprogramming of fibroblasts into functional cardiomyocytes by defined factors. *Cell* **142**, 375–386 (2010).
461. Hirai, H. *et al.* Direct reprogramming of fibroblasts into smooth muscle-like cells with defined transcription factors-brief report. *Arterioscler. Thromb. Vasc. Biol.* **38**, 2191–2197 (2018).
462. Di Giorgio, E., Gagliostro, E., Clocchiatti, A. & Brancolini, C. The Control Operated by the Cell Cycle Machinery on MEF2 Stability Contributes to the Downregulation of CDKN1A and Entry into S Phase. *Mol. Cell. Biol.* **35**, 1633–1647 (2015).
463. Kliem, V. *et al.* Mechanisms involved in the pathogenesis of tubulointerstitial

fibrosis in 5/6-nephrectomized rats. *Kidney International* vol. 49 666–678 (1996).
464. Liu, P. Y., Tian, Y. & Xu, S. Y. Mediated protective effect of electroacupuncture pretreatment by miR-214 on myocardial ischemia/reperfusion injury. *J. Geriatr. Cardiol.* **11**, 303–310 (2014).
465. Aurora, A. B. *et al.* MicroRNA-214 protects the mouse heart from ischemic injury by controlling Ca^{2+} overload and cell death. *J. Clin. Invest.* **122**, 1222–32 (2012).
466. Deng, L. *et al.* Regulation and Function of miR-214 in Pulmonary Arterial Hypertension. *Pulm. Circ.* **6**, 109–117 (2016).
467. Svíglerová, J. *et al.* Cardiovascular parameters in rat model of chronic renal failure induced by subtotal nephrectomy. *Physiol. Res.* **59 Suppl 1**, S81-8 (2010).
468. Y, Zhang, K. A., Zhang, Y. & Kompa, A. R. A practical guide to subtotal nephrectomy in the rat with subsequent methodology for assessing renal and cardiac function. *Nephrology (Carlton).* **19**, 552 (2014).
469. Prescott, M. J. & Lidster, K. Improving quality of science through better animal welfare: The NC3Rs strategy. *Lab Anim. (NY).* **46**, 152–156 (2017).
470. Ding, W., Wang, B., Zhang, M. & Gu, Y. Tempol, a superoxide dismutase-mimetic drug, ameliorates progression of renal disease in CKD mice. *Cell. Physiol. Biochem.* **36**, 2170–2182 (2015).
471. Scharenberg, M. A. *et al.* TGF-β-induced differentiation into myofibroblasts involves specific regulation of two MKL1 isoforms. *J. Cell Sci.* **127**, 1079–1091 (2014).
472. Rockey, D. C., Weymouth, N. & Shi, Z. Smooth muscle α actin (Acta2) and myofibroblast function during hepatic wound healing. *PLoS One* **8**, (2013).